UNIVERSITÉ DE STRASBOURG

ÉCOLE DOCTORALE DES SCIENCES CHIMIQUES

Laboratoire de Bioimagerie et Pathologies – UMR 7021

THÈSE présentée par :

Anne RUNSER

soutenue le : **11 juin 2020**

pour obtenir le grade de : **Docteur de l'Université de Strasbourg**

Discipline/ Spécialité : chimie-biologie

Nanoparticules de polymères fluorescentes, ultrapetites, ultrabrillantes et furtives pour le suivi intracellulaire et l'imagerie super-résolutive

THÈSE dirigée par :

M. KLYMCHENKO Andrey	Directeur de recherche CNRS, Université de Strasbourg
M. REISCH Andreas	Maitre de conférences, Université de Strasbourg

RAPPORTEURS :

Mme MEALLET-RENAULT Rachel	Professeur, Université Paris-Sud
M. PONS Thomas	Chargé de recherche CNRS, ESPCI

EXAMINATEURS:

Mme GAUFFRE Fabienne	Directeur de recherche, Institut des sciences chimiques de Rennes, Université de Rennes
M. ANTON Nicolas	Maitre de conférences, Université de Strasbourg

Remerciements

Je souhaite dans un premier temps remercier tout particulièrement mon directeur de thèse, Andrey Klymchenko, et mon co-directeur de thèse, Andreas Reisch, qui m'ont encadrée tout au long de cette thèse. Je leur suis extrêmement reconnaissante de m'avoir confié ce projet et de leur aide pour le mener à bien. Leur disponibilité, leurs brillantes intuitions, et leurs encouragements m'ont permis de surmonter de nombreux obstacles pendant ces trois années de doctorat.

Je tiens aussi à remercier Yves Mély de m'avoir accueillie dans les locaux du laboratoire.

J'exprime également toute ma gratitude aux membres du jury : à Mme Gauffre, directrice de recherche à l'université de Rennes, pour l'honneur qu'elle m'a fait en acceptant d'être présidente de mon jury ; à Mme Meallet-Renault, Professeure à l'université Paris-Sud, et M. Pons, chargé de recherche à l'ESPCI pour avoir accepté d'être rapporteurs de cette thèse ; à M. Anton, maitres de conférences à l'université de Strasbourg pour avoir accepté de faire partie du jury.

Je tiens à remercier tous mes collaborateurs en particulier Marcellina Cardoso Dos Santos, Loic Charbonnière, Aline Nonat, Denis Dujardin, Pascal Didier, Vitalii Rosiuk et Sylvie Egloff qui ont contribué à ce travail.

Merci également aux personnes du laboratoire, Oleksii Dukhno, Nicolas Humbert mais aussi à Romain Vauchelles de la plateforme PIQ, à Christine Ruhlmann et Corinne Crucifix, de la plateforme FRISBI, à Delphine Garnier et Oliva Estefania de la plateforme PACSI qui m'ont aidée à résoudre des problèmes d'ordre technique.

Je voudrais aussi remercier Marlyse Wernert et Ingrid Barthel pour leur redoutable efficacité concernant les papiers administratifs.

Un grand merci à mes collègues et amis qui m'ont aidée à décompresser : Sylvie Egloff, Sophie Bou, Mary Tanoo et Pauline Gosset pour les mémorables soirées « fromage » ; Mélanie Saenger et Kyong Fam pour avoir été mes partenaires de cross-training.

Enfin j’adresse mes remerciements à mes proches et amis pour les attentions et leurs encouragements avec un merci tout particulier à ma mère pour le travail de relecture.

Mes derniers remerciements vont à mon conjoint, Laurent Hakim, pour son amour et son soutien infaillible pendant cette thèse et dans tout ce que j’entreprends.

Table des matières

LISTE DES ABREVIATIONS 8

INTRODUCTION 11

PARTIE 1 : ETAT DE L'ART 14

1.1 Généralités sur la fluorescence 14

1.2 Caractéristiques de l'émission de fluorescence 16

1.2.1 Spectres d'absorption, d'émission et coefficient d'extinction molaire .. 16

1.2.2 Temps de vie 17

1.2.3 Rendement quantique 17

1.3 Marqueurs fluorescents 18

1.3.1 Molécules organiques fluorescentes 18

1.3.2 Protéines fluorescentes 19

1.3.3 Nanoparticules luminescentes 20

1.4 Nanoparticules de polymère encapsulant une grande quantité de fluorophores 27

1.4.1 Méthodes de préparations des NPs de polymères fluorescentes 28

1.4.2 Encapsulation des fluorophores 30

1.4.3 Propriétés photo-physiques des nanoparticules 31

1.4.4 Chimie de surface 33

1.5 Imagerie de fluorescence intracellulaire 35

1.5.1 Imagerie de fluorescence et ses limites 35

1.5.2 Imagerie de molécules uniques 36

1.5.3 Imagerie super-résolutive 37

1.5.4 Les contraintes de l'imagerie intracellulaire 38

1.5.5 Les sondes utilisées pour l'imagerie intracellulaire 39

PARTIE 2 : MATERIEL ET METHODES 41

2.1 Matériel 41

2.2 Synthèses 42

2.2.1 Synthèse des polymères 42

2.2.2 Synthèse de l'espaceur boc-NH-L-SO_3H-N_3 45

2.2.3 Modification du polymère PMMA-ZI 10%-PFMA 1% 46

2.3 Préparation des nanoparticules 47

2.4 Fonctionnalisation des NPs-N_3 avec DBCO-sulfoCy5 47
2.5 Caractérisation des nanoparticules 47
2.5.1 Diffusion dynamique de la lumière 47
2.5.2 Microscopie électronique à transmission 48
2.5.3 Spectroscopie de corrélation de fluorescence..... 49
2.5.4 UV/vis, fluorescence 51
2.5.5 Microscopie TIRF 51
2.6 Microinjection et microscopie cellulaire 53

PARTIE 3 : CONTROLE DE LA TAILLE DES NANOPARTICULES 54

3.1 Développement de nanoparticules de taille contrôlée 54
Article 1 : Charge-Controlled Nanoprecipitation as a Modular Approach to Ultrasmall Polymer Nanocarriers: Making Bright and Stable Nanoparticles. 67
3.2 Application pour la biologie 88

PARTIE 4 : OPTIMISATION DE LA LUMINESCENCE POUR L'IMAGERIE INTRACELLULAIRE 92

4.1 Nanoparticules de lanthanides 92
Article 4 : Lanthanide-Complex-Loaded Polymer Nanoparticles for Background-Free Single-Particle and Live-Cell Imaging. 95
4.2 Fluorescence et clignotement des nanoparticules à base de rhodamine . 115

PARTIE 5 : INTERACTIONS DES NANOPARTICULES 124

5.1 Nanoparticules zwittérioniques 124
Article 5 : Zwitterionic Stealth Dye-Loaded Polymer Nanoparticles for Intracellular Imaging. 127
5.2 Fonctionnalisation des nanoparticules 146

CONCLUSION ET PERSPECTIVES 151

RÉFÉRENCES 154

ANNEXES 172

Article 2 : Protein-Sized Dye-Loaded Polymer Nanoparticles for Free Particle Diffusion in Cytosol. 173
Article 3 : Controlling Size and Fluorescence of Dye-Loaded Polymer Nanoparticles through Polymer Design 192

Liste des abréviations

ACQ	fluorescence causée par agrégation
AIBN	azobis isobutyronitrile
AIE	émission induite par agrégation
AMA	méthacrylate de 2-amino-2-oxoéthyle
BG	O6-benzylguanine
BMA	méthacrylate de butyle
BODIPY	boron-dipyrrométhène
BzMA	méthacrylate de benzyle
CCM	chromatographie sur couche mince
CMC	concentration micellaire critique
DBCO	dibenzocyclooctyne-amine
DCC	N,N'-dicyclohexylcarbodiimide
DCM	dichlorométhane
DIPEA	N,N-Diisopropyléthylamine
DLS	diffusion dynamique de la lumière
DMAP	4-diméthylaminopyridine
DMEM	« Dulbecco’s modified eagle medium »
DMF	diméthylformamide
DMSO	diméthylsulfoxide
DSPE	1,2-distéaroyl-sn-glycéro-3-phosphoéthanolamine
EMA	méthacrylate d’éthyle
F5-TPB	tétrakis(pentafluorophényl)borate
FBS	sérum de veau fœtal
FCS	spectroscopie de corrélation de fluorescence
FITC	isothiocyanate de fluorescéine
FRET	transfert d'énergie par résonance de Förster
GFP	« green fluorescent protein »
HEMA	méthacrylate d’hydroxyéthyle
LR	« lumogen red »
MAA	acide méthacrylique

Liste des abréviations

MAMA	méthacrylate de 2-acétamidoéthyle
MMA	méthacrylate de méthyle
MSD	déplacement quadratique moyen
NA	ouverture numérique
NHS	N-hydroxysuccinimide
NP	nanoparticule
PALM	microscopie par localisation activée
PBS	tampon phosphate salin
PCL	poly(caprolactone)
PEG	poly(éthylène glycol)
PEI	poly(éthylèneimine)
PFMA	méthacrylate de pentafluorophényle
PLGA	poly(D,L-lactide-co-glycolide)
PMA	méthacrylate de propyle
PMMA	poly(méthacrylate de méthyle)
QD	quantum dot
QY	rendement quantique
R18	octadécylrhodamine B
RMN	résonance magnétique nucléaire
ROI	région d’intérêt
SEC	chromatographie d’exclusion stérique
SMA	méthacrylate de sulfopropyle
STED	microscopie de déplétion par émission stimulée
STORM	microscopie de reconstruction optique stochastique
T80	tween 80
TEM	microscopie électronique à transmission
TFA	acide trifluoroacétique
TIRF	microscopie de fluorescence par réflexion totale interne
TMR	6-carboxy-tétraméthylrhodamine
UV-vis	ultraviolet-visible
ZI	zwittérion

Introduction

L'imagerie de molécules biologiques dans les cellules vivantes par microscopie de fluorescence promet d'apporter de nouvelles informations sur les processus moléculaires, comme par exemple des paramètres de cinétiques et de dynamiques qui ne peuvent être obtenus par des méthodes d'ensemble de microscopie ou biochimiques.[1,2] En microscopie de fluorescence, le suivi de molécules repose sur la précision de localisation de l'émetteur fluorescent. Celle-ci dépend directement du nombre de photons récoltés lors de l'acquisition.[3] Plus l'émetteur est brillant, plus le nombre de photons récoltés est élevé pour une intensité donnée. Cela se traduit par un meilleur rapport signal/bruit. Mais le nombre de photons émis et récoltés est également lié à l'intensité lumineuse qui excite l'émetteur. Enfin plus le temps d'acquisition est long, plus on peut localiser précisément l'émetteur. Malheureusement des puissances d'excitation élevées et des temps d'acquisition trop longs sont responsables de phototoxicité sur les cellules accompagnée d'une dégradation de la sonde fluorescente. De plus si la molécule à suivre bouge trop rapidement, des temps d'acquisition trop longs ne permettront pas de localiser l'émetteur dans l'espace. Augmenter la brillance de l'émetteur permet cependant de le localiser avec précision à la fois dans le temps et l'espace sans interférer avec les processus cellulaires. De surcroit, il est aujourd'hui également possible de résoudre deux émetteurs à une distance inférieure aux limites de diffraction de la lumière par microscopie de reconstruction optique stochastique directe (dSTORM)[4] ou microscopie par localisation activée (PALM)[5] mais uniquement si l'émetteur est photocommutable ou photoactivable.

La limite de brillance des fluorophores conventionnels (fluorophores organiques et protéines fluorescentes) peut être surmontée par l'utilisation de NPs luminescentes. Aujourd'hui les NPs de semiconducteurs (QDs)[6] et les NPs de silice[7] dominent le domaine des NPs luminescentes. Parmi ces dernières, les NPs de polymères fluorescentes ont l'avantage d'être biocompatibles et d'avoir une plus grande flexibilité. Ces NPs peuvent donc être une excellente alternative aux NPs inorganiques. Notre groupe a notamment développé des NPs de polymères fluorescentes par nanoprécipitation.[8] Ces NPs, constituée de polymères biocompatibles, peuvent facilement être chargées avec de grandes concentrations en fluorophores organiques.

Dernièrement, les problèmes d'auto-inhibition de fluorescence généralement rencontrés dans ces systèmes ont été résolus.[8,9] Les NPs de polymères fluorescentes peuvent donc égaler voir surpasser la brillance des QDs. Il a également été démontré que ces NPs contenant de grande quantité de fluorophores conduisaient au clignotement de la particule entière résultant d'une forte coopération entre les fluorophores. Cette propriété les rend tout à fait appropriés à l'imagerie super-résolutive par dSTORM. Outre les propriétés photophysiques décrites ci-dessus, l'utilisation de NPs fluorescentes demandent un contrôle de la taille ainsi que des interactions spécifiques et non spécifiques. Le cytoplasme est un espace très encombré, composé de nombreuses macromolécules, d'un réseau dense formé par le cytosquelette et de divers organites cellulaires.[10,11] Les NPs doivent être suffisamment petites pour se frayer un chemin dans cet amas de molécules sans pour autant perturber la trajectoire des biomolécules d'intérêts.[12] Pour cela, leur taille doit être du même ordre de grandeur que les biomolécules destinées à être marquées. Cependant la taille des NPs obtenues par nanoprécipitation est entre 40 et 250 nm.[13] En même temps, les surfaces des particules influencent fortement leur comportement dans les systèmes biologiques au niveau extra- et intracellulaire.[12,14] L'adsorption non spécifique de protéines à la surface des particules va conduire à une perte de contrôle de leur comportement et masquer les éventuels ligands attachés à la surface de la particule. La stratégie la plus utilisée est l'ajout de polyéthylène glycol (PEG) en guise de traitement de surface.[15] Mais le risque de la PEGylation est dans un premier temps, d'augmenter significativement le diamètre hydrodynamique de la particule et dans un deuxième temps, d'accroitre la distance entre l'émetteur et la molécule marquée. Une alternative à la PEGylation est l'utilisation de groupements zwittérioniques.[16] Ces groupements ont l'avantage de former une fine couche avec une efficacité contre l'adsorption de protéines comparable à la PEGylation.

L'objectif de ce travail consiste à développer des NPs de polymères fluorescentes en tant que sondes pour l'imagerie intracellulaire. Le développement de ces NPs peut se résumer en trois parties bien distinctes. (i) Le premier objectif est d'optimiser la fluorescence des NPs pour augmenter la vitesse et la précision de localisation. La combinaison de la brillance avec un contrôle du clignotement des NPs augmenterait également la résolution. (ii) Ensuite les NPs doivent être rendues complètement furtives dans le cytoplasme. Pour cela deux aspects doivent être considérés. L'un est

de diminuer au maximum le diamètre des NPs tout en conservant une efficacité d'encapsulation des fluorophores. Et l'autre consiste à adapter la surface des NPs pour éviter les interactions non spécifiques avec l'environnement intracellulaire. (iii) Enfin ces NPs ultrapetites, ultrabrillantes et non-interactives devront être fonctionnalisées pour marquer des biomolécules intracellulaires.

Dans un premier temps, nous verrons les principes généraux de fluorescence ainsi que l'état de l'art sur les NPs fluorescentes en particulier les NPs de polymères encapsulant des grandes quantités de fluorophores et l'imagerie intracellulaire. Ensuite la seconde partie traitera du contrôle de la taille des NPs par ajout de fractions de groupements chargés sur les polymères ou en variant la composition du polymère. Nous verrons également quelques exemples du comportement des NPs en fonction de leur taille dans le cytosol après microinjection et électroporation. Ensuite, nous nous intéresserons aux propriétés optiques de ces NPs. Deux types de NPs ont été optimisées en termes de brillance : les NPs chargées de complexes de lanthanides et les NPs chargées de rhodamine. Enfin dans une dernière partie, nous proposerons une nouvelle approche de traitement de surface à base de groupements zwittérioniques pour réduire les interactions non spécifiques dans le cytoplasme. Nous verrons également le comportement des NPs résultantes dans le cytosol après microinjection ainsi que la stratégie de fonctionnalisation choisie pour les NPs afin de marquer des biomolécules intracellulaires telles que les dynéines.

Partie 1 : Etat de l’art

1.1 Généralités sur la fluorescence

La lumière est probablement l’outil le plus versatile pour observer un objet. Nous l’employons nous-mêmes constamment et tous les jours pour fournir une image à notre cerveau. Son caractère non-invasif, capable d’interagir de différentes manières avec la matière en fait une radiation primordiale en imagerie. Par définition, la lumière est un ensemble d’ondes électromagnétiques avec des λ de 10^{-3} à 10^{-8} m.[17] Ces fluctuations électriques et magnétiques sont capables de se propager aussi bien dans le vide que dans la matière. L’œil humain est sensible aux ondes comprises entre 400 et 800 nm qui constituent le spectre de la lumière visible. La lumière regroupe également, les rayonnements infra-rouges (de 800 nm à 1 mm) et les rayonnements ultra-violets (de 100 à 400 nm).

En mécanique quantique, la lumière est décrite selon le principe fondamental de la dualité onde-particule. Cela signifie qu’elle se comporte à la fois comme une onde électromagnétique et comme une particule transportant un quantum d’énergie, appelée, photon. Ainsi un photon de fréquence ν a une énergie égale à $h\nu$ avec h la constante de Planck de magnitude $6{,}63 \times 10^{-34}$ Js.[17] En tant que particule, la lumière est alors capable d’interagir avec la matière par échange d’énergie. L’absorption d’un photon ne peut se faire que si son énergie est égale à la différence d’énergie entre l’état fondamental et l’un des états excités de la molécule. L’énergie est alors absorbée par la molécule qui passe dans un état électroniquement excité. Les molécules restituent l’énergie perçue sous divers processus de désexcitation. Le retour à l’état fondamental, peut se faire par émission de photons après un transfert de charge intramoléculaire ou un changement de conformation. Les interactions avec d’autres molécules peuvent aussi se produire telles qu’un transfert d’électron ou de proton ou un transfert d’énergie.[18]

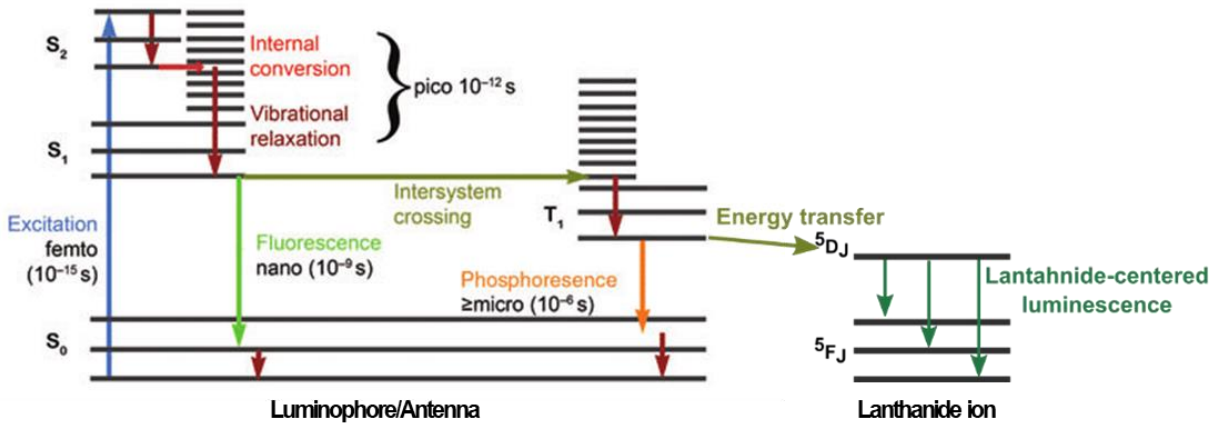

Figure 1. Diagramme de Jablonski. Reproduit à partir des références [19,20].

Parmi les différents mécanismes de désactivation, le phénomène de luminescence résulte de l'émission de photons par la matière. La luminescence distingue la fluorescence de la phosphorescence par des mécanismes de restitutions des photons différents. Le diagramme de Jablonski (Figure 1) schématise l'ensemble des processus d'excitation et de désactivation. Le niveau d'énergie électronique fondamental singlet, ainsi que les premier et second niveaux d'énergie sont désignés respectivement par S_0, S_1 et S_2. Les niveaux d'énergie intermédiaires correspondent aux niveaux vibrationnels. Lorsqu'une molécule rencontre un photon ayant une énergie correspondante à une transition entre ses niveaux d'énergie, la molécule absorbe l'énergie du photon et passe du niveau électronique fondamental S_0 à un état électronique de plus haute énergie, S_1 ou S_2. La molécule promue perd ensuite une partie de son énergie sous forme non radiative pour atteindre le niveau vibrationnel le plus bas de S_1. Lorsque celle-ci est permise, la transition $S_1 \rightarrow S_0$ s'accompagne de l'émission d'un photon de fluorescence.

Si cette transition n'est pas permise, c'est-à-dire qu'il y a une modification du spin de départ de l'électron, le retour à l'état fondamental est plus lent et s'accompagne tout d'abord d'un retournement de spin de l'électron qui passe par l'état triplet T_1 avant de pouvoir revenir à l'état fondamental par émission d'un photon de phosphorescence. Dans certains cas, le mécanisme est un peu plus complexe. Pour les ions de lanthanides trivalents, la luminescence s'effectue par des transitions des électrons de l'orbitale 4*f*. Habituellement ces transitions sont dites interdites (selon la règle de Laporte) et l'excitation directe est donc très peu efficace. L'excitation s'effectue alors

à travers un transfert d'énergie d'un ligand/chélateur au lanthanide, appelé effet d'antenne. Une fois le ligand excité, la conversion intersystème est suivie d'un transfert d'énergie intramoléculaire qui conduit à l'excitation de l'ion lanthanide. Le retour à l'état fondamental s'effectue par une émission de luminescence avec des temps de vie extrêmement longs de l'ordre de la micro- ou milliseconde.[20]

1.2 Caractéristiques de l'émission de fluorescence

1.2.1 Spectres d'absorption, d'émission et coefficient d'extinction molaire

Le diagramme de Jablonski révèle que l'énergie d'émission de fluorescence est systématiquement plus faible que l'énergie d'excitation. L'électron excité perd en effet rapidement une partie de l'énergie absorbée par relaxation vibrationnelle pour atteindre le niveau vibrationnel le plus bas de S_1. Par conséquent, la longueur d'onde d'absorption est donc toujours plus courte que la longueur d'onde d'émission. Cette différence entre les longueurs d'onde d'excitation et d'émission est appelé déplacement de Stokes. En filtrant la lumière incidente sans bloquer l'émission de fluorescence, il est possible de discriminer la lumière d'excitation de la lumière d'émission et donc d'observer uniquement l'objet fluorescent. Cela fait de la fluorescence une méthode d'imagerie extrêmement sensible avec un contraste bien supérieur aux autres techniques d'imagerie optique.

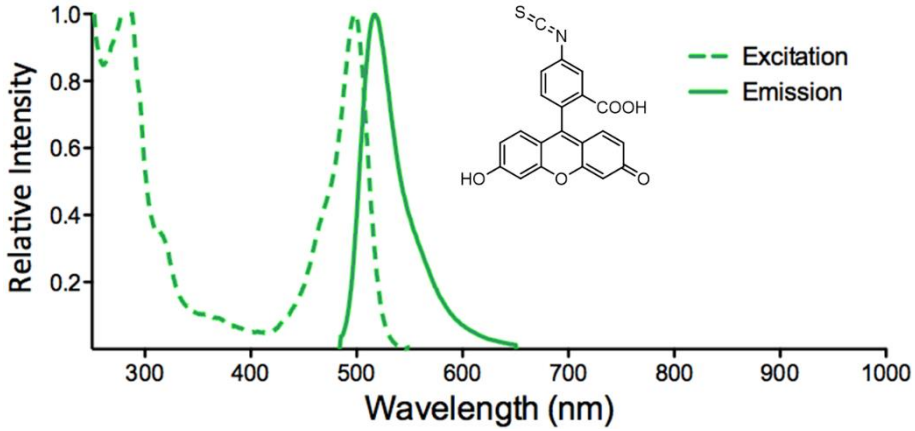

Figure 2. Spectres d'absorption et d'émission de FITC. Reproduit à partir de la référence [21].

Le coefficient d'extinction molaire, ε, représente la probabilité qu'un fluorophore absorbe un photon. Il est exprimé en $M^{-1}cm^{-1}$ et dépend de la longueur d'onde. On parle aussi quelques fois de section d'absorption efficace, σ, exprimée en m^2.

1.2.2 Temps de vie

En considérant, k_r comme la constante cinétique de désexcitation par émission de fluorescence et k_{nr}, la constante cinétique de désexcitation non radiative, le temps de vie d'un fluorophore est :

$$\tau = \frac{1}{k_r + k_{nr}}$$

Il correspond au temps caractéristique pendant lequel le fluorophore reste à l'état excité avant de revenir à l'état fondamental en produisant un photon de fluorescence. Le temps de vie va définir la fenêtre temporelle d'observation pendant laquelle le fluorophore peut interagir ou diffuser et donc fournir des informations concernant des processus d'une durée similaire.[18]

1.2.3 Rendement quantique

Le rendement quantique, Φ_f, est le rapport du nombre de photons émis sur le nombre de photons absorbés par un fluorophore. Il représente la fraction de molécules excitées qui retourne à l'état fondamental en émettant un photon de fluorescence et est donné par l'équation suivante :

$$\Phi_f = \frac{nombre\ de\ photons\ émis}{nombre\ de\ photons\ absorbés} = \frac{k_r}{k_r + k_{nr}} = k_r\tau$$

Le rendement quantique et le coefficient d'extinction molaire sont étroitement liés à la brillance du fluorophore. La brillance caractérise le nombre de photons émis en fluorescence par unité de temps pour une intensité de lumière donnée. Cette dernière est donnée par la formule suivante :

$$B = \varepsilon \times \Phi_f$$

Ce sont donc les fluorophores ayant les plus grands rendements quantiques et coefficients d'extinction molaire qui sont les plus brillants.

1.3 Marqueurs fluorescents

1.3.1 Molécules organiques fluorescentes

Les fluorophores sont généralement des molécules de structure plane composées de plusieurs noyaux aromatiques conjugués. La figure 3 donne une vue d'ensemble des principales classes de molécules fluorescentes utilisées à ce jour en fluorescence. Parmi elles, les plus importantes et les plus connues sont les acides aminés fluorescents, les xanthènes (fluorescéines et rhodamines), les BODIPYs, les cyanines et les coumarines. Beaucoup d'entre-eux ont été modifiés chimiquement pour améliorer leurs paramètres physico-chimiques tels que la solubilité, la photostabilité ou la brillance. Cependant les fluorophores organiques ont un coefficient d'extinction molaire qui est généralement compris entre 25 000 et 250 000 $M^{-1}cm^{-1}$ et leur rendement quantique est modéré à élevé (30 à 90 %).[22–24] Ainsi, les plus performants atteignent des valeurs de l'ordre de $2x10^4$ à $9x10^4$ $M^{-1}cm^{-1}$ en brillance.[22,23]

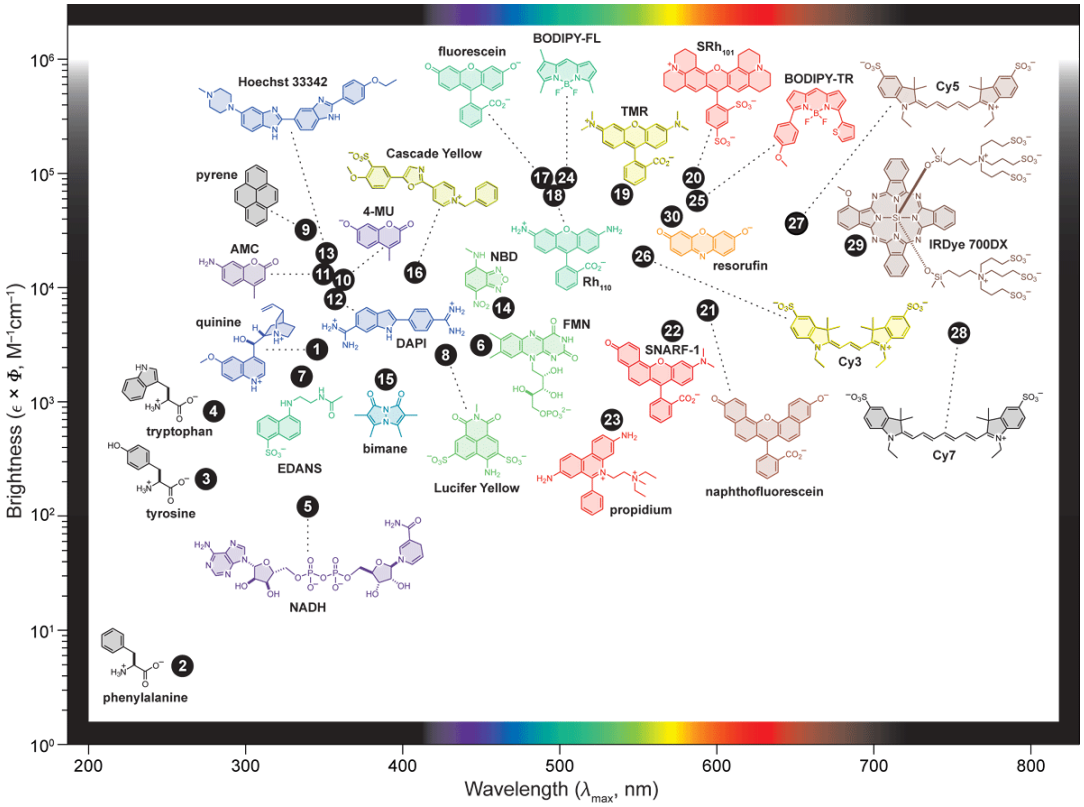

Figure 3. Graphique représentant la brillance des principales classes de fluorophores organiques en fonction de la longueur d'onde du maximum d'absorption. La couleur de la structure chimique indique la longueur du maximum d'émission. Reproduit à partir de la référence [22].

Compte tenu de leur petite taille et de la variété existante, leurs applications sont nombreuses allant du marquage de biomolécules,[25] au suivi des réactions enzymatiques,[26] aux indicateurs de pH[27] ou d'ions[28] en passant par la coloration des cellules.[29]

1.3.2 Protéines fluorescentes

A l'origine, la GFP (« green fluorescent protein ») est une protéine naturelle que l'on retrouve dans la méduse *Aequorea Victoria*.[30] L'ingénierie des protéines recombinantes a permis la création de milliers de GFP mutants dont la diversité, aujourd'hui, recouvre tout le spectre visible (Figure 4). Les modifications concernent leur spectre d'absorption et d'émission,[31–33] leur brillance,[34] leur photostabilité,[31] certaines sont mêmes photoconvertibles[35] ou photoactivables.[36]

L'application première des protéines fluorescentes est le marquage de protéines. La séquence codante pour la protéine fluorescente peut être fusionnée au gène d'une protéine d'intérêt. L'expression de la protéine d'intérêt peut alors être suivie en temps réel, on obtient des informations sur son expression, sa localisation, ses translocations et interactions jusqu'à sa dégradation.[37]

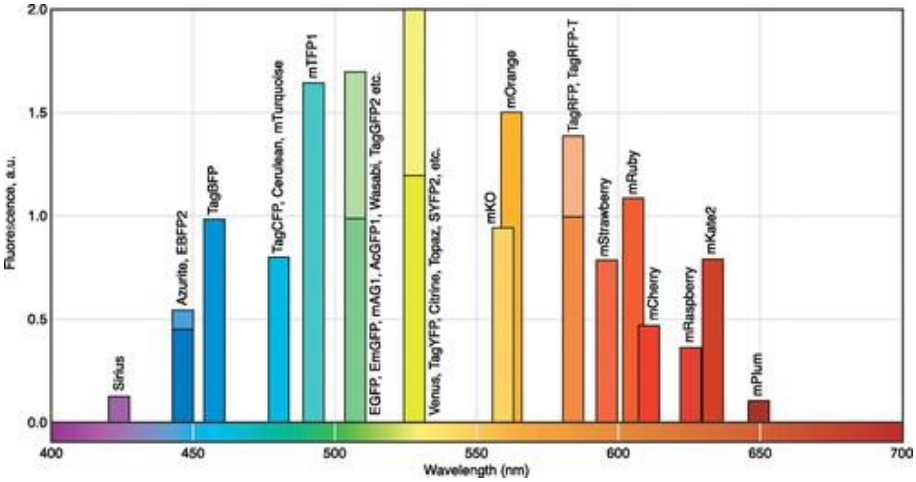

Figure 4. Diversité spectrale des protéines fluorescentes monomériques. Les colonnes montrent les positions des maxima d'émission et de leur brillance relative à celle de l'EGFP. Reproduit à partir de la référence [37].

Récemment, d'autres classes de protéines fluorescentes génériques sont apparues utilisant des protéines complexant des fluorogènes naturels tels que les flavines[38–40] ou les bilirubines.[41] Ces protéines ont l'avantage d'être plus petites que la GFP et peuvent être utilisées en conditions anaérobies, contrairement à la GFP. Certaines classes de protéines fluorescentes issues de photochromes bactériens et complexant la biliverdine, ont également été ingéniées pour émettre dans le proche infrarouge ouvrant l'accès à l'imagerie *in vivo*.[42] Malgré tous ces efforts dans le développement de protéines fluorescentes, leur coefficient d'extinction molaire est très souvent inférieur à $5x10^4$ $M^{-1}cm^{-1}$, limitant fortement leur brillance, en plus d'une faible photostabilité.[37,42]

1.3.3 Nanoparticules luminescentes

Compte tenu de la diversité des NPs luminescentes, nous nous limiterons aux NPs connues pour leur grande brillance et leur utilisation pour le suivi intracellulaire ou l'imagerie super-résolutive.

Quantum dots

Depuis la fin des années 90, les QDs ont été très largement utilisés en tant que marqueurs luminescents. Les QDs ont une taille variant de 1-6 nm.[24] Les QDs généralement utilisés pour la bioimagerie, sont constitués de semi-conducteurs de classe II/VI ou III/V tels que CdSe, CdTe, InP ou InGaP. Leurs propriétés optiques vont dépendre des semi-conducteurs utilisés, de leur taille, de leur dispersité et de la chimie de surface. Leur spectre d'absorption est généralement assez large alors que le spectre d'émission est plutôt étroit et symétrique. Leurs caractéristiques spectrales permettent ainsi une excellente séparation de la lumière d'excitation de la lumière d'émission et une détection de plusieurs QDs émettant à différentes longueur d'onde avec une seule source d'excitation. La largeur du pic d'émission dépend en grande partie de la distribution de taille des QDs. En effet, la taille du cœur des QDs détermine les longueurs d'ondes d'absorption et d'émission (Figure 5). Généralement, leur coefficient d'extinction varie de 100,000–1,000,000 M^{-1} cm^{-1}.[24] Cela s'accompagne dans la plupart des cas de rendements quantiques assez élevés entre 20 et 60 % qui donnent des brillances entre $6x10^4$-$6x10^5$ $M^{-1}cm^{-1}$.[23,24] Le cœur de semi-conducteur peut être entouré d'une enveloppe en ZnS pour les QDs de CdSe, qui va permettre

d'optimiser le rendement quantique et la stabilité des QDs.[43] Il en résulte que les QDs possèdent une brillance et une photostabilité bien supérieures comparées aux fluorophores organiques ou protéines fluorescentes, accompagnées de temps de vie plus longs. Cependant des défauts à la surface du crystal conduisent à un signal luminescent intermittent visible lorsqu'on observe les NPs de manière individuelle.[44] Ce phénomène diminue le rendement quantique et peut nuire à l'observation en microscopie de luminescence conventionnelle.[45] Mais cette propriété à clignoter peut être utilisée, si maitrisée, pour l'imagerie super-résolutive.[46,47] Les QDs ne peuvent pas être utilisés tels quels dans les milieux biologiques car leur solubilité dans l'eau est très faible. Il est donc nécessaire de modifier la surface des QDs pour assurer leur dispersion dans les milieux aqueux. Cela peut être effectué par un revêtement à base de ligands chargés,[48] de polymères amphiphiles,[49] de polyélectrolytes,[50] d'une couche supplémentaire inorganique de silice[51] ou de phospholipides.[52] Cela a aussi conduit au développement de diverses stratégies de fonctionnalisation des particules.[53–55] Malgré ces efforts, la chimie de surface des QDs reste cependant compliquée car toute modification à la surface de la particule risque d'affecter les propriétés optiques des QDs.[56] A cela, s'ajoute également la toxicité élevée des métaux lourds constituants les QDs qui est un réel frein dans leur utilisation en imagerie du vivant.[57]

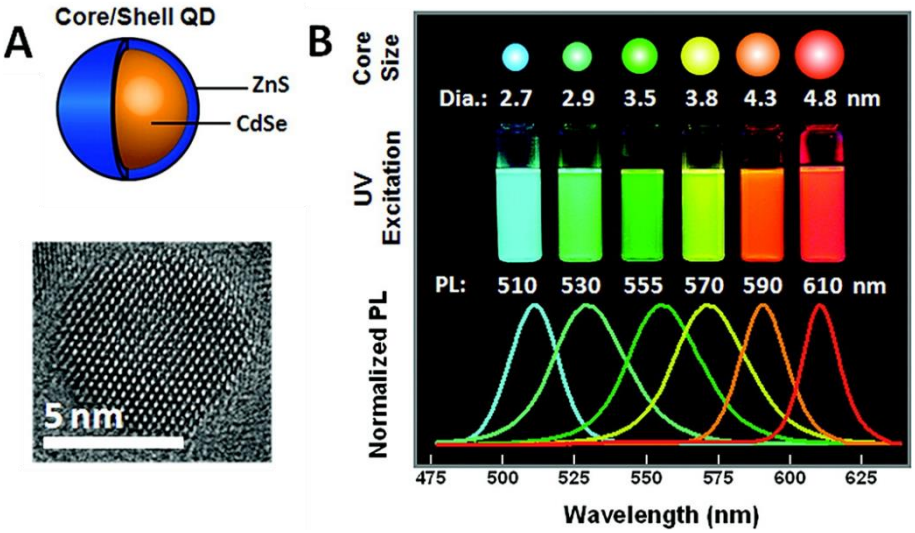

Figure 5. (A) Schéma et image TEM d'un QD composé du noyau et d'une enveloppe. (B) Relation entre la taille et la longueur d'onde d'émission des QDs. Le spectre d'émission se déplace vers les plus grandes longueurs d'onde lorsque le diamètre des QDs augmente. Reproduit à partir la référence [58].

Nanoparticules d’or

Si les QDs dominent le marché des particules fluorescentes, d’autres types de particules luminescentes ont été développées ces dernières années. Parmi elles, les particules d’or sont une alternative aux QDs. Les NPs d’or sont reconnues pour leur propriétés de résonance plasmonique de surface résultant de l’interaction avec la lumière.[59] En plus de cela, les NPs d’or absorbent fortement dans la lumière visible[60] et peuvent être utilisées en imageries de luminescence à deux photons dans le proche infrarouge.[61] Les NPs d’or ont l’avantage d’avoir une bonne biocompatibilité ainsi que d’être faciles à synthétiser et à fonctionnaliser.[62] Elles possèdent des sections efficaces élevées et une excellente photostabilité mais des rendements quantiques très faibles.[62,63] Leurs propriétés de luminescence sont également difficiles à maitriser car elles dépendent de paramètres tels que la taille des particules[62,64] ou la nature de l’habillage.[64,65] La photocommutation des NPs d’or est notamment possible grâce à un revêtement de surface avec des molécules photocomutables ou photoactivables.[66]

Nanoparticules de carbone

Les particules de carbone, appelées « carbon dots », sont de diamètre inférieur à 10 nm. Elles sont une bonne alternative aux QDs car elles sont moins toxiques, plus économiques et ont une meilleure biocompatibilité.[67,68] Tout comme pour les particules d’or et les quantum dots, leur section d’absorption efficace est élevée aussi bien dans le visible par excitation à un photon que dans le proche infrarouge par excitation à deux photons.[61] Les particules de carbone présentent des rendements quantiques généralement compris entre 5 et 40% ainsi qu’une bonne photostabilité.[69] Ces NPs montrent une émission de luminescence sans clignotement. Mais elles peuvent être photocommutables dans certains cas particuliers.[67] Leur surface est hautement sensible à l’environnement et les propriétés optiques des particules de carbone peuvent être affectées par des contaminants même à faibles doses.[69] C’est pourquoi les particules de carbones sont souvent passivées par des PEG afin d’obtenir des intensités de fluorescence suffisamment élevées.[70]

Nanoparticules à conversion ascendante de photon

Les NPs à conversion ascendante de photon ou « up conversion » sont capables d'une émission de luminescence appelée « anti-Stockes » grâce à un processus optique non linéaire. Cela signifie que le photon de luminescence est émis à une longueur d'onde plus courte que la longueur d'onde d'excitation contrairement aux fluorophores conventionnels.[71] Généralement ce phénomène nécessite un transfert d'énergie entre un sensibilisateur et un émetteur. Le sensibilisateur est excité après absorption d'un photon généralement dans le proche infrarouge. Il a la possibilité de transférer son énergie d'excitation à l'émetteur qui lui peut absorber un ou plusieurs photons et ainsi accumuler l'énergie d'excitation. Il émet ensuite un photon de luminescence de plus faible longueur d'onde. Ces NPs sont généralement composées d'une matrice cristalline, typiquement $NaYF_4$, dopée d'ions lanthanides trivalents dont 20 % de sensibilisateur tel que Yb^{3+} et 2% d'émetteur comme Er^{3+}.[72] La taille joue un rôle important dans la brillance de ces NPs à conversion ascendante de photon. Il a notamment été démontré que l'excitation du réseau cristallin est inhibée par des défauts de surface. Ainsi les particules présentant le plus de défauts de surface, généralement les plus petites, vont présenter une intensité d'émission réduite.[73]

Nanoparticules de complexes de lanthanides

Les complexes de lanthanides peuvent être encapsulés dans des NPs de polymère,[74,75] de silice[76] ou simplement enrobés de surfactant.[77] Généralement ce sont des complexes d'europium[74,77,78] ou de terbium trivalents.[76,79] Le principal inconvénient de ces complexes est leur faible coefficient d'extinction venant des ions lanthanides. C'est pourquoi ils sont excités à travers un ligand qui contient un groupement « antenne » qui va absorber l'énergie d'excitation avant de le transférer à l'ion lanthanide qui émet de la luminescence.[80] Concernant leurs propriétés spectrales, les complexes de lanthanides ont des pics d'émission très fins (<10 nm), des déplacements de Stokes larges (>150 nm) ainsi qu'une excellente photostabilité accompagnés de temps de vie de photoluminescence extrêmement longs (plusieurs dizaines de µs à quelques ms).[76,79] Ces temps de vie très longs sont particulièrement adaptés à l'imagerie à déclenchement périodique avec la possibilité de supprimer l'autofluorescence des milieux biologiques.[80]

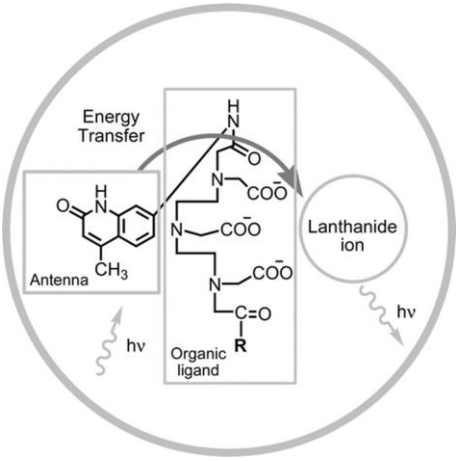

Figure 6. Les ions de lanthanides sont excités par l'effet d'antenne. Reproduit à partir de la référence [76].

Les NPs de complexes de lanthanides sont souvent fonctionnalisées avec de la streptavidine[74,77,79], quelques fois avec des anticorps[81] ou des oligonnucléotides.[76] Elles sont notamment très utilisées dans les tests immunochimiques où elles peuvent atteindre des sensibilités 100 fois supérieures aux fluorophores organiques en utilisant une détection à déclenchement périodique.[76]

Nanoparticules de silice dopées avec des fluorophores

Les particules de silice sont inertes et transparentes dans le visible. De quelques dizaines à des milliers de molécules organiques et ou nanoobjets inorganiques peuvent y être incorporées.[82] Suivant la méthode de synthèse des NPs, les fluorophores peuvent être simplement piègés dans la NPs[83] ou attachés de manière covalente.[84] La quantité de fluorophores organiques incorporée est cependant limitée du fait du caractère hydrophobe de ces derniers alors que la silice est plutôt hydrophile. Cela pose également problème au niveau des possibles fuites des fluorophores qui diminuent l'intensité de fluorescence mais en même temps augmente le bruit de fond en imagerie.[85] Malgré cela, l'encapsulation de plusieurs fluorophores dans les particules de silice augmente considérablement le coefficient d'extinction résultant, qui correspond à la somme des coefficients d'extinction individuels des fluorophores encapsulés. Il en résulte que ces NPs atteignent des brillances plus élévées que les fluorophores organiques seuls. Néanmoins, à concentrations trop élevées en fluorophores, des phénomènes d'auto inhibition de fluorescence induit par agrégation des fluorophores apparaissent, diminuant le rendement quantique des

NPs.[86] La matrice de silice protège efficacement les fluorophores de l'environnement extérieur minimisant leur photoblanchiment. Ceci permet de les illuminer à des intensités lumineuses élevées et des excitations prolongées. En outre, la surface de silice rend ces NPs chimiquement inertes et physiquement stables. Elle peut être modifiée facilement par l'introduction de divers groupements fonctionnels tels que des groupements PEG, hydroxyle, carboxyle, phosphonate ou amine.[85] En terme de toxicité, les NPs de silice montrent une excellente biocompatibilité. A cela s'ajoute leur capacité à encapsuler, en plus de fluorophores, d'autres matériels comme des principes actifs ou des agents de contrastes magnétiques ou radioactifs.[87,88] C'est pourquoi, les NPs de silice ont un grand potentiel en imagerie multimodale ou en diagnostic et thérapie combinés pour des pathologies telles que les cancers.[89]

NPs de polymères conjugués

Les particules de polymères conjugués sont à base de polymères π-conjugués fluorescents. Elles peuvent atteindre des tailles très petites ~ 4 nm. On obtient des sections d'absorption efficaces typiquement entre 10^{-15}-10^{-14} cm^2, soit trois à quatre ordres de grandeurs supérieurs aux fluorophores conventionnels et un ordre de grandeur plus grand que les particules inorganiques.[82,90] Contrairement aux nanoparticules de silice, il y a peu de phénomènes d'inhibition de fluorescence induit par agrégation. Néanmoins leur rendement quantique est généralement modéré entre 1 et 20 %.[91] Mais dans certains cas il peut atteindre 70%. [92,93] Ces NPs atteignent donc des brillances très élevées entre 10^4 et 10^8 $M^{-1}cm^{-1}$.[94]

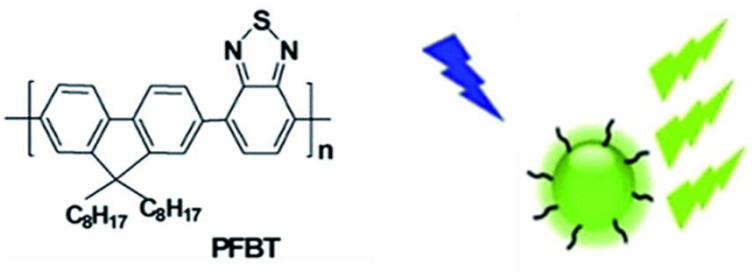

Figure 7. Nanoparticule de polymères conjugués PFBT. Reproduit à partir de la référence [95].

Lorsque les polymères conjugués sont dispersés dans une matrice polymérique inerte, les particules résultantes montrent un signal fluorescent intermittent.[96,97] Les NPs de polymères conjugués sont pourvues d'une photostabilité trois fois supérieure

comparée aux fluorophores conventionnels. On peut également facilement encapsuler des fluorophores organiques à l’intérieur des NPs de polymères conjugués ce qui permet d’obtenir des déplacements de Stockes supérieurs.[98] Enfin, la modification de surface avec des polymère amphiphiles est facile et n’altère pas les propriétés optiques du polymère conjugué.[99,100]

1.4 Nanoparticules de polymère encapsulant une grande quantité de fluorophores

Parmi les nanoparticules luminescentes non citées précédemment, les NPs de polymères encapsulant une grande quantité de fluorophores sont également très intéressantes. Elles ont l'avantage d'être composées de polymère non fluorescent biocompatible voire biodégradable. A l'intérieur, des fluorophores organiques sont piégés dans la matrice polymérique.

$$\text{Brillance} = N \times \varepsilon_{fluo} \times \Phi_{NP}$$

Figure 8. Représentation schématique d'une nanoparticule polymérique encapsulant une grande quantité de fluorophores. La brillance de la nanoparticule est proportionnelle au nombre de fluorophores encapsulés (N), à leur coefficient d'extinction (ε) et au rendement quantique de la nanoparticule (Φ).

Le principe de ces NPs repose sur l'encapsulation d'une grande quantité de fluorophores dans un espace confiné. Le coefficient d'absorption de la NP correspond à la somme des coefficients d'absorption des fluorophores encapsulés (figure 8). La brillance résultante est d'autant plus élevée, qu'elle est le produit du coefficient d'absorption multiplié par le rendement quantique. Le coefficient d'absorption de la nanoparticule va également dépendre de la taille des NPs : plus le volume de la particule est grand, plus on peut encapsuler de fluorophores à l'intérieur.

1.4.1 Méthodes de préparations des NPs de polymères fluorescentes

A partir de monomères

Les NPs peuvent être préparées directement à partir des monomères par les méthodes de mini-, micro-émulsion et émulsion (figure 9). Elles reposent sur la dispersion du monomère dans une phase dispersante. Les micelles formées sont ainsi stabilisées par un tensioactif plus ou moins en grande quantité. La réaction de polymérisation est ensuite amorcée par un initiateur. La différence entre les émulsions repose principalement sur les concentrations en tensioactifs et sur la méthode d'homogénéisation des émulsions.[94] Le diamètre des particules formées varie de 50 à plusieurs centaines de nm pour l'émulsion et dépend essentiellement de la cinétique de polymérisation et de l'utilisation ou non de surfactant. Les NPs obtenues sont de l'ordre de 100 nm pour la mini-émulsion et inférieur à 50 nm pour la microémulsion. Les fluorophores sont encapsulés le plus souvent de manière covalente dans les particules[101] mais l'encapsulation physique des fluorophores est également possible.[102] La difficulté avec ces techniques de préparations de NPs est d'obtenir des particules de polymères très concentrées en fluorophores et d'avoir une répartition homogène des fluorophores dans les particules. Certaines de ces méthodes de synthèse comme la polymérisation RAFT par mini-émulsion permettent néanmoins d'incorporer de manière covalente des quantités importantes de fluorophores dans des NPs de poly(styrène).[103]

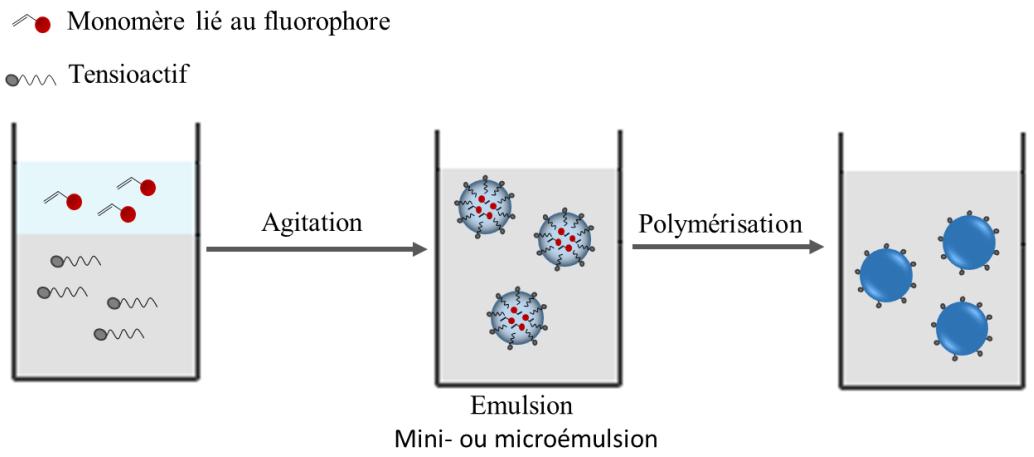

Figure 9. Préparation des nanoparticules à partir de monomères.

A partir de polymères

L'évaporation de solvant, l'auto-assemblage ainsi que la nanoprécipitation sont les trois principales méthodes permettant l'obtention de NPs de polymères à partir de polymères (figure 10).

Parmi elles, l'évaporation de solvant repose sur la formation d'une émulsion en prérequis. Le polymère est dissous dans la phase organique. Une émulsion de type huile dans eau se forme grâce à l'ajout d'un surfactant et d'une forte agitation (homogénéisation à haute vitesse ou sonication). Puis l'émulsion est suivie de l'évaporation du solvant organique résiduel volatil. Ceci provoque la précipitation du polymère et la formation de NPs.[104] Cette méthode est principalement limitée par la taille de NPs obtenue, de l'ordre d'une à plusieurs centaines de nm, malgré l'ajout de tensioactif et l'homogénéisation énergique.

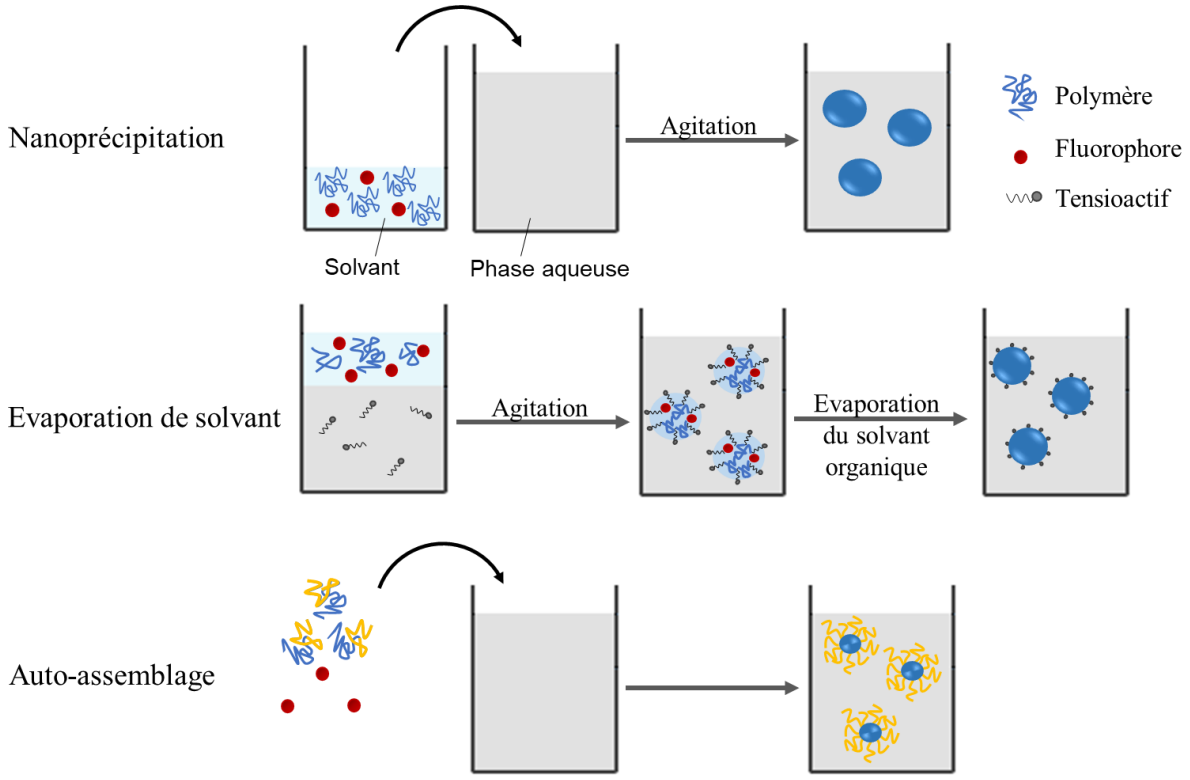

Figure 10. Préparation des nanoparticules à partir de polymères.

L'auto-assemblage de NPs de polymères requiert quant à elle des copolymères à blocs composés de séquences ou blocs à partir d'au moins deux monomères différents, l'un hydrophile et l'autre hydrophobe.[105] La micellisation de ces polymères nécessite un solvant dans lequel l'un des blocs est dissous et l'autre non.

Au-delà de la concentration micellaire critique (CMC), les chaines de copolymères s'associent formant des micelles dont le centre est composé des blocs insolubles dans le solvant entourés par les blocs solubles. L'auto-assemblage de copolymères à blocs permet d'obtenir des tailles de NPs variant entre moins de 10 à 100 nm. Cependant en cas de dilution, l'équilibre thermodynamique n'est plus stable et peut conduire à des échanges de chaine polymérique et à la fuite des fluorophores encapsulés. Pour éviter ce problème, le fluorophore peut être covalemment attaché au polymère à blocs[106] ou les polymères réticulés une fois sous forme de particules.[107]

D'un point de vue, efficacité d'encapsulation, la nanoprécipitation ou déplacement de solvant est une des méthodes les plus intéressantes. Elle est aussi souvent choisie pour sa simplicité et son économie en temps et énergie vis-à-vis de l'évaporation de solvant.[108] Elle requiert deux phases dont l'une est un solvant et l'autre, un non-solvant du polymère. La phase solvant, typiquement organique qui sert à solubiliser les polymères et doit être miscible à la phase non-solvant. Cette dernière est aqueuse et peut ou non contenir des tensioactifs. La phase organique est additionnée à la fraction aqueuse en une seule fois ou en plusieurs, soit par goutte à goutte ou en continu par des systèmes microfluidiques. La formation des NPs résulte de la diffusion rapide des solvants (aqueux et organique) qui conduit à un mélange dans lequel le polymère n'est plus soluble qu'on appelle supersaturation du polymère. La gamme de taille de NPs obtenue est très large allant de moins de 10 nm à plusieurs centaines de nm. La taille des particules formées par nanoprécipitation va dépendre de nombreux paramètres tel que la concentration en polymère, la présence ou non de tensioactifs, la vitesse et le type de mélange des différentes phases, la quantité relative des deux solvants.

1.4.2 Encapsulation des fluorophores

Le confinement des fluorophores dans les NPs de polymères peut être fait de différentes manières. La première stratégie est de lier par liaison covalente le fluorophore à la matrice polymérique.[109–111] Cela nécessite l'introduction de groupement réactifs sur les polymères ou des groupements de polymérisation sur le fluorophore afin de lier le fluorophore au polymère. L'inconvénient de cette méthode est d'être limitée dans la quantité de groupements réactionnels ou le degré de polymérisation du fluorophore et donc de la quantité de fluorophores encapsulés. Dans

les autres cas, le fluorophore n'est pas lié covalemment au polymère mais piégé physiquement dans la particule de polymère. [8,112–118] Le risque dans ce cas est d'avoir une fuite des fluorophores vers le milieu extérieur. Pour éviter cela et avoir une encapsulation efficace, il est nécessaire que les fluorophores encapsulés soient très apolaires afin d'être piégés dans le cœur de la nanoparticule très hydrophobe.

1.4.3 Propriétés photo-physiques des nanoparticules

Tout comme les NPs de silice, l'encapsulation de fluorophores à l'intérieur de la matrice de polymère protège les fluorophores encapsulés de l'environnement extérieur et augmente par conséquent leur photostabilité. Cependant à forte concentration en fluorophore, des phénomènes d'agrégation des fluorophores dans la particule qui forment des agrégats H non fluorescents conduisent à une auto-inhibition de la fluorescence (appelée auto-inhibition de la fluorescence causée par agrégation (ACQ)) et donc à une diminution de la brillance.[115,119,120] L'encapsulation d'une grande quantité de fluorophores dans les NPs de polymères nécessite une adaptation au niveau du design des fluorophores utilisés.

Afin d'éviter la formation d'agrégats H, il est possible d'ajouter des groupements volumineux qui vont venir se placer perpendiculairement par rapport au plan du fluorophore et procurer un espacement suffisant entre chaque fluorophore dans la particule.[117,121,122] Par exemple, des NPs de PLGA chargées avec le lumogen red (LR) d'une teneur de 5 %m possède un rendement quantique de 50 % (figure 11).[117] Dans le cas des fluorophores chargés comme les dérivés de la rhodamine B (R18) et les cyanines, il est possible d'utiliser des contre-ions volumineux et hydrophobes comme par exemple les dérivés fluorés de tétraphényl borate ou des bis(2-éthylhéxyl)sulfosuccinate (AOT).[123,124] De charge négative très volumineux et hydrophobe, le contre-ion s'insère entre les fluorophores chargés positivement et évite leur agrégation. Les résultats de mesure de fluorescence indiquent qu'avec un contre-ion volumineux, F5-TBP (figure 11), associé à R18 dans des NPs de PLGA, le rendement quantique est de 20 % avec une teneur de fluorophores de 5 %m.[8] Alternativement, l'encapsulation de fluorophores qui montre une émission induite par agrégation (AIE) peut être utilisée (figure 11).[125–127] Ces fluorophores ont la particularité d'être non fluorescents en solution mais de fluorescer sous forme d'agrégats ou à l'état solide. Ainsi des NPs de DSPE-PEG contenant des fluorophores

de type AIE à 33 %m possèdent un rendement quantique de 58 %.[128] Concernant les fluorophores covalemment liés au polymère, l'insertion de fluorophore directement sur le polymère peut conduire également à des NPs avec des chargements en fluorophores et des rendements quantiques très élevés.[103,129] Par exemple, un monomère de type BODIPY, a été incorporé dans le polymère par mini-émulsion (figure 11). Les NPs résultantes contiennent un chargement de 8%m de fluorophore avec un rendement quantique de 35 %.[103] En terme de brillance, les NPs contenant les fluorophores précédemment décrits atteignent des valeurs de brillance entre 10^5 à 10^8 $M^{-1}cm^{-1}$.[94]

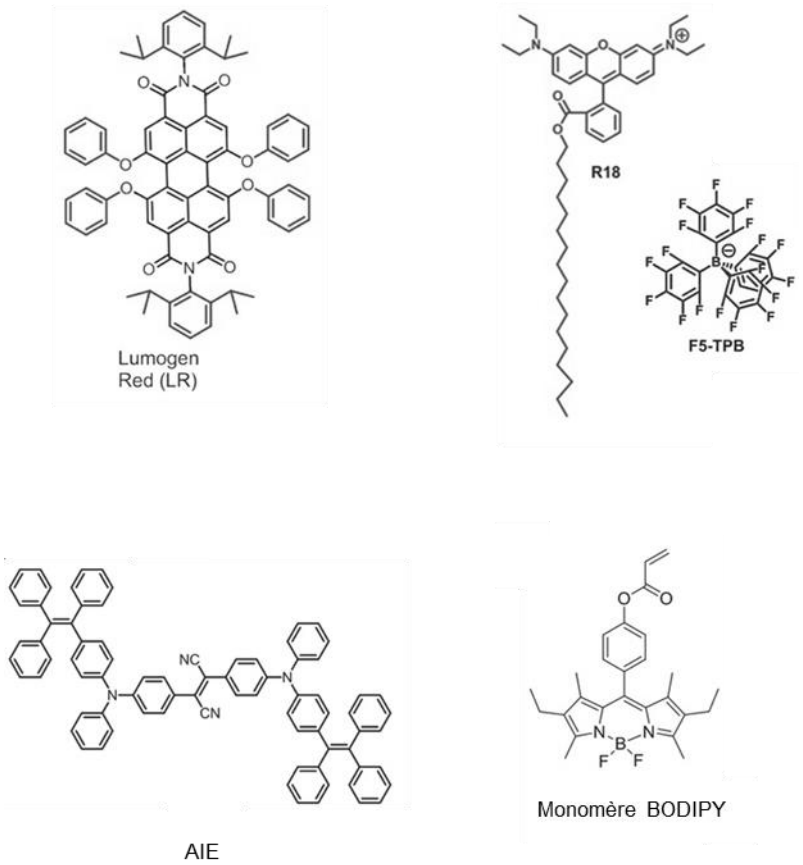

Figure 11. Exemples de fluorophores utilisés pour les NPs de polymères fluorescentes permettant d'atteindre des brillances élevées.

En les observant de manière individuelle, les NPs chargées avec des concentrations élevées en fluorophores R18/F5-TPB ont un comportement photocommutable.[8] Ce phénomène résulte d'un transfert d'énergie ultra-rapide entre fluorophores identiques.[130] A fortes concentrations, le transfert d'énergie augmente ainsi que la probabilité de transférer l'énergie d'excitation à un agrégat non fluorescent. Associé à

un comportement collectif des fluorophores au sein de la particule, cela se traduit par un clignotement de la particule entière. Cette propriété permet d'envisager leur utilisation pour l'imagerie super-résolutive.

De plus, ce transfert d'énergie ultra-rapide entre les fluorophores permet de transférer l'énergie d'excitation de milliers de fluorophores donneurs à un seul fluorophore accepteur. Ces NPs de polymères chargées avec beaucoup de fluorophores fonctionnent alors comme des nano-antennes, capables d'amplifier le signal de trois ordres de grandeur par rapport à un seul fluorophore. Grâce à ce système, il est alors possible de détecter une molécule unique dans des conditions d'illumination semblables à la lumière ambiante.[131–133]

1.4.4 Chimie de surface

La modification de surface des NPs consiste en l'insertion de groupements hydrophiles à la surface qui permettront dans un premier temps de stabiliser les NPs dans les milieux biologiques. Les NPs ne doivent pas agréger en présence de sels et dans les conditions de pH physiologique. De plus la modification de surface permet de minimiser les interactions non spécifiques notamment avec les protéines afin de rendre les NPs furtives et de prolonger leur temps de circulation *in vivo*. Enfin le contrôle des propriétés de surface des NPs combiné à la fonctionnalisation, c'est-à-dire l'ajout de ligand, permet l'adressage spécifique des NPs à des récepteurs moléculaires.

La stratégie la plus répandue pour assurer la stabilité des NPs dans les milieux biologiques est l'ajout de groupement poly(éthylène glycol) (PEG). Ce dernier est connu pour empêcher l'adsorption des protéines sur la particule par encombrement stérique.[134] L'insertion du groupement PEG peut être réalisée par l'insertion de lipides PEGylés comme le DSPE-PEG, au sein de la matrice polymérique.[128] Le groupement PEG peut également être lié de manière covalent sur le polymère.[115] D'autres groupes ont utilisé des copolymères à blocs comprenant un domaine hydrophobe à base de poly(styrène) (PS) suivis par un bloc d'acide poly(acrylique) (PAA) et puis du groupement PEG.[103] Certaines NPs ont également été enrobées de surfactants PEGylées comme le tween 80 ou le pluronic F127.[135] Enfin des polymères amphiphiles tel que le poly(phosphoester)[136] ou encore des polysaccharides[137] peuvent être utilisés alternativement.

L’interaction des NPs avec des récepteurs biologiques spécifiques nécessite en plus d’une surface non interactive, l’insertion de groupements chimiques réactifs. La fonctionnalisation des particules est souvent effectuée à la fin de la chaine PEG *via* des groupements tels que les groupements carboxylates, thiols ou amines.[138] Par une réaction de bioconjugaison il est possible d’attacher des ligands comme l’acide folique,[128] la streptavidine,[139] des anticorps[116] ou encore des peptides tels que RGD[140] ou TAT.[126] En dehors de ces réactions conventionnelles, d’autres réactions telles que la chimie clic peut être employée. Elle a l’avantage d’être simple, rapide avec des rendements élevés en milieu aqueux.[141,142]

1.5 Imagerie de fluorescence intracellulaire

1.5.1 Imagerie de fluorescence et ses limites

L'imagerie de fluorescence est très utilisée en biologie notamment grâce à son caractère non-invasif, sa grande sensibilité et sa compatibilité avec le vivant. A l'aide de marquages fluorescents il est possible d'imager de manière spécifique des molécules, des constituants cellulaires, des cellules ou des tissus dans des organismes vivants ou fixés. La microcopie de fluorescence est donc devenue, au cours de ces dernières années, un outil fondamental en biologie allant de la compréhension de processus moléculaires jusqu'à la visualisation d'organisme entier.

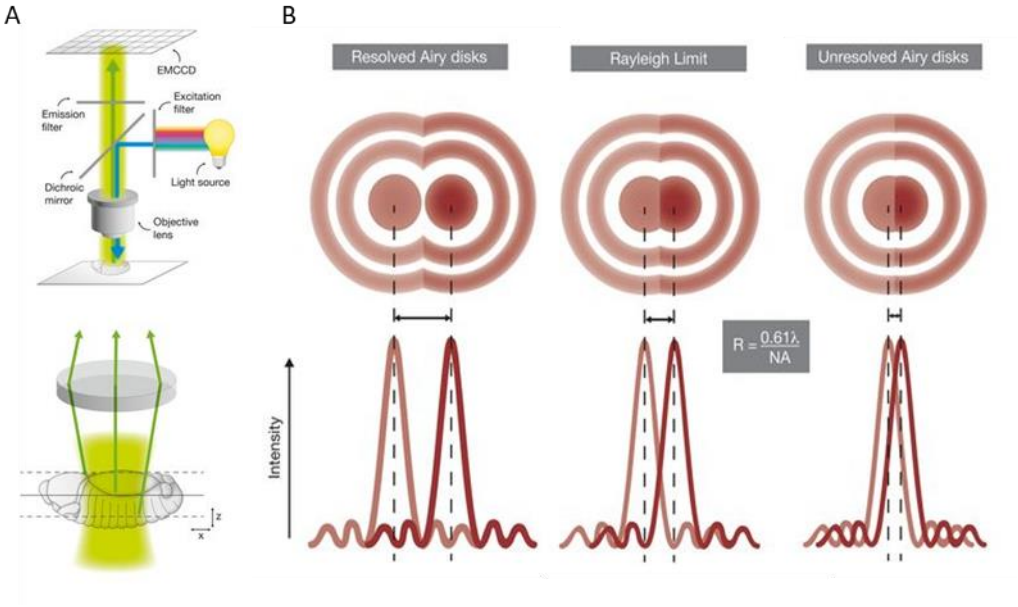

Figure 12. (A) Principe d'un microscope à épifluorescence. (B) Capacité d'un microscope de fluorescence à résoudre deux émetteurs de lumière qui sont proches. La résolution est définie par le critère de Rayleigh (R = 0.61λ/ON). Reproduit à partir de la référence [143].

L'image d'une source ponctuelle lumineuse à travers un système optique tel qu'un microscope à épifluorescence (Figure 12A) est représentée par la tâche d'Airy. Elle est formée de disques représentant les maxima et minima d'intensité lumineuse qui résultent des effets de diffraction de la lumière (Figure 12B). Selon le critère de Rayleigh, les figures de diffraction sont résolues lorsque la région centrale de la tâche d'Airy chevauche le premier disque de minima d'une autre tâche.[143]

La résolution spatiale d'un microscope est définie comme :

$$R = 0.61\frac{\lambda}{ON}$$

avec λ la longueur d'onde et ON (ou NA) l'ouverture numérique. Ainsi pour une ouverture numérique maximale de 1,4 avec un grossissement x100, un objectif à immersion huile et une longueur d'onde de 500 nm, la résolution sera de 214 nm. La résolution est limitée à ~ 200-250 nm en microscopie à fluorescence.[2] Cela signifie qu'il est impossible de séparer et d'imager des objets ou détails dont la taille est inférieure à cette limite.

1.5.2 Imagerie de molécules uniques

A côté de cela, l'observation de molécules uniques nécessite une précision de localisation de l'émetteur ou de la sonde fluorescent(e). Cela dépend du nombre de photons détectés par rapport au bruit de fond de l'échantillon. Plus ce ratio est grand, plus la localisation sera précise et rapide.[3] Ce rapport signal/bruit peut être augmenté de différentes manières. Le bruit de fond fluorescent est non négligeable lorsqu'on veut localiser une molécule individuelle dans la cellule.[72] Les composés tels que les acides aminés aromatiques, les flavines, NAD(P)H, l'élastine et les porphyrines fluorescentes recouvrent le spectre entier du visible et contribuent à l'autofluorescence des cellules et tissus.[144] Ce bruit de fond fluorescent peut être réduit à l'aide de méthodes de microscopie telles que la microscopie confocale, la microsopie TIRF ou l'imagerie à déclenchement périodique. Les microscopies confocale et TIRF vont permettre de réduire le champs observé ou excité sur des profondeurs < 400 nm et 100 nm respectivement.[1] L'imagerie à déclenchement périodique utilise des sondes luminescentes ayant des temps de vie très longs et permet de supprimer l'autofluorescence des composants cellulaires.[145] Une autre solution est d'augmenter le nombre de photons récoltés venant de la sonde fluorescente. Celui-ci peut être amélioré soit en utilisant une sonde plus brillante, soit par augmentation de l'intensité de la lumière d'excitation, ou encore par prolongation du temps d'acquisition. La méthode FIONA (fluorescence imaging with one-nanometer accuracy) par exemple combine la microscopie TIRF avec l'acquisition d'un grand nombre d'images permettant d'augmenter considérablement le ratio signal/bruit.[146]

1.5.3 Imagerie super-résolutive

Dernièrement, le développement de techniques de microscopie optique capables de franchir la limite de diffraction de la lumière ont permis d'avoir des images avec une meilleure résolution. Les techniques d'imagerie de super-résolution regroupent quatre techniques reposant sur les propriétés photo-physiques des fluorophores : la microscopie de déplétion par émission stimulée (STED),[147,148] la microscopie par localisation photoactivée (PALM),[5,149] la microscopie de reconstruction optique stochastique (STORM)[4] et PAINT (point accumulation for imaging in nanoscale topography).[150]

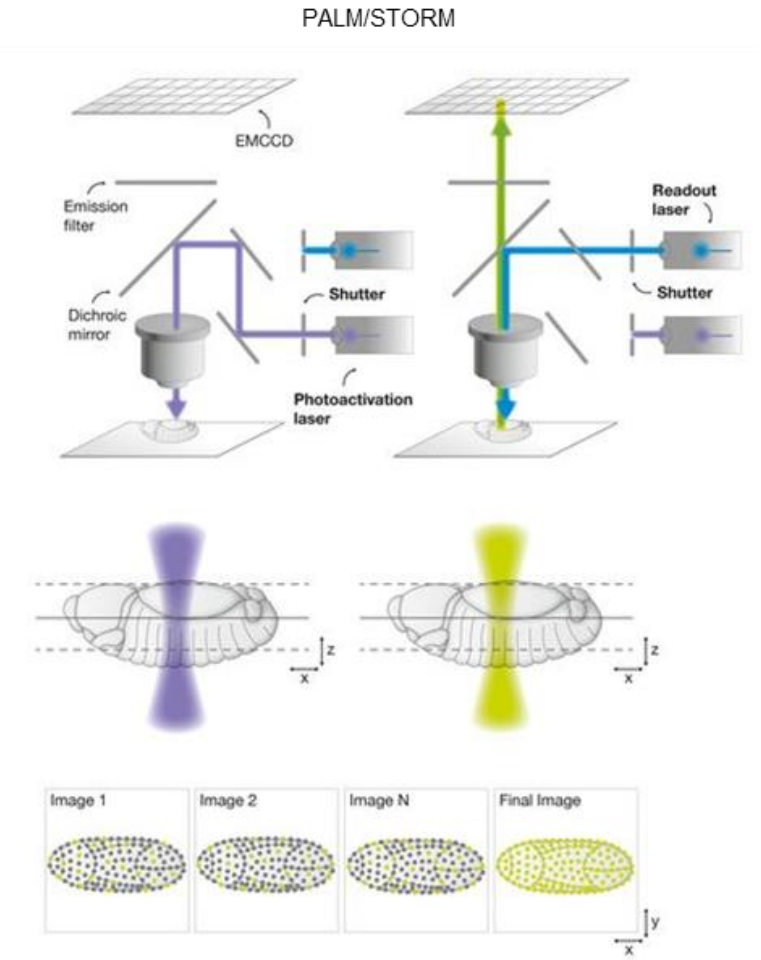

Figure 13. Principe des microscopies super-résolutives : PALM et STORM. Reproduit à partir de la référence [151].

PALM et STORM sont tous les deux basés sur la détection de molécules individuelles. Ils requièrent des fluorophores photoactivables ou photocommutables (figure 13). Les émetteurs fluorescents sont dans un premier temps activés/excités de manière aléatoire ou non par un laser. L'image est enregistrée puis les fluorophores activés sont photoblanchis dans le cas de PALM ou passent par un état noir non fluorescent réversible pour STORM à l'aide d'un laser d'inactivation ou non. Durant chaque cycle d'activation/inactivation, seuls une poignée de fluorophores s'illuminent. L'image finale est une reconstruction des images résultantes des n cycles et regroupant toutes molécules individuelles détectées. Il en résulte une résolution latérale de 20 nm et 50 nm en axial.[151]

1.5.4 Les contraintes de l'imagerie intracellulaire

Suivre des biomolécules intracellulaires de manière individuelle implique de travailler sur des cellules vivantes. Par conséquent, le temps d'exposition et l'intensité d'excitation des fluorophores sont non seulement limités par le nombre de photons qu'ils peuvent délivrer avant leur photoblanchiment mais aussi par la phototoxicité induite sur les cellules vivantes.[152] Pourtant les techniques de suivi de molécules individuelles nécessitent de récolter un nombre de photons important. La brillance de l'émetteur fluorescent doit alors être suffisamment élevée pour sa détection et sa localisation. Les NPs fluorescentes sont de plus en plus utilisées dans l'imagerie intracellulaire pour leur brillance et leur photostabilité. Cependant ils sont également considérablement plus volumineux par rapport aux fluorophores organiques et protéines fluorescentes et doivent répondre, en dehors des propriétés photophysiques, à des critères de taille et de chimie de surface. En effet le cytoplasme est un espace particulièrement encombré, composé de nombreuses macromolécules et d'un réseau dense formé par le cytosquelette et de divers organites cellulaires.[10,11] Le premier événement qui se produit lorsqu'une NP entre dans un système biologique est l'adsorption de protéines recouvrant la surface de la particule.[153] La composition et la structure de cette couche de protéine va déterminer le sort de la particule dans les milieux biologiques. Rendre les NPs furtives est d'autant plus indispensable pour cibler une biomolécule spécifique puisque la couche de protéines adsorbées risque de masquer les ligands insérés à la surface de la particule. En même temps, les NPs doivent être suffisamment petites pour se frayer un chemin à travers le maillage du

cytosquelette et l'encombrement cytoplasmique sans pour autant perturber la trajectoire des biomolécules d'intérêts.[12]

1.5.5 Les sondes utilisées pour l'imagerie intracellulaire

Les fluorophores organiques, les protéines fluorescentes et les QDs sont les sondes fluorescentes les plus utilisées pour le suivi de molécules individuelles.[54] Pour obtenir une brillance suffisante, les biomolécules peuvent être marquées avec plusieurs copies de protéines fluorescentes.[154,155] Des dérivés de GFP ont permis de suivre des transporteurs de la sérotonine au niveau de la membrane plasmique et du réticulum endoplasmique[156,157],d'ARNm dans les cellules[154,155] ou encore de protéines régulatrices et d'étudier leurs interactions au niveau des moteurs flagellaires d'Escherichia coli. [158] L'inconvénient majeur des protéines fluorescentes est qu'elles peuvent interférer avec la molécule/protéine cible et altérer son comportement ou même sa fonction.[54,158]

Les fluorophores organiques sont également très employés notamment pour l'exploration des dynamiques d'association/dissociation des finalement d'actine,[159,160] la visualisation du déplacement des myosines le long de ces filaments,[161] ou encore le suivi de protéines régulatrices des filaments d'actines.[162]

Les QDs ont été utilisés dans un premier temps pour marquer des protéines membranaires tels que les récepteurs EGF, les récepteurs GABA, les canaux potassiques ou les intégrines.[54] Cela a permis d'obtenir des informations sur les mécanismes de transport dans les cellules. Le marquage de biomolécules intracellulaires nécessite néanmoins des exigences particulières pour les particules fluorescentes comparées aux fluorophores organiques ou protéines fluorescentes. Tout d'abord, il faut un moyen de faire entrer les NPs dans la cellule et délivrer le matériel dans le cytosol. Ensuite ces NPs doivent se déplacer dans un environnement extrêmement encombré. Plusieurs exemples traitent des kinésines et myosines, moteurs moléculaires, impliqués dans le transport et la division cellulaire. La brillance des QDs permet de visualiser les pas individuels de myosine-V se déplaçant le long de filament d'actine.[163,164]

Parmi les autres nanoparticules fluorescentes, des nanoparticules de fluorophores ont montré une grande brillance et peuvent être imagées au niveau de particule individuelle avec une grande précision pendant des périodes prolongées dans des milieux cellulaires.[165] Des NPs d’AIE de 14 nm de diamètre ont également permis de marquer des structures intracellulaires telles que les microtubules par microscopie STED.[166] Récemment, des NPs à conversion ascendante de photons ont montré des brillances adaptées à l’imagerie de molécule unique.[167] Certaines de ces NPs ont permis d’imager la structure de protéines du cytosquelette en imagerie super-résolutive à haut débit.[168] Grâce à leur taille ultrapetite et leurs propriétés photophysiques, les carbon dots sont aussi d’excellents candidats pour l’imagerie intracellulaire et la visualisation de dynamiques cellulaires.[169] Ils peuvent également être utilisés en imagerie super-résolutive.[167] Des NPs de polymères conjugués sont aussi très prometteuses au niveau de leur brillance et de leur stabilité permettant de les localiser avec précision au niveau individuelle.[170] Ces NPs ont notamment été utilisées pour imager des structures subcellulaires telles que des mitochondries, l’enveloppe nucléaire ou des microtubules en imagerie super-résolutive.[171] Enfin, des NPs d’or ont permis d’étudier les processus d’endocytose en temps réel avec une méthode d’imagerie basée sur la résonnance plasmonique de surface et la luminescence.[172]

Partie 2 : Matériel et méthodes

2.1 Matériel

Le méthacrylate de méthyle (99%, M55909), le méthacrylate d'éthyle (99%, 234893), le méthacrylate de butyle (99%, 235865), l'acide méthacrylique (99%, 155721), le méthacrylate de 3-sulfopropyle (99%, 251658), le méthacrylate de 2-(N-3-Sulfopropyl-N,N-diméthylammonium)éthyle (99%, 537284), le chlorure de 2-(méthacryloyloxy)éthyl]triméthylammonium (75 % dans l'eau, 408107) et le méthacrylate de pentafluorophényle (95%, 741108) ont été achetés chez Sigma-Aldrich. Le méthacrylate de propyle (Sigma-Aldrich, 97%, 751162) a été purifié en utilisant une colonne de chromatographie et l'azobis isobutyronitrile (Aldrich, ≥ 98%) a été recristallisé dans l'éthanol. Le diméthylsulfoxide (DMSO, grade analytique) a été obtenu de Fisher-Scientific. L'eau Milli-Q (Millipore), l'acétonitrile (≥ 99.9%, Sigma-Aldrich) et le méthanol (≥ 99.9%, Carlo Erba reagents) ont été utilisés pour la préparation de nanoparticules. La 6-carboxy-tétraméthylrhodamine (TMR, Sigma-Aldrich), le tampon phosphate salin (PBS, Fisher Scientific), le sérum de veau fœtal (FBS, Lonza) ont été utilisés pour les études de stabilité *in vitro*. L'azobis isobutyronitrile (Aldrich, ≥ 98%) a été recristallisé dans l'éthanol. Le R18/F5-TPB a été synthétisé à partir de l'octadécyl ester perchlorure de rhodamine B (Aldrich, >98.0%) et le lithium tétrakis(pentafluorophényl)borate éthyl éthérate (AlfaAesar, 97%) par échange d'ions suivi d'une purification par colonne de chromatographie comme décrit précédemment.[8,173] Les cellules de carcinome cervical humain (HeLa), le milieu DMEM (Dulbecco's modified eagle medium), le sérum de veau fœtal (FBS), la solution d'antibiotiques (penicillin-strepomycine, Gibco-Invitrogen), la L-glutamine and la trypsine ont été employés pour la culture cellulaire. Des plaques 6-puits de cultures tissulaires (TPP®) ont été utilisées pour l'imagerie cellulaire.

2.2 Synthèses

2.2.1 Synthèse des polymères

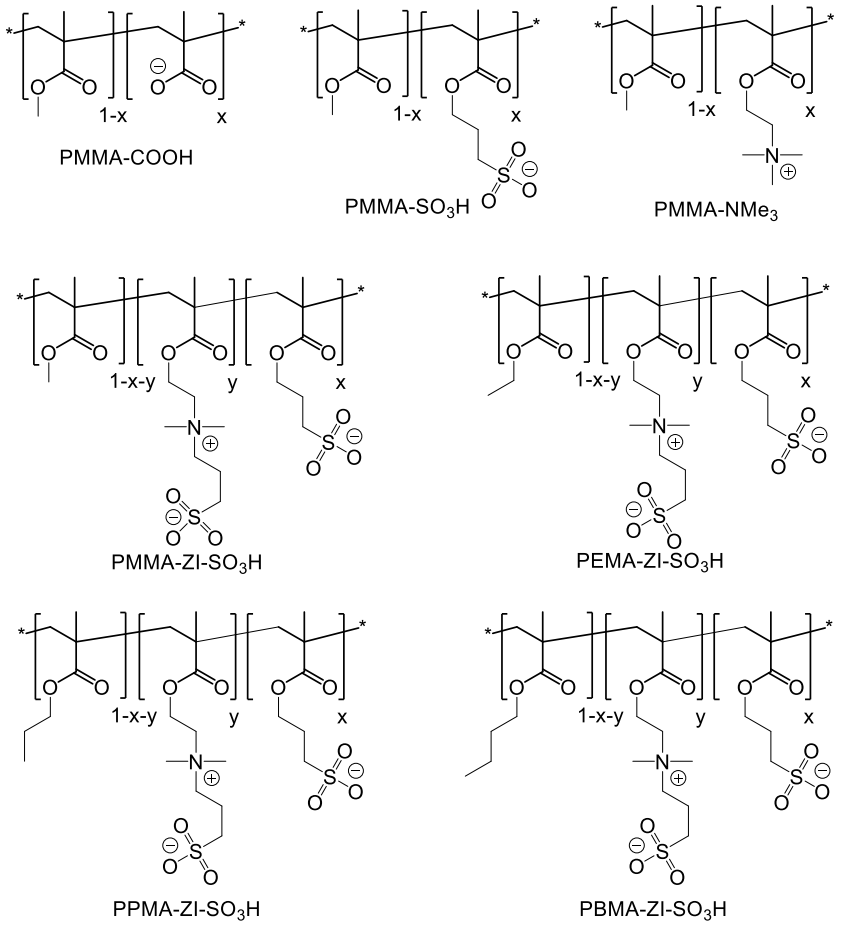

Figure 14. Principaux polymères synthétisés.

Procédure générale pour la polymérisation radicalaire : les monomères ont été dissous dans du DMSO ou de l'acétonitrile dégazés et mélangés au ratio désiré. Ensuite 0.01 eq d'AIBN ont été ajoutés au mélange. L'ensemble a été placé dans un bain d'huile préchauffé à 70°C. La réaction a été arrêtée une fois atteint une conversion de 25 % déterminée par RMN-^{1}H. Les polymères ont été ensuite précipités deux fois dans un mélange de méthanol et/ou d'eau. Après séchage, les polymères ont été caractérisés par RMN et lorsque c'était possible, par chromatographie d'exclusion stérique. Pour les polymères contenant de grandes quantités de ZI, aucun solvant adapté à la chromatographie d'exclusion stérique n'a été trouvé. La synthèse du PMMA-SO_3H est donnée comme exemple ci-dessous :

Poly(méthacrylate de méthyle-co-méthacrylate de 3-sulfopropyle) (PMMA-SO_3H) : le méthacrylate de méthyle et méthacrylate de 3-sulfopropyle ont été dissous dans du DMSO dégazé à des concentrations respectives de 2 et 0.5 M. Les deux solutions ont été ajoutées et mixées dans un ballon bicol de 50 ml au ratio désiré à l'aide d'un barreau magnétique pour donner un volume final de 20ml. Le mélange a été dégazé en faisant buller de l'argon pendant 5 min puis placé sous atmosphère argon. 0.01 éq d'AIBN (en solution dans DMSO à 40 mg/ml) a été ajouté. Le ballon a ensuite été placé dans un bain d'huile à 70°C. A intervalles réguliers, des échantillons du mélange réactionnel ont été prélevés, dissous dans DMSO-d6 et analysés par RMN-^{1}H. Lorsque la conversion a atteint 25 %, la réaction a été arrêtée et rapidement refroidie à température ambiante. Le mélange réactionnel a ensuite été ajouté goutte à goutte au méthanol (ou un mélange méthanol/eau pour les pourcentages les plus élevés en groupements chargés). Après filtration, le précipité récupéré a été redissous dans un petit volume d'acétonitrile (avec si besoin un petit volume de méthanol) et reprécipité deux fois dans le méthanol (méthanol/eau pour des pourcentages de charges plus élevés). RMN-^{1}H (400 MHz, DMSO-d6, δ): 3.97 (br. s, 0.02-0.2 H), 3.57 (s, 3 H), 2.45 (m, partiellement recouvert par le pic du solvant), 2.1–0.5 (m, 6 H). Fraction de groupements SO_3H basée sur le pic à 3.97 ppm (théorique: obtenu) : 1%:1.1%; 2%:2.3%; 5%:5.5%, 10%:12%. Poids moléculaire par chromatographie d'exclusion stérique (SEC) : 1%: M_w = 51 200, M_w/M_n = 1.58; 5%: M_w = 48 400, M_w/M_n = 1.08.

Caractérisation des principaux polymères utilisés

Poly(méthacrylate de méthyle-co-acide méthacrylique) (PMMA-COOH) : RMN-^{1}H (400 MHz, CDCl3, δ): 3.60 (s, 3 H), 2.2–0.5 (m, 6 H). Poids moléculaire par SEC : 1%: M_w = 38 100, M_w/M_n = 1.35; 5%: M_w = 46 800, M_w/M_n = 1.34.

Poly(méthacrylate de méthyle-co-[2-(méthacryloyloxy)éthyl]triméthylammonium) (PMMA-NMe_3) : RMN-^{1}H (400 MHz, DMSO-d6, δ): 4.37 (br. s, 0.02-0.2 H), 3.70 (br. S, 0.02-0.2), 3.55 (s, 3 H), 3.17 (s, 0.09–0.9 H), 2.1–0.4 (m, 6 H). Fraction des groupements NMe_3 basée sur le pic à 3.17 ppm (théorique: obtenu) : 1%:1.1%; 2%:2.4%; 5%:5.8%; 10%:12.2%. Poids moléculaire par SEC : 1%:M_w = 99 900, M_w/M_n = 1.62; 5%: M_w = 95 300, M_w/M_n = 1.22.

Poly(méthacrylate de méthyle-co-méthacrylate de 3-sulfopropyle-co-méthacrylate de 2-(N-3-Sulfopropyl-N,N-diméthyl ammonium)éthyle) (PMMA-ZI-SO_3H) : RMN-^{1}H (400

MHz, DMSO-d6, δ): 4.36 (br, 0.04-0.2 H), 3.96 (br. s, 0.02-0.04 H), 3.55 (m, 3.4 H), 3.13 (br, 0.12-0.6 H), 2.45 (br, recouvert par le pic de solvant), 2.04 (br, 0.04-0.2 H), 2.00-0.30 (m, 6 H). Fraction obtenue des groupements ZI et SO3H basée sur les pics à 4.36 et 3.97 ppm, respectivement (théorique: obtenu) : ZI 10 %: 10.2 % - SO3H 1 %: 1.4%; ZI 10 %: 11 %- SO3H 2 %: 2.8%. Poids moléculaire par SEC : 1% ZI: M_w = 43 100, M_w /M_n = 1.14. Pour les polymères avec des quantités plus grandes de ZI aucun solvant adapté à la chromatographie d'exclusion stérique n'a été trouvé.

Poly(méthacrylate d'éthyle-co-méthacrylate de 3-sulfopropyle-co-méthacrylate de 2-(N-3-Sulfopropyl-N,N-diméthylammonium)éthyle) (PEMA-ZI-SO_3H): RMN-^{1}H (400 MHz, MeOD, δ): 4.50 (br, 0.2 H), 4.34-3.92 (m, 2.02 H), 3.81 (br, 0.2 H), 3.70 (br, 0.2 H), 3.29 (br, partiellement recouvert par le pic du solvant), 2.92 (br, 0.2 H), 2.31 (br, 0.2 H), 2.23-0.5 (m, 9 H). Fraction obtenue des groupements ZI basée sur le pic à 4.50 ppm: 10.3 %.

Poly(méthacrylate de propyle-co-méthacrylate de 3-sulfopropyle-co-méthacrylate de 2-(N-3-Sulfopropyl-N,N-diméthyl ammonium)éthyle) (PPMA-ZI-SO_3H): RMN-^{1}H (400 MHz, MeOD, δ): 4.50 (br, 0.2 H), 4.29-3.54 (m, 2.42 H), 3.29 (br, partiellement recouvert par le pic du solvant), 2.92 (br, 0.2 H), 2.31 (br, 0.2 H), 2.23-0.5 (m, 11 H). Fraction obtenue des groupements ZI basée sur le pic à 4.50 ppm: 9.4%.

Poly(méthacrylate de butyle-co- méthacrylate de 3-sulfopropyle -co- méthacrylate de 2-(N-3-Sulfopropyl-N,N-diméthylammonium)éthyle) (PBMA-ZI-SO_3H): RMN-^{1}H (400 MHz, CDCl3, δ): 4.40 (br, 0.2H), 4.30-3.55 (m, 2.42 H), 3.33 (br, 0.6 H), 2.99 (br, 0.2 H), 2.36 (br, 0.2 H), 2.28-0.4 (m, 13 H). Fraction obtenue des groupements ZI basée sur le pic à 4.40 ppm: 8.3%.

Poly(méthacrylate de méthyle-co-méthacryalte de pentafluorophényle-co-méthacrylate de 2-(N-3-Sulfopropyl-N,N-diméthylammonium)éthyle) (PMMA-ZI-PFMA): RMN-^{1}H (400 MHz, DMSO-d6, δ): 4.36 (br, 0.04-0.2 H), 3.55 (m, 3 H), 3.13 (br, 0.6 H), 2.45 (br, recouvert par le pic de solvant), 2.04 (br, 0.2 H), 2.00-0.30 (m, 6 H). Fraction obtenue des groupements ZI basée sur les pics à 4.36 ppm : 11.2%. RMN-^{19}F (400 MHz, ACN-d3, δ): -150 (s, 1F), 152 (s, 1F), -157 (s, 1F), -162 (s, 2F).

2.2.2 Synthèse de l'espaceur boc-NH-L-SO_3H-N_3

*Synthèse du synthon **1*** : L'acide homocystéique (1,00 g, 5,46 mmol, 1 eq.) et le di-tert-butyl dicarbonate (Boc_2O, 1,56 g, 7,18 mmol, 1,3 eq) ont été mis dans 20 mL d'un mélange eau methanol (1:1) et suivi par l'ajout de DIPEA (2,1 mL, 12,8 mmol, 2,3 eq). Après 24 h à température ambiante, le solvant a été évaporé sous pression réduite. Le résidu a ensuite été purifié par chromatographie avec un gradient de concentration DCM/MeOH de 95:5 à 50:50 (deux colonnes). Après séchage sous vide on obtient 1,2 g du produit (rendement 78%). RMN-^{1}H (400 MHz, MeOD, δ): 4.06 (m, 1H), 3.25 (h, 2H, J = 6.6 Hz), 3.22 (q, 2H, J= 7.4 Hz), 2.87 (m, 2H), 2.31 (m, 2H), 2.31 (m, 2H), 1.45 (s, 9H), 1.36 (s, 3H).

Par la suite, le produit purifié (610 mg, 2.16 mmol,1 eq) et l'azido propanamine (247 mg, 2.5 mmol, 1.2 eq) ont été dissous dans 6 ml de DMF anhydre. HATU (980 mg, 2.6 mmol, 1.2 eq) et la triéthanolamine (600 µl, 4.32 mmol, 2 eq) ont été dissous à part dans 2 ml DMF puis ajouter au mélange réactionnel. L'ensemble a été placé sous agitation et sous argon à température ambiante. La réaction a été suivie par CCM (DCM/MeOH 8:2, révélation ninhydrine). Après 18h de réaction, le solvant a été évaporé à l'évaporateur rotatif. Le produit brut redissous dans un mélange DCM/MeOH (1:1) a ensuite été purifié par flash chromatographie sur une colonne de silice avec un gradient de concentration DCM/MeOH 95:5 à 70:30 (répété une fois). Le produit obtenu (428 mg, 54% de rendement) a été analysé par RMN-^{1}H. RMN-^{1}H (400 MHz, MeOD, δ): 4.09 (q, 1H), 3.36 (m, 2H), 3.27 (m, partiellement recouvert par le pic du solvant), 2.85 (t, 2H), 2.24-1.97 (m, 2H), 1.44 (s, 9 : H).

*Synthèse de l'ester NHS (synthon **2**)* : le boc-β-Ala-OH (400 mg, 2.11 mmol, 1eq) et le NHS (255mg, 2.22 mmol, 1.05 eq) ont été dissous dans 2.5 ml de DCM anhydre. DCC (458 mg, 1.05 eq) et DMAP (129 mg, 0.5eq) ont été dissous dans 2.5 ml de DCM anhydre puis ajoutés au mélange réactionnel goutte à goutte. Le tout a été placé sous agitation et sous argon pendant 18h à température ambiante. La réaction a été filtrée pour éliminer le précipité. Le filtrat récupéré a ensuite été séché à l'évaporateur rotatif puis conservé à -20°C après analyse RMN-^{1}H. RMN-^{1}H (400 MHz, MeOD, δ): 4.44-3.24 (m, partiellement recouvert du pic du solvant), 2.65 (s, 4H), 2.49 (t, 1H), 2.35 (t, 1H), 1.43 (s, 9H).

Synthèse de l'espaceur final (boc-NH-L-SO_3H-N_3) : Le synthon **1** (29 mg, 0.079 mmol 1eq) a été dissous avec 2 ml de DCM/TFA 1:1 et placé sous agitation pendant 1h. L'achèvement de la déprotection a été vérifié par CCM (DCM/MeOH 8:2, révélation ninhydrine). Après 1 h, la réaction a été stoppée et le solvant enlevé par évaporation sous pression réduite. Le produit brut a ensuite été lavé au MeOH suivi d'une évaporation, trois fois de suite. Le produit sec obtenu sous forme d'une poudre blanche et l'ester NHS (synthon **2**, 46 mg, 0.160 mmol, 2 eq) ont ensuite été dissous dans 600 µl d'un mélange DMF/H2O 3:1. La réaction a été suivie par CCM (DCM/MeOH 8:2, révélation ninhydrine). Après 48h de réaction, 35 mg (0.122 mmol, 1.6 eq) d'ester NHS ont été ajoutés à la réaction avec 200 µl de DMF/H_2O 3:1 et le tout a été laissé pendant encore 24h. Le solvant a ensuite été éliminé par évaporation sous pression réduite et le produit brut a été purifié par flash chromatographie avec un gradient de concentration DCM/MeOH de 95:5 à 70:30. Le produit purifié collecté (19 mg, 0.044 mmol, 56% de rendement) a été analysé par RMN-^{1}H et spectrométrie de masse. RMN-^{1}H (400 MHz, MeOD, δ): 4.38 (q, 1H), 3.37 (t, 2H), 3.28 (m, recouvert par le pic du solvant), 2.86 (t, 2H), 2.43 (t, 2H), 2.29-2.03 (m, 2H), 1.77 (m, 2H), 1.43 (s, 9H). m/z : 437.1806 (+2H), calculée 435.4765.

2.2.3 Modification du polymère PMMA-ZI 10%-PFMA 1%

L'espaceur boc-NH-L-SO_3H-N_3 (5.2mg, 0.012mmol, 2 eq) a été dissous dans 1 ml DCM/TFA 1:1. L'achèvement de la déprotection a été suivi par CCM (DCM/MeOH 8:2). Après 1h de réaction, le solvant a été évaporé. Le produit brut a été lavé avec du MeOH avant d'être séché à l'évaporateur rotatif. Cette étape a été répétée 2 fois. Le produit sec a ensuite été dissous avec le polymère PMMA-ZI 10 %-PFMA 1% (64 mg soit 0.006 mmol de groupements PFMA,1eq) dans 500 µl de DMF anhydre. Une solution de triéthylamine anhydre diluée 20x dans le DMF anhydre a été préparée à part avant d'ajouter 2 eq au mélange réactionnel. La réaction a été placée sous agitation et sous argon pendant 120h à température ambiante. Le polymère a ensuite été redissous dans 1 ml de CH_3CN/MeOH 5:2. Puis le polymère a été précipité dans le MeOH à 4°C puis séché. Il a ensuite été redissous dans 1 ml de DCM/MeOH 1:1 et purifié sur colonne LH-20. Le polymère collecté puis séché donne une masse de 41 mg.

2.3 Préparation des nanoparticules

Des solutions stocks de polymères ont été préparées à une concentration de 10 $g.l^{-1}$ dans l'acétonitrile (avec 20 % (vol.) méthanol pour les polymères ZI). Ces solutions ont été diluées à 2 $g.l^{-1}$ dans le solvant correspondant contenant 1, 10 ou 20 % (en masse relative au polymère) de R18/F5-TPB. 50 µl de cette solution ont été ensuite ajoutés rapidement à 450 µl d'eau sous agitation (Thermomixer comfort, Eppendorf, 1000 rpm, à 21°C) suivi d'une seconde dilution (x5) dans l'eau.

Dans le cas de l'étude du comportement des NPs non ZI destinées à être microinjectées ou introduites dans le cytosol par électroporation, les solutions de NPs ont ensuite été additionnées d'une solution de T80 afin d'obtenir une concentration finale de 0.05 $g.l^{-1}$.

2.4 Fonctionnalisation des NPs-N_3 avec DBCO-sulfoCy5

Les NPs-N_3 à 20 % R18/F5-TPB ont été préparées comme décrit précédemment à partir du polymère modifié PMMA-ZI 10%-N_3 1%. 4.8 µl d'une solution de DBCO-sulfoCy5 à 100 µM ont été ajoutés à 1 ml de solution de NPs. Après homogénéisation, l'ensemble a été placé à température ambiante, protégé de la lumière pendant 18h. Les NPs ont ensuite été purifiées par chromatographie d'exclusion stérique à l'aide d'une colonne de déssalage PD-10 (GE Healthcare, Life Science). La fraction de NPs collectée a ensuite été analysée par spectrofluorométrie.

2.5 Caractérisation des nanoparticules

2.5.1 Diffusion dynamique de la lumière

La diffusion dynamique de la lumière (DLS) est une méthode non-invasive permettant de mesurer la taille de particules en solution ou suspension. La DLS est composée d'un laser qui éclaire l'échantillon et d'un détecteur qui enregistre la lumière diffusée par les particules. Le mouvement des particules crée des interférences constructives et destructives qui se traduit par une variation de l'intensité de la lumière

diffusée en fonction du temps. [174] La corrélation de l'intensité du signal en fonction du temps permet d'obtenir le coefficient de diffusion. Celui-ci est lié au rayon hydrodynamique de la particule par la relation de Stokes-Einstein :

$$R_H = \frac{kT}{6\pi\eta D}$$

Avec R_H le rayon hydrodynamique, D le coefficient de diffusion, η la viscosité du liquide dispersant, T la température et k la constante de Boltzmann.[174]

Les solutions de particules préparées par nanoprécipitation sont utilisées telles quelles pour les mesures de taille en DLS. Toutes les mesures en DLS ont été réalisées sur un Zetasizer Nano ZSP (Malvern Instruments S.A.). Il est équipé d'une source laser à 633 nm qui éclaire l'échantillon. Le détecteur est placé à un angle de 173° et enregistre les variations d'intensités diffusées par les particules pendant 20 s à 25°C. Pour chaque mesure de taille, nous avons pris la moyenne des diamètres moyens pondérés en fonction du volume obtenus sur 10 cycles de 20 s.

2.5.2 Microscopie électronique à transmission

L'imagerie par microscopie électronique à transmission (TEM) repose sur l'utilisation d'un faisceau d'électrons qui passe à travers l'échantillon déposé en fine couche sur une grille. Le microscope est composé d'un ensemble de lentilles magnétiques permettant de focaliser le faisceau d'électrons sur l'échantillon et de former l'image sur un écran fluorescent, le tout sous un vide poussé (figure 15).

Préparation des échantillons : Les solutions de NPs peuvent être diluées selon la concentration en particules de la solution. 5µl de l'échantillon est déposé sur une grille de cuivre-rhodium recouverte d'un film de carbone CF-300-Cu 300 Mesh préalablement traitée à l'amylamine par décharge luminescente grâce à un système d'effluvage ELMO™. Une solution à 2% d'acétate d'uranyle est ensuite appliquée pendant 20 s pour la coloration. La grille est séchée avant d'être observée au microscope.

Microscopie : Le microscope utilisé est un microscope électronique à transmission Philips CM120. Un faisceau d'électrons est généré par un filament LaB6 et accéléré par un potentiel de 100 kV sous vide. L'acquisition d'images numériques est réalisée par une caméra CDD Peltier (Model 794, Gatan, Pleasanton,CA). Les images

obtenues sont ensuite analysées avec le logiciel Fiji. Pour chaque condition, au moins 100 NPs ont été analysées.

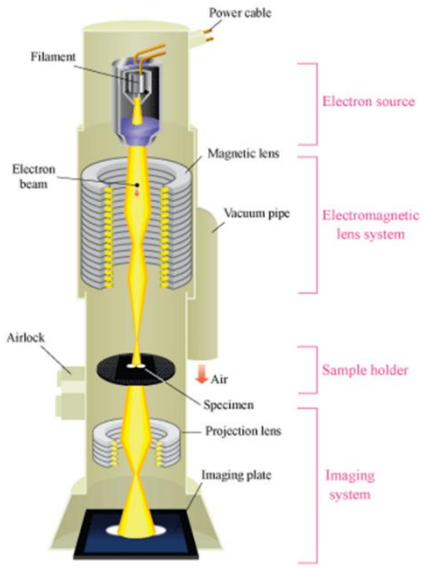

Figure 15. Principe de la microscopie électronique à transmission. Reproduit à partir de la référence [175].

2.5.3 Spectroscopie de corrélation de fluorescence

La spectroscopie de corrélation de fluorescence (FCS) est basée sur l'analyse des corrélations des fluctuations du signal de fluorescence de fluorophores (figure 16). Cette technique est très similaire à la DLS. La différence ici, est qu'on s'intéresse aux fluctuations de la fluorescence et non à celles de la lumière diffusée. La FCS mesure dans un petit volume d'observation les variations de l'intensité de fluorescence en fonction du temps, $F(t)$, qui fluctue comme la particule ou molécule fluorescente (en faible concentration) bouge à travers le volume confocal excité. Les fluctuations du signal sont analysées par une fonction d'autocorrélation temporelle $G(\tau)$ qui détermine le degré de corrélation entre l'intensité de fluorescence au temps t et celle au temps $t+\tau$ [176]:

$$G(\tau) = \frac{\langle \delta F(t).\delta F(t+\tau) \rangle}{\langle \delta F(t) \rangle^2}$$

A partir de cette fonction, on détermine le temps de diffusion du fluorophore qui traduit le temps moyen que reste un fluorophore dans le volume excité. $G(0)$, correspondant

à l'amplitude de la courbe d'autocorrélation, est inversement proportionnel au nombre moyen de fluorophores ou particules diffusantes dans le volume d'observation.[177]. La FCS est une méthode généralement utilisée pour des études d'association-dissociation, de colocalisation ou de changement conformationel.[18,178]

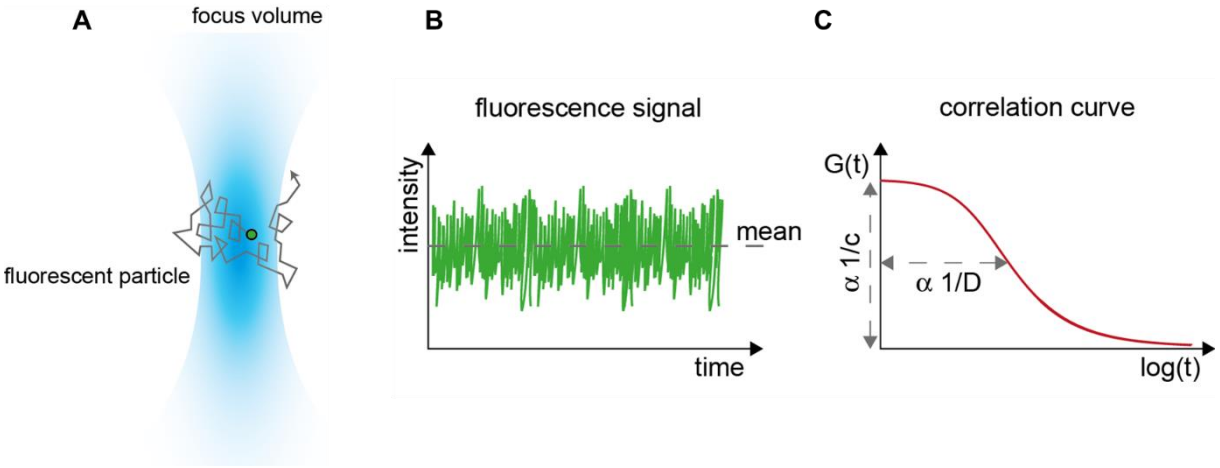

Figure 16. Principe de la FCS : (A) volume d'observation dans lequel une particule fluorescente se déplace ; (B) fluctuations de l'intensité de fluorescence en fonction du temps ; (C) fonction d'autocorrélation. Reproduit à partir de la référence [179].

Les mesures de FCS ont été réalisées sur un équipement fait-maison composé d'un microscope inversé Nikon avec un objectif Nikon 60 × 1.2 NA à immersion dans l'eau. La source d'excitation est produite par une diode laser à émission continue (532 nm, Oxxius) et les photons sont collectés avec une photodiode à avalanche (APD SPCM-AQR-14-FC, Perkin Elmer) connectée à un corrélateur (ALV7000-USB, ALV GmbH, Germany). Pour les mesures de FCS, nous avons utilisé des solutions de NPs chargées à 1 % de fluorophores, diluées 2 fois avant d'en déposer 200 µl dans une plaque 96-puits. La stabilité des NPs en présence de sels et de protéines a été évaluée par ajout goutte à goutte de 50 % du volume final d'une solution de PBS (10x) diluée 10 fois, d'une solution de FBS ou d'eau mQ aux solutions de NPs dans des tubes (low-binding, Eppendorf) de 1,5 ml. L'acquisition a été réalisée directement après l'ajout. Les données obtenues ont été ensuite analysées avec le logiciel PyCorrFit.

2.5.4 UV/vis, fluorescence

Pour les NPs de rhodamine, les spectres d'absorption et d'émission ont été enregistrés respectivement, sur un spectrophotomètre Cary 4000 Scan ultraviolet–visible (Varian) et un spectrofluoromètre FS5 (Edinburgh Instruments) équipé d'un compartiment thermostaté. Les échantillons ont été excités à 530 nm et l'émission de fluorescence a été enregistrée de 540 à 750 nm. Les rendements quantiques ont été calculés en utilisant la rhodamine 101 dans l'éthanol comme référence (QY=0.9).[180]

Pour les NPs de lanthanides, les spectres d'absorption et d'émission ont été enregistrés respectivement avec un spectrophotomètre Cary 4000 Scan ultraviolet–visible (Varian) et un spectrofluoromètre FluoroMax-4 (Horiba Jobin Yvon) équipé d'un compartiment thermostaté. La longueur d'onde d'excitation a été réglée à 345 nm et l'émission a été enregistrée de 550 à 720 nm. Les rendements quantiques ont été ensuite calculés en utilisant le complexe [Eu(tta)3phen] dans l'acétonitrile comme référence (QY=0.32).

2.5.5 Microscopie TIRF

Pour l'étude du clignotement des NPs, celles-ci ont été déposées sur une surface traitée au préalable avec du polyéthylèneimine (PEI) avant d'être observées par microscopie de fluorescence par réflexion totale interne (TIRF). Le principe de la microscopie TIRF repose sur une illumination de l'échantillon par des ondes évanescentes qui sont générées par la réflexion totale interne de la lumière incidente à l'interface de deux milieux ayant des indices de réfraction différents (figure 17). Seuls les fluorophores compris dans les premiers 100 nm de hauteur seront excités.

Préparation des échantillons : La solution de NPs obtenue après nanoprécipitation a été diluée à une concentration de 6 pM. Après centrifugation (MiniSpin plus, Eppendorf, 12 000 rpm, 15 min), 200 µl de cette solution ont ensuite été déposés dans des puits d'une plaque LabTek® dont la surface en verre a été recouverte de PEI (25k, 1 $g.l^{-1}$ dans tampon Tris pH 7.4) 15 min avant d'être lavée deux fois avec de l'eau Milli-Q. La surface a ensuite été laissée en contact avec de l'eau Milli-Q pendant toute la durée de la microscopie.

Microscopie : L'équipement est composé d'un microscope Olympus IX-71 avec un objectif à immersion d'huile (NA = 1.49, 100×). La source lumineuse d'excitation est un laser DPPS (Cobolt) qui émet en continu à une longueur d'onde de 532 nm à une intensité de 0.5 ou 5 W/cm^2. Le signal de fluorescence a été enregistré avec une caméra EMCCD (ImagEM Hamamatsu) avec un temps d'exposition de 30 ms par image. Les acquisitions ont ensuite été analysées par le logiciel Fiji.

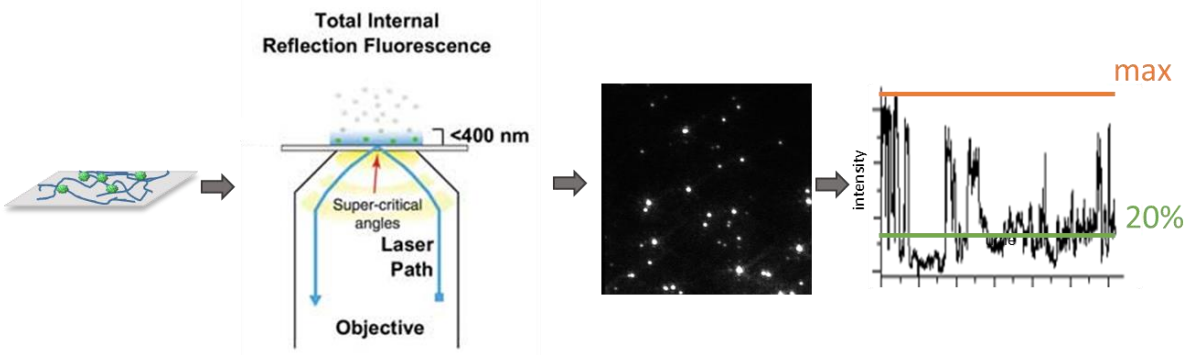

Figure 17. Etude du clignotement des NPs. Après avoir déposé les NPs sur une surface, elles sont imagées par microscopie TIRF. A partir des images obtenues, la variation de l'intensité de fluorescence en fonction du temps est analysée pour chaque spot lumineux. Le clignotement de la particule est défini comme le franchissement au moins une fois d'une limite correspondant à 20 % du maximum d'intensité de fluorescence de la NP. Reproduit à partir de la référence [181].

Analyse des images : L'intensité moyenne des régions d'intérêt (ROIs, cercles de diamètre 5 pixels autour de la localisation de la particule) a été mesurée pour la projection du maximum d'intensité. Le bruit de fond a été soustrait en mesurant l'intensité moyenne des anneaux autour des ROIs. Pour chaque particule localisée, la fluctuation de l'intensité de fluorescence ainsi que celle du bruit de fond sur 30 s ont été mesurées sur les images initiales. Au moins 50 particules ont été analysées par échantillons. La distribution de l'intensité moyenne des NPs a permis d'exclure les agrégats. La variation de l'intensité de fluorescence corrigée par le bruit de fond a été tracée sur R pour chaque NP détectée. Le clignotement de la particule est défini comme le franchissement au moins une fois sur le temps d'acquisition de la limite correspondant à 20 % du maximum d'intensité de fluorescence de la NP.

2.6 Microinjection et microscopie cellulaire

Les cellules HeLa ont été cultivées dans un milieu DMEM supplémenté avec 10 % de FBS, L-glutamine et 1 % de solution d'antibiotiques à 37°C sous atmosphère humidifiée avec 5 % de CO_2. Pour la microinjection, elles ont été ensemencées sur des lamelles en verre (diamètre 16 mm) déposées ensuite dans une plaque 6-puits à une densité de $125x10^3$ celllules/puit pendant 24h. Les cellules HeLa en sous confluence ont ensuite été montées dans une chambre Ludin ((Life Imaging Services, Bâle, Suisse). Les cellules ont été placées sur un microscope Leica DMIRE 2 et les différentes solutions de NPs de 0.5 à 2 nM ont été microinjectées dans le cytoplasme, et plus précisément dans le cytosol, au niveau de la région périnucléaire à l'aide d'un microinjecteur Femtojet/InjectMan NI2 (Eppendorf). L'acquisition a été réalisée soit avec le même équipement (Objectif 100x Plan APO 1.4 NA, lampe Xénon, et caméra Photometrics Prime), soit sur un microsocpe iMIC (Till Photonics) équipé d'une source multi-LED spectra X (Lumencor), un objectif Olympus 60x TIRFM (1.45 NA), et une caméra Flash 4 V2+ (Hamamatsu) après transfert des cellules. Durant l'expérience, les cellules ont été maintenues à 37°C dans une atmosphère humidifiée contenant 5% CO_2 en utilisant un système de contrôle environnemental (Life Imgaging Services). Les vidéos ont été enregistrées sur 60 s avec un temps d'exposition de 50 ms et un binning 2. Les images et vidéos ont été analysées avec le logiciel ImageJ (National Institutes of Health, USA). Pour le suivi de particules individuelles, l'acquisition a été réalisée sur 30 s avec un temps d'exposition de 43 ms pour le microsocpie iMIC ou 50ms pour le microscope Leica DMIRE 2 avec un binning 1. Les trajectoires des NPs ont été obtenues en utilisant le plugin TrackMate pour Fiji.[182] Les courbes de déplacement quadratique moyen (MSD) ont été tracées et extraites avec un script MATLAB pour l'analyse des trajectoires de NPs. Au moins 50 trajectoires ont été analysées par condition sur au moins trois cellules différentes.

Partie 3 : Contrôle de la taille des nanoparticules

3.1 Développement de nanoparticules de taille contrôlée

La taille des particules est un point essentiel à prendre en compte pour les applications en biologie et en particulier pour l'imagerie intracellulaire.[183] Le cytosol est un environnement extrêmement dense en macromolécules et autres constituants cellulaires. La particule fluorescente doit donc être suffisamment petite pour se frayer un chemin à travers le milieu intracellulaire en évitant par la même occasion, les interactions non-spécifiques qui conduiraient inévitablement à une perte de contrôle de la NP.[184] Cependant dans le cas des NPs de polymères fluorescentes, la brillance est également dépendante de la taille des NPs. Plus les NPs sont petites, plus la quantité de fluorophores encapsulés diminue. Il faut donc trouver le bon compromis entre une taille suffisamment petite pour se déplacer dans le cytosol tout en conservant une brillance suffisamment élevée pour une localisation précise dans le temps et l'espace.

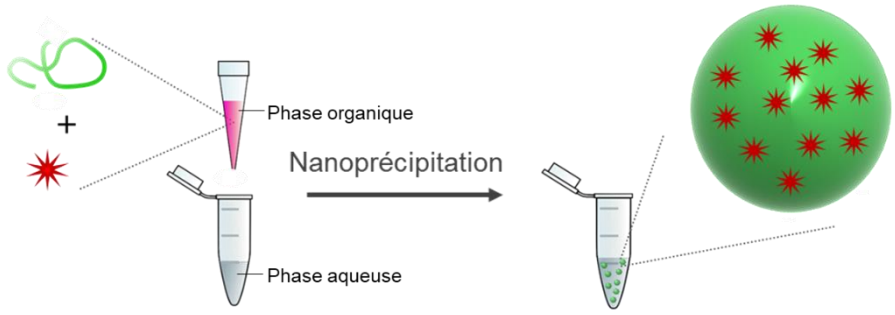

Figure 18. Schéma représentant le principe de la nanoprécipitation et l'encapsulation de fluorophores (en rouge) dans la matrice polymérique (en vert).

Parmi les méthodes de préparation des NPs, la nanoprécipitation permet une encapsulation d'une grande quantité de fluorophores dans la matrice polymérique à partir de polymères préformés (figure 18). Le principe consiste à dissoudre le polymère dans un solvant organique miscible à l'eau. Puis cette solution est ajoutée à un excès de non-solvant du polymère, généralement de l'eau. La diffusion rapide des deux

solvants provoque la précipitation du polymère qui conduit à la formation des premiers noyaux de polymères ou particules primaires auxquelles peuvent venir s'ajouter des chaines de polymère pour faire grossir la particule. C'est un processus cinétiquement contrôlé par différents paramètres tels que la concentration,[185] le type et la vitesse de mélange,[186,187] le type de solvant,[188] la présence et la nature de composés stabilisants.[189] Mais la plupart des NPs formées par nanoprécipitation ne descendent pas en-dessous de 30 nm de diamètre. Dans notre groupe, des NPs de PLGA six fois plus brillantes que les QDs ont été formulées. Même en optimisant le protocole de nanoprécipitation et en diminuant la concentration du polymère, les NPs synthétisées atteignent au mieux 40 nm.[8] Dans la littérature, il est souvent observé que les plus petites NPs sont obtenues en utilisant des polymères ou des tensio-actifs chargés.[190–192] A partir de ces observations, nous avons postulé que le ou les groupements chargés présents sur le polymère pouvaient réduire la taille des particules.

Ci-dessous sont résumées les différentes étapes auxquelles j'ai contribué pour le contrôle de la taille des particules. Ces résultats sont répartis initialement dans trois articles différents. Pour plus de clarté, j'ai donc inséré uniquement l'article principal. Les deux autres publications se trouvent en annexe.

Dans un premier temps nous avons démontré l'influence de un ou deux groupements chargés en fin de chaine du polymère sur la taille des nanoparticules. Nous avons ensuite synthétisé des polymères par polymérisation radicalaire en contrôlant le pourcentage de groupements chargés insérés sur le polymère pour obtenir des tailles de particules $<$ 10 nm. Enfin, l'influence de la composition du polymère, sa concentration et le milieu de nanoprécipitation sur la taille des particules a été explorée plus en détail.

Influence de un ou deux groupements chargés sur la taille

Dans une étude préliminaire, nous nous sommes intéressés à l'influence de groupements chargés portés par la chaine polymérique sur la taille des particules formées par nanoprécipitation. Pour cela nous avons modifié des polymères commerciaux souvent utilisés dans le domaine des biomatériaux : le poly(D,L-lactide-*co*-glycolide) (PLGA), le polycaprolactone (PCL) et le poly(méthacrylate de méthyle) (PMMA). Ces polymères ont été modifiés par des groupements non chargés, ou

chargés dont les groupements carboxylate, sulfonate ou triméthylammonium (figure 19).

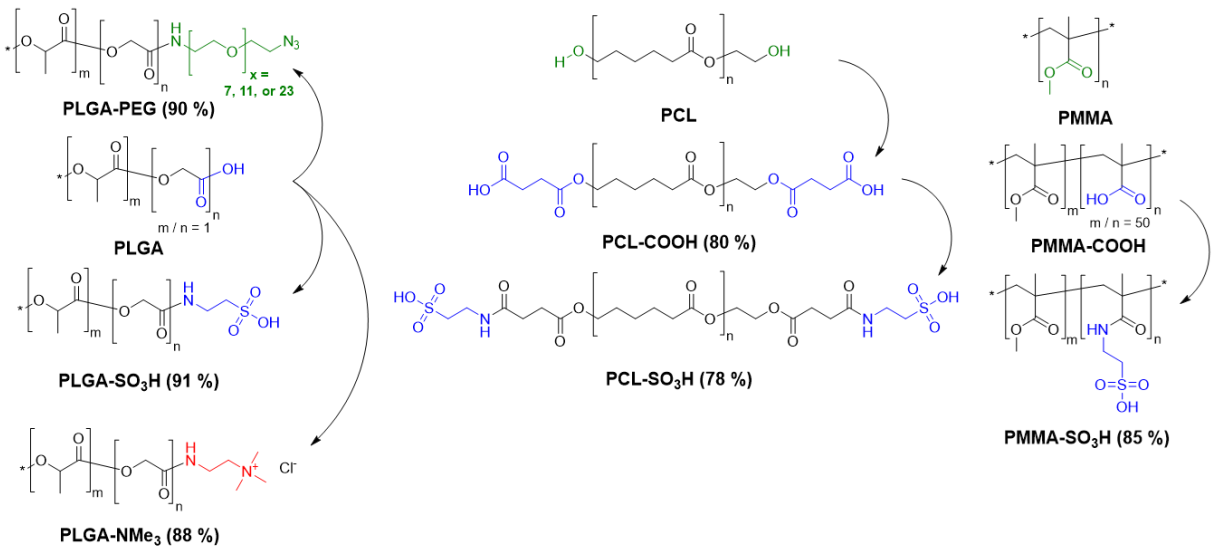

Figure 19. Polymères modifiés chimiquement : le poly(D,L-lactide-co-glycolide) (PLGA), le polycaprolactone (PCL) et le poly(méthacrylate de méthyle) (PMMA) ont été modifiés avec des groupements PEG, carboxylate, sulfonate, et triméthylammonium.

Les polymères obtenus ont été dissous dans l'acétonitrile pour former ensuite des NPs après nanoprécipitation dans l'eau. Les tailles mesurées par DLS sont reportées figure 20. Les indices de polydispersité sont assez faibles $< 0,2$. Pour les trois polymères portant des groupements non chargés, la taille des particules est systématiquement au-dessus de 100 nm. Les polymères portant des groupements carboxylates donnent des particules de diamètre intermédiaire entre 60 et 100 nm. Les polymères portant des groupements sulfonate ou triméthylammonium conduisent aux tailles les plus petites, inférieures à 25 nm. Ici, la nature du polymère n'a, quant à elle, qu'une très faible influence sur la taille des particules. Néanmoins, dans certains cas (que nous verrons plus loin), la composition du polymère peut jouer un rôle plus important sur la taille.

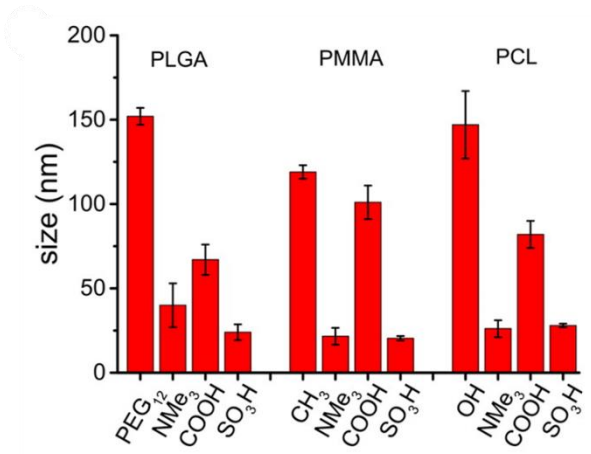

Figure 20. Tailles obtenues par diffusion dynamique de la lumière de trois types de polymères PLGA, PMMA et PCL portant différents groupements chargés ou non. Les tailles sont les moyennes des valeurs obtenues pour trois mesures indépendantes du diamètre moyen pondéré en fonction du volume par DLS. Les barres d'erreurs correspondent à l'écart-type.

Influence de fractions de groupements chargés sur la taille

Par la suite, les polymères PMMA ont été synthétisés par polymérisation radicalaire (figure 21A) nous permettant d'augmenter ou de réduire le pourcentage de groupements chargés introduit sur le polymère. Ainsi trois séries de copolymères de type PMMA ont été synthétisés portant des groupements carboxylate, sulfonate ou triméthylammonium dont le pourcentage varie entre 1 et 10% (mol) (figure 21B). La polymérisation et la fraction de groupements chargés a été suivi par RMN-^{1}H. Les spectres RMN des polymères après purification et séchage révèlent que la fraction des groupements chargés est bien contrôlée par polymérisation radicalaire. Le poids moléculaire moyen en masse mesuré par chromatographie d'exclusion est d'environ 50 000 g.mol^{-1} pour les PMMA-COOH et -SO_3H et 90 000 g.mol^{-1} pour les PMMA-NMe_3.

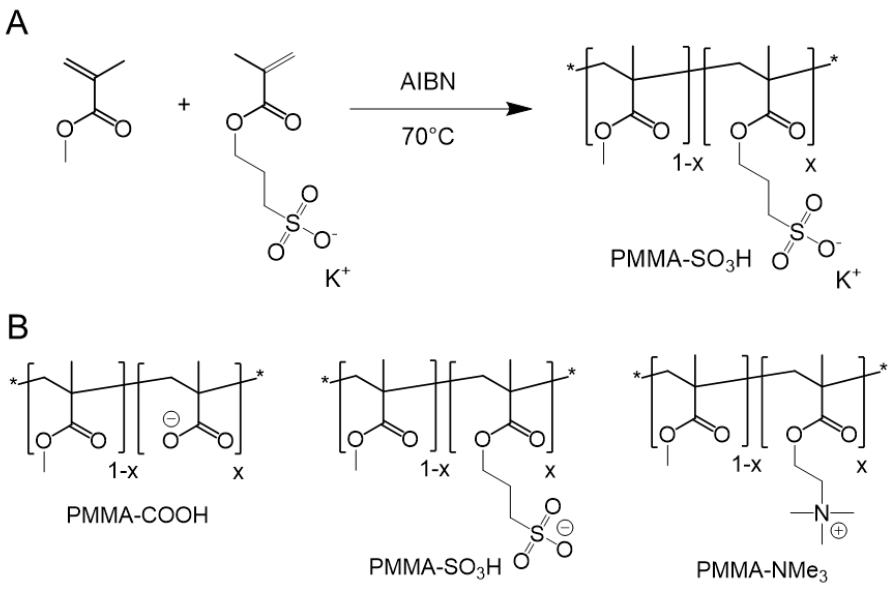

Figure 21. Synthèse (A) par polymérisation radicalaire du PMMA-SO_3H et structure chimique (B) des polymères utilisés.

Après nanoprécipitation dans l'eau, la taille des nanoparticules obtenues a été mesurée par TEM et reportée figure 22. On observe une diminution du diamètre des NPs avec l'augmentation de la fraction de groupements chargés sur le polymère. Au-delà de 5% de groupements -SO_3H ou -NMe_3, la taille des NPs atteint 8 et 7 nm respectivement. La même tendance est observée pour les NPs PMMA-COOH. Toutefois, la taille des NPs de PMMA-COOH est systématiquement plus grande. En effet à 10 % de groupement carboxylate sur le polymère, la taille des NPs descend seulement à 29 nm.

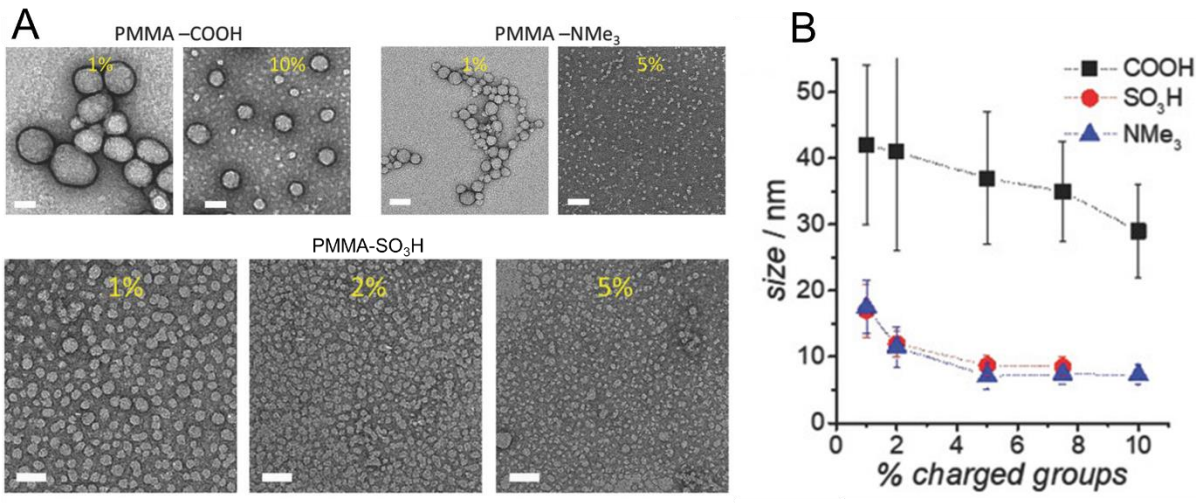

Figure 22. Tailles des NPs obtenues par nanoprécipitation. (A) Images de TEM de NPs de différents polymères dans l'eau. Les barres d'échelle correspondent à 50 nm. (B) Influence de la fraction de groupements chargés sur la taille des particules. Les NPs sont chargées à 10 % en fluorophores R18/F5-TPB. Au moins 200 particules ont été analysées par condition. Les barres d'erreur correspondent à la largeur à mi-hauteur de la distribution.

Influence de la composition et de l'hydrophobie du polymère sur la taille

Afin d'aller plus loin dans la compréhension de l'importance de la chimie des polymères dans le processus de nanoprécipitation, nous avons étudié l'influence de la nature du polymère sur la taille des NPs. Pour cela, nous avons synthétisé par polymérisation radicalaire des copolymères avec différents types et ratios de monomères méthacrylates. Les types de monomères utilisés, hydrophiles, hydrophobes et chargés sont représentés figure 23. Les copolymères synthétisés contiennent généralement un monomère de chaque type à différents pourcentages. La fraction des groupements chargés varie entre 1 et 5 % (mol) pour l'acide méthacrylique (MAA) et est de 1% (mol) pour le méthacrylate de sulfopropyle (SMA). Les fractions de groupements hydrophiles varient de 0 à 75 %. Les polymères ont été analysés par RMN-^{1}H. Les ratios entre groupements hydrophiles et hydrophobes sur les polymères purifiés correspondent aux ratios de monomères ajoutés dans le mélange réactionnel (± 2 %).

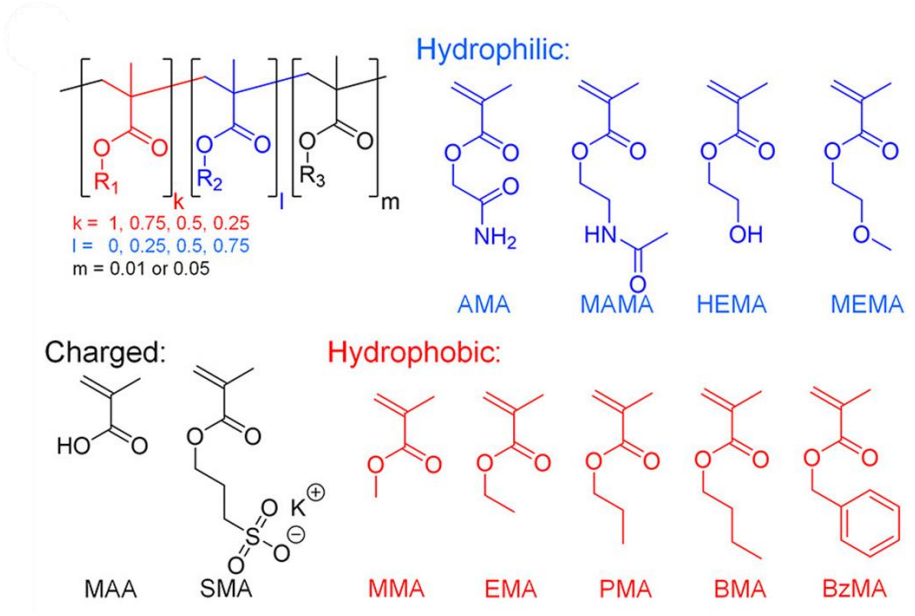

Figure 23. Monomères utilisés pour la conception des copolymères.

Pour chaque polymère, la fraction d'eau critique a été déterminée par mesure de turbidité. Celle-ci a été réalisée par ajout croissant de quantité d'eau aux solutions de polymères dissous dans un mélange acétonitrile/acétone. En parallèle, l'hydrophobie des polymères a été estimé en calculant le coefficient de partage (log P) sur ChemDraw pour quatre unités répétitives. Les fractions d'eau critique sont corrélées aux valeurs de log P pour les différents polymères. Cela signifie que l'hydrophobie globale des polymères est directement liée à la solubilité des polymères dans des mélanges de solvants organiques/aqueux.

Les NPs ont été ensuite formulées par nanoprécipitation dans l'eau et leur taille mesurée par DLS. Pour toutes les combinaisons de monomères, l'augmentation de la fraction hydrophile du polymère conduit à une diminution de la taille des particules (Figure 24A). Les polymères contenant 100% de groupement hydrophobe et 1% de MAA donnent des particules de plus de 100 nm. A 75% de groupements hydrophiles, la taille diminue en dessous de 40 nm.

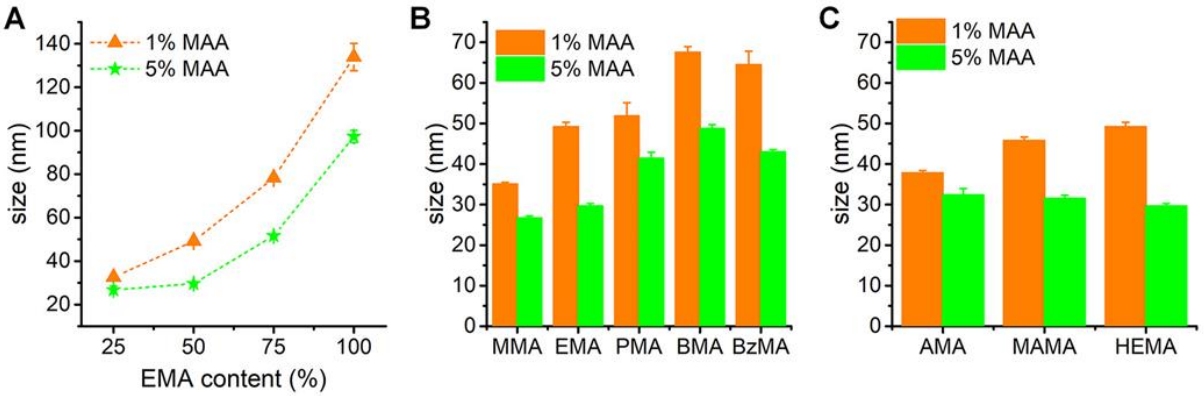

Figure 24. Influence de la composition des copolymères sur la taille des NPs. (A) Influence du ratio de monomères pour le copolymère HEMA-EMA-MAA. (B) Influence du type de monomère hydrophobe pour les copolymères avec 50 % HEMA et 1 ou 5 % MAA. (C) Influence du type de monomère hydrophile pour les copolymères avec 50 % EMA et 1 ou 5 % MAA. Les tailles sont les moyennes des valeurs obtenues pour trois mesures indépendantes du diamètre moyen pondéré en fonction du volume par DLS. Les barres d'erreur correspondent à l'écart-type.

Le type de monomère hydrophobe influence également la taille des particules. Pour une série de copolymères constitués de monomères hydrophiles HEMA et de monomères hydrophobes divers avec un ratio 1:1, le diamètre des NPs résultantes augmente dans l'ordre des monomères hydrophobes suivants : MMA < EMA < PMA < BMA ~ BzMA correspondant à une augmentation de l'hydrophobie (figure 24B). De manière similaire le type de monomère hydrophile a également une influence (figure 24C). Pour un même monomère hydrophobe, la taille des NPs augmente dans l'ordre AMA < MAMA < HEMA, toujours avec l'augmentation de l'hydrophobie. Ceci est vrai pour les copolymères portant 1 % de groupements chargés MAA. Mais à 5 % de MAA, l'effet du groupement chargé prend le dessus et l'influence de l'hydrophobie des monomères hydrophiles disparait complètement.

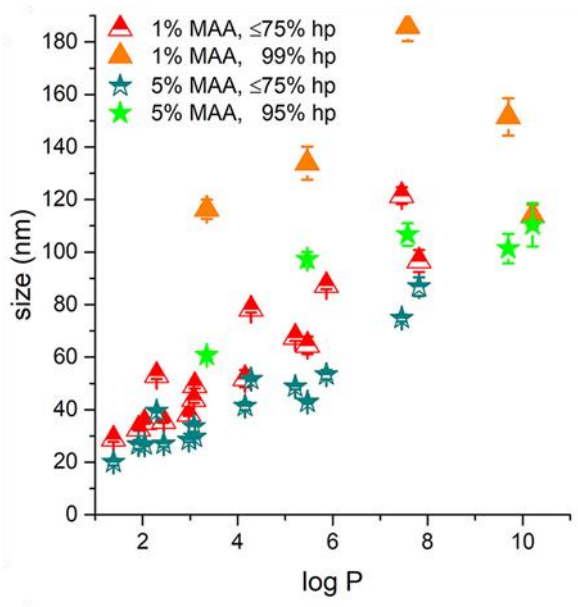

Figure 25. Tailles des NPs en fonction des valeurs de log P calculées des copolymères. Les résultats sont donnés pour les copolymères contenant 1 % (triangles) et 5 % (étoiles) de MAA. Les symboles mi-remplis correspondent aux NPs obtenues à partir des polymères contenant des monomères hydrophiles et hydrophobes (≤ 75% hp). Les symboles pleins sont utilisés pour ceux contenant uniquement le monomère hydrophobe (99 ou 95 % hp). Les barres d'erreur correspondent à l'écart-type sur au minimum trois mesures.

Dans la Figure 25, la taille des NPs obtenues par nanoprécipitation est tracée en fonction de l'hydrophobie globale du polymère et résume les résultats de cette étude. Nous pouvons établir que l'influence de la chimie des polymères sur la taille s'observe à plusieurs niveaux. (i) De manière générale, la taille augmente avec l'hydrophobie du polymère. (ii) A hydrophobies égales, la taille est plus petite pour les polymères contenant de plus grands pourcentages en groupements chargés. L'influence de l'hydrophobie est également plus marquée pour les faibles pourcentages de groupements chargés (1 % MAA) que pour les polymères portant plus de monomères chargés (5 % MAA). (iii) Les polymères composés uniquement de groupements hydrophobes et chargés donnent des NPs beaucoup plus grandes. L'influence de l'hydrophobie globale du polymère est également moins nette pour ces polymères.

Influence du milieu et de la concentration en polymère

Lorsque les NPs sont formulées dans le tampon phosphate à pH 7,4, la taille diminue assez fortement pour les polymères -COOH (figure 26A). Pour le PLGA par exemple, la taille passe de plus de 60 nm dans l'eau à 40 nm dans le tampon phosphate.

L'augmentation du pH du milieu de nanoprécipitation permet d'ioniser complétement le groupement -COOH et donc d'augmenter la charge nette sur le polymère qui se traduit par une diminution de taille des NPs. Cela explique également que les NPs des polymères -COOH sont systématiquement plus grandes que les NPs -SO_3H dans l'eau (figure 20). En effet le groupement COOH n'est pas complètement déprotoné dans l'eau contrairement au groupement SO_3H. A l'inverse l'ajout de sel dans la phase aqueuse de précipitation augmente la taille des NPs de PMMA-SO3H 1% qui passe de 17 nm à 32 nm avec 30 mM NaCl (figure 26B). Le NaCl, ici, permet de masquer les groupements chargés et d'augmenter la taille des particules pour un même polymère.

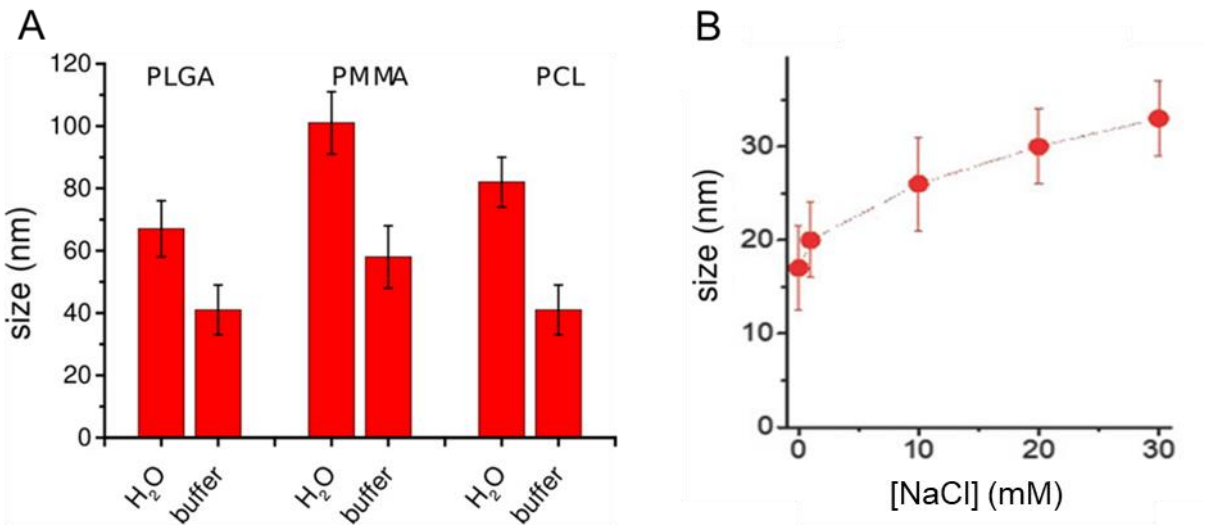

Figure 26. Influence du milieu : (A) tailles de NPs de polymères carboxylates obtenues dans différents non-solvants : l'eau ou le tampon phosphate à pH 7,4. Les tailles sont les moyennes des valeurs obtenues pour trois mesures indépendantes du diamètre moyen pondéré en fonction du volume par DLS. Les barres d'erreurs correspondent à l'écart-type. (B) Influence de la concentration en NaCl dans le milieu de précipitation sur la taille des NPs PMMA-SO_3H 1%. Les NPs sont chargées à 10 % en fluorophores R18/F5-TPB. Au moins 200 particules ont été analysées par condition. Les barres d'erreur correspondent à la largeur à mi-hauteur de la distribution.

Un autre paramètre ayant un effet sur la taille des NPs est la concentration du polymère. En réduisant la concentration du polymère dans l'acétonitrile de 2 $g.L^{-1}$ à 0,2 $g.L^{-1}$, nous pouvons réduire la taille jusqu'à 14 nm pour les NPs de PMMA-SO_3H (figure 27). Le système atteint cependant ses limites lorsqu'on arrive à une concentration de 0.1 $g.L^{-1}$ en polymère. A cette concentration, nous observons une augmentation de la taille moyenne des NPs qui résulte d'une distribution de taille beaucoup plus hétérogène.

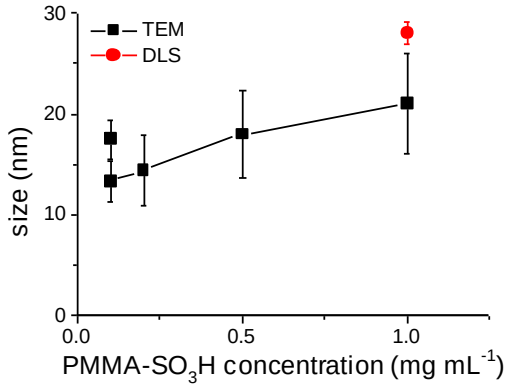

Figure 27. Taille des NPs de PMMA-SO_3H mesurées par DLS et TEM. Les tailles sont les moyennes des valeurs obtenues pour trois mesures indépendantes du diamètre moyen pondéré en fonction du volume. Les valeurs de TEM correspondent à la moyenne des valeurs d'au moins 50 particules. Les barres d'erreurs correspondent à l'écart-type.

L'ensemble de ces observations ont permis de mieux comprendre les paramètres qui interviennent sur le mécanisme de formation des NPs par nanoprécipitation.[185,193,194] Lorsque les phases aqueuse et organique diffusent l'une dans l'autre, cela crée une surpersaturation conduisant à une nucléation spontanée, c'est-à-dire la formation de noyaux primaires de polymère. Les particules grossissent ensuite par incorporation de nouvelles chaines de polymère au sein des NPs. En absence de stabilisation des NPs, celles-ci peuvent agréger. La taille finale des NPs résulte alors des taux relatifs de nucléation, grossissement et d'agrégation. Le taux de nucléation dépend essentiellement de la tension de surface et de la supersaturation.

En supposant que les groupements chargés se situent préférentiellement à la surface des particules, la présence de groupements chargés dans le polymère diminue la tension de surface lors de la formation des nucléi qui a pour conséquence d'augmenter le taux de nucléation. Les groupements hydrophiles permettent également de stabiliser les particules à leur niveau mais moins efficacement.

A partir des tailles déterminées par TEM, nous pouvons estimer le nombre de groupements chargés par particule. Ainsi pour les particules de PMMA-SO_3H ou PMMA-NMe_3, le nombre de groupements –SO_3H ou NMe_3 par particule est de 100 quelle que soit la taille de la particule. Cela signifie qu'une fois cette limite atteinte, la phase de grossissement des particules s'arrête, due probablement à la répulsion

électrostatique entre la surface chargée des particules et les groupements chargés des polymères. Dans l'eau, la longueur de Debye est > 10 nm. De par leurs petites tailles, toutes les charges présentes à la surface de la particule participent à la répulsion d'un nouvel ajout de chaine polymérique. Il en est de même pour l'agrégation des particules qui est limitée par la répulsion des particules chargées entre-elles. Pour les NPs de PMMA-COOH, la charge effective dans l'eau est plus faible et les particules sont également plus grandes. Le grossissement de la NP ne s'arrête que lorsqu'une densité de charge de surface donnée est atteinte. Plus le polymère sera donc chargé, plus les particules seront petites résultant d'un taux de nucléation élevé associé à des taux de grossissement et d'agrégation bas. Au contraire, l'ajout de sel dans la phase aqueuse de nanoprécipitation permet de diminuer les forces de répulsion conduisant à une augmentation de taille des NPs pour un polymère donné. L'augmentation de la taille avec l'hydrophobie du polymère est liée à l'augmentation de la supersaturation du polymère. Cela semble favoriser le grossissement des particules par rapport à la nucléation. Cela explique également l'augmentation de la taille lorsqu'on augmente la concentration en polymère.

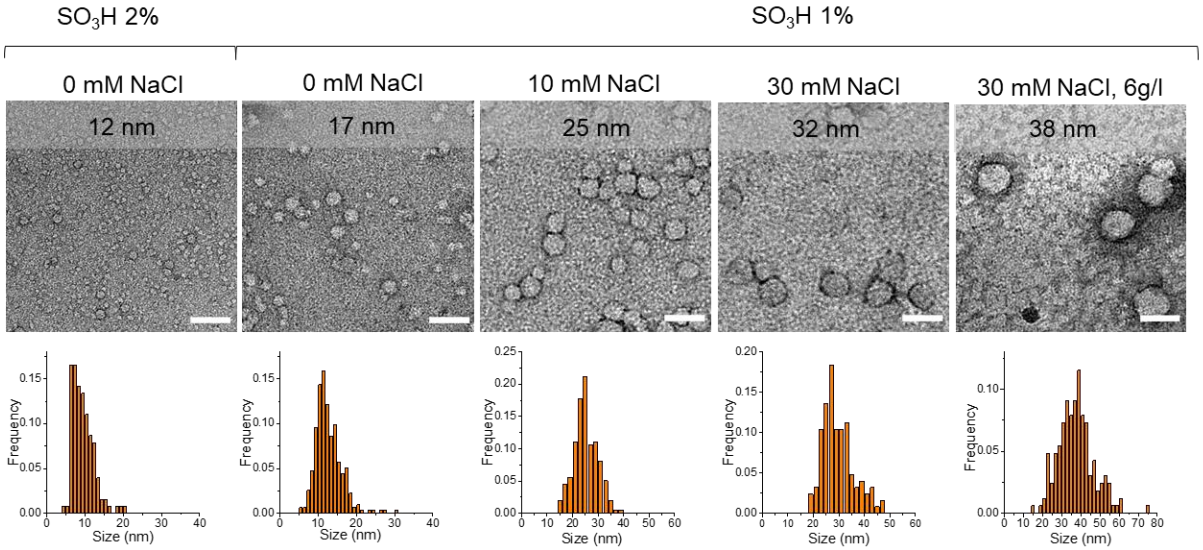

Figure 28. Images de TEM des NPs de PMMA-SO_3H 1 et 2 % faites dans l'eau ou dans $10x10^{-3}$ ou $30x10^{-3}$ M NaCl. La nanoprécipitation a été réalisée avec une concentration en polymère de 2 $g.L^{-1}$ excepté pour les NPs de 38 nm pour lesquelles la concentration en polymère est de 6 $g.L^{-1}$. La taille indiquée correspond à la taille moyenne sur au moins 100 NPs. Les distributions de taille sont indiquées en bas de chaque image. Barre d'échelle : 50 nm.

La figure 28 montre un exemple d'une gamme de taille pour un polymère de PMMA-SO_3H. En variant la fraction de groupements chargés sur le polymère, sa concentration et le milieu de précipitation, nous obtenons des NPs dont la taille varie entre 12 et 38 nm.

Pour conclure, l'introduction de quelques groupements chargés sur les polymères influence fortement la formation des NPs par nanoprécipitation. Outre les groupements chargés, la composition générale du polymère influe également considérablement la taille des particules obtenues. Selon le cas, l'hydrophobie du polymère va prendre le dessus sur l'influence du groupement chargé ou inversement. Ces deux paramètres combinés permettent d'obtenir une gamme de taille de NPs très large. A plus faible niveau, le milieu de nanoprécipitation et la concentration du polymère jouent un rôle également sur la taille. Ces deux derniers paramètres vont plutôt être utilisés pour moduler plus finement le diamètre des particules. Grâce à cela, nous pouvons formuler des NPs ultrapetites $<$ 15 nm. Nous sommes également en mesure de contrôler efficacement la taille des NPs et de produire des gammes de taille de NPs pour un polymère donné ou des gammes de NPs de même taille mais de composition (en termes de polymère) différente.

Une partie de ces résultats a été publié *ACS Nano* et est joint ci-dessous. Une autre partie de ces résultats a été publié dans les articles joints en annexe :

Article 2 : Protein-Sized Dye-Loaded Polymer Nanoparticles for Free Particle Diffusion in Cytosol. Andreas Reisch, Doriane Heimburger, Pauline Ernst, Anne Runser, Pascal Didier, Denis Dujardin, Andrey S. Klymchenko. *Advanced Functional Materials* **28**, 1805157 (2018).

Article 3 : Controlling Size and Fluorescence of Dye-Loaded Polymer Nanoparticles through Polymer Design. Rosiuk, V., Runser, A., Klymchenko, A. & Reisch, A. *Langmuir* **35**, 7009–7017 (2019).

Article 1 : Charge-Controlled Nanoprecipitation as a Modular Approach to Ultrasmall Polymer Nanocarriers: Making Bright and Stable Nanoparticles.

ARTICLE

Charge-Controlled Nanoprecipitation as a Modular Approach to Ultrasmall Polymer Nanocarriers: Making Bright and Stable Nanoparticles

Andreas Reisch,* Anne Runser, Youri Arntz, Yves Mély, and Andrey S. Klymchenko*

Laboratoire de Biophotonique et Pharmacologie, UMR 7213 CNRS, Université de Strasbourg, Faculté de Pharmacie, 74 Route du Rhin, 67401 Illkirch, France

ABSTRACT Ultrasmall polymer nanoparticles are rapidly gaining importance as nanocarriers for drugs and contrast agents. Here, a straightforward modular approach to efficiently loaded and stable sub-20-nm polymer particles is developed. In order to obtain ultrasmall polymer nanoparticles, we investigated the influence of one to two charged groups per polymer chain on the size of particles obtained by nanoprecipitation. Negatively charged carboxylate and sulfonate or positively charged trimethylammonium groups were introduced into the polymers poly(D,L-lactide-*co*-glycolide) (PLGA), polycaprolactone (PCL), and poly(methyl methacrylate) (PMMA). According to dynamic light scattering, atomic force and electron microscopy, the presence of one to two charged groups per polymer chain can strongly reduce the size of polymer nanoparticles made by nanoprecipitation. The particle size can be further decreased to less than 15 nm by decreasing the concentration of polymer in the solvent used for nanoprecipitation. We then show that even very small nanocarriers of 15 nm size preserve the capacity to encapsulate large amounts of ionic dyes with bulky counterions at efficiencies >90%, which generates polymer nanoparticles 10-fold brighter than quantum dots of the same size. Postmodification of their surface with the PEG containing amphiphiles Tween 80 and pluronic F-127 led to particles that were stable under physiological conditions and in the presence of 10% fetal bovine serum. This modular route could become a general method for the preparation of ultrasmall polymer nanoparticles as nanocarriers of contrast agents and drugs.

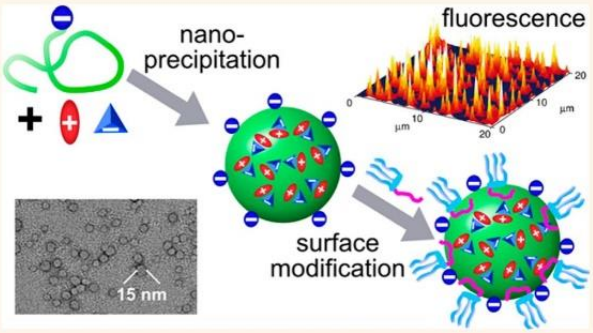

KEYWORDS: polymer nanoparticles · nanocarriers · size · nanoprecipitation · encapsulation efficiency · fluorescent nanoparticles · surface modification

In the past decades, polymer nanoparticles (polymer NPs) have gained a high degree of importance as carriers in drug delivery.[1−3] They allow facile encapsulation of a vast choice of small molecules and their controlled release over time and/or following external stimuli. However, this research was mainly focused on NPs in the range of 50 to 250 nm, because they should be small enough to avoid fast clearance by the reticuloendothelial system,[4] but large enough to avoid rapid elimination through the kidneys.[5] Though the field of NPs below 50 nm is underexplored, recent works showed that these NPs may have a great future in biomedical research. First, the enhanced permeation and retention effect (EPR) that allows passive targeting of tumors is further enhanced for NPs of 50 nm and less.[6−8] Second, some NPs of very small size can enter cells by crossing directly the membrane barrier,[9,10] unlike larger particles, which enter the cells by endocytosis or pinocytosis.[11] Finally, polymeric nanocarriers are rapidly gaining interest as contrast agents and especially as ultrabright fluorescent markers,[12−15] a field, up to now, dominated by inorganic particles especially by quantum dots (QDs).[16,17] For fluorescence imaging, NPs should be as small as possible, in order to be useful for detecting/tracking biomolecules[18,19] and super-resolution microscopy,[15,20] while being able to access small intracellular compartments.[21] These

* Address correspondence to andreas.reisch@unistra.fr, andrey.klymchenko@unistra.fr.

Received for review January 12, 2015 and accepted April 20, 2015.

Published online April 20, 2015
10.1021/acsnano.5b00214

© 2015 American Chemical Society

applications require robust and flexible synthesis of nanocarriers, combining ultrasmall size, efficient loading, adjustable core and surface properties.[18,22] The latter have notably to be adapted to the use in biological environments, which impose challenges in view of particle stabilization and suppression of nonspecific interactions.[23,24]

The classical techniques used for the preparation of NPs below 50 nm are based on *in situ* polymerization (notably miniemulsion and microemulsion polymerization)[25,26] or on the formation of polymeric micelles from block copolymers.[27−30] Polymerization approaches have several limitations: (1) the molecules have to be stable in the conditions of polymerization; (2) the quantity of remaining monomers is difficult to control; and (3) relatively large concentrations of surfactant are needed, which complicates the control of the NP surface chemistry. In contrast, polymeric micelles can be directly assembled from block copolymers containing polyethylene glycol (PEG) as the hydrophilic part that forms a biocompatible shell preventing aggregation and nonspecific interactions.[31] However, achieving ultrasmall polymeric micelles requires generally short block copolymers with a high ratio of the hydrophilic to the hydrophobic block length.[32,33] This leads to a thick shell with respect to the core and a higher solubility of the individual block copolymers in water, thus decreasing the encapsulation efficiency and the stability of the resulting NPs, as well as increasing unwanted fast initial (burst) release of the encapsulated compounds.[34−39]

An alternative and straightforward approach for producing loaded polymer NPs is nanoprecipitation, also called solvent displacement. Nanoprecipitation only requires dissolving the polymer together with the small molecule cargo in a water miscible solvent, and adding this solution into a nonsolvent for the polymer, most often water.[40,41] Diffusion of the solvent into the aqueous phase (and of the water into the organic phase) leads to supersaturation and thus to the formation of polymer NPs encapsulating the cargo molecules. This simple and flexible protocol makes nanoprecipitation an attractive technique for producing loaded polymer NPs.[22,42−45] However, most particles formed by this technique have sizes in the range of 50 to 500 nm.[25,41,46−50] Recently, we described the synthesis of 40 nm NPs from poly(D,L-lactide-*co*-glycolide) (PLGA) by optimizing the mixing protocol and decreasing the polymer concentration.[15] This protocol enabled preparation of fluorescent polymer NPs several times brighter than QDs. We hypothesized that the charge at the end of the polymer chain might help in reducing the particle size. This is in line with scattered data in the literature, where the smallest particles are often obtained using polymers bearing charged groups or using charged surfactants.[41,46,51−53] However, no systematic study on the influence of polymer charge is available, and polymer charge has not been exploited to prepare ultrasmall polymer NPs.

In the present work we propose a modular approach for preparation of ultrasmall NPs with efficient dye loading based on charge-controlled nanoprecipitation and further stabilization of the NPs by surfactants. We first showed that nanoprecipitation into ultrasmall NPs can be controlled by one to two charged groups in a polymer. The concept was validated on polymers frequently used in the biomaterials field, namely poly(D,L-lactide-*co*-glycolide) (PLGA) and polycaprolactone (PCL), two biodegradable polyesters, and poly(methyl methacrylate) (PMMA), a nonbiodegradable, acrylic polymer. Optimizing the experimental conditions enabled preparation of particles of ~15 nm mean diameter. Despite their small size, the particles encapsulated almost quantitatively large amounts of dyes, leading to NPs more than 10 times as bright as QDs. Finally, the NP stability in biological media (salts and serum proteins) was ensured using PEGylated amphiphiles that formed very thin protective shells at the particle surface. Thus, our simple two-step modular approach enables preparation of ultrasmall polymer NPs stable in biological media and featuring excellent fluorescence brightness due to efficient encapsulation of organic dyes.

RESULTS

Modification of Polymers with Different Charged Groups. In order to investigate the influence of the charge of the polymer end groups, we modified the chain ends of PLGA and PCL (Figure 1). The PLGA used had one terminal carboxylic acid group, which allowed us introducing end groups through amide coupling using HBTU and HOBt with the corresponding amines: (1) amine terminated PEGs, to introduce neutral PEG with different chain lengths; (2) (2-aminoethyl)trimethylammonium chloride, to introduce positively charged trimethylammonium groups; and (3) taurine, to introduce negatively charged sulfonate groups. In order to evaluate the degree of modification of the end groups we employed NMR spectroscopy (Figure 2, Supporting Information Figure S1 for PCL and PMMA). For instance, the introduction of a PEG comprising 24 ethylene glycol (CH_2CH_2O) units led to the appearance of signals at 3.66, 3.64, 3.48, and 3.38 ppm corresponding to the CH_2 groups of the PEG. Together the intensity of these signals was 0.44 compared to one proton in one of the repeat units. The expected value for the total of 48 CH_2 groups of a PEG of 24 units at the end of a chain containing 185 lactic and 185 glycolic acid units would be $1/185 \times 2 \times 48 = 0.52$. This yields a degree of modification of the terminal acid groups of the PLGA of 85%. Taking into account that the reprecipitation procedure probably led to an increase of the mean molecular weight of the polymer, the actual degree of modification might even be higher than 85%. Similar

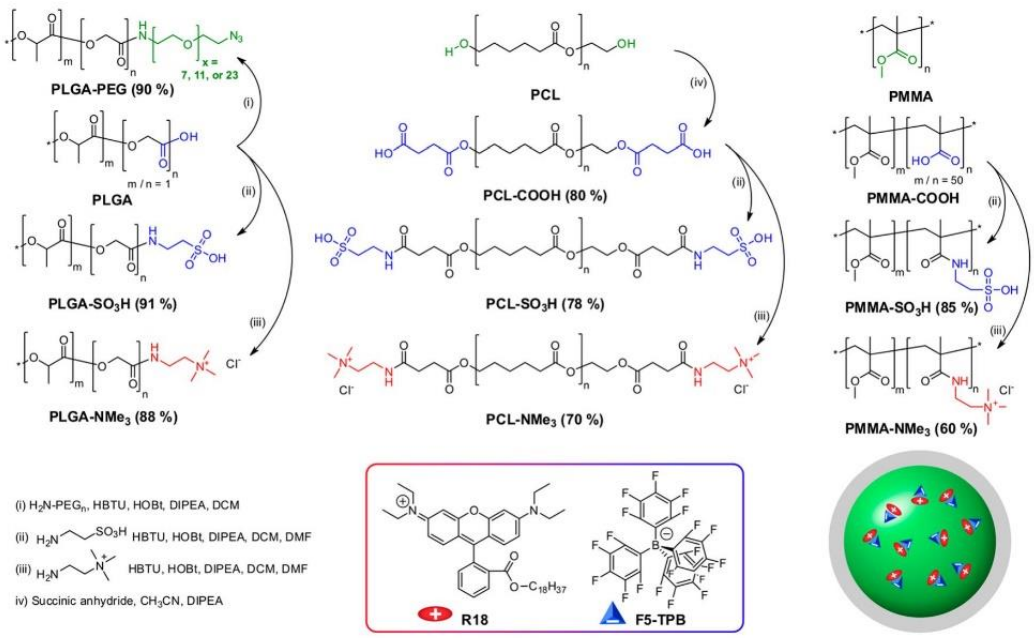

Figure 1. Chemically modified polymers used in this study and schematic view of synthesis of dye loaded NPs. Poly(D,L-lactide-*co*-glycolide) (PLGA) bearing a carboxylate group at one chain end, polycaprolactone (PCL) bearing hydroxyl groups at both chain ends, and a copolymer of poly(methyl methacrylate) (PMMA) with methacrylic acid were modified with PEG, carboxylate, sulfonate, and trimethylammonium groups. A salt of rhodamine B octadecyl ester (R18) with tetrakis-(pentafluorophenyl)borate (F5-TPB) as counterion was used as dye for encapsulation.

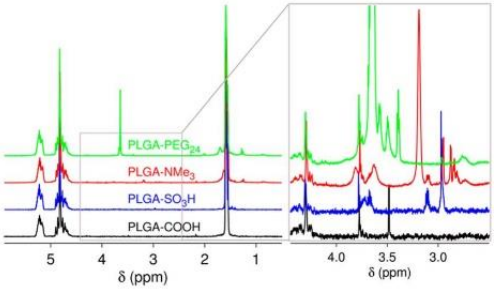

Figure 2. ^{1}H NMR spectra of parent PLGA (PLGA-COOH) and PLGA modified with different terminal groups.

analysis was applied to the other types of modification, yielding a degree of modification of 88 and 90% for trimethylammonium and sulfonate groups, respectively. The PCL used bears two terminal hydroxy groups, which were reacted with succinic anhydride to introduce carboxyl functionalities. The resulting spectra showed a multiplet at 2.63 ppm attributed to the CH_2 groups of the succinic amide (Supporting Information Figure S1). The associated intensity gave a degree of modification of around 80%. The resulting PCL-COOH was then reacted with taurine and 2-(aminoethyl)trimethylammonium chloride in the same way as PLGA, giving degrees of modification of 77 and 70% for introduction of the sulfonate and trimethylammonium groups, respectively, which accounts for the modification of both chain ends (*i.e.*, about 1.5 groups per chain). As a carboxylate bearing form of PMMA we used a copolymer of methyl methacrylate with 1.3% methacrylic acid (Figure 1), which corresponds on average to 2 carboxylate groups per chain. Reaction with taurine and 2-(aminoethyl) trimethylammonium chloride yielded a degree of modification of about 85 and 60%, respectively.

Influence of the End Groups on Particle Size and Zeta-Potential. The influence of a single polar group at the polymer chain end on the size of NPs, made by nanoprecipitation, was then investigated. Earlier we showed that nanoprecipitation of PLGA-COOH from acetonitrile solution into 20 mM phosphate buffer gave ~40 nm particles. To maximize the effect of charge we first performed nanoprecipitation of PLGA polymers bearing different end groups in Milli-Q water. Dynamic light scattering (DLS) showed that the size of the obtained NPs decreased in the following order with respect to the end groups PEG_{12} > PEG_{24} > COOH > NMe_3 > SO_3H (Figure 3a), for PLGA polymers of two different molecular weights (7000 and 24 000) (Figure 3). The size decreased from 150 nm for PEG_{12} end groups to 25 nm for SO_3H end groups. Noticeably, NPs obtained from PLGA-COOH, *i.e.*, the parent PLGA, were the largest among polymers bearing charged groups. Transmission electron microscopy (TEM) confirmed the observed trends in the particle sizes (Figure 3c), but gave somewhat smaller mean size values as compared to DLS data. Though the polydispersity index given by DLS remained below 0.2 for all particles, TEM showed some inhomogeneities in the

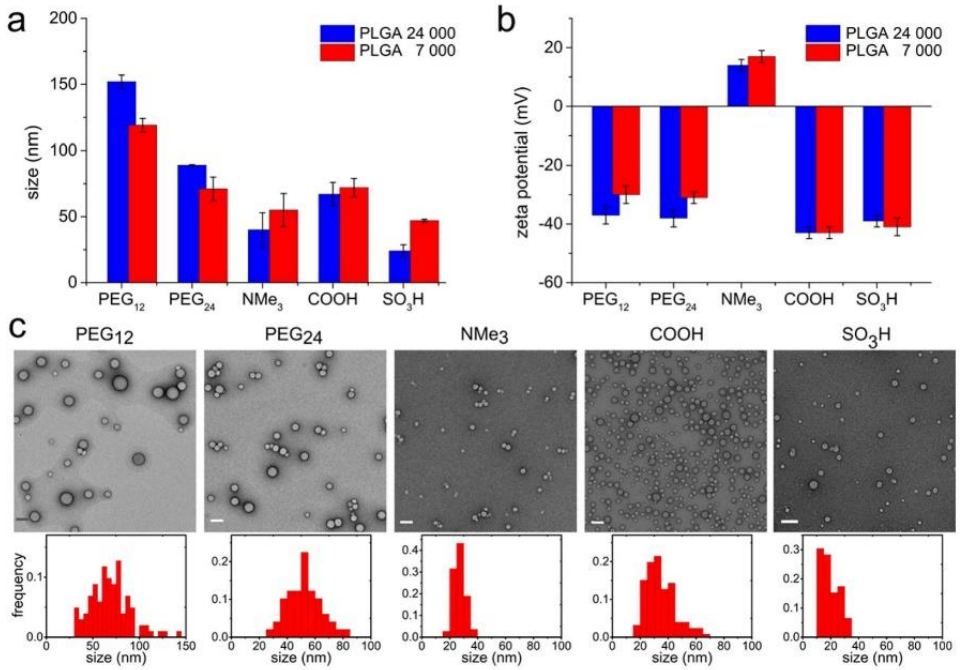

Figure 3. Influence of the end groups on size and zeta potential of PLGA nanoparticles. (a) Size and (b) zeta potential of nanoparticles made from PLGA with different end groups as measured by dynamic light scattering. Nanoparticles were made from PLGA of two different molecular weights (24 000 and 7000). (c) TEM images and size histograms of nanoparticles from PLGA 24 000 with different end groups. In all cases the PLGA concentration was 2 mg mL^{-1} in acetonitrile, and water was used as the nonsolvent. Values for the size are averages of volume distribution mean values; the error bars correspond to s.e.m. The scale bars correspond to 100 nm.

particle sizes for the PEGylated PLGA. The zeta potentials of the obtained NPs were clearly negative for PLGAs with carboxy and sulfonate end groups (−40 mV) and positive for PLGA-NMe$_3$ (+15 mV) (Figure 3b). In the case of PLGA−PEG, they were between −30 and −40 mV. The NPs thus showed a general tendency to be negatively charged, probably due to the ~10% remaining unreacted carboxy groups and deprotonation at the particle surface. Interestingly, uncharged PLGA−PEG gave smaller NPs for lower molecular weight, while charged PLGA polymers, especially bearing amine and sulfonate groups, gave smaller NPs for higher molecular weight (Figure 3a).

We then investigated whether this behavior as a function of the charge was limited to PLGA, or if it occurred more generally for different types of polymer backbones. We, hence, chose two other polymers, PCL and PMMA frequently used in biomedical applications. The former is, as PLGA, an aliphatic polyester, yet with a longer hydrocarbon chain between the ester groups, making it more hydrophobic and crystalline. PMMA is an acrylate polymer with an all carbon backbone characterized by a relatively high glass transition temperature >100 °C. For PCL the charged groups were introduced at the chain ends, though in this case both ends were modified. On the other hand, in PMMA the charged groups occurred at random positions along the chain. As for PLGA, the particle size of modified PMMA and PCL depended strongly on the nature of the polar group (Figure 4). For all three polymers the size of particles made from uncharged chains was largest, being typically above 100 nm. Carboxylate bearing polymers led to medium-sized particles between 60 and 100 nm. The TEM images of particles from uncharged and carboxy PMMA revealed a strong tendency of aggregate formation (this also made an analysis of the particle sizes difficult). Sulfonate and trimethylammonium-bearing polymers gave the smallest particles with sizes typically below 25 nm. The influence of one to two charged groups per chain thus outweighed largely the influence of the polymer type on the particle size. The only noticeable influence of the polymer type was that a minor population of larger particles (about 1% by volume of 250 nm particles) was systematically observed by DLS for PCL and its derivatives.

In the light of the small influence of the polymer type and molecular weight on particle size, the strong difference between sulfonate and carboxylate groups was surprising. We hypothesized that this might be due to the carboxylate group being protonated more readily, so that its (average) charge is reduced. Our earlier studies showed effectively that in phosphate buffer at pH 7.4, in which the carboxylate groups should be completely ionized, PLGA gives much smaller particles (~40 nm)[15] than in Milli-Q water, reported

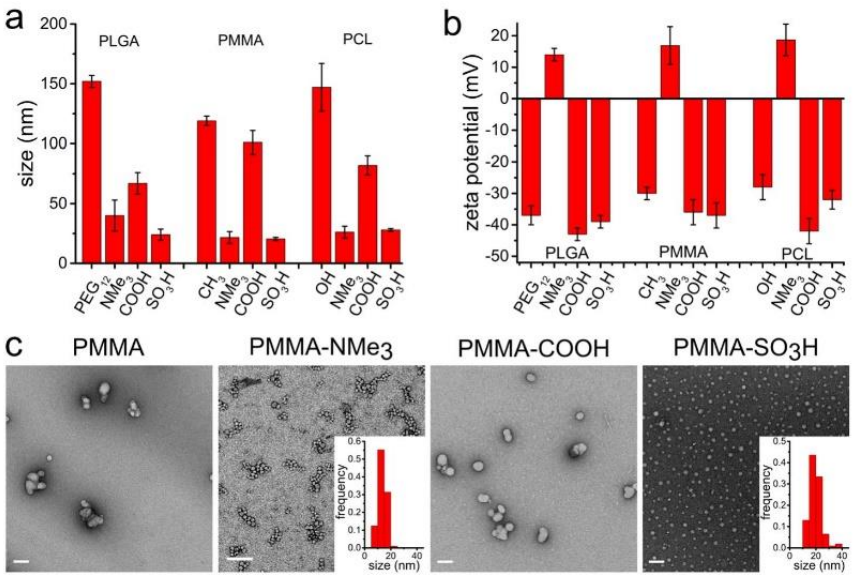

Figure 4. Influence of the end groups on size and zeta potential of nanoparticles from different polymers. (a) Size and (b) zeta potential of nanoparticles made from PLGA, PMMA, and PCL with different end or side groups as measured by dynamic light scattering. Nanoparticles were made using 2 mg mL^{-1} of PLGA (24 000) and 1 mg mL^{-1} for the other polymers in acetonitrile and water as the nonsolvent. (c) TEM images and size histograms of nanoparticles from PMMA, PMMA-NMe$_3$, PMMA-COOH, and PMMA-SO$_3$H. Values for the size are averages of volume distribution mean values; the error bars correspond to s.e.m. The scale bars correspond to 100 nm.

here. Nanoprecipitation of all three carboxylate bearing polymers in phosphate buffer at pH 7.4 showed indeed that the obtained particles were in the range of 40 to 55 nm as measured by DLS, and thus significantly smaller than in Milli-Q water (Figure 5). This indicated that the observed difference between sulfonate and carboxylate groups in water was effectively due to the carboxylate groups being not completely deprotonated and hence bearing fewer charges.

By introducing one to two charged groups per polymer chain we were hence able to reduce the size of the polymer NPs made by nanoprecipitation from over 100 to less than 25 nm. In order to decrease their size further, we then reduced the concentration of the polymer in acetonitrile for two representative examples: PLGA-COOH (M_n 7000) and PMMA-SO$_3$H. This led to very dilute particle solutions that could not be measured with high precision using DLS. Atomic force microscopy (AFM) and TEM were thus used instead. Decreasing the concentration did lead to a decrease of the particle size (Figure 6, Supporting Information Figure S2 and S3). For PLGA-COOH a decrease of the concentration down to 0.2 mg mL^{-1} decreased the mean diameter to about 14 nm. When the concentration was decreased further, no particles were detected by AFM. We could speculate that at too low concentrations the majority of the polymer was adsorbed on the surface of the sample tube. In the case of PMMA-SO$_3$H the particle diameter could be decreased to 14.5 nm when decreasing the polymer concentration to 0.2 mg mL^{-1}. When the concentration was further

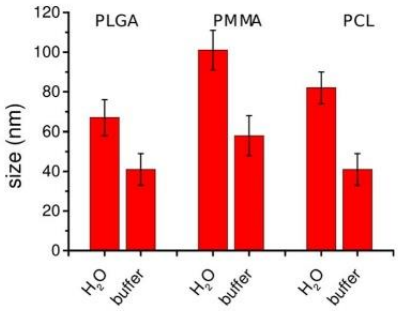

Figure 5. Influence of the nonsolvent on the particle size for carboxylate bearing polymers. Nanoparticles were made using solutions in acetonitrile (2 mg mL^{-1} for PLGA, 1 mg mL^{-1} for the other polymers) and either water or 20 mM phosphate buffer (pH of 7.4) as nonsolvent. Values are averages of volume distribution means; the error bars correspond to s.e.m.

reduced to 0.1 mg mL^{-1}, there was a further decrease of the size but only for a part of the NPs, while another part of the particles showed larger sizes of around 18 nm (Figure 6b, Supporting Information Figure S3), thus indicating that again the system was close to the limits of controlled particle formation.

Ultrasmall Nanocarriers as Fluorescent Nanoparticles. In the next step we verified whether charge controlled nanoprecipitation is suitable for encapsulating molecules in our ultrasmall nanoparticles. As a model system we chose a fluorescent dye which can be readily detected and should lead to dye-doped fluorescent nanoparticles—organic analogues of quantum

dots. The selected fluorescent dopant was a salt of a cationic dye, rhodamine B octadecyl ester (R18), with a bulky hydrophobic counterion, tetrakis(pentafluorophenyl)borate (F5-TPB) (Figure 1). In this system the hydrophobic counterion plays the role of a spacer that prevents aggregation-induced self-quenching of ionic dyes and facilitates their encapsulation.[15] Encapsulation is achieved simply by mixing the dye solution at the desired concentration with the polymer solution in acetonitrile followed by nanoprecipitation. Using ultracentrifugation, we were able to keep the ultrasmall PMMA-SO_3H NPs in suspension and to remove the nonencapsulated dye salt, which presumably formed large aggregates in water. Measuring the absorbance of the precipitation solutions showed that in the presence of polymer the dye concentration decreased by less than 10% upon ultracentrifugation (Supporting Information Figure S4). In the absence of the polymer, however, more than 95% of the dye salt were removed from the solution after ultracentrifugation. These measurements thus enabled evaluation of the degree of dye encapsulation in our nanoparticles. For the tested 0.5 to 5 wt % range the dye salt could be encapsulated into PMMA-SO_3H NPs with at least 90% efficiency (Figure 7a). Using a polymer concentration of 0.2 mg mL^{-1}, we could obtain NPs of 15 nm loaded with 5 wt % of R18/F5-TPB (Figure 7b). Fluorescence microscopy of these NPs immobilized on a surface revealed their excellent brightness. Indeed, the

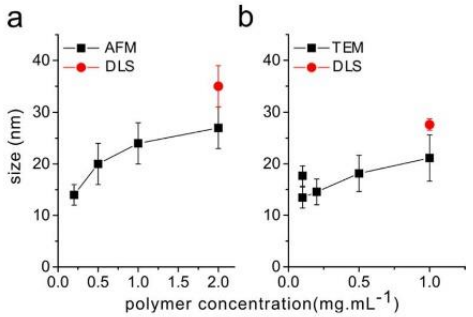

Figure 6. Influence of the polymer concentration on the particle size for (a) PLGA-COOH (M_n 7000) precipitated in 20 mM phosphate buffer (pH 7.4) and (b) PMMA-SO_3H precipitated in water. Values given for DLS are averages of volume distribution means; the error bars correspond to s.e.m. Values given for AFM and TEM are averages over at least 50 particles; the error bars correspond to the standard deviation.

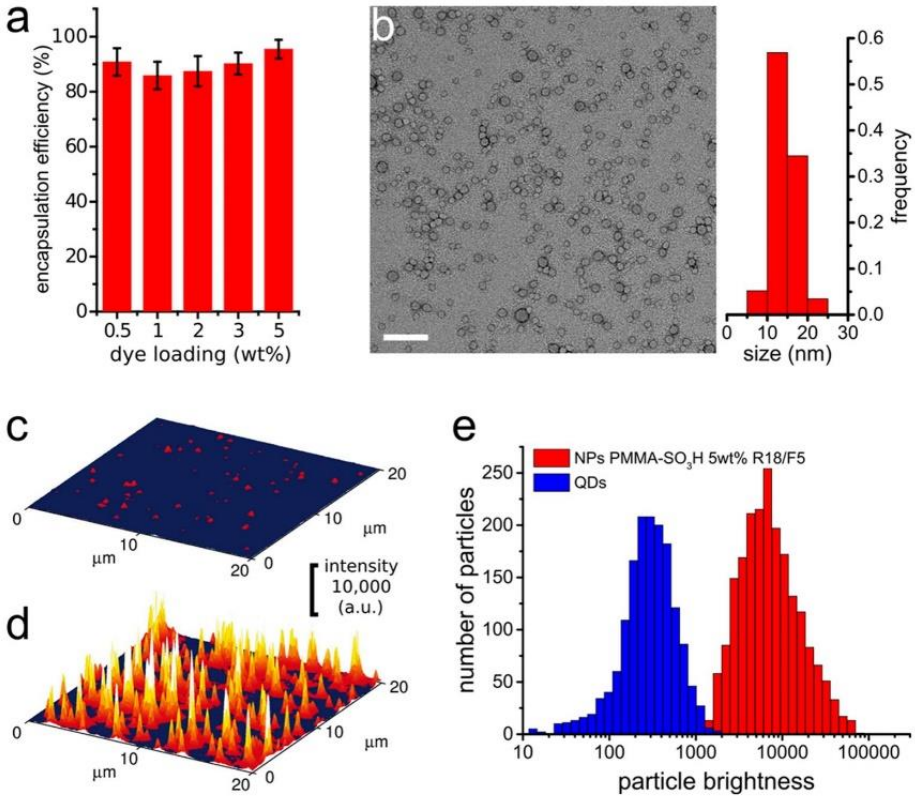

Figure 7. Dye-loaded fluorescent polymer nanoparticles. (a) Encapsulation efficiencies (estimated minimum percentage of the dye that was encapsulated in NPs) for R18/F5-TPB in PMMA-SO_3H nanoparticles. (b) TEM image and size histogram of the dye loaded PMMA-SO_3H nanoparticles. Scale bar 100 nm. Fluorescence microscopy images of (c) quantum dots (QDs, Qdot 585 Streptavidin Conjugates, Life Technologies) and (d) PMMA-SO_3H nanoparticles loaded with 5 wt % R18/F5-TPB obtained under the same conditions of illumination and recording, and (e) the corresponding distributions of single particle brightnesses.

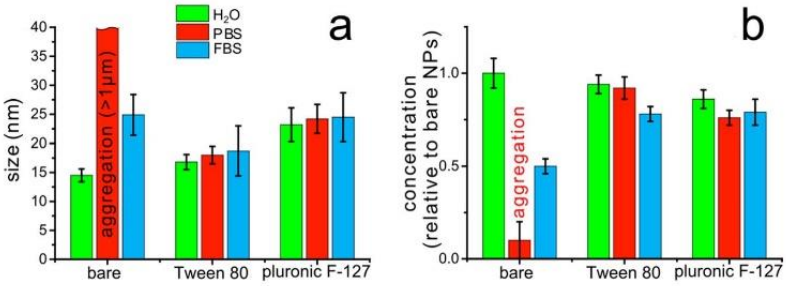

Figure 8. Stabilization of nanoparticles by surfactants. (a) Size and (b) concentration of PMMA-SO_3H NPs in Milli-Q-water, phosphate buffered saline (PBS), and 10 vol % fetal bovine serum (FBS) as measured by FCS. NPs were either used as made or treated with 0.05 mg mL^{-1} of Tween 80 or pluronic F-127. The NPs were obtained from 0.2 mg mL^{-1} solutions of PMMA-SO_3H. Error bars give the standard deviation over the 40 FCS measurements of a single sample.

dye loaded NPs were found to have a median single particle brightness of 6000 au and thus to be more than 10-fold brighter than commercial streptavidin bearing quantum dots of about the same size (15–20 nm according to the manufacturer) that had a median brightness of 400 au when imaged under the same conditions (Figure 7c,d,e).

Nanoparticle Stability and Interaction with Proteins. In order to be of practical use as nanocarriers, NPs have to be stable in biological media; *i.e.*, they should not aggregate at physiological salt concentrations and show minimal interaction with proteins. The influence of the medium on fluorescent NPs can be conveniently tested by fluorescence correlation spectroscopy (FCS), which allows measuring simultaneously their hydrodynamic diameter and concentration as well as estimating the dye release of NPs.[54,55] For our native 15 nm PMMA-SO_3H NPs loaded with R18/F5-TPB, FCS measurements showed a nearly complete precipitation of the NPs in phosphate buffered saline (PBS, Figure 8). In the presence of 10% fetal bovine serum (FBS) the hydrodynamic diameter of the NPs was observed to increase from 15 to 27 nm, while their concentration decreased by a factor close to 2. These NPs were hence not stable under physiological conditions. This was not really surprising as the average density of the sulfonate groups on their surface is one per 6.5 nm^2, and proteins adsorb even on like-charged NPs.[56] This means that the major part of the NP surface is occupied by relatively hydrophobic PMMA, which may favor adsorption of serum proteins and aggregation, when the repulsive forces of the sulfonate groups are screened by salt. On the other hand, this partially hydrophobic surface offers the possibility of surface modification using amphiphilic compounds. In order to reduce the effects of proteins and salts, amphiphiles containing PEG as the hydrophilic part are of particular interest.[18,31,57] According to FCS, addition of the nonionic surfactant Tween 80 (Polysorbate 80) and the amphiphilic block copolymer pluronic F-127 to our 15 nm NPs led only to a slight increase of their hydrodynamic diameter by 3 and 9 nm, respectively, indicating formation of a thin surfactant shell (Figure 8). Importantly, this surface modification made our NPs stable in PBS, as shown by the marginal changes in their size and concentration, in contrast to bare NPs (Figure 8). Furthermore, the particle size and concentrations remained stable after addition of 10% FBS, indicating that protein adsorption was largely inhibited after NP treatment with the surfactants. In addition, no increase in the concentration and no significant change of the particle brightness were observed (Figure 8b, Supporting Information Figure S6), indicating that no dye release occurred. Remarkably, the stabilization of NPs in physiological media was achieved at very low surfactant concentrations, namely 0.01–0.025 g/L (Supporting Information Figure S5), which are close to the critical micellar concentration (CMC) of Tween 80 (0.015 g/L),[58] but far below the CMC of pluronic F-127 (2.6–8.0 g/L).[59] Thus, a two-step modular approach, based on nanoprecipitation and further stabilization by a surfactant, allows obtaining sub-20-nm particles that are stable in physiological conditions and that show minimal interaction with proteins.

DISCUSSION

In the first part of this work we studied the influence of charged groups in PLGA, PCL, and PMMA polymers on the formation of particles through nanoprecipitation. Surprisingly, we found that the size of the resulting NPs was controlled by only one to two charged groups per polymer chain, while the nature of the polymer backbone and the molecular weight had a minor influence. Sulfonate and trimethylammonium groups, which are assumed to be fully charged under the used conditions, were the most effective for obtaining small particles. The size could be further decreased by decreasing the polymer concentration, which led to sub-15-nm particles. To better understand the origin of this phenomenon, the mechanism of particle formation has to be considered. In the case of low organic to aqueous phase ratios and low polymer concentrations, a nucleation and growth (or binodal) process is generally considered to prevail over spinodal decomposition, which consists in a rapid unmixing giving separate solid and liquid

phases.[41,45,46,60,61] Upon mixing of the organic and aqueous phase diffusion of the solvent into the aqueous phase (and *vice versa*) leads to a local supersaturation of the polymer. This supersaturation is the driving force for spontaneous nucleation and further growth of the so-formed primary particles. The final size of the particles then depends on the relative rates of nucleation, growth, and aggregation, with the smallest particles being formed at high nucleation rates, low growth rates, and very low aggregation rates.[45,61] The nucleation rate increases with decreasing nucleation parameter: $\gamma^3/\ln[S]^2$, where γ is the interfacial tension between the formed particles and the solution, and S is the supersaturation parameter. Turbidity measurements showed that the solubility in acetonitrile−water mixtures did not vary significantly for polymers having different end groups (Supporting Information Figure S7). As a consequence, for the identical concentrations used, the S value should not change drastically either. On the other hand, as the most hydrophilic groups are probably at the surface of the particles, the interfacial tension γ should be reduced strongly by charged groups and PEG. Thus, the presence of charged groups should reduce the nucleation parameter and hence increase the nucleation rate, leading to formation of smaller particles. The particle growth rate is proportional to the supersaturation S and the mass transfer coefficient k_m, corresponding to the rate constant of transport of mass to the growing particle. The latter decreases if charged polymers have to be brought to particles bearing the same charge. The decrease in the growth rate due to the presence of charges should then favor the formation of smaller particles. Finally, aggregation is prevented by a zeta potential more positive (negative) than +(−)30 mV. For negatively charged (and uncharged) polymers, the zeta potentials of the formed particles were indeed at least −30 mV, independently of their size. The zeta potential depends on the density of charges on the surface. Charged groups on the polymer thus help reach a potential necessary for preventing aggregation at smaller particle sizes and hence help stabilize small particles. This is in agreement with TEM micrographs that showed a tendency of aggregation notably for uncharged PMMA (Figure 4). The mechanism should be similar for the positively charged polymers, though the zeta potentials of their NPs were slightly smaller (15−20 mV). In summary, the presence of charged groups thus increases nucleation rates and decreases growth and aggregation rates. All three processes occurring during particle formation are hence pushed toward formation of smaller particles, which can explain the strong influence of the presence of one to two charged groups per polymer chain. The observed smaller particle size for higher molecular weight in case of charged PLGAs can be explained by a kinetic control of the growth step, where the mass transfer coefficient k_m decreases with increasing molecular weight. In the presence of neutral PEG groups a larger influence of thermodynamic factors on the control of the particle growth is assumed. Stabilization and repulsion is then reached through optimization of the density of PEG on the surface, and for lower polymer molecular weight a given density is reached for smaller particle sizes.

A remarkable feature of the NPs prepared by charge-controlled nanoprecipitation is the nearly quantitative encapsulation of organic dyes. Moreover, according to the FCS data, no burst release of the dye was observed in a biological medium, PBS with 10% serum, which is an excellent recipient of apolar molecules. In contrast, small micellar NPs prepared from block copolymers present relatively low encapsulation efficiency[62,63] together with significant burst release.[34−38] This is probably related to the dynamic equilibrium between the micelles and individual polymer molecules, due to their partial solubility in aqueous solution. In contrast, the polymers used here for the preparation of NPs through charge-controlled nanoprecipitation have only a minimal number of charges and thus a very low water solubility (Supporting Information Figure S7). The latter should favor the stable and nearly quantitative encapsulation of hydrophobic molecules inside these particles and the undetectable burst release in serum. It should be noted, that the choice of the hydrophobic molecule for encapsulation is also important. As we showed earlier,[15] efficient encapsulation of cationic dye R18 can be achieved using bulky hydrophobic counterions that make the dye more hydrophobic and prevent it from accumulating at the negatively charged particle surface.

The third important feature is the effective stabilization of our charged NPs by remarkably small concentrations of surfactants, which are significantly lower than those normally used in nanoprecipitation.[64−66] Tween and pluronic amphiphiles are known to stabilize uncoated NPs after their preparation.[67,68] Here we showed using FCS that the surfactant shell is only 1.5 and 4.5 nm thick for Tween 80 and pluronic F-127, respectively. This thickness is smaller than the hydrodynamic radius of 3−5 nm[69] and 10−12 nm[70] of the micelles formed by Tween 80 and pluronic F-127, respectively. Therefore, we can speculate that surfactants at these low concentrations underwent a strong adsorption of their alkyl chains at the hydrophobic sites of the NPs without forming a lipid monolayer, and thus gave an ultrathin protective shell (Figure 9). Remarkably, this shell was sufficiently stable to prevent particle aggregation in salts and protect the NPs from adsorption of serum proteins. Some reports showed that surfactants are not absolutely necessary for preparation of polyester NPs.[71,72] According to our data, the surfactants are indeed not necessary for particle preparation, but they are important as "corona" that

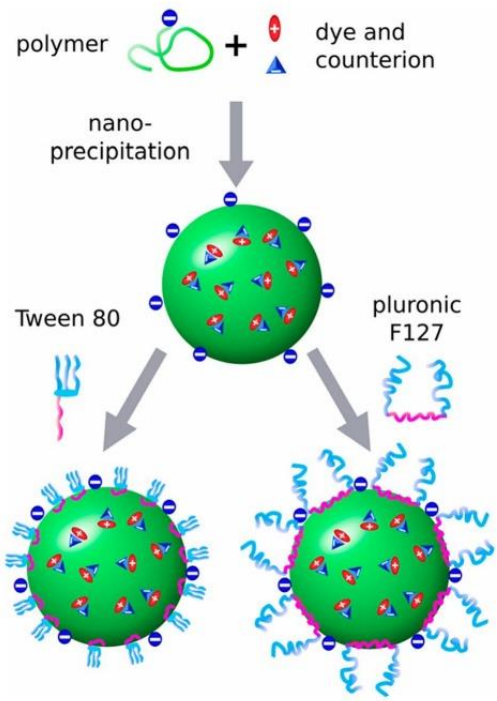

Figure 9. Scheme of the modular two-steps approach used to prepare stable nanocarriers through charge-controlled nanoprecipitation. A polymer bearing a charged group is mixed with a cargo molecule (the dye salt) in an organic solvent and precipitated in water. The resulting particles are stabilized in a second step using Tween 80 or pluronic F-127.

can be added after particle preparation and serve to protect the NPs from aggregation and nonspecific interactions. Thus, we propose a two-step modular approach for the synthesis of ultrasmall nanoparticles, consisting in (1) charge controlled nanoprecipitation in low-salt conditions, followed by (2) stabilization of the particle surface by a surfactant (Figure 9). This highly flexible approach can be, in principle, extended to other polymers and other types of surface modification.

CONCLUSION

Ultrasmall nanoparticles are of special interest as nanocarriers of contrast agents and drugs. Here we have developed charge controlled nanoprecipiation as a modular approach to the assembly of ultrasmall stable polymeric nanocarriers. We showed that the presence of only one to two charged groups per polymer chain can strongly reduce the size of polymer nanoparticles made by nanoprecipitation. This concept works with negatively charged groups, such as carboxyl and sulfonate as well as with positively charged trimethylammonium. Its success with three quite different types of polymers (PLGA, PCL, and PMMA) suggests its general usefulness for the preparation of polymer nanocarriers. Moreover, the particle size can be further decreased to less than 15 nm by minimizing the concentration of polymer in the solvent used for nanoprecipitation. We further showed that even very small nanoparticles of 15 nm size preserve the capacity to encapsulate efficiently large amounts of ionic dyes with bulky counterions, which generates polymer nanoparticles 10-fold brighter than quantum dots of the same size. These nanocarriers could be stabilized by surface modification using PEG-containing amphiphiles, leading to particles that show minimal interactions with proteins. This straightforward and modular route could become a general approach for the preparation of ultrasmall polymer nanoparticles as nanocarriers of contrast agents and drugs.

MATERIALS AND METHODS

Materials. Poly(D,L-lactide-*co*-glycolide) (PLGA noted here as PLGA-COOH, lactide 50 mol %, glycolide 50 mol %, acid terminated, M_n 24 000, PDI 1.7, and M_n 8800, PDI 1.7), polycaprolactone (α,ω-dihydroxy functional, M_n ~10 000, M_w ~14 000), poly(methyl methacrylate) (PMMA, M_w 120 000), poly(methyl methacrylate-*co*-methacrylic acid) (PMMAMA noted here as PMMA-COOH, 1,3% methacrylic acid, M_n ~15 000, M_w ~34 000), *N,N,N′,N′*-tetramethyl-*O*-(1*H*-benzotriazol-1-yl)uronium hexafluorophosphate (HBTU, >98.0%), 1-hydroxybenzotriazole hydrate (HOBt, >99.0%), *N,N*-diisopropylethylamine (DIPEA, 99,5%), acetonitrile (anhydrous, 99.8%), dichloromethane (anhydrous, >99.8%), (2-aminoethyl) trimethylammonium chloride hydrochloride (99%), rhodamine B octadecyl ester perchlorate (>98.0%), lithium tetrakis(pentafluorophenyl)borate ethyl etherate, Tween 80, pluronic F-127 were purchased from Sigma-Aldrich. Amine terminated polyethylene glycols (H_2N-PEG(8)N_3, H_2N-PEG(12)N_3, H_2N-PEG(24)N_3) were purchased from Iris Biotech. *N,N′*-dimethylformamide (absolute >99.8%) and succinic anhydride were purchased from AlfaAesar. 2-Aminoethanesulfonic acid (taurine, >98%) was obtained from TCI. Sodium phosphate monobasic (>99.0%, Sigma-Aldrich) and sodium phosphate dibasic dihydrate (>99.0%, Sigma-Aldrich) were used to prepare 20 mM phosphate buffer solutions at pH 7.4; tris(hydroxymethyl)aminomethane (Tris base, >99.8%, Sigma-Aldrich) and HCl (1 M) were used to prepare 20 mM Tris buffer with a pH of 7.4. Milli-Q water (Millipore) was used in all experiments. Qdot 585 Streptavidin Conjugates were purchased from Life-Technologies.

Synthesis. *Rhodamine B Octadecyl Ester Tetrakis(pentafluorophenyl)borate (R18/F5-TPB).* Title compound was synthesized by ion exchange and purified by column chromatography as described previously.[15]

PLGA−PEG. Given is, as an example, the procedure for PLGA−PEG_{24} 24 000: 40 mg of PLGA (0.0017 mmol, 1 equiv of COOH) were dissolved in anhydrous dichloromethane (2 mL). To this solution DIPEA (3 μL, 0.017 mmol, 10 equiv), HOBt (0.55 mg, 0.004 mmol, 2.4 equiv) and HBTU (1.27 mg, 0.003 mmol, 2 equiv) were added as solutions in anhydrous dimethylformamide (total of 1 mL) under argon. 3.7 mg of NH_2-PEG(23)-N_3 (0.003 mmol, 2 equiv) were dissolved in 0.3 mL of DMF and added to the reaction mixture. After stirring for 18 h at room temperature, part of the solvent was evaporated at 40 °C under reduced pressure. The obtained solution was precipitated in methanol. The precipitate was washed with methanol, redissolved in acetonitrile, and reprecipitated twice in methanol. After drying under a vacuum, 27 mg of a white solid were obtained (yield 65%). ^{1}H NMR (400 MHz, $CDCl_3$): δ/ppm 5.3−5.1 (m, 1 H), 4.9−4.6 (m, 2 H), 4.30 (m, 0.011 H), 3.64 (m, 0.4 H), 3.47

(br, 0.016 H), 3.38 (t, 0.011 H), 1.8−1.4 (m, 3 H). Degree of modification 86%.

PLGA−PEG_{12} 24 000: 32 mg obtained (yield 79%). Degree of modification 96%.

PLGA−PEG_8 24 000: 15 mg obtained (yield 75%). Degree of modification 94%.

PLGA−PEG_{24} 7000: 42 mg obtained (yield 73%). Degree of modification 67%.

PLGA−PEG_{12} 7000: 35 mg obtained (yield 65%). Degree of modification 69%.

PLGA−PEG_8 7000: 17 mg obtained (yield 80%). Degree of modification 66%.

PCL-COOH. The PCL (244 mg, 0.0244 mmol, 2 equiv of OH) was dissolved in anhydrous acetonitrile (4,8 mL) at 40 °C. Succinic anhydride (12.3 mg, 0.123 mmol, 5 equiv) and DIPEA (50 μL, 0.302 mmol) were added under stirring. The mixture was stirred at 45 °C under argon atmosphere for 18 h. The solvent was evaporated under reduced pressure. After redissolution in a small amount of acetonitrile the solution was precipitated in methanol. The precipitate was washed with methanol, redissolved in acetonitrile, and reprecipitated twice in methanol. After drying under a vacuum, 102 mg of a white solid were obtained (yield 41%). ^{1}H NMR (400 MHz, $CDCl_3$): δ/ppm 4.05 (t, 2 H), 3.7−3.6 (m, 0.09 H), 2.63 (m, 0.08 H), 2.30 (t, 2 H), 1.64 (m, 4 H), 1.38 (m, 2 H). Degree of modification 80%.

Trimethylammonium Bearing Polymers. The basic procedure was the same for all polymers except that PCL-COOH and PMMA-COOH were reacted at 40 °C; given are the quantities used for PLGA-NMe_3 24 000: The PLGA (40 mg, 0.0017 mmol, 1 equiv of COOH) was dissolved in anhydrous dichloromethane (3 mL). 2-(Aminoethyl)trimethylammonium chloride hydrochloride (3 mg, 0.017 mmol, 10 equiv), DIPEA (25 μL, 0.15 mmol, 88 equiv), HOBt (2.3 mg, 0.017 mmol, 10 equiv) and HBTU (6.4 mg, 0.017 mmol, 10 equiv) were dissolved in anhydrous dimethylformamide (total of 2 mL) and added to the PLGA solution under argon. The mixture was stirred for 20 h at room temperature. After evaporating part of the solvent at 40 °C under reduced pressure, the solution was precipitated in methanol. The precipitate was washed with methanol, redissolved in acetonitrile, and reprecipitated twice in methanol. After drying under a vacuum, 25 mg of a white solid were obtained (yield 63%). ^{1}H NMR (400 MHz, $CDCl_3$): δ/ppm 5.3−5.1 (m, 1 H), 4.9−4.6 (m, 2H), 4.27 (m, 0.013 H), 3.76 (m, 0.009 H), 3.64 (br, 0.008 H), 3.26 (br, 0.043 H), 1.8−1.4 (m, 3 H).

PLGA-NMe_3 7000 18 mg were obtained (yield 45%). Degree of modification 88%.

PCL-NMe_3: 12 mg obtained (yield 42%). Degree of modification 70%.

PMMA-NMe_3: 82 mg obtained (yield 55%). Degree of modification 60%.

Sulfonate Bearing Polymers. The same procedure was used for the introduction of sulfonate groups into all polymers starting from the corresponding carboxyl bearing polymers. Given is, as an example, the detailed procedure for PLGA-SO_3H 24 000: The PLGA (102 mg, 0,0042 mmol, 1 equiv of COOH) was dissolved in anhydrous DMF (1.5 mL) under argon. Taurine (5.2 mg, 0.042 mmol, 10 equiv) and DIPEA (30 μL, 0.18 mmol) were added to the solution, followed by the addition of HOBt (4.6 mg, 0.034 mmol, 8 equiv) and HBTU (12.5 mg, 0.033 mmol, 8 equiv). The mixture was stirred under argon for 20 h at 40 °C. After evaporating part of the solvent at 40 °C under reduced pressure, the solution was precipitated in methanol. The precipitate was washed with methanol, redissolved in acetonitrile, and reprecipitated twice in methanol. After drying under a vacuum, 57 mg of a white solid were obtained (yield 55%). ^{1}H NMR (400 MHz, $CDCl_3$): δ/ppm 5.3−5.1 (m, 1 H), 4.9−4.6 (m, 2 H), 4.30 (m, 0.011 H), 3.80−3.65 (m, 0.020 H), 3.10 (0.006 H), 2.98 (m, 0.010 H), 1.8−1.4 (m, 3 H). Degree of modification 91%.

PLGA-SO_3H 7000: 75 mg obtained (yield 74%). Degree of modification 86%.

PCL-SO_3H: 157 mg obtained (yield 62%). Degree of modification 78%.

PMMA-SO_3H: 114 mg obtained (yield 78%). Degree of modification 85%.

Nanoparticle Preparation. Stock solutions of the polymers in acetonitrile were prepared at a concentration of 10 mg mL^{-1}. These solutions were then diluted with acetonitrile to the desired concentration (between 0.05 and 2 mg mL^{-1}). 50 μL of the polymer solutions were then added quickly using a micropipette and under shaking (Thermomixer comfort, Eppendorf, 1000 rpm) to 450 μL of water or buffer. PLGA and PMMA based nanoparticles were prepared at 21 °C, PCL nanoparticles were prepared at 27 °C. The particle solution was then quickly diluted 5-fold with the same buffer. For preparation of fluorescent nanoparticles, different concentrations of R18/F5-TPB (0.5 to 5 wt % relative to the polymer) were added to the acetonitrile solution used for particle preparation, and the particles were prepared as described above. For stabilization of NPs, different amounts of 1 or 0.1 mg mL^{-1} solutions of Tween 80 or pluronic F-127 were added under stirring to the NP solutions.

Nanoparticle Characterization. *Dynamic Light Scattering.* measurements for the determination of the size, size distribution, and zeta-potential of the nanoparticles were performed on a Zetasizer Nano series DTS 1060 (Malvern Instruments S.A.). The mean value of the diameter of the size distribution per volume was used for analysis. Each sample was measured three times and each condition was tested at least in triplicate in independent measurements. The errors (bars) are given as the standard error of the mean.

Electron Microscopy. Five microliters of the particle solution were deposited onto carbon-coated copper−rhodium electron microscopy grids that were used either as obtained or following an air or amylamine glow-discharge. The grids were then treated for 1 min with a 2% uranyl acetate solution for staining. They were then observed with a Philips CM120 transmission electron microscope equipped with a LaB_6 filament and operating at 100 kV. Areas covered with nanoparticles of interest were recorded at different magnifications on a Peltier cooled CCD camera (Model 794, Gatan, Pleasanton, CA). Image analysis was performed using the Fiji software.

Atomic Force Microscopy. AFM measurements were performed using a commercial instrument (Solver Pro-M, NT-MDT, Moscow) in the tapping mode in liquid phase. The cantilever used were CSG01 (NT-MDT, Moscow) with a typical spring constant of 0.06 N/m and a resonance frequency of 11 kHz. Images were acquired with a resolution of 512 × 512 points and a scan rate of 1 Hz. The samples were prepared using 100 μL deposed on cleaved mica coated with polyethylenimine (PEI) as described below. The measurements were performed 10 min after sample preparation. Analysis of particle populations was done using Gwydion 2.31 and Origin 8.0.

Encapsulation Efficiency. Eight milliliters of NP solution (at a polymer concentration of 0.02 mg μL^{-1} and containing between 0.5 and 5 wt % R18/F5-TPB) were ultracentrifuged using polycarbonate thick-wall centrifuge tubes (Beckman Coulter Inc.) in a Beckman Coulter Ultracentrifuge using a Ti90 rotor at 125000*g* for 12 min at 23 °C. Absorbances at 555 nm before and after ultracentrifugation were measured in the supernatant. The same procedure was applied to the same amounts of dye in water without the polymer. The encapsulation efficiency was calculated from the percentage of absorbance remaining after ultracentrifugation. To take into account the nonencapsulated dye that might not be removed by ultracentrifugation, the percentage of remaining absorbance in the absence of polymer after ultracentrifugation was subtracted: encapsulation efficiency = $A_{NP}^{after}/A_{NP}^{before} - A_{dye}^{after}/A_{dye}^{before}$.

Fluorescence Microscopy. For single particle fluorescence microscopy measurements, the NPs were immobilized on glass surfaces on which a polyethylenimine (PEI) layer was initially adsorbed. The solutions of NPs were diluted to a particle concentration of about 6 pM with water or buffer (particle concentration before the dilution was estimated by fluorescence correlation spectroscopy, see below). 400 μL of these solutions per cm^2 were then brought in contact with the PEI covered glass for 15 min, followed by extensive rinsing with Milli-Q-water. The surfaces were left in Milli-Q water during microscopy. Quantum dots (Qdot 585 Streptavidin Conjugates, life technologies) at 6 pM concentration were immobilized and imaged in the same way as the NPs.

Single particle measurements were performed in the TIRF (Total Internal Reflection Fluorescence) mode on a homemade wide-field setup based on an Olympus IX-71 microscope with an oil immersion objective (NA = 1.49, 100×). A DPPS (Cobolt) continuous wave (CW) laser emitting at 532 nm was used for excitation. The laser intensity was set to 4.5 W cm^{-2} by using a polarizer and a half-wave plate (532 nm). The fluorescence signal was recorded with an EMCCD (ImagEM Hamamatsu) using an exposure of 30 ms per image frame. Single particle analysis was performed using the Fiji software as described previously.[15,73] Briefly, particle locations were detected through a Fiji routine applied to a projection (maximum intensity) of 100 frames. The mean intensities of circular regions of interest with a diameter of 5 pixels around the found particle locations were then measured. Background subtraction was then achieved by measuring the mean intensities in circular bands around the circular regions of interest and subtracting them. Three image sequences (55 μm × 55 μm) per condition were analyzed with, on average, 680 and 530 particles per image for PMMA-SO_3H NPs and QDs, respectively.

Fluorescence Correlation Spectroscopy (FCS) and NP Stability. FCS measurements were performed on a two-photon platform including an Olympus IX70 inverted microscope, as described previously.[55,74] Two-photon excitation at 830 nm (10 mW laser output power) was provided by an InSight DeepSee laser (Spectra Physics). The measurements were carried out in 96-well optical-bottom plates, using 125 μL per well. The focal spot was set about 20 μm above the cover- slip. The normalized autocorrelation function, $G(\tau)$, was calculated online using an ALV-5000E correlator (ALV, Germany) from the fluorescence fluctuations, $\delta F(t)$, by $G(\tau) = \langle \delta F(t)\delta F(t+\tau)\rangle / \langle F(t)\rangle^2$ where $\langle F(t)\rangle$ is the mean fluorescence signal and τ is the lag time. Assuming that NPs diffuse freely in a Gaussian excitation volume, the correlation function, $G(\tau)$, calculated from the fluorescence fluctuations was fitted according to[54]

$$G(\tau) = \frac{1}{N}\left(1+\frac{\tau}{\tau_d}\right)^{-2}\left(1+\frac{1}{S^2}\frac{\tau}{\tau_d}\right)^{-1/2}$$

where τ_d is the diffusion time, N is the mean number of fluorescent species within the two-photon excitation volume, and S is the ratio between the axial and lateral radii of the excitation volume. The excitation volume is about 0.34 fL and S is about 3 to 4. The typical data recording time was 5 min, using freshly prepared NPs without further dilution. The measurements were done with respect to 6-carboxy- tetramethylrhodamine (TMR from Sigma-Aldrich) in water, used as a reference. The hydrodynamic diameter, d, of NPs was calculated as $d_{NPs} = \tau_{d(NPs)} / \tau_{d(TMR)} \times d_{TMR}$, where d_{TMR} is the hydrodynamic diameter of TMR (1.0 nm). The concentration of NPs was calculated from the number of species by $C(NPs) = N(NPs)/N(TMR) \times C(TMR)$, using a TMR concentration of 140 nM.

NP stability in PBS was tested by adding 10 vol % of 10-fold concentrated PBS to the solutions of the corresponding NPs containing 1 wt % of R18/F5-TPB and measuring the hydrodynamic diameter and concentration. Interaction with 10 vol % fetal bovine serum was tested in the same way.

Conflict of Interest: The authors declare no competing financial interest.

Acknowledgment. The authors thank C. Ruhlmann for help with electron microscopy and C. Antheaume and J. Viéville for help with NMR spectroscopy. This work was supported by ANR JCJC (ANR-11-JS07-014-01), CNRS, and the University of Strasbourg.

Supporting Information Available: Includes additional NMR spectra, AFM and additional TEM images, data on encapsulation efficiencies, NP stability, and polymer solubilities. This material is available free of charge *via* the Internet at http://pubs.acs.org.

REFERENCES AND NOTES

1. Panyam, J.; Labhasetwar, V. Biodegradable Nanoparticles for Drug and Gene Delivery to Cells and Tissue. *Adv. Drug Delivery Rev.* **2003**, *55*, 329–347.
2. Danhier, F.; Ansorena, E.; Silva, J. M.; Coco, R.; Le Breton, A.; Preat, V. PLGA-Based Nanoparticles: An Overview of Biomedical Applications. *J. Controlled Release* **2012**, *161*, 505–522.
3. Kumari, A.; Yadav, S. K.; Yadav, S. C. Biodegradable Polymeric Nanoparticles Based Drug Delivery Systems. *Colloids Surf., B* **2010**, *75*, 1–18.
4. Kulkarni, S. A.; Feng, S.-S. Effects of Particle Size and Surface Modification on Cellular Uptake and Biodistribution of Polymeric Nanoparticles for Drug Delivery. *Pharm. Res.* **2013**, *30*, 2512–2522.
5. Choi, H. S.; Liu, W.; Misra, P.; Tanaka, E.; Zimmer, J. P.; Ipe, B. I.; Bawendi, M. G.; Frangioni, J. V. Renal Clearance of Nanoparticles. *Nat. Biotechnol.* **2007**, *25*, 1165–1170.
6. Huo, S.; Ma, H.; Huang, K.; Liu, J.; Wei, T.; Jin, S.; Zhang, J.; He, S.; Liang, X.-J. Superior Penetration and Retention Behavior of 50 nm Gold Nanoparticles in Tumors. *Cancer Res.* **2013**, *73*, 319–330.
7. Cabral, H.; Matsumoto, Y.; Mizuno, K.; Chen, Q.; Murakami, M.; Kimura, M.; Terada, Y.; Kano, M. R.; Miyazono, K.; Uesaka, M.; *et al.* Accumulation of Sub-100 nm Polymeric Micelles in Poorly Permeable Tumours Depends on Size. *Nat. Nanotechnol.* **2011**, *6*, 815–823.
8. Wong, C.; Stylianopoulos, T.; Cui, J.; Martin, J.; Chauhan, V. P.; Jiang, W.; Popović, Z.; Jain, R. K.; Bawendi, M. G.; Fukumura, D. Multistage Nanoparticle Delivery System for Deep Penetration into Tumor Tissue. *Proc. Natl. Acad. Sci. U. S. A.* **2011**, *108*, 2426–2431.
9. Rosi, N. L.; Giljohann, D. A.; Thaxton, C. S.; Lytton-Jean, A. K. R.; Han, M. S.; Mirkin, C. A. Oligonucleotide-Modified Gold Nanoparticles for Intracellular Gene Regulation. *Science* **2006**, *312*, 1027–1030.
10. Verma, A.; Uzun, O.; Hu, Y.; Hu, Y.; Han, H.-S.; Watson, N.; Chen, S.; Irvine, D. J.; Stellacci, F. Surface-Structure-Regulated Cell-Membrane Penetration by Monolayer-Protected Nanoparticles. *Nat. Mater.* **2008**, *7*, 588–595.
11. Sahay, G.; Alakhova, D. Y.; Kabanov, A. V. Endocytosis of Nanomedicines. *J. Controlled Release* **2010**, *145*, 182–195.
12. Maria Coto-Garcia, A.; Sotelo-Gonzalez, E.; Teresa Fernandez-Argueelles, M.; Pereiro, R.; Costa-Fernandez, J. M.; Sanz-Medel, A. Nanoparticles as Fluorescent Labels for Optical Imaging and Sensing in Genomics and Proteomics. *Anal. Bioanal. Chem.* **2011**, *399*, 29–42.
13. Wagh, A.; Qian, S. Y.; Law, B. Development of Biocompatible Polymeric Nanoparticles for *in Vivo* NIR and FRET Imaging. *Bioconjugate Chem.* **2012**, *23*, 981–992.
14. Wagh, A.; Jyoti, F.; Mallik, S.; Qian, S.; Leclerc, E.; Law, B. Polymeric Nanoparticles with Sequential and Multiple FRET Cascade Mechanisms for Multicolor and Multiplexed Imaging. *Small* **2013**, *9*, 2129–2139.
15. Reisch, A.; Didier, P.; Richert, L.; Oncul, S.; Arntz, Y.; Mély, Y.; Klymchenko, A. S. Collective Fluorescence Switching of Counterion-Assembled Dyes in Polymer Nanoparticles. *Nat. Commun.* **2014**, *5*, 4089.
16. Michalet, X.; Pinaud, F. F.; Bentolila, L. A.; Tsay, J. M.; Doose, S.; Li, J. J.; Sundaresan, G.; Wu, A. M.; Gambhir, S. S.; Weiss, S. Quantum Dots for Live Cells, *in Vivo* Imaging, and Diagnostics. *Science* **2005**, *307*, 538–544.
17. Wang, M.; Abbineni, G.; Clevenger, A.; Mao, C.; Xu, S. Upconversion Nanoparticles: Synthesis, Surface Modification and Biological Applications. *Nanomedicine* **2011**, *7*, 710–729.
18. Howes, P. D.; Chandrawati, R.; Stevens, M. M. Colloidal Nanoparticles as Advanced Biological Sensors. *Science* **2014**, *346*, 1247390.
19. Li, Z.; Sun, Q.; Zhu, Y.; Tan, B.; Xu, Z. P.; Dou, S. X. Ultra-Small Fluorescent Inorganic Nanoparticles for Bioimaging. *J. Mater. Chem. B* **2014**, *2*, 2793–2818.
20. Cognet, L.; Leduc, C.; Lounis, B. Advances in Live-Cell Single-Particle Tracking and Dynamic Super-Resolution Imaging. *Curr. Opin. Chem. Biol.* **2014**, *20*, 78–85.
21. Wang, X.; Stolwijk, J. A.; Lang, T.; Sperber, M.; Meier, R. J.; Wegener, J.; Wolfbeis, O. S. Ultra-Small, Highly Stable, and Sensitive Dual Nanosensors for Imaging Intracellular Oxygen and pH in Cytosol. *J. Am. Chem. Soc.* **2012**, *134*, 17011–17014.

22. Zhang, L.; Chan, J. M.; Gu, F. X.; Rhee, J.-W.; Wang, A. Z.; Radovic-Moreno, A. F.; Alexis, F.; Langer, R.; Farokhzad, O. C. Self-Assembled Lipid–Polymer Hybrid Nanoparticles: A Robust Drug Delivery Platform. *ACS Nano* **2008**, *2*, 1696–1702.
23. Santander-Ortega, M. J.; Jódar-Reyes, A. B.; Csaba, N.; Bastos-González, D.; Ortega-Vinuesa, J. L. Colloidal Stability of Pluronic F68-Coated PLGA Nanoparticles: A Variety of Stabilisation Mechanisms. *J. Colloid Interface Sci.* **2006**, *302*, 522–529.
24. Gillich, T.; Acikgöz, C.; Isa, L.; Schlüter, A. D.; Spencer, N. D.; Textor, M. PEG-Stabilized Core–Shell Nanoparticles: Impact of Linear *versus* Dendritic Polymer Shell Architecture on Colloidal Properties and the Reversibility of Temperature-Induced Aggregation. *ACS Nano* **2012**, *7*, 316–329.
25. Rao, J. P.; Geckeler, K. E. Polymer Nanoparticles: Preparation Techniques and Size-Control Parameters. *Prog. Polym. Sci.* **2011**, *36*, 887–913.
26. Landfester, K. Miniemulsion Polymerization and the Structure of Polymer and Hybrid Nanoparticles. *Angew. Chem., Int. Ed.* **2009**, *48*, 4488–4507.
27. Allen, C.; Maysinger, D.; Eisenberg, A. Nano-Engineering Block Copolymer Aggregates for Drug Delivery. *Colloids Surf., B* **1999**, *16*, 3–27.
28. Kataoka, K.; Harada, A.; Nagasaki, Y. Block Copolymer Micelles for Drug Delivery: Design, Characterization and Biological Significance. *Adv. Drug Delivery Rev.* **2001**, *47*, 113–131.
29. Riess, G. Micellization of Block Copolymers. *Prog. Polym. Sci.* **2003**, *28*, 1107–1170.
30. Gohy, J.-F.; Willet, N.; Varshney, S.; Zhang, J.-X.; Jérôme, R. Core–Shell–Corona Micelles with a Responsive Shell. *Angew. Chem., Int. Ed.* **2001**, *40*, 3214–3216.
31. Otsuka, H.; Nagasaki, Y.; Kataoka, K. PEGylated Nanoparticles for Biological and Pharmaceutical Applications. *Adv. Drug Delivery Rev.* **2012**, *64* (Supplement), 246–255.
32. Nagarajan, R.; Ganesh, K. Block Copolymer Self-assembly in Selective Solvents: Spherical Micelles with Segregated Cores. *J. Chem. Phys.* **1989**, *90*, 5843–5856.
33. Mortensen, K.; Brown, W. Poly(ethylene Oxide)-Poly(propylene Oxide)-Poly(ethylene Oxide) Triblock Copolymers in Aqueous Solution. The Influence of Relative Block Size. *Macromolecules* **1993**, *26*, 4128–4135.
34. Zou, P.; Chen, H. W.; Paholak, H. J.; Sun, D. X. Burst Release of Lipophilic Drugs from Poly (Ethylene Oxide)- B-Polystyrene Micelles Is Not Caused by Micelle Disassembly. *J. Tumor* **2013**, *1*, 7–15.
35. Bae, Y. H.; Yin, H. Stability Issues of Polymeric Micelles. *J. Controlled Release* **2008**, *131*, 2–4.
36. Chen, H.; Kim, S.; He, W.; Wang, H.; Low, P. S.; Park, K.; Cheng, J.-X. Fast Release of Lipophilic Agents from Circulating PEG-PDLLA Micelles Revealed by *in Vivo* Förster Resonance Energy Transfer Imaging. *Langmuir* **2008**, *24*, 5213–5217.
37. Chen, H.; Kim, S.; Li, L.; Wang, S.; Park, K.; Cheng, J.-X. Release of Hydrophobic Molecules from Polymer Micelles into Cell Membranes Revealed by Förster Resonance Energy Transfer Imaging. *Proc. Natl. Acad. Sci. U. S. A.* **2008**, *105*, 6596–6601.
38. Zhao, X.; Poon, Z.; Engler, A. C.; Bonner, D. K.; Hammond, P. T. Enhanced Stability of Polymeric Micelles Based on Postfunctionalized Poly(ethylene Glycol)-B-Poly(γ-Propargyl L-Glutamate): The Substituent Effect. *Biomacromolecules* **2012**, *13*, 1315–1322.
39. Schulz, A.; Jaksch, S.; Schubel, R.; Wegener, E.; Di, Z.; Han, Y.; Meister, A.; Kressler, J.; Kabanov, A. V.; Luxenhofer, R.; *et al.* Drug-Induced Morphology Switch in Drug Delivery Systems Based on Poly(2-Oxazoline)s. *ACS Nano* **2014**, *8*, 2686–2696.
40. Fessi, H.; Puisieux, F.; Devissaguet, J. P.; Ammoury, N.; Benita, S. Nanocapsule Formation by Interfacial Polymer Deposition Following Solvent Displacement. *Int. J. Pharm.* **1989**, *55*, R1–R4.
41. Mora-Huertas, C. E.; Fessi, H.; Elaissari, A. Influence of Process and Formulation Parameters on the Formation of Submicron Particles by Solvent Displacement and Emulsification–Diffusion Methods: Critical Comparison. *Adv. Colloid Interface Sci.* **2011**, *163*, 90–122.
42. Govender, T.; Stolnik, S.; Garnett, M. C.; Illum, L.; Davis, S. S. PLGA Nanoparticles Prepared by Nanoprecipitation: Drug Loading and Release Studies of a Water Soluble Drug. *J. Controlled Release* **1999**, *57*, 171–185.
43. Chan, J. M.; Zhang, L.; Yuet, K. P.; Liao, G.; Rhee, J.-W.; Langer, R.; Farokhzad, O. C. PLGA-Lecithin-PEG Core-Shell Nanoparticles for Controlled Drug Delivery. *Biomaterials* **2009**, *30*, 1627–1634.
44. Danhier, F.; Lecouturier, N.; Vroman, B.; Jérôme, C.; Marchand-Brynaert, J.; Feron, O.; Préat, V. Paclitaxel-Loaded PEGylated PLGA-Based Nanoparticles: *In Vitro* and *in Vivo* Evaluation. *J. Controlled Release* **2009**, *133*, 11–17.
45. D'Addio, S. M.; Prud'homme, R. K. Controlling Drug Nanoparticle Formation by Rapid Precipitation. *Adv. Drug Delivery Rev.* **2011**, *63*, 417–426.
46. Ganachaud, F.; Katz, J. L. Nanoparticles and Nanocapsules Created Using the Ouzo Effect: Spontaneous Emulsification as an Alternative to Ultrasonic and High-Shear Devices. *ChemPhysChem* **2005**, *6*, 209–216.
47. Hornig, S.; Heinze, T.; Becer, C. R.; Schubert, U. S. Synthetic Polymeric Nanoparticles by Nanoprecipitation. *J. Mater. Chem.* **2009**, *19*, 3838–3840.
48. Aubry, J.; Ganachaud, F.; Cohen Addad, J.-P.; Cabane, B. Nanoprecipitation of Polymethylmethacrylate by Solvent Shifting: 1. Boundaries. *Langmuir* **2009**, *25*, 1970–1979.
49. Perevyazko, I. Y.; Vollrath, A.; Pietsch, C.; Schubert, S.; Pavlov, G. M.; Schubert, U. S. Nanoprecipitation of Poly(methyl Methacrylate)-Based Nanoparticles: Effect of the Molar Mass and Polymer Behavior. *J. Polym. Sci., Part A: Polym. Chem.* **2012**, *50*, 2906–2913.
50. De Oliveira, A. M.; Jäger, E.; Jäger, A.; Stepánek, P.; Giacomelli, F. C. Physicochemical Aspects behind the Size of Biodegradable Polymeric Nanoparticles: A Step Forward. *Colloids Surf., A* **2013**, *436*, 1092–1102.
51. Perevyazko, I.; Vollrath, A.; Hornig, S.; Pavlov, G. M.; Schubert, U. S. Characterization of Poly(methyl Methacrylate) Nanoparticles Prepared by Nanoprecipitation Using Analytical Ultracentrifugation, Dynamic Light Scattering, and Scanning Electron Microscopy. *J. Polym. Sci., Part A: Polym. Chem.* **2010**, *48*, 3924–3931.
52. Schneider, J.; Jallouk, A. P.; Vasquez, D.; Thomann, R.; Forget, A.; Pino, C. J.; Shastri, V. P. Surface Functionality as a Means to Impact Polymer Nanoparticle Size and Structure. *Langmuir* **2013**, *29*, 4092–4095.
53. Seremeta, K. P.; Chiappetta, D. A.; Sosnik, A. Poly(epsilon-Caprolactone), Eudragit (R) RS 100 and Poly(epsilon-caprolactone)/Eudragit (R) RS 100 Blend Submicron Particles for the Sustained Release of the Antiretroviral Efavirenz. *Colloids Surf., B* **2013**, *102*, 441–449.
54. Koynov, K.; Butt, H.-J. Fluorescence Correlation Spectroscopy in Colloid and Interface Science. *Curr. Opin. Colloid Interface Sci.* **2012**, *17*, 377–387.
55. Klymchenko, A. S.; Roger, E.; Anton, N.; Anton, H.; Shulov, I.; Vermot, J.; Mely, Y.; Vandamme, T. F. Highly Lipophilic Fluorescent Dyes in Nano-Emulsions: Towards Bright Non-Leaking Nano-Droplets. *RSC Adv.* **2012**, *2*, 11876–11886.
56. Hühn, D.; Kantner, K.; Geidel, C.; Brandholt, S.; De Cock, I.; Soenen, S. J. H.; Rivera_Gil, P.; Montenegro, J.-M.; Braeckmans, K.; Müllen, K.; *et al.* Polymer-Coated Nanoparticles Interacting with Proteins and Cells: Focusing on the Sign of the Net Charge. *ACS Nano* **2013**, *7*, 3253–3263.
57. Ren, W.; Tian, G.; Jian, S.; Gu, Z.; Zhou, L.; Yan, L.; Jin, S.; Yin, W.; Zhao, Y. TWEEN Coated NaYF4:Yb,Er/NaYF4 Core/Shell Upconversion Nanoparticles for Bioimaging and Drug Delivery. *RSC Adv.* **2012**, *2*, 7037–7041.
58. Le Maire, M.; Champeil, P.; Møller, J. V. Interaction of Membrane Proteins and Lipids with Solubilizing Detergents. *Biochim. Biophys. Acta, Biomembr.* **2000**, *1508*, 86–111.

59. Zhang, Y.; Lam, Y. M. Controlled Synthesis and Association Behavior of Graft Pluronic in Aqueous Solutions. *J. Colloid Interface Sci.* **2007**, *306*, 398–404.
60. Vitale, S. A.; Katz, J. L. Liquid Droplet Dispersions Formed by Homogeneous Liquid–Liquid Nucleation: "The Ouzo Effect". *Langmuir* **2003**, *19*, 4105–4110.
61. Lince, F.; Marchisio, D. L.; Barresi, A. A. Strategies to Control the Particle Size Distribution of Poly-E-Caprolactone Nanoparticles for Pharmaceutical Applications. *J. Colloid Interface Sci.* **2008**, *322*, 505–515.
62. Kowalczuk, A.; Trzcinska, R.; Trzebicka, B.; Müller, A. H. E.; Dworak, A.; Tsvetanov, C. B. Loading of Polymer Nanocarriers: Factors, Mechanisms and Applications. *Prog. Polym. Sci.* **2014**, *39*, 43–86.
63. Torchilin, V. P. Micellar Nanocarriers: Pharmaceutical Perspectives. *Pharm. Res.* **2007**, *24*, 1–16.
64. Chorny, M.; Fishbein, I.; Danenberg, H. D.; Golomb, G. Lipophilic Drug Loaded Nanospheres Prepared by Nanoprecipitation: Effect of Formulation Variables on Size, Drug Recovery and Release Kinetics. *J. Controlled Release* **2002**, *83*, 389–400.
65. Contado, C.; Vighi, E.; Dalpiaz, A.; Leo, E. Influence of Secondary Preparative Parameters and Aging Effects on PLGA Particle Size Distribution: A Sedimentation Field Flow Fractionation Investigation. *Anal. Bioanal. Chem.* **2013**, *405*, 703–711.
66. Khoee, S.; Yaghoobian, M. An Investigation into the Role of Surfactants in Controlling Particle Size of Polymeric Nanocapsules Containing Penicillin-G in Double Emulsion. *Eur. J. Med. Chem.* **2009**, *44*, 2392–2399.
67. Redhead, H. M.; Davis, S. S.; Illum, L. Drug Delivery in Poly(lactide-Co-Glycolide) Nanoparticles Surface Modified with Poloxamer 407 and Poloxamine 908: *In Vitro* Characterisation and *in Vivo* Evaluation. *J. Controlled Release* **2001**, *70*, 353–363.
68. Duy, J.; Connell, L. B.; Eck, W.; Collins, S. D.; Smith, R. L. Preparation of Surfactant-Stabilized Gold Nanoparticle–Peptide Nucleic Acid Conjugates. *J. Nanopart. Res.* **2010**, *12*, 2363–2369.
69. Croy, S. R.; Kwon, G. S. Polysorbate 80 and Cremophor EL Micelles Deaggregate and Solubilize Nystatin at the Core–Corona Interface. *J. Pharm. Sci.* **2005**, *94*, 2345–2354.
70. Chaibundit, C.; Ricardo, N. M. P. S.; Costa, F.; de, M. L. L.; Yeates, S. G.; Booth, C. Micellization and Gelation of Mixed Copolymers P123 and F127 in Aqueous Solution. *Langmuir* **2007**, *23*, 9229–9236.
71. Schubert, S.; Delaney, J. T.; Schubert, U. S. Nanoprecipitation and Nanoformulation of Polymers: From History to Powerful Possibilities beyond Poly(lactic Acid). *Soft Matter* **2011**, *7*, 1581–1588.
72. Nehilla, B. J.; Allen, P. G.; Desai, T. A. Surfactant-Free, Drug-Quantum-Dot Coloaded Poly(lactide-Co-Glycolide) Nanoparticles: Towards Multifunctional Nanoparticles. *ACS Nano* **2008**, *2*, 538–544.
73. Trofymchuk, K.; Reisch, A.; Shulov, I.; Mély, Y.; Klymchenko, A. S. Tuning the Color and Photostability of Perylene Diimides Inside Polymer Nanoparticles: Towards Biodegradable Substitutes of Quantum Dots. *Nanoscale* **2014**, *6*, 12934–12942.
74. Clamme, J. P.; Azoulay, J.; Mély, Y. Monitoring of the Formation and Dissociation of Polyethylenimine/DNA Complexes by Two Photon Fluorescence Correlation Spectroscopy. *Biophys. J.* **2003**, *84*, 1960–1968.

Supporting Information for:

Charge-Controlled Nanoprecipitation as a Modular Approach to Ultrasmall Polymer Nanocarriers: Making Bright and Stable Nanoparticles

Andreas Reisch, Anne Runser, Youri Arntz, Yves Mély, Andrey S. Klymchenko

Laboratoire de Biophotonique et Pharmacologie, UMR 7213 CNRS, Université de Strasbourg,

Faculté de Pharmacie, 74, Route du Rhin, 67401 Illkirch, France

NMR spectra of PMMA and PCL modifications

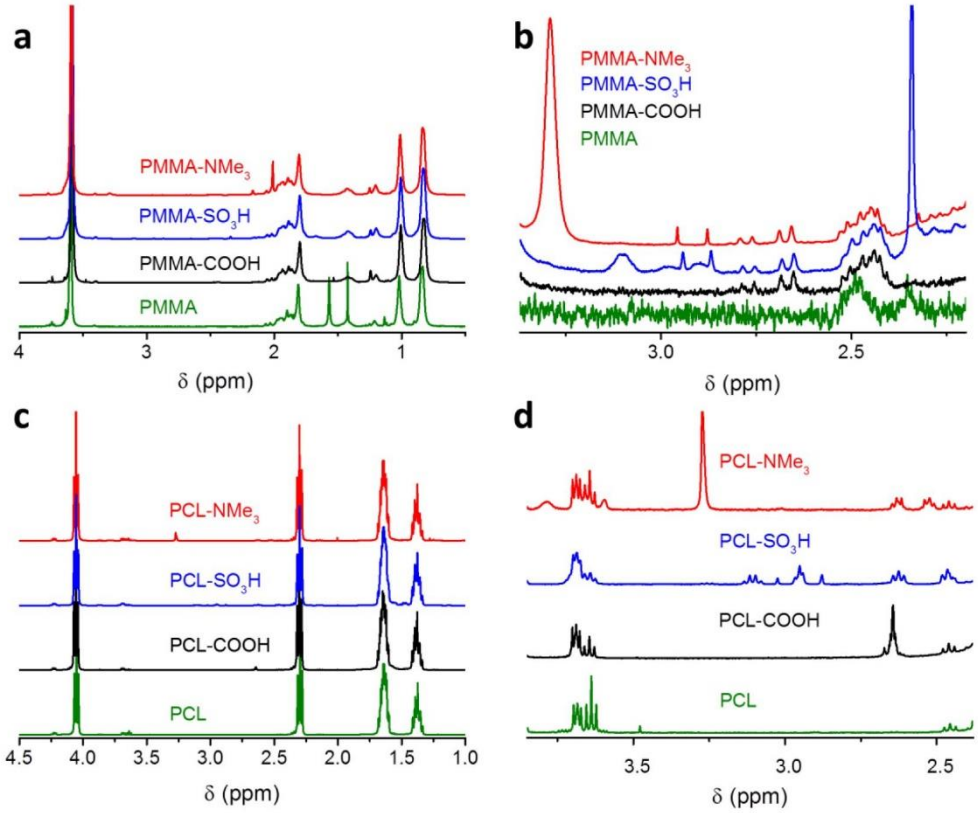

Fig. S1. ^{1}H-NMR spectra of PMMAs and PCLs. (a, b) Spectra of PMMA, parent poly(methyl methacrylate-*co*-methacrylic acid) (PMMA-COOH), and PMMA-COOH modified with sulfonate and trimethylammonium side groups (b: zoom on the region between 3.4 and 2.2 ppm). (c, d) Spectra of parent PCL, and PCL modified with carboxylate, sulfonate, and trimethylammonium side groups (b: zoom on the region between 3.8 and 2.4 ppm).

Atomic force microscopy of PLGA-COOH NPs

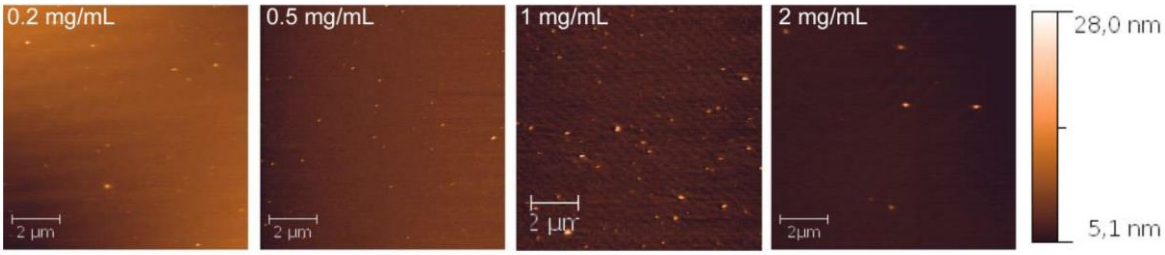

Fig. S2. AFM images of PLGA-COOH NPs made at different PLGA concentrations and immobilized on PEI coated mica substrates.

Electron microscopy of PMMA-SO_3H NPs

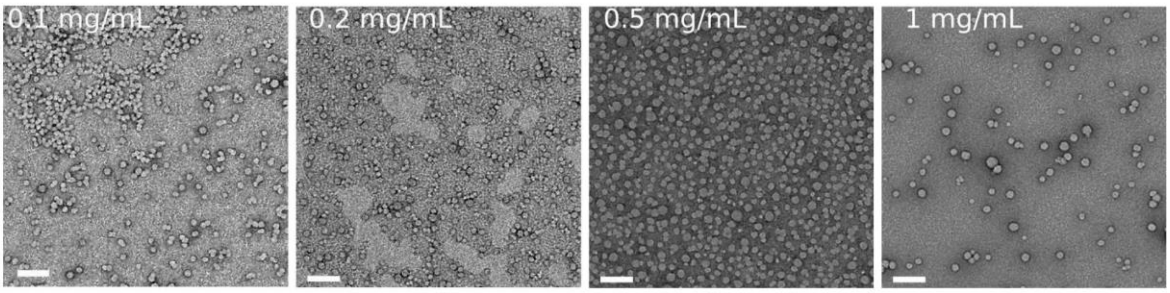

Fig. S3. TEM images of PMMA-SO_3H NPs made at different PMMA-SO_3H concentrations and immobilized on amylamine glow discharge treated carbon-coated copper-rhodium electron microscopy grids, followed by staining with uranyl acetate. The scale bars correspond to 100 nm.

Encapsulation efficiencies

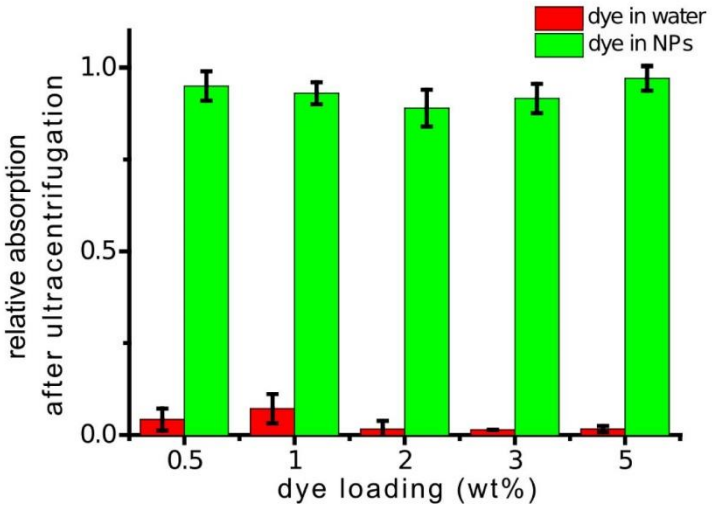

Fig S4. Absorbance ratios before and after ultracentrifugation at 560 nm of water solutions of NPs containing different amounts of R18/F5-TPB dye and of the dye without polymer at equivalent concentrations.

Stability of NPs in PBS and serum

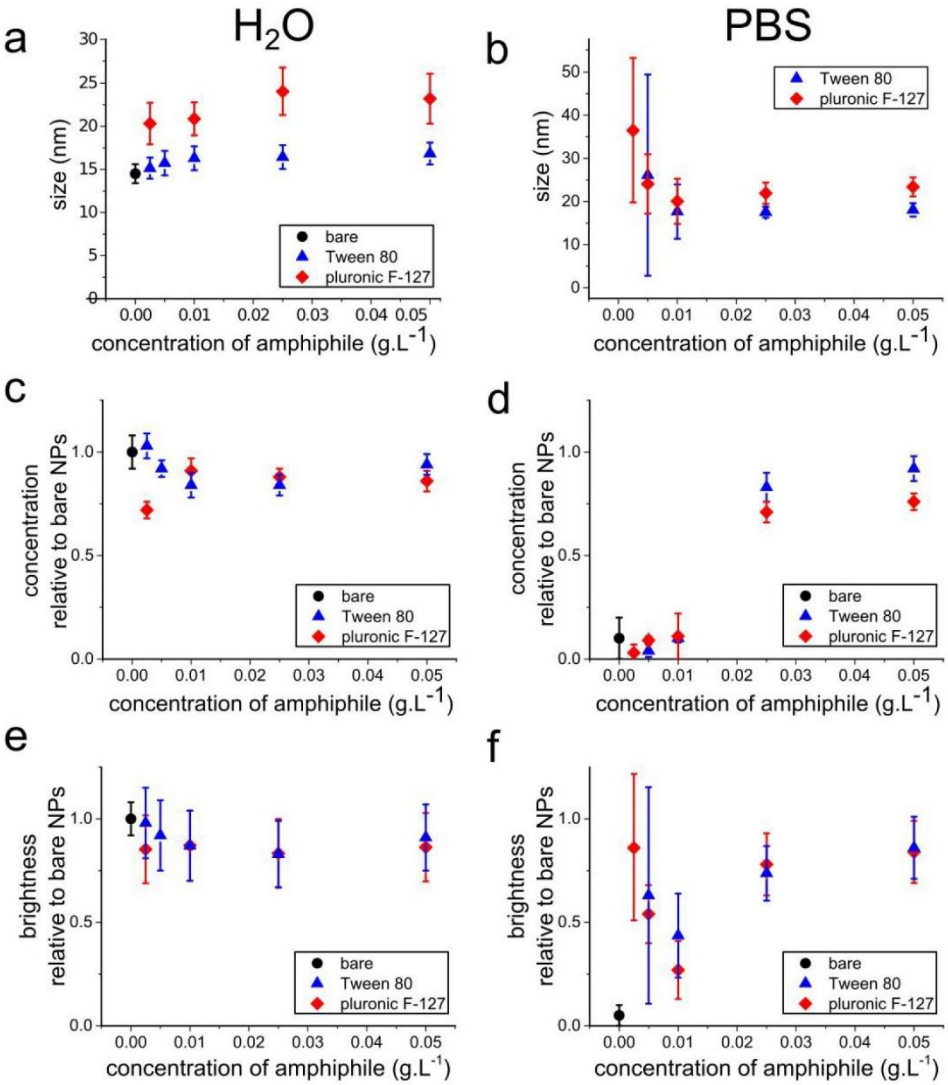

Fig. S5. Stabilization of nanoparticles by surfactants. (a, b) Size, (b, c) concentration, and (e, f) brightness of PMMA-SO_3H NPs in milliQ-water (a, c, e) and phosphate buffered saline (PBS, b, d, f) as measured by FCS for different amphiphile concentrations (Tween 80 or pluronic F-127). The NPs were obtained from 0.2 mg.mL^{-1} solutions of PMMA-SO_3H. Concentration and brightness are given relative to bare NPs in water. Error bars give the standard deviation over the individual FCS measurements.

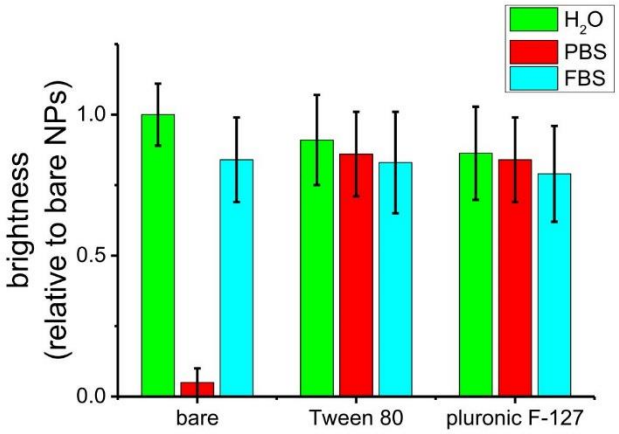

Fig. S6. Stabilization of nanoparticles by surfactants. Brightness of PMMA-SO_3H NPs in MilliQ-water, phosphate buffered saline (PBS), and 10 vol.% fetal bovine serum (FBS) as measured by FCS relative to bare NPs in water. NPs were either used as made or treated with 0.05 $mg.mL^{-1}$ of Tween 80 or pluronic F127. The NPs were obtained from 0.2 $mg.mL^{-1}$ solutions of PMMA-SO_3H. Error bars give the standard deviation over the 40 FCS measurements of a single sample.

Solubility of PLGAs in acetonitrile-water mixtures

Turbidity measurements were used to access the solubility of PLGA with different end-groups in mixtures of acetonitrile and water. For this, the PLGA was dissolved at a concentration of 1 mg mL^{-1} in acetonitrile. 1 mL of these solutions was placed in a 1 mL quartz cuvette. Then different amounts of water were added and after mixing, the absorbance spectra were recorded. The absorbance at 400 nm of these mixtures is given in Fig. S5. Independently of the end-group, no turbidity was observed up to a water content of 0.17 (that is the absorbance remained 0), and turbidity occurred for all PLGAs starting from a water content of 0.20. The nature of the end-group thus did not have a significant influence on the solubility of the PLGA.

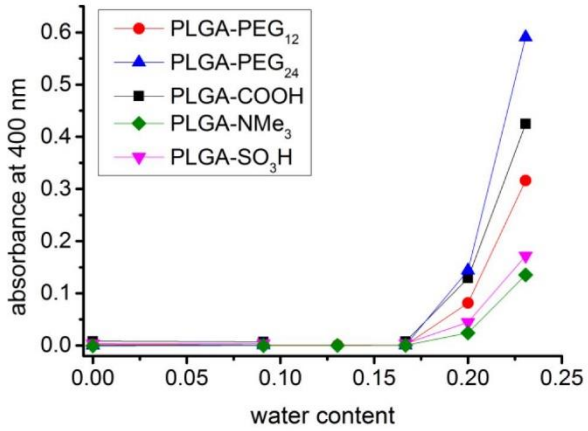

Fig. S7. Absorbance at 400 nm of solutions of PLGA with different end-groups in water-acetonitrile mixtures containing different amounts of water. The original PLGA concentration was 1 mg mL^{-1}. The water content is the volume ratio of added water to total volume of the solution.

3.2 Application pour la biologie

En collaboration avec Sylvie Egloff et Doriane Heimburger, ces NPs ont permis d'observer leur comportement dans le cytosol de cellules vivantes après microinjection ou électroporation des cellules. Nous avons utilisé la gamme de NPs décrites précédemment (figure 28) dont la taille varie entre 12 et 38 nm. Ces NPs sont chargées avec 10 % R18/F5-TPB les rendant extrêmement brillantes. Pour éviter les interactions non spécifiques, les NPs ont été traitées avec du tween 80 (T80), un surfactant portant du polyéthylène glycol (PEG), par simple adsorption sur la surface. Les NPs ont ensuite été introduites dans le cytosol *via* deux différentes méthodes : la microinjection ou l'électroporation.

Etude du comportement des NPs par microinjection

Une série de NPs de 17 et 32 nm ont été microinjectées dans le cytosol de cellules HeLa vivantes. Grâce à leur grande brillance, les NPs ont pu être observées de manière individuelle. La majorité des plus grandes NPs (32 nm) reste proche du point d'injection comme le montre la figure 29. Quelques particules bougent dans le cytosol mais leur mouvement est restreint au niveau du pourtour du point d'injection. Les NPs de 17 nm réalisées à partir de PMMA-SO_3H 1% dans l'eau, montrent cependant une bonne dispersion dans le cytosol. La quasi-totalité des NPs se retrouve dans le cytosol et se déplacent rapidement occupant tout l'espace. Seules 10% de ces NPs restent bloquées au point d'injection. En observant la distribution de taille des NPs de 17 et 32 nm, 10% des NPs ont des tailles plus grandes que 23 nm pour les NPs de 17 nm alors que 5 % des NPs sont en-dessous de 23 nm pour les NPs de 32 nm. La taille critique permettant une diffusion libre dans le cytosol se situe donc à 23 nm. Les particules plus petites de 9 et 12 nm montrent une meilleure accessibilité dans le cytosol en particulier au niveau des régions cytoplasmiques plus encombrées ou difficiles d'accès.

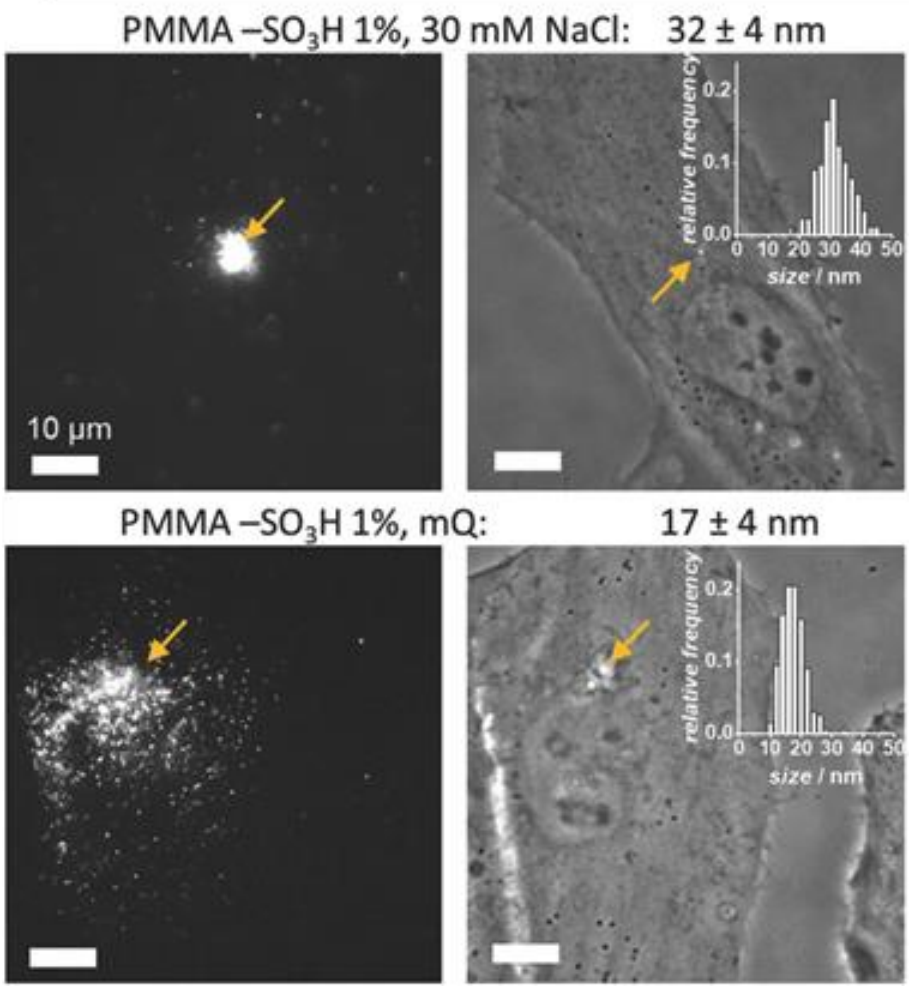

Figure 29. Images de microscopie de NPs de PMMA-SO_3H 1% chargées à 10 % R18/F5-TPB traitées avec du tween 80 microinjectées dans des cellules HeLa vivantes. A gauche : image de microscopie d'épifluorescence de NPs de 32 et 17 nm préparées dans $30x10^{-3}$ M NaCl et dans l'eau, respectivement. A droite : image en contraste de phase des cellules correspondantes. Les points d'injections sont indiqués par des flèches. Les histogrammes montrent les distributions des tailles des NPs mesurées par TEM. Barres d'échelle : 10 μm.

Etude du comportement des NPs par électroporation

Parmi les différentes manières de faire entrer du matériel dans la cellule, l'électroporation a l'avantage de transférer des molécules ou particules dans le cytosol sur un large nombre de cellules en même temps.[195] L'électroporation repose sur la perméabilisation de la membrane plasmique. Cependant cette méthode demande une optimisation des conditions d'électroporation. En effet il s'agit de trouver des conditions suffisamment douces pour créer une perméabilité réversible sans provoquer des pores trop larges qui conduiraient à la mort cellulaire. A l'inverse, le matériel, en l'occurrence

ici, les NPs, risquent de rester bloquées à l'entrée ou dans le milieu extracellulaire si leur taille est trop grande par rapport aux pores. Nous avons donc déterminé la taille limite des NPs pour entrer dans le cytoplasme *via* les pores d'électroporation. Pour cela, nous avons utilisé une gamme de NPs de PMMA-SO_3H de cinq tailles différentes : 12, 17, 25, 32 et 38 nm (figure 28). Ces NPs ont été ajoutées aux cellules électroporées avant d'être rincées pour éliminer les NPs restant dans le milieu extracellulaire. Après un repos des cellules de 2h, elles ont été imagées par microscopie de fluorescence. Les plus petites NPs de 12 et 17 nm rentrent en grande quantité dans les cellules électroporées (figure 30). Par contre la quantité de NPs dans les cellules est nettement plus faible pour les NPs de 25 nm. La quantité de NPs dans les cellules diminue d'autant plus que la taille augmente pour les NPs de PMMA-SO3H 1 % de 32 et 38 nm. Les contrôles sans électroporation ne montrent aucune NPs indiquant qu'il n'y a pas d'interactions non spécifiques entre les NPs et la membrane plasmique.

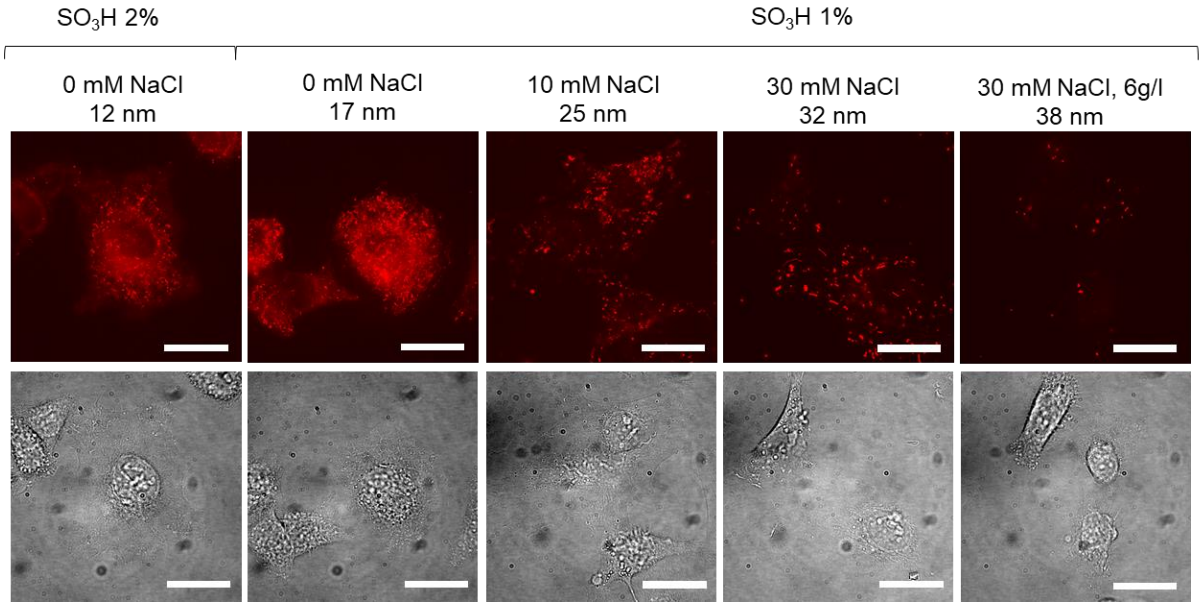

Figure 30. Cellules HeLa vivantes électroporées et incubées avec les NPs de PMMA-SO3H 2 et 1 % de différentes tailles. Les cellules ont été lavées pour ôter les NPs résiduelles dans le milieu extracellulaire avant d'être imagées par microscopie d'épifluorescence. En haut : projection du maximum de l'intensité de fluorescence. En bas : images en contraste de phase des cellules correspondantes. Elles sont chargées avec 10 % de R18/F5-TPB et traitées avec du tween 80. Barre d'échelle : 25 µm.

De plus, les vidéos correspondant aux images de microscopie figure 30, montrent une bonne mobilité des plus petites NPs de 12 et 17 nm dans les cellules. Ainsi pour franchir la membrane plasmique perméabilisée par électroporation, les NPs doivent avoir un diamètre inférieur à 25 nm.

Les différences de comportement et de diffusion des NPs sont donc extrêmement dépendantes de leur taille. Celle-ci va déterminer leur capacité à traverser la membrane dans le cas de l'électroporation puis à passer à travers le maillage du cytosquelette[196] et l'encombrement cytoplasmique[197] ainsi que d'atteindre des régions de diffusion restreintes telle que les zones proches du réticulum endoplasmique ou de l'appareil de golgi.[10,198] L'étude du comportement des NPs dans le cytoplasme a permis de déterminer une taille critique < 25 nm permettant de franchir la membrane cytoplasmique par électroporation puis une taille ≤ 23 nm pour diffuser librement dans le cytosol. Néanmoins, si les NPs doivent avoir accès à des zones plus encombrées où la diffusion est restreinte dans le cytosol notamment au niveau des régions péri-nucléaires, le diamètre doit alors être diminué au maximum pour être de l'ordre des tailles des protéines (~10 nm).

Une partie de ces résultats a été publié dans l'article joint en annexe :

Article 2 : Protein-Sized Dye-Loaded Polymer Nanoparticles for Free Particle Diffusion in Cytosol. Andreas Reisch, Doriane Heimburger, Pauline Ernst, Anne Runser, Pascal Didier, Denis Dujardin, Andrey S. Klymchenko. *Advanced Functional Materials* **28**, 1805157 (2018).

Partie 4 : Optimisation de la luminescence pour l'imagerie intracellulaire

Observer et suivre des NPs individuelles est particulièrement difficile dans les milieux biologiques. L'autofluorescence résultant des cellules et tissus, réduit considérablement le signal sur bruit résultant.[144] La visualisation de molécules ou particules individuelles nécessite alors des puissances d'illumination généralement élevées pour obtenir un signal d'émission qui se détache du bruit de fond.[72] L'optimisation du signal/bruit se fait soit en augmentant la brillance de la sonde luminescente, soit en diminuant le bruit de fond résultant de l'autofluorescence des cellules.

Dans un premier temps, nous avons choisi d'utiliser une technique permettant d'éliminer l'autofluorescence venant de l'échantillon : l'imagerie à déclenchement périodique (ou « time-gated imaging ») en utilisant des complexes de lanthanides encapsulés dans les NPs de polymères. Ensuite, nous sommes revenus vers un système de NPs de polymères contenant des fluorophores plus conventionnels, des sels cationiques de rhodamine, en optimisant la brillance de ces NPs et en essayant également de moduler leur clignotement.

4.1 Nanoparticules de lanthanides

Les complexes de lanthanides ont la particularité de posséder des temps de vie de plusieurs µs à quelques dizaines de ms.[145] Ce sont par conséquent, d'excellents candidats pour l'imagerie à déclenchement périodique. Le principe de cette méthode d'imagerie repose sur l'application d'un délai entre l'excitation de l'émetteur luminescent et l'acquisition de l'image. Ce délai permet la suppression du signal luminescent des émetteurs à temps de vie courts (ns à µs). Par conséquent, le signal sur bruit obtenu est nettement supérieur comparé aux méthodes d'imagerie de luminescence conventionnelles. Associé à une grande brillance des émetteurs, cela permettrait d'obtenir une précision de localisation sans précèdent et la possibilité de suivre en temps réel des biomolécules individuelles. Néanmoins, les ions trivalents de lanthanides seuls possèdent des coefficients d'extinction extrêmement bas. La présence de ligands aromatiques coordinant les ions lanthanides permettent

néanmoins d'augmenter considérablement leur coefficient d'extinction et l'émission de luminescence grâce à l'effet d'antenne. Toutefois cela suffit à peine à égaler les capacités d'absorption des fluorophores organiques. Leur brillance reste donc limitée par leur coefficient d'extinction et rend l'imagerie de molécules uniques à base de lanthanides extrêmement difficile.

Pour répondre à ce problème, nous avons encapsulé de grandes quantités de complexes d'europium [Eu(tta)$_3$phen] dans des particules de polymères. Des poly(méthacrylate de méthyle)s (PMMA) ont été synthétisés par polymérisation radicalaire. Ces PMMA portent des groupements chargés -SO_3H à 1 ou 3% ou COOH à 10 %. Les complexes [Eu(tta)$_3$phen] ont été encapsulés dans les particules par nanoprécipitation avec les polymères avec des chargements de 0, 5, 10, 20 ou 40%m. A un chargement de 40% [Eu(tta)$_3$phen], les mesures par TEM donnent trois tailles différentes de 13, 23 et 34 nm pour les NPs à base de PMMA-SO_3H 3%, 1% et PMMA-COOH 10% respectivement.

L'encapsulation du complexe dans les particules permet d'obtenir des rendements quantiques supérieurs à 20% dans l'eau pour des chargements à 40%. De plus le taux de décroissance bien supérieur pour les complexes [Eu(tta)$_3$phen] dans les particules (τ = 1.26 ± 0.04 ms) comparé à celui du complexe [Eu(tta)$_3$phen] dans l'acétonitrile (τ = 0.63 ms) montre que la matrice polymérique protège les complexes d'Eu^{3+} des milieux aqueux. Cela indique également une encapsulation efficace du complexe dans les NPs de polymères même à pourcentage de chargement élevé. Ainsi pour les NPs de PMMA-COOH 10% à 40% [Eu(tta)$_3$phen], nous avons estimé une moyenne de 5 000 complexes encapsulés par particules permettant d'atteindre des brillances de $4x10^7$ $M^{-1}.cm^{-1}$. Cette valeur est en adéquation avec la brillance mesurée expérimentalement par microscopie de particules individuelles qui est de 2.9×10^7 $M^{-1}.cm^{-1}$.

Par la suite, les NPs ont été observées par imagerie de luminescence à déclenchement périodique avec des intensités lumineuses de 0.24 W cm^{-2} soit 10 000 fois plus faibles qu'habituellement pour l'imagerie à base de lanthanides. L'incubation des NPs avec des cellules vivantes montrent une internalisation de ces dernières par endocytose.

En résumé, la combinaison de l'imagerie à déclenchement périodique et les NPs chargées avec de grandes quantités de lanthanides ont permis l'observation de ces dernières dans les cellules vivantes à des puissances lumineuses et des temps d'acquisition très faibles limitant la phototoxicité pour les cellules et permettant d'envisager l'observation de processus rapides.

Ce travail a été publié dans *Chemistry of Materials* et est joint ci-dessous.

Article 4 : Lanthanide-Complex-Loaded Polymer Nanoparticles for Background-Free Single-Particle and Live-Cell Imaging.

CHEMISTRY OF MATERIALS
Article
Cite This: Chem. Mater. 2019, 31, 4034−4041
pubs.acs.org/cm

Lanthanide-Complex-Loaded Polymer Nanoparticles for Background-Free Single-Particle and Live-Cell Imaging

Marcelina Cardoso Dos Santos,[†,∥] Anne Runser,[‡,∥] Hortense Bartenlian,[†] Aline M. Nonat,[§] Loïc J. Charbonnière,[§] Andrey S. Klymchenko,[‡] Niko Hildebrandt,[*,†] and Andreas Reisch[*,‡]

[†]NanoBioPhotonics (nanofret.com), Institute for Integrative Biology of the Cell (I2BC), Université Paris-Saclay, Université Paris-Sud, CNRS, CEA, 91405 Orsay Cedex, France

[‡]Laboratoire de Bioimagerie et Pathologies, CNRS UMR 7021, Université de Strasbourg, Faculté de Pharmacie, 67401 Illkirch Cedex, France

[§]Equipe de Synthèse pour l'analyse (SynPA), IPHC, UMR 7178 CNRS, Université de Strasbourg, ECPM, 25 rue Becquerel, 67087 Strasbourg Cedex, France

Supporting Information

ABSTRACT: Imaging single molecules and nanoparticles in complex biological media is highly challenging notably due to autofluorescence of cells and tissues. Lanthanides and lanthanide complexes, with their particularly long luminescence lifetimes, offer the possibility to perform time-gated imaging and thus to strongly reduce the autofluorescence background. However, their very low brightness and photon flux have limited their use in single-molecule imaging. Here, we encapsulate high amounts of Europium complexes into poly(methyl methacrylate)-based particles of 10, 20, and 30 nm size. The resulting particles contain up to 5000 copies of the complex with a quantum yield of ≥0.2, resulting in a per particle brightness of up to 4×10^7 M^{-1} cm^{-1}. They can be imaged at the single-particle level using low illumination intensities (0.24 W cm^{-2}) and low acquisition times (300 ms) and internalize well into living cells, where they can be monitored through time-gated imaging at illumination conditions compatible with living specimen. These Eu-complex-loaded nanoparticles can thus be applied for highly sensitive and autofluorescence-free imaging and have the potential to become very performant probes for fast intracellular tracking of single biomolecules.

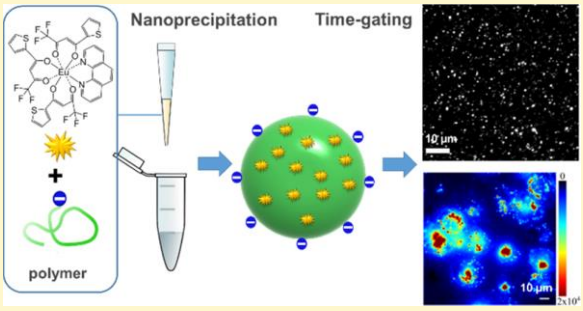

The field of luminescent nanoparticles (NPs)[1,2] for bioimaging and sensing is in constant expansion, and emerging NPs, such as semiconductor quantum dots,[3,4] upconverting NPs,[5−8] graphene or carbon dots,[9,10] lanthanide nanoparticles,[11−13] organic nanoparticles based on dyes and polymers,[14−18] and nanodiamonds,[19,20] have significantly advanced the versatility and capabilities of bioimaging applications. Detection and tracking of single NPs remain, however, challenging and often require very high illumination power and sensitive detectors to observe the particles in the presence of autofluorescence of cells and tissues.[6] Indeed, various compounds inherently present in cells or tissues, including aromatic amino acids, flavins and NAD(P)H, elastin, and porphyrins, and emitting in different wavelength regions, contribute an autofluorescence background over practically the entire visible spectrum.[21] Very bright NP probes that can be imaged while suppressing cell autofluorescence would hence offer the possibility to significantly increase the signal-to-background ratio. They would thus be valuable probes for monitoring single biomolecules with unprecedented precision directly inside living cells and thus obtain a wealth of information on biological processes at the molecular level in real time.[22,23]

Lanthanides have particularly long photoluminescence (PL) lifetimes, which offer the possibility to strongly reduce the autofluorescence background of living samples by time-gated (TG) imaging. Numerous studies have used inorganic lanthanide particles for immunodetection,[24−26] or for imaging in vitro[11,27−30] or in tissues and small animals.[31,32] However, the low photon flux of long-lived lanthanide PL (PL decay times up to milliseconds)[12] has strongly limited their use in single-particle imaging.[26,33−35] Imaging of single lanthanide particles requires near infrared irradiance power on the order of 10^3−10^6 W cm^{-2},[6,33,34] which can cause high phototoxicity,[36] or extremely long exposure times (30 s),[26] which are not compatible with single-molecule dynamics.

In the case of fluorescent dyes, the limits of brightness can be overcome by the so-called dye-doped or dye-loaded

Received: February 8, 2019
Revised: May 9, 2019
Published: May 29, 2019

ACS Publications © 2019 American Chemical Society

DOI: 10.1021/acs.chemmater.9b00576
Chem. Mater. 2019, 31, 4034−4041

Downloaded via UNIV STRASBOURG on November 14, 2019 at 09:34:32 (UTC).
See https://pubs.acs.org/sharingguidelines for options on how to legitimately share published articles.

polymer NPs.[16,18,37−39] Encapsulation of large amounts of fluorescent dyes in these NPs allows exceeding largely the brightness of fluorescent proteins or quantum dots (up to 100-fold), while the NPs are compatible with cellular imaging.[40−42] Application of this approach to lanthanide compounds would thus offer the possibility to combine high signal with suppression of the autofluorescence background but remains largely unexplored, especially in view of high loadings, which are needed to achieve high absorbance.[43−47] Indeed, attempts to directly load high amounts of Ln complexes led to either significant quenching of the PL intensity or leakage and instability of the resulting NPs.[48,49] This was either due to insufficient retention of the complexes in the host polymer or to the formation of clusters of complexes. As a consequence, most Ln complex-loaded polymer NPs are limited with respect to their loadings and often an optimum loading of about 2 wt % was used.[45,49−53] Particularly interesting candidates for encapsulation are lanthanide complexes (chelates or cryptates), which provide much higher absorption cross sections and PL quantum yields (QYs) than those of the pure lanthanide ions and have been used in many biosensing applications.[12,54] Loading of high amounts of these bright lanthanide complexes with long PL lifetimes into small polymeric NPs has the potential to extend NP-based PL imaging to challenging biological samples (e.g., tissues) with high intrinsic autofluorescence through the use of TG. In this work, we demonstrate that single-particle and live-cell imaging of small polymer NPs (down to 10 nm) loaded with lanthanide complexes can be performed with short acquisition times and low irradiation power (Figure 1). Our proof-of-concept study demonstrates the possibility to extend lanthanide-NP imaging toward single-particle tracking and thus their potential as probes for the investigation of cellular and molecular dynamics.

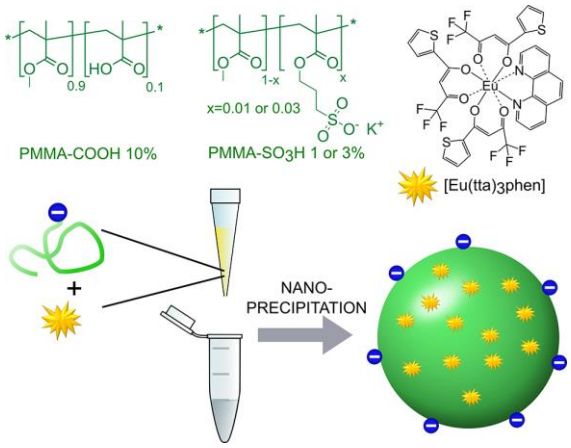

Figure 1. Chemical structures of the polymers and the lanthanide complex used in this study, and schematic representation of the synthesis of Europium-complex-loaded polymer NPs (ECP-NPs).

■ RESULTS AND DISCUSSION

Europium-complex-loaded polymer NPs (ECP-NPs) were prepared through nanoprecipitation of acetonitrile solutions containing the Eu^{3+}-complex and methyl methacrylate-based copolymers (PMMA) bearing sulfonate (1 and 3 mol %) or carboxylate (10 mol %) groups in water (Figure 1). The charged groups were introduced during polymerization to reduce and control the size of the particles.[55,56] We encapsulated 1−40 wt % (relative to the polymer) of $Eu(tta)_3phen$ (Eu^{3+} surrounded by three [4,4,4-trifluoro-1-(2-thienyl)-1,3-butanedionate] and 1,10-phenantroline ligands)[57] inside the NPs. This resulted in three series of ECP-NPs with mean diameters, as obtained from transmission electron microscopy (TEM), of ∼30, ∼20, and ∼10 nm for PMMA-COOH 10%, PMMA-SO_3H 1%, and PMMA-SO_3H 3%, respectively (Figure 2). Particle sizes slightly increased with increasing $Eu(tta)_3phen$ loading. At the highest loading of 40 wt % $Eu(tta)_3phen$, TEM showed spherical NPs with sizes of 13, 23, and 34 nm, respectively, and relatively narrow size distributions (Figure 2B). Especially, in view of their future use as labels for intracellular imaging, small sizes are important.[56,58] The smallest ECP-NPs obtained here have sizes on the order of those of antibodies, which makes them particularly attractive as labels for single biomolecules. Encapsulation of the Eu^{3+} complex was confirmed by the higher contrast of the loaded NPs in TEM (Figure S1).

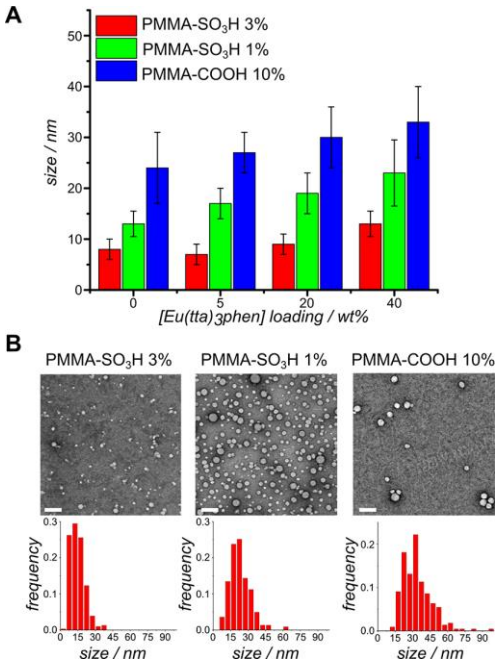

Figure 2. (A) Size measurements of ECP-NPs by TEM. NPs of PMMA-SO_3H 1 and 3% and PMMA-COOH 10% were loaded with different amounts of $[Eu(tta)_3phen]$. Sizes are mean values over at least 200 particles; error bars correspond to width at half-maximum of the size distributions. (B) TEM images and size distribution of NPs at 40 wt % $[Eu(tta)_3phen]$ loading made from different polymers. Scale bars correspond to 100 nm. At least 100 NPs were analyzed per condition.

We then characterized the photophysical properties of these ECP-NPs. Their absorption showed no spectral variations (compared to those for $Eu(tta)_3phen$ in organic solution) and the absorbance increased with $Eu(tta)_3phen$ loading (Figure S2). ECP-NP emission spectra clearly showed the $Eu(tta)_3phen$ characteristics with intense PL of the hypersensitive $^5D_0 \rightarrow {}^7F_2$ transition of Eu^{3+} between 610 and 630 nm (Figures 3A and S2).[59] PL quantum yields (QYs) in water

DOI: 10.1021/acs.chemmater.9b00576
Chem. Mater. 2019, 31, 4034−4041

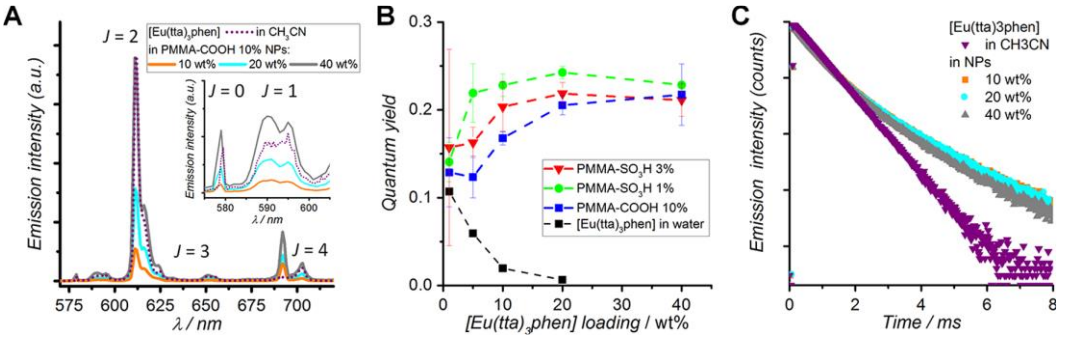

Figure 3. (A) Emission spectra (λ_{exc} = 350 nm) recorded in aqueous solution for PMMA-COOH 10% NPs loaded with different amounts of [Eu(tta)$_3$phen], as well as of [Eu(tta)$_3$phen] in CH_3CN. Inset: Zoom on the $^5D_0 \rightarrow {}^7F_{J=0,1}$ transitions. (B) Photoluminescence quantum yields of ECP-NPs vs [Eu(tta)$_3$phen] loading. Data points correspond to mean values from three independent measurements. Error bars correspond to standard error of the mean. ([Eu(tta)$_3$phen] in water at a concentration corresponding to 40 wt % in the NPs led to the formation of sedimenting aggregates.) (C) Time-resolved emission decay profiles (rt, λ_{exc} = 350 nm) measured for solutions of [Eu(tta)$_3$phen] in acetonitrile and of PMMA-COOH 10% NPs loaded with different amounts of [Eu(tta)$_3$phen]. Note: Log scale for emission intensity.

Table 1. Lifetimes of [Eu(tta)$_3$phen] in Acetonitrile and of ECP-NPs in Water[a,b]

	τ_1		τ_2	
	ms	%	ms	%
[Eu(tta)$_3$phen] in CH_3CN	0.625	100		
PMMA-COOH 10%−10% [Eu(tta)$_3$phen]	0.524	50	1.301	50
PMMA-COOH 10%−20% [Eu(tta)$_3$phen]	0.524	50	1.301	50
PMMA-COOH 10%−40% [Eu(tta)$_3$phen]	0.553	65	1.218	34

[a]Room temperature (rt), λ_{exc} = 350 nm. [b]Estimated errors: ±10% on lifetimes.

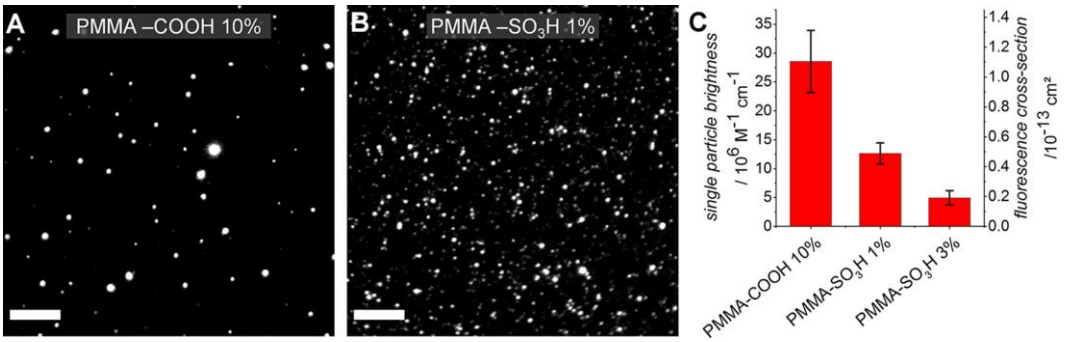

Figure 4. TG single-particle images of PMMA-COOH 10% (A) and PMMA-SO_3H 1% (B) at 40% [Eu(tta)$_3$phen] loading. Scale bars: 10 μm. (C) Average single-particle PL brightness in M^{-1} cm^{-1} and their correspondence in luminescence cross section as obtained from single-particle microscopy. At least 100 particles were analyzed for each condition. Error bars correspond to SD.

increased with Eu(tta)$_3$phen loading and reached a maximum of ~0.25 at around 20 wt % (Figure 3B). QYs were highest in PMMA-SO_3H 1%, followed by PMMA-SO_3H 3% and PMMA-COOH 10% (Table S1). The biexponential PL decays of ECP-NPs indicated two distinct populations of Eu(tta)$_3$phen inside the NPs (Figure 3C and Table 1). The shorter decay time (τ_1 = 0.54 ± 0.02 ms) was in the same range as for Eu(tta)$_3$phen in acetonitrile (τ = 0.63 ms) and therefore assigned to a population close to the surface of the NPs. The longer decay (τ_2 = 1.26 ± 0.04 ms) exceeded the lifetime of Eu(tta)$_3$phen measured in solid state (τ = 0.87 ms)[60] and was therefore assigned to a population in the core of the NPs.

These results indicate an efficient encapsulation of Eu(tta)$_3$phen in the polymer NPs and a good protection of the Eu cations from water deactivation. Indeed, addition of Eu(tta)$_3$phen to water (in the absence of polymer) led to aggregation and thus a strong decrease in the absorbance together with QYs close to zero (Figure 3B). The influence of the nature of the polymer on the QY could stem from the differences in size of the resulting NPs, the number of charged groups, or their nature. No clear correlation with size was observed. At the same time, the QYs decreased with increasing fraction of charged groups on the polymer. These might hence interact with part of the complexes, as their concentrations lie in a similar range. The nature of the charged groups could also play a role, with carboxylates interacting more strongly with the complexes than sulfonates. The observed increase in QY with loading of the complex could be explained by a higher fraction of the complex encapsulated in the core of the NPs, which is characterized by a prolonged lifetime. The increase of the PL decay time upon encapsulation is of high interest for applications such as time-resolved microscopy or fluoroimmu-

DOI: 10.1021/acs.chemmater.9b00576
Chem. Mater. 2019, 31, 4034−4041

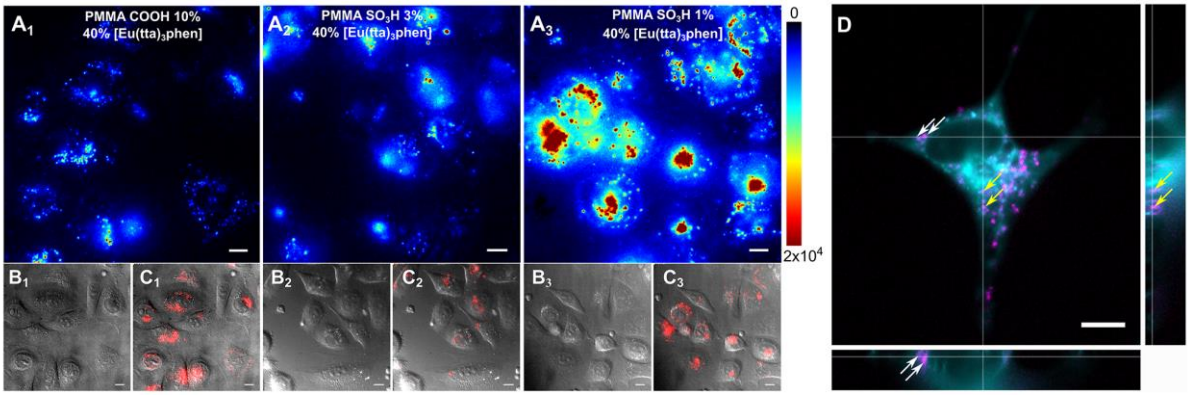

Figure 5. Live-cell images of HeLa cells incubated with ECP-NPs. (A) TG PL images with PMMA-COOH 10% (A_1), PMMA-SO_3H 3% (A_2), and PMMA-SO_3H 1% (A_3) NPs at 40% [$Eu(tta)_3phen$] loading. For a better comparison between the different images, the intensity scale was fixed at 0 to 2×10^4 counts. (B) Differential interference contrast (DIC) images. (C) Overlay of images from A and B (ECP-NP PL is shown in red, PL intensities were normalized to the highest values in A1, A2, and A3). (D) Projections of a z-stack of images of a HeLa cell incubated with ECP-NPs (PMMA-COOH 10% at 40% [$Eu(tta)_3phen$]). ECP-NPs are shown in magenta and the cell membranes in turquoise (costained with DiD). Large image: x/y-optical section at 6 μm from the surface; small images are optical sections of cell along the x- and y-axis of the z-stack with a x/z side view (bottom) and y/z side view (right). Lines in the images indicate positions of the sections; white and yellow arrows point to ECP-NPs in endosomes/lysosomes. Scale bars in all images: 10 μm.

noassay because it allows for a more efficient autofluorescence background suppression. Interestingly, practically, no concentration quenching was observed for these complexes, at least up to 20 wt %. This results in a very high brightness of the obtained luminescent NPs: the PMMA-COOH 10% NPs of 34 nm encapsulate about 5000 complexes per particle (based on NP size for 40 wt % loading) with a QY of 21%, yielding a brightness, B, of $0.21 \times 40\,000\ M^{-1}\ cm^{-1} \times 5000 = 4.2 \times 10^7\ M^{-1}\ cm^{-1}$ and a luminescence cross section, σ, of $1.6 \times 10^{-13}\ cm^2$ (see the Methods section for calculations). For the PMMA-SO_3H 1 and 3% NPs, the corresponding brightness is 1.2×10^7 and $0.34 \times 10^7\ M^{-1}\ cm^{-1}$, respectively. These differences are first of all due to the differences in size and the resulting variation of the number of complexes per particle. Indeed, dividing the particle brightness by the particle volume gives similar values of $(2100 \pm 200)\ M^{-1}\ cm^{-1}\ nm^{-3}$ for all three polymers. The brightness of our ECP-NPs thus largely exceeds that of classical molecular fluorophores (on the order of $10^5\ M^{-1}\ cm^{-1}$) and even that of the brightest quantum dots (e.g., $7.4. \times 10^6\ M^{-1}\ cm^{-1}$ for QDot 625 from Invitrogen).

Taking advantage of the exceptional brightness of our ECP-NPs, we assessed their performance for single-particle imaging using both continuous illumination (for photon counting) and TG imaging. For this, very dilute solutions of the NPs were deposited on polyethylenimine (PEI)-treated glass or in poly(vinyl alcohol) (PVA) gels under conditions favoring immobilization as single particles.[40,41] The NPs could be imaged at the single-particle level in both imaging modes (Figures 4, S3, and S4): using a setup for photon counting and steady-state illumination allowed us to determine the absolute brightness of the particles as 2.9×10^7, 1.2×10^7, and $0.5 \times 10^7\ M^{-1}\ cm^{-1}$, respectively, for the 40 wt % PMMA-COOH 10%, PMMASO_3H 1%, and PMMASO_3H 3% particles (σ = 1.1, 0.48, and $0.18 \times 10^{-13}\ cm^2$, respectively). These values are in reasonable agreement with the particle brightness obtained from spectroscopic data, and in line with their size and thus the number of encapsulated complexes per particle (see the Supporting Information for details on calculations). In TG imaging (detection window from 0.01 to 0.61 ms after pulsed excitation),[61] efficient detection of single particles of all three types of ECP-NPs loaded with 40 wt % of $Eu(tta)_3phen$ was accomplished with excitation power densities as low as 0.24 W cm^{-2} and an impressively short total acquisition time (for lanthanide detection) of 666 ms (Figures 4 and S3). The brightness of the particles in TG imaging also increased in the order PMMA-SO_3H 3% < PMMASO_3H 1% < PMMA-COOH 10%. It should be noted that these results could be obtained on an imaging setup that used extremely low light doses in the sub μJ cm^{-2} range, which is several orders of magnitude lower than those used in conventional fluorescence imaging studies and thus avoids cytotoxic effects.[11] Besides being even brighter than QDs, the ECP-NPs have thus the distinct advantage that they are suitable for TG imaging down to the single-particle level, which opens the way to suppression of autofluorescence background in cellular imaging.

Encouraged by the single-particle imaging capability of the ECP-NPs, we investigated their potential for live-cell imaging. For this purpose, the NPs were incubated for 3 h with HeLa cells and TG imaging was performed with a very low excitation power density of 0.24 W cm^{-2}, which is compatible with biological samples and 4 orders of magnitude lower compared to conventional lanthanide-based imaging.[62] Figure 5 shows strong PL signals from endocytosed ECP-NPs, for both the sulfonate- and the carboxylate-based particles. Highest luminescence was observed for the PMMA-SO_3H 1% particles followed by PMMA-SO_3H 3% and PMMA-COOH 10% particles, which indicates the highest uptake efficiency for the former NPs. These differences indicate that sulfonate bearing NPs are more readily internalized than those bearing carboxylate. However, as size and NP concentration change at the same time, it is difficult to derive general relations. An acquisition time of 333 ms (0.01 ms delay, 0.6 ms gate, 100 gates/exposure), corresponding to acquisition times used in conventional imaging, was sufficient to clearly image our NPs inside cells. To better appreciate the localization of NPs inside the cells, PL and differential interference contrast (DIC) images were overlayed and the intensity scale adapted according to the PL level (Figure 5C). In addition, TG

DOI: 10.1021/acs.chemmater.9b00576
Chem. Mater. 2019, 31, 4034−4041

imaging eliminates all autofluorescence, such that the experiments could be performed in complete cell culture medium (Figure S8). The intracellular position of the ECP-NPs was studied by optical sectioning of HeLa cells in the *Z*-direction (Figure 5D, Supporting Information Movie S1), by imaging after different incubation times (Figure S9), and by costaining with LysoTracker (Figure S6). These experiments indicated that the ECP-NPs first adsorbed on the membrane and then located in endosomes or lysosomes inside the cells. To investigate intracellular brightness as a function of Eu-$(tta)_3$phen loading, cells were incubated with carboxylate polymer NPs at 40, 20, 10, and 5% doping ratios (Figure S7). At the highest loading ratio, PL intensities of the brightest points inside the cells exceeded 10 000 counts, whereas those at the lowest loading ratio still reached 1000 counts, confirming increasing luminescence intensity of the particles with increasing loading directly in the cells.

To investigate a long-term effect of NPs on live cells, we controlled cell development within 7 days for cells incubated with NPs PMMA-SO_3H 3% at 20% [Eu$(tta)_3$phen] loading (Figure S10A). The results showed no influence of the NPs on cell development. Furthermore, the presence of NPs was observed in cells even after 7 days postincubation (Figure S10B), even though their luminescence decreases according to cell division.

■ CONCLUSIONS

ECP-NPs with diameters of 10, 20, and 30 nm and up to 40 wt % of Eu-complex loading were successfully assembled by nanoprecipitation. This corresponds to encapsulation of up to 5000 emitters per particle, thus reaching very high absorbance. The ECP-NPs showed high PL QYs in water (up to 0.26) and long PL decay times (up to 1.3 ms). High loading together with high QYs led to an exceptionally high brightness of more than 10^7 M^{-1} cm^{-1}. Together with their millisecond lifetimes, this allowed us to use ECP-NPs for TG imaging at the single-particle level at low laser powers and short acquisition times. ECP-NPs were spontaneously endocytosed and detected by autofluorescence-free TG imaging inside live HeLa cells in the presence of whole culture medium. Our Eu-complex-doped polymer NPs successfully demonstrated that lanthanide-based NPs can be applied for highly sensitive and autofluorescence-free imaging using a standard TG wide-field fluorescence microscope and low excitation powers. Upon suitable functionalization, they could thus be applied to label biomolecules and allow their imaging at the single-particle level with high spatial and temporal resolution, even in complex biological systems. The ECP-NPs presented here thus open a whole new field of high-precision tracking of single biomolecules at low excitation light conditions inside living cells.

■ METHODS

Materials. Milli-Q water (Millipore) and acetonitrile (≥99.9%, Sigma-Aldrich) were used for the preparation of NPs. CELLview Petri dishes (35 × 10 mm, Greiner Bio-One, 627860), Nunclon Delta Petri dishes (35 × 12 mm, Nunc, 150318), and LabTek II (8 well, Nunc, 155409) cell culture chambers were used for cell and single NP imaging. Polyethylenimine (PEI, 408727) and poly(vinyl alcohol) (PVA, Sigma-Aldrich, 341584) were used to immobilize single NPs on the glass surface. Human cervical carcinoma (HeLa) cells were purchased from American Type Culture Collection (CCL-2). Dulbecco's modified Eagle medium (DMEM, D6546), fetal bovine serum (FBS, F0804), antibiotics (Pen Strep, P4333), L-glutamine (G7513), and trypsin−ethylenediaminetetraacetic acid (EDTA) 0.05% (59417C) for cell culture were purchased from Sigma-Aldrich. Opti-MEM I reduced serum medium (1×, Gibco, 11058-021), Hank's balanced salt solution (HBSS, Sigma-Aldrich, H6648), and fibronectin (Sigma-Aldrich, F1141) were used for cell imaging. DID probe (1,1′-dioctadecyl-3,3,3′,3′-tetramethylindodicarbocyanine, 4-chlorobenzenesulfonate salt, D7757, Molecular Probes, Invitrogen) and LysoTracker green DND-26 (ThermoFisher Scientific, L7526) were used for colocalization imaging.

Polymer Synthesis. Poly(methyl methacrylate)s bearing carboxylate groups at 10 mol % (PMMA-COOH 10%) and sulfonate groups at 1 or 3 mol % (PMMA-SO_3H 1 and 3%) were synthetized through copolymerization of methyl methacrylate (Sigma-Aldrich, M55909) with methacrylic acid (Sigma-Aldrich, 155721) or 3-sulfopropyl methacrylate potassium salt (Sigma-Aldrich, 251658), respectively, via radical polymerization at 70 °C using azobisisobutyronitrile as an initiator, and reprecipitated twice in methanol. PMMA-COOH 10%: ^{1}H NMR (400 MHz, $CDCl_3$, δ): 3.60 (s, 3 H), 2.2−0.5 (m, 6 H). Molecular weight by size exclusion chromatography (SEC): M_w = 35 200, M_w/M_n = 1.29. PMMA-SO_3H: ^{1}H NMR (400 MHz, DMSO-d_6, δ): 3.97 (br. s, 0.02; 0.06 H), 3.57 (s, 3 H), 2.45 (m, partial covered by the solvent peak), 2.1−0.5 (m, 6 H). % Molecular weight by SEC: 1%: M_w = 51,200, M_w/M_n = 1.58; 3%: M_w = 106,600, M_w/M_n = 1.37.

Preparation of Nanoparticles. Stock solutions of PMMA-COOH 10% and PMMA-SO_3H 1 and 3% were prepared at a concentration of 10 g L^{-1} in acetonitrile. These solutions were diluted to 2 g L^{-1} for PMMA-COOH 10% and PMMA-SO_3H 1% and 1.2 g L^{-1} for PMMA-SO_3H 3% in acetonitrile containing different amounts of [Eu$(tta)_3$phen] (0−40 wt % relative to the polymer). Polymer solution (50 μL) was added in 450 μL of water with a micropipette under shaking at 21 °C. Then, the obtained suspension was quickly diluted 5-fold in water.

Characterization of Nanoparticles. *Transmission Electron Microscopy (TEM).* Nanoparticle solution (5 μL) at 40 μg mL^{-1} was deposited onto carbon-coated copper−rhodium electron microscopy grids following amylamine glow discharge. They were then treated for 1 min with a 2% uranyl acetate solution for staining. The obtained grids were observed using a Philips CM120 TEM equipped with a LaB6 filament and operating at 100 kV. The acquisition of areas of interest was performed with a Peltier-cooled charge-coupled device (CCD) camera (model 794, Gatan, Pleasanton, CA). Images were analyzed using Fiji software.

Spectroscopy. Absorption and emission spectra of NPs were recorded on a Cary 4000 Scan ultraviolet−visible spectrophotometer (Varian) and a FluoroMax-4 spectrofluorometer (Horiba Jobin Yvon) equipped with a thermostated cell compartment, respectively. The excitation wavelength was set to 345 nm, and emission was recorded from 550 to 720 nm. QYs of the NPs were calculated using [Eu$(tta)_3$phen] in acetonitrile as a reference (QY = 0.30, see below). For [Eu$(tta)_3$phen] in acetonitrile, UV−visible absorption spectra were recorded on a Specord 205 (Analytik Jena) spectrometer, whereas steady-state emission and excitation spectra were recorded on a FLP920 spectrometer from Edinburgh Instruments working with a continuous 450W Xe lamp and a red-sensitive Hamamatsu R928 photomultiplier in a Peltier housing. All spectra were corrected for the instrumental functions. A 455 nm highpass filter was used to remove second-order artifacts. Phosphorescence lifetimes were measured on the same instrument working in a multichannel scaling mode and using a Xenon flash lamp as the excitation source. Errors on the PL lifetimes were estimated to ±10%. PL quantum yields of [Eu-$(tta)_3$phen] in acetonitrile were determined independently using an absolute method (QY= 0.32) on a Horiba Jobin Yvon Fluorolog 3 spectrometer equipped with a G8 integration sphere (GMP SA, Switzerland) and by comparison with a reference sample, [TbL-(H_2O)] in water (QY = 0.31, λ_{exc} = 308 nm)[63], using optically diluted solutions (optical density <0.05) and yielding QY of 0.28. Estimated errors on the PL quantum yields were ±15%, and the reported value for [Eu$(tta)_3$phen] in acetonitrile (0.30) was taken as the average of both methods. The particle brightness is then obtained as follows: the number of emitters can be calculated based on the wt % of

DOI: 10.1021/acs.chemmater.9b00576
Chem. Mater. 2019, 31, 4034−4041

encapsulated complexes and the mean particle size as obtained from TEM. Multiplication with the per complex extinction coefficient (40 000 M^{-1} cm^{-1} at 350 nm) and the QY then yields the brightness

$$B = N\,\varepsilon\,QY$$

The fluorescence cross section, in cm^2, can be obtained by multiplying this value with 3.82×10^{-21}.

Immobilization of ECP-NPs. The surface of CELLview Petri dishes was treated overnight with 1 M NaOH. Then, the Petri dish surface was extensively rinsed with ultrapure water and incubated with PEI solution (2 mg mL^{-1} in 20 mM tris-buffer at pH 7.4, 150 mM NaCl) at 37 °C for 1.5 h followed by rinsing with ultrapure water. Solutions of ECP-NPs in water at 40 μg mL^{-1} were sonicated for 15 min and diluted in ultrapure water to 0.8 μg mL^{-1} (for PMMA-SO_3H 1%, 40% [Eu(tta)$_3$phen]) or 0.4 μg mL^{-1} (for PMMA-COOH 10%, 40% [Eu(tta)$_3$phen]). Petri dishes were incubated with NPs for 2 h, rinsed, and immersed in ultrapure water. PMMA-SO_3H 3% and 40% [Eu(tta)$_3$phen] NPs were also sonicated for 15 min and diluted to 2 μg mL^{-1} in PVA at 15% in water and heated to 70 °C.

Cell Culture. Cells were grown in DMEM supplemented with 10% FBS, 1% penicillin/streptomycin, and 2 mM L-glutamine at 37 °C and 5% CO_2. The cells were passaged with trypsin−EDTA 0.05%.

Cell Incubation with ECP-NPs. HeLa cells were seeded at 3×10^5 cells/dish in Nunclon Delta Petri dishes and incubated at 37 °C and 5% CO_2 overnight. The following day, ECP-NPs were sonicated for 15 min and then mixed rapidly with Opti-MEM at 4 μg mL^{-1}. Cells were washed with HBSS and incubated with ECP-NPs in Opti-MEM for 3 h at 37 °C, followed by rinsing with phosphate-buffered saline. Cells were detached using trypsin and centrifuged for 5 min at 37 °C and 1500 rpm. Cells were resuspended and seeded at 5×10^4 cells/well in LabTek chambers previously coated with fibronectin at 10 μg mL^{-1}. Cells were incubated for 1 h and then imaged at 37 °C.

Costaining with DiD and LysoTracker. DiD was used for plasma membrane labeling of HeLa cells following 20 h of incubation with ECP-NPs. First, cells were suspended using trypsin in 1 mL of complete culture medium. Then, DiD in dimethylformamide was added at the final concentration of 5 μM and gently mixed. Cells were incubated for 10 min at 37 °C and 5% CO_2. To remove nonincorporated DiD, cells were washed three times using centrifugation at 1500 rpm and 37 °C for 5 min. After each spin, cells were resuspended in a fresh complete culture medium. For labeling of endosomes/lysosomes, HeLa cells were first incubated with ECP-NPs for 24 h and then coincubated with green LysoTracker in complete DMEM at 50 nM for 30 min. In both cases, cells were imaged in Opti-MEM.

TG PL Microscopy. Single NP imaging and cell imaging were performed using a wide-field, inverted microscope (Olympus IX71) that uses a UV laser (349 nm, 300 Hz, Nd:YLF, Triton, Spectra Physics) for pulsed excitation and an intensified CCD camera (ICCD, PI-MAX3, Princeton Instruments) for TG detection. Laser irradiance on the sample was 0.24 W cm^{-2}, which corresponds to a UV light dose of 1 μJ cm^{-2}. The laser beam was redirected onto the sample with a 405 nm dichroic mirror (Di02-R405, Semrock Inc.). PL signals of ECP-NPs were collected with a high numerical aperture (NA = 1.35) immersion oil objective (UPLSAPO 60× O, Olympus) and detected using a 605 nm bandpass filter (FF01-605/15-25, Semrock Inc.). Acquisition settings in Winview software controlling the camera were fixed at a delay time of 10 μs, gatewidth of 0.6 ms, gates/exposure of 200 (for single NP imaging) or 100 (for cell imaging), and intensifier gain of 100 V. DIC images were acquired with no delay time, a gatewidth of 300 ms, gates/exposure of 1, accumulations of 10, and an intensifier gain at 6 V. The background acquired on a bare substrate with the same acquisition settings (gating sequence, laser frequency) was subtracted from the raw images. For single NP imaging, the mean intensities of circular regions of 6 pixels around the particles were measured for at least 200 particles and the background signal was subtracted. Zones with intensities above four times the mean per particle intensity were excluded from the analysis.

Details on steady-state and 3D imaging as well as on Photon counting can be found in the Supporting Information

■ ASSOCIATED CONTENT

Supporting Information

The Supporting Information is available free of charge on the ACS Publications website at DOI: 10.1021/acs.chemmater.9b00576.

Additional experimental details, as well as TEM images, absorption and emission spectra, and micrographs of single NPs and cells incubated with ECP-NPs (PDF)

Scan through a cell after incubation with PMMA-COOH 10% NPs loaded with 40 wt % of [Eu(tta)$_3$phen] (AVI)

■ AUTHOR INFORMATION

Corresponding Authors

*E-mail: niko.hildebrandt@u-psud.fr (N.H.).
*E-mail: reisch@unistra.fr (A.R.).

ORCID

Aline M. Nonat: 0000-0003-0478-5039
Loïc J. Charbonnière: 0000-0003-0328-9842
Andrey S. Klymchenko: 0000-0002-2423-830X
Niko Hildebrandt: 0000-0001-8767-9623
Andreas Reisch: 0000-0003-1154-7637

Author Contributions

[‖]M.C.D.S. and A.R. contributed equally to this work.

Author Contributions

The manuscript was written through contributions of all authors. All authors have given approval to the final version of the manuscript.

Notes

The authors declare no competing financial interest.

■ ACKNOWLEDGMENTS

The authors thank the French Agence National de la Recherche (ANR project "neutrinos", ANR JC/JC project "supertrack" 16-CE09-0007) and the European Commission (Horizon2020, FET-Open project "PROSEQO", ERC Consolidator Grant "BRIGHTSENS") for financial support and C. Ruhlmann and C. Crucifix from the FRISBI platform (ANR-10-INBS-05) for help with electron microscopy.

■ REFERENCES

(1) Wolfbeis, O. S. An Overview of Nanoparticles Commonly Used in Fluorescent Bioimaging. *Chem. Soc. Rev.* **2015**, *44*, 4743−4768.

(2) Howes, P. D.; Chandrawati, R.; Stevens, M. M. Colloidal Nanoparticles as Advanced Biological Sensors. *Science* **2014**, *346*, No. 1247390.

(3) Wegner, K. D.; Hildebrandt, N. Quantum Dots: Bright and Versatile in Vitro and in Vivo Fluorescence Imaging Biosensors. *Chem. Soc. Rev.* **2015**, *44*, 4792−4834.

(4) Zhou, J.; Yang, Y.; Zhang, C. Toward Biocompatible Semiconductor Quantum Dots: From Biosynthesis and Bioconjugation to Biomedical Application. *Chem. Rev.* **2015**, *115*, 11669−11717.

(5) Haase, M.; Schäfer, H. Upconverting Nanoparticles. *Angew. Chem., Int. Ed.* **2011**, *50*, 5808−5829.

(6) Gargas, D. J.; Chan, E. M.; Ostrowski, A. D.; Aloni, S.; Altoe, M. V. P.; Barnard, E. S.; Sanii, B.; Urban, J. J.; Milliron, D. J.; Cohen, B. E.; et al. Engineering Bright Sub-10-Nm Upconverting Nanocrystals for Single-Molecule Imaging. *Nat. Nanotechnol.* **2014**, *9*, 300−305.

(7) Ostrowski, A. D.; Chan, E. M.; Gargas, D. J.; Katz, E. M.; Han, G.; Schuck, P. J.; Milliron, D. J.; Cohen, B. E. Controlled Synthesis and Single-Particle Imaging of Bright, Sub-10 Nm Lanthanide-Doped Upconverting Nanocrystals. *ACS Nano* **2012**, *6*, 2686−2692.

DOI: 10.1021/acs.chemmater.9b00576
Chem. Mater. 2019, 31, 4034−4041

(8) Resch-Genger, U.; Gorris, H. H. Perspectives and Challenges of Photon-Upconversion Nanoparticles - Part I: Routes to Brighter Particles and Quantitative Spectroscopic Studies. *Anal. Bioanal. Chem.* **2017**, *409*, 5855−5874.
(9) Zheng, X. T.; Ananthanarayanan, A.; Luo, K. Q.; Chen, P. Glowing Graphene Quantum Dots and Carbon Dots: Properties, Syntheses, and Biological Applications. *Small* **2015**, *11*, 1620−1636.
(10) Kang, Z.; Liu, Y.; Gao, J.; Zhu, M. Carbon Dots for Environmental and Energy Applications: Advances, Challenges and Promises. *Inorg. Chem. Front.* **2017**, *4*, 1963−1986.
(11) Cardoso Dos Santos, M.; Goetz, J.; Bartenlian, H.; Wong, K.-L.; Charbonnière, L. J.; Hildebrandt, N. Autofluorescence-Free Live-Cell Imaging Using Terbium Nanoparticles. *Bioconjug. Chem.* **2018**, *29*, 1327−1334.
(12) Sy, M.; Nonat, A.; Hildebrandt, N.; Charbonnière, L. J. Lanthanide-Based Luminescence Biolabelling. *Chem. Commun.* **2016**, *52*, 5080−5095.
(13) Dong, H.; Du, S.-R.; Zheng, X.-Y.; Lyu, G.-M.; Sun, L.-D.; Li, L.-D.; Zhang, P.-Z.; Zhang, C.; Yan, C.-H. Lanthanide Nanoparticles: From Design toward Bioimaging and Therapy. *Chem. Rev.* **2015**, *115*, 10725−10815.
(14) Kaeser, A.; Schenning, A. P. H. J. Fluorescent Nanoparticles Based on Self-Assembled π-Conjugated Systems. *Adv. Mater.* **2010**, *22*, 2985−2997.
(15) Görl, D.; Zhang, X.; Würthner, F. Molecular Assemblies of Perylene Bisimide Dyes in Water. *Angew. Chem., Int. Ed.* **2012**, *51*, 6328−6348.
(16) Li, K.; Liu, B. Polymer-Encapsulated Organic Nanoparticles for Fluorescence and Photoacoustic Imaging. *Chem. Soc. Rev.* **2014**, *43*, 6570−6597.
(17) Peng, H.-S.; Chiu, D. T. Soft Fluorescent Nanomaterials for Biological and Biomedical Imaging. *Chem. Soc. Rev.* **2014**, *44*, 4699−4722.
(18) Reisch, A.; Klymchenko, A. S. Fluorescent Polymer Nanoparticles Based on Dyes: Seeking Brighter Tools for Bioimaging. *Small* **2016**, *12*, 1968−1992.
(19) Mochalin, V. N.; Shenderova, O.; Ho, D.; Gogotsi, Y. The Properties and Applications of Nanodiamonds. *Nat. Nanotechnol.* **2012**, *7*, 11−23.
(20) Haziza, S.; Mohan, N.; Loe-Mie, Y.; Lepagnol-Bestel, A. M.; Massou, S.; Adam, M. P.; Le, X. L.; Viard, J.; Plancon, C.; Daudin, R.; et al. Fluorescent Nanodiamond Tracking Reveals Intraneuronal Transport Abnormalities Induced by Brain-Disease-Related Genetic Risk Factors. *Nat. Nanotechnol.* **2017**, *12*, 322−328.
(21) Croce, A. C.; Bottiroli, G. Autofluorescence Spectroscopy and Imaging: A Tool for Biomedical Research and Diagnosis. *Eur. J. Histochem.* **2014**, *58*, No. 2461.
(22) Kusumi, A.; Tsunoyama, T. A.; Hirosawa, K. M.; Kasai, R. S.; Fujiwara, T. K. Tracking Single Molecules at Work in Living Cells. *Nat. Chem. Biol.* **2014**, *10*, 524−532.
(23) Shen, H.; Tauzin, L. J.; Baiyasi, R.; Wang, W.; Moringo, N.; Shuang, B.; Landes, C. F. Single Particle Tracking: From Theory to Biophysical Applications. *Chem. Rev.* **2017**, *117*, 7331−7376.
(24) Tang, S.; Moayeri, M.; Chen, Z.; Harma, H.; Zhao, J.; Hu, H.; Purcell, R. H.; Leppla, S. H.; Hewlett, I. K. Detection of Anthrax Toxin by an Ultrasensitive Immunoassay Using Europium Nanoparticles. *Clin. Vaccine Immunol.* **2009**, *16*, 408−413.
(25) Tan, W.; Wang, K.; He, X.; Zhao, X. J.; Drake, T.; Wang, L.; Bagwe, R. P. Bionanotechnology Based on Silica Nanoparticles. *Med. Res. Rev.* **2004**, *24*, 621−638.
(26) Härmä, H.; Soukka, T.; Lövgren, T. Europium Nanoparticles and Time-Resolved Fluorescence for Ultrasensitive Detection of Prostate-Specific Antigen. *Clin. Chem.* **2001**, *47*, 561−568.
(27) Davies, A.; Lewis, D. J.; Watson, S. P.; Thomas, S. G.; Pikramenou, Z. PH-Controlled Delivery of Luminescent Europium Coated Nanoparticles into Platelets. *Proc. Natl. Acad. Sci. U.S.A.* **2012**, *109*, 1862−1867.
(28) Wong, K. L.; Law, G. L.; Murphy, M. B.; Tanner, P. A.; Wong, W. T.; Lam, P. K. S.; Lam, M. H. W. Functionalized Europium Nanorods for in Vitro Imaging. *Inorg. Chem.* **2008**, *47*, 5190−5196.
(29) Di, W.; Li, J.; Shirahata, N.; Sakka, Y.; Willinger, M.; Pinna, N. Photoluminescence, Cytotoxicity and in Vitro Imaging of Hexagonal Terbium Phosphate Nanoparticles Doped with Europium. *Nanoscale* **2011**, *3*, 1263−1269.
(30) Manning, H. C.; Goebel, T.; Thompson, R. C.; Price, R. R.; Lee, H.; Bornhop, D. J. Targeted Molecular Imaging Agents for Cellular-Scale Bimodal Imaging. *Bioconjug. Chem.* **2004**, *15*, 1488−1495.
(31) Väisänen, V.; Härmä, H.; Lilja, H.; Bjartell, A. Time-Resolved Fluorescence Imaging for Quantitative Histochemistry Using Lanthanide Chelates in Nanoparticles and Conjugated to Monoclonal Antibodies. *Luminescence* **2000**, *15*, 389−397.
(32) Kattel, K.; Park, J. Y.; Xu, W.; Kim, H. G.; Lee, E. J.; Bony, B. A.; Heo, W. C.; Chang, Y.; Kim, T. J.; Do, J. Y.; et al. Water-Soluble Ultrasmall Eu2O3 Nanoparticles as a Fluorescent Imaging Agent: In Vitro and in Vivo Studies. *Colloids Surf., A* **2012**, *394*, 85−91.
(33) Beaurepaire, E.; Buissette, V.; Sauviat, M. P.; Giaume, D.; Lahlil, K.; Mercuri, A.; Casanova, D.; Huignard, A.; Martin, J. L.; Gacoin, T.; et al. Functionalized Fluorescent Oxide Nanoparticles: Artificial Toxins for Sodium Channel Targeting and Imaging at the Single-Molecule Level. *Nano Lett.* **2004**, *4*, 2079−2083.
(34) Wu, S.; Han, G.; Milliron, D. J.; Aloni, S.; Altoe, V.; Talapin, D. V.; Cohen, B. E. Non-Blinking and Photostable Upconverted Luminescence from Single Lanthanide- Doped Nanocrystals. *Proc. Natl. Acad. Sci. U.S.A.* **2009**, *106*, 1−5.
(35) Zhang, J.; Ray, K.; Fu, Y.; Lakowicz, J. R. First Observation to Enhanced Luminescence from Single Lanthanide Chelate on Silver Nanorod. *Chem. Commun.* **2014**, *50*, 9383−9386.
(36) Laissue, P. P.; Alghamdi, R. A.; Tomancak, P.; Reynaud, E. G.; Shroff, H. Assessing Phototoxicity in Live Fluorescence Imaging. *Nat. Methods* **2017**, *14*, 657−661.
(37) Trofymchuk, K.; Reisch, A.; Didier, P.; Fras, F.; Gilliot, P.; Mely, Y.; Klymchenko, A. S. Giant Light-Harvesting Nanoantenna for Single-Molecule Detection in Ambient Light. *Nat. Photonics* **2017**, *11*, No. 657.
(38) Robin, M. P.; O'Reilly, R. K. Strategies for Preparing Fluorescently Labelled Polymer Nanoparticles. *Polym. Int.* **2015**, *64*, 174−182.
(39) Robin, M. P.; Raymond, J. E.; O'Reilly, R. K. One-Pot Synthesis of Super-Bright Fluorescent Nanogel Contrast Agents Containing a Dithiomaleimide Fluorophore. *Mater. Horiz.* **2014**, *2*, 54−59.
(40) Reisch, A.; Didier, P.; Richert, L.; Oncul, S.; Arntz, Y.; Mély, Y.; Klymchenko, A. S. Collective Fluorescence Switching of Counterion-Assembled Dyes in Polymer Nanoparticles. *Nat. Commun.* **2014**, *5*, No. 4089.
(41) Reisch, A.; Trofymchuk, K.; Runser, A.; Fleith, G.; Rawiso, M.; Klymchenko, A. S. Tailoring Fluorescence Brightness and Switching of Nanoparticles through Dye Organization in the Polymer Matrix. *ACS Appl. Mater. Interfaces* **2017**, *9*, 43030−43042.
(42) Qin, W.; Li, K.; Feng, G.; Li, M.; Yang, Z.; Liu, B.; Tang, B. Z. Bright and Photostable Organic Fluorescent Dots with Aggregation-Induced Emission Characteristics for Noninvasive Long-Term Cell Imaging. *Adv. Funct. Mater.* **2014**, *24*, 635−643.
(43) Binnemans, K. Lanthanide-Based Luminescent Hybrid Materials. *Chem. Rev.* **2009**, *109*, 4283−4374.
(44) Feng, J.; Zhang, H. Hybrid Materials Based on Lanthanide Organic Complexes: A Review. *Chem. Soc. Rev.* **2012**, *42*, 387−410.
(45) Desbiens, J.; Bergeron, B.; Patry, M.; Ritcey, A. M. Polystyrene Nanoparticles Doped with a Luminescent Europium Complex. *J. Colloid Interface Sci.* **2012**, *376*, 12−19.
(46) Bai, G.; Tsang, M.-K.; Hao, J. Luminescent Ions in Advanced Composite Materials for Multifunctional Applications. *Adv. Funct. Mater.* **2016**, *26*, 6330−635.
(47) Sun, W.; Yu, J.; Deng, R.; Rong, Y.; Fujimoto, B.; Wu, C.; Zhang, H.; Chiu, D. T. Semiconducting Polymer Dots Doped with Europium Complexes Showing Ultranarrow Emission and Long

DOI: 10.1021/acs.chemmater.9b00576
Chem. Mater. 2019, 31, 4034−4041

Luminescence Lifetime for Time-Gated Cellular Imaging. *Angew. Chem., Int. Ed.* **2013**, *52*, 11294−11297.
(48) Li, Q.; Zhang, J.; Sun, W.; Yu, J.; Wu, C.; Qin, W.; Chiu, D. T. Europium-Complex-Grafted Polymer Dots for Amplified Quenching and Cellular Imaging Applications. *Langmuir* **2014**, *30*, 8607−8614.
(49) Peng, H.; Stich, M. I. J.; Yu, J.; Sun, L.; Fischer, L. H.; Wolfbeis, O. S. Luminescent Europium(III) Nanoparticles for Sensing and Imaging of Temperature in the Physiological Range. *Adv. Mater.* **2010**, *22*, 716−719.
(50) Huhtinen, P.; Kivelä, M.; Kuronen, O.; Hagren, V.; Takalo, H.; Tenhu, H.; Lövgren, T.; Härmä, H. Synthesis, Characterization, and Application of Eu(III), Tb(III), Sm(III), and Dy(III) Lanthanide Chelate Nanoparticle Labels. *Anal. Chem.* **2005**, *77*, 2643−2648.
(51) Wartenberg, N.; Raccurt, O.; Imbert, D.; Mazzanti, M.; Bourgeat-Lami, E. Luminescent Latex Particles Loaded with Anionic Lanthanide Complexes: A Versatile Platform for Multicolour Optical Coding. *J. Mater. Chem. C* **2013**, *1*, 2061−2068.
(52) Pihlasalo, S.; Mariani, L.; Härmä, H. Quantitative and Discriminative Analysis of Nucleic Acid Samples Using Luminometric Nonspecific Nanoparticle Methods. *Nanoscale* **2016**, *8*, 5902−5911.
(53) Takei, Y.; Arai, S.; Murata, A.; Takabayashi, M.; Oyama, K.; Ishiwata, S.; Takeoka, S.; Suzuki, M. A Nanoparticle-Based Ratiometric and Self-Calibrated Fluorescent Thermometer for Single Living Cells. *ACS Nano* **2014**, *8*, 198−206.
(54) Hildebrandt, N.; Wegner, K. D.; Algar, W. R. Luminescent Terbium Complexes: Superior Förster Resonance Energy Transfer Donors for Flexible and Sensitive Multiplexed Biosensing. *Coord. Chem. Rev.* **2014**, *273*−*274*, 125−138.
(55) Reisch, A.; Runser, A.; Arntz, Y.; Mély, Y.; Klymchenko, A. S. Charge-Controlled Nanoprecipitation as a Modular Approach to Ultrasmall Polymer Nanocarriers: Making Bright and Stable Nanoparticles. *ACS Nano* **2015**, *9*, 5104−5116.
(56) Reisch, A.; Heimburger, D.; Ernst, P.; Runser, A.; Didier, P.; Dujardin, D.; Klymchenko, A. S. Protein-Sized Dye-Loaded Polymer Nanoparticles for Free Particle Diffusion in Cytosol. *Adv. Funct. Mater.* **2018**, *28*, No. 1805157.
(57) Stanimirov, S. S.; Hadjichristov, G. B.; Petkov, I. K. Emission Efficiency of Diamine Derivatives of Tris[4,4,4-Trifluoro-1-(2-Thienyl)-1,3-Butanediono]Europium. *Spectrochim. Acta, Part A* **2007**, *67*, 1326−1332.
(58) Etoc, F.; Balloul, E.; Vicario, C.; Normanno, D.; Liße, D.; Sittner, A.; Piehler, J.; Dahan, M.; Coppey, M. Non-Specific Interactions Govern Cytosolic Diffusion of Nanosized Objects in Mammalian Cells. *Nat. Mater.* **2018**, *17*, 740−746.
(59) Eliseeva, S. V.; Bünzli, J.-C. G. Lanthanide Luminescence for Functional Materials and Bio-Sciences. *Chem. Soc. Rev.* **2009**, *39*, 189−227.
(60) Fix, T.; Nonat, A.; Imbert, D.; Di Pietro, S.; Mazzanti, M.; Slaoui, A.; Charbonnière, L. J. Enhancement of Silicon Solar Cells by Downshifting with Eu and Tb Coordination Complexes. *Prog. Photovoltaics* **2016**, *24*, 1251−1260.
(61) Cardoso Dos Santos, M.; Hildebrandt, N. Recent Developments in Lanthanide-to-Quantum Dot FRET Using Time-Gated Fluorescence Detection and Photon Upconversion. *TrAC, Trends Anal. Chem.* **2016**, *84*, 60−71.
(62) Zhang, K. Y.; Yu, Q.; Wei, H.; Liu, S.; Zhao, Q.; Huang, W. Long-Lived Emissive Probes for Time-Resolved Photoluminescence Bioimaging and Biosensing. *Chem. Rev.* **2018**, *118*, 1770−1839.
(63) Weibel, N.; Charbonnière, L. J.; Guardigli, M.; Roda, A.; Ziessel, R. Engineering of Highly Luminescent Lanthanide Tags Suitable for Protein Labeling and Time-Resolved Luminescence Imaging. *J. Am. Chem. Soc.* **2004**, *126*, 4888−4896.

DOI: 10.1021/acs.chemmater.9b00576
Chem. Mater. 2019, 31, 4034−4041

Supporting Information

Lanthanide-Complex-Loaded Polymer Nanoparticles for Background-Free Single-Particle and Live-Cell Imaging

Marcelina Cardoso Dos Santos, Anne Runser, Hortense Bartenlian, Aline M. Nonat, Loïc J. Charbonnière, Andrey S. Klymchenko, Niko Hildebrandt* and Andreas Reisch *

Experimental Details

Microscopy

Steady-state imaging.

For ECP-NP detection, cells were imaged with an Olympus IX71 microscope and illuminated with an X-Cite 120Q mercury source (EXFO Photonic Solutions Inc.) at ~15 W through a 365 nm excitation band-pass filter (Hg01-365-25, Semrock Inc.) and 495 nm dichroic mirror (FF495-Di03, Semrock Inc.). The fluorescent signal was detected using a 60x objective (UPLSAPO, Olympus) and a 605 nm emission filter (FF01-605/15-25, Semrock Inc.). PL signal was recorded using a CMOS camera (pco.edge, PCO) with an acquisition time of 333 ms.

3D imaging.

Fluorescent images of HeLa cells were acquired on a wide-field inverted microscope Olympus IX83 using an X-Cite Exacte illumination source (Excelitas Technologies) and iXon Ultra 888 EMCCD camera (Andor). ECP-NPs were excited with a 100 W source power using 320 nm excitation filter (FF01−320/40−25, Semrock Inc.) and 355 dichroic mirror (Di01-R355, Semrock Inc.) and their emission collected using 605 nm filter (FF01−605/15−25, Semrock Inc.). DiD was excited with 10 W illumination power using 623 nm band-pass filter (FF01−623/24−25, Semrock Inc.), 649 nm dichroic mirror (FF649-Di01, Semrock Inc.) and the emission was collected through a 676 nm bandpass-filter (FF01−676/29−25, Semrock Inc.). Sample was imaged using UPLSAPO 60x objective (Olympus). Z-stack images were obtained by a displacement of a step of 0.25 µm. Images of ECP-NPs were acquired with x750 EM gain, 30 MHz readout speed, 1.1 µs vertical shift speed, and x2 preamplifier sensitivity. Images of plasma membrane stained with DiD were acquired with the same parameters except EM gain at x2. iXon camera and Olympus microscope were controlled by the Micromanager software.

Photon counting

Photon counting imaging was performed for PMMA-COOH 10% particles loaded with 40wt% [Eu(tta)$_3$phen] as a reference on a wide-field inverted microscope Olympus IX83 using X-Cite Exacte illumination source at 2 W (Excelitas Technologies) and iXon Ultra 888 EMCCD camera (Andor), 365 nm excitation filter (Hg01-365-25, Semrock Inc.) and 405 dichroic mirror (Di02-R405, Semrock Inc.). The excitation power density was measured to be 0.02 W/cm² at the sample plane and the illumination area was 0.005 cm².

The number of photons collected by the camera per pixel can be calculated from the equation:

$$Nb\ of\ collected\ photons = \frac{(signal - background) \times camera\ sensitivity}{analog\ gain \times EM\ gain \times QE} \quad (1)$$

Where the camera sensitivity (electrons to counts conversion) was 5.17, analog gain 2, EM gain 1000 and quantum efficiency (QE) 95 % at 605 nm. To obtain the total number of collected photons per particle, the measured numbers of photons per pixel were integrated over an area of typically 21 pixels (circular region of diameter 5 pixels, containing > 95 % of the detected photons) The number of emitted photons per particle can then be determined using:

$$Nb\ of\ emitted\ photons = \frac{\int Nb\ of\ collected\ photons}{\%photons\ into\ objective \times T\ obj \times T\ filter} \quad (2)$$

Objective transmittance (*T obj*) of UPLSAPO 60x in ECP-NPs emission wavelength range and FF01-605/15-25 emission filter transmittance (*T filter*) were 90% and 33%, respectively. The collection half-angle of the objective was 64.4°, corresponding to a solid angle of 3.6 sr. 28 % of the emitted photons are thus collected by the objective. The number of photons emitted per particle per second can be obtained using the following equation:

$$Nb\ of\ emitted\ photons/s = \frac{Nb\ of\ emitted\ photons}{t_{exposure}} \quad (3)$$

Exposure time ($t_{exposure}$) was fixed at 50 ms.

Dividing the number of emitted photons by the number of incoming photons per second (3.6 x 10^{16} cm^{-2}) yields the fluorescence cross section σ.

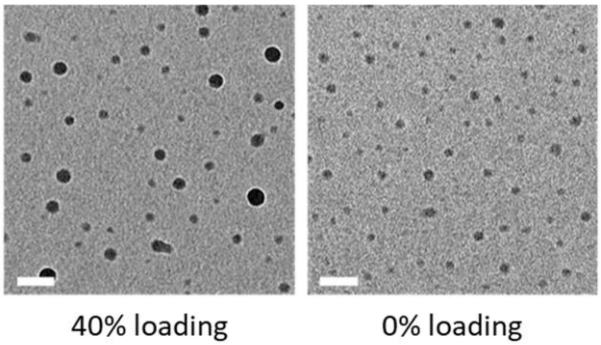

Figure S1. Comparison of TEM images of PMMA-COOH 10% ECP-NPs with (left) or without (right) [Eu(tta)$_3$phen] loading. Here no staining with uranyl acetate was applied. The scale bars correspond to 100 nm.

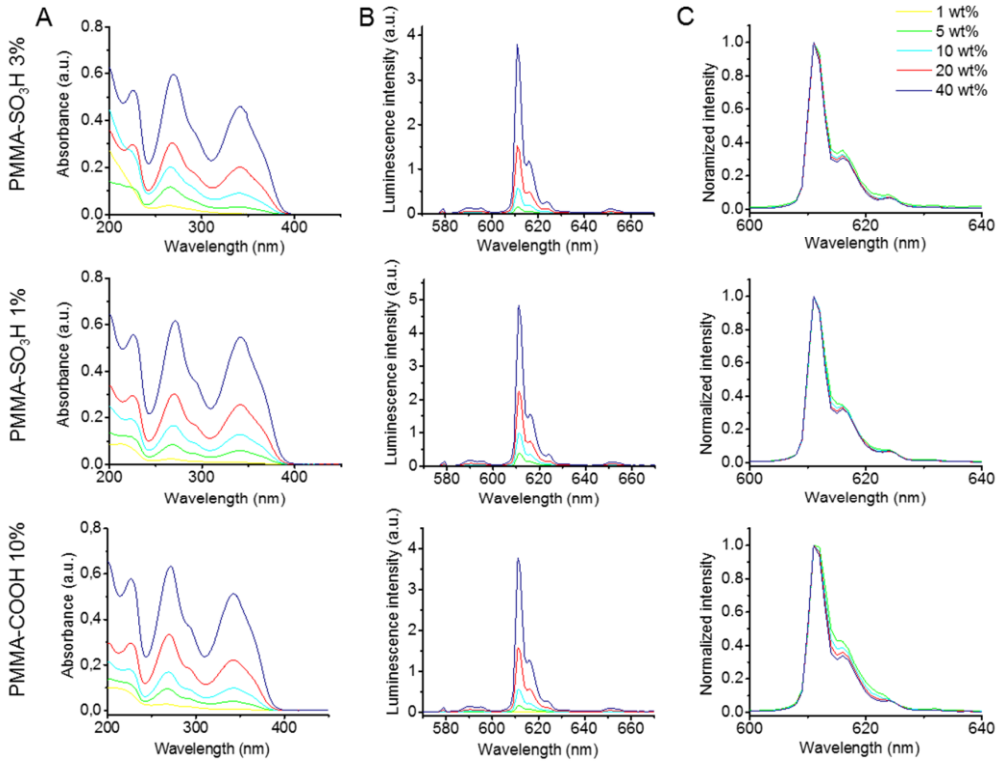

Figure S2. Absorbance (A), emission (B), and normalized emission (C) spectra of PMMA-SO_3H 1% and 3 % and PMMA-COOH 10% NPs loaded with 1, 5, 10, 20, and 40 wt% $[Eu(tta)_3phen]$ (λ_{exc} = 350 nm).

Table S1. PL quantum yields (ϕ) of solutions of [Eu(tta)$_3$phen] in acetonitrile and of ECP-NPs in water (r.t., λ_{exc} = 350 nm). The Eu^{III}-centered QY (ϕ_{Eu}^{Eu} =0.50) was calculated according to Equation 1,[1] from which a sensitization efficiency η_{sens} = 0.56 was calculated using Equation 5.

Sample	ϕ_{Eu}^{L} (%)	ϕ_{Eu}^{Eu} (%)[a)]
[Eu(tta)$_3$phen]	0.30	0.50
PMMA-COOH 10% - 40% [Eu(tta)$_3$phen]	0.26	0.52
PMMA-COOH 10% - 20% [Eu(tta)$_3$phen]	0.21	0.54
PMMA-COOH 10% - 10% [Eu(tta)$_3$phen]	0.16	0.59

[a)] according to Equation 4. Estimated errors: ± 15% .

$$\phi_{Eu}^{Eu} = \tau_{H2O}/\tau_R \text{ , with } \tau_R = \left(1/A_{MD,0}n^3\right)(I_{MD}/I_{tot}) \quad (4)$$

where $A_{MD,0} = 14.65\ s^{-1}$ arises for the spontaneous emission probability for the $^5D_0 \rightarrow {}^7F_1$ transition in vacuum, n is the refractive index of the solution (n = 1.341 at 25°C for acetonitrile), I_{MD} and I_{tot} are the area of emission of the $^5D_0 \rightarrow {}^7F_1$ transition and of all the transitions respectively.

$$\phi_{Eu}^{L} = \eta_{sens} \times \phi_{Eu}^{Eu} \quad (5)$$

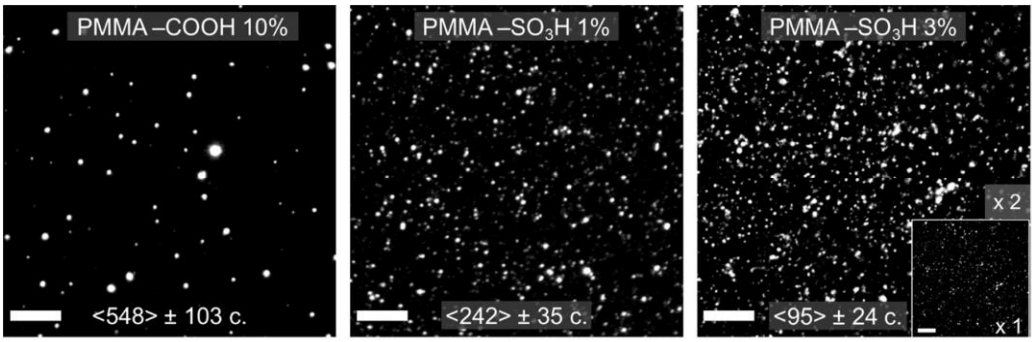

Figure S3. TG single-particle images of PMMA-COOH 10 %, PMMA-SO_3H 1%, and PMMA-SO_3H 3% at 40% [Eu(tta)$_3$phen] loading. Values at the bottom of the images are average PL intensities (in photon counts: c. ±SD). For better visibility the intensity was increased twofold for PMMA- SO_3H 3% (original in inset). Scale bars: 10 µm.

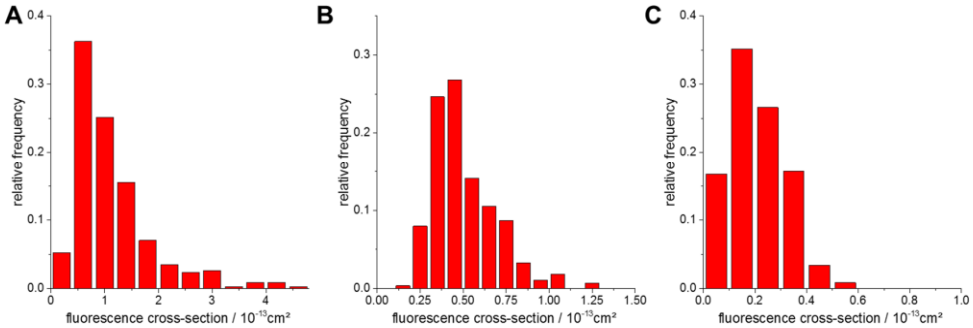

Figure S4. Histograms of single particle brightnesses of (A) PMMA-COOH 10 % NPs, (B) PMMA-SO_3H 1%, (C) PMMA-SO_3H 3%, all loaded with 40% [Eu(tta)$_3$phen]. At least 250 particles have been analyzed per condition.

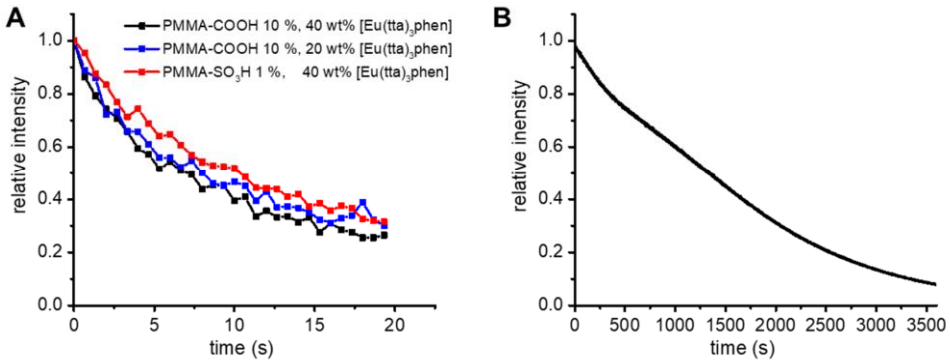

Figure S5. (A) Single particle photostability of Eu(tta)$_3$phen loaded NPs in TG imaging in water. Pulsed excitation with a Nd:YLF laser at 349 nm and 300 Hz was used. Acquisition was performed using a delay time of 10 µs, a gate width of 0.6 ms, and 200 gates/exposure. NPs: PMMA-COOH 10% NPs loaded with 20 or 40 wt % [Eu(tta)$_3$phen] and PMMA-SO$_3$H 1% NPs loaded with 40 wt % Eu(tta)$_3$phen. (B) Ensemble photostability of Eu(tta)$_3$phen in acetonitrile solution as measured in a fluorometer (l_{ex} = 345 nm, l_{em} = 612 nm).

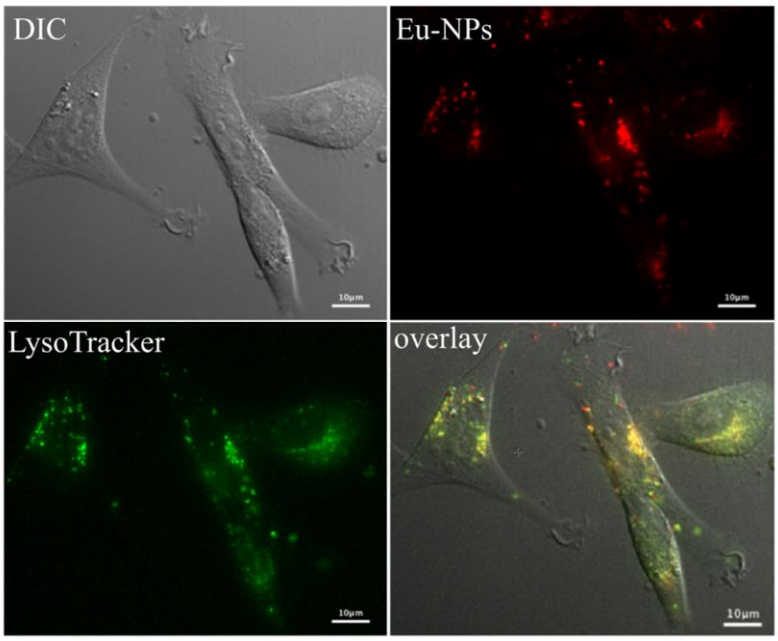

Figure S6. Live-cell images of HeLa cells costained with ECP-NPs (PMMA-COOH 10%, 40% [Eu(tta)$_3$phen]) and green LysoTracker. PL of ECP-NPs (red) and fluorescence of LysoTracker (green) were measured with steady-state detection. Cells were left with ECP-NPs for 24 h at 37°C. Before imaging, cells were incubated with green Lysotracker in complete DMEM at the final concentration of 50 nM for 30 minutes at 37°C. Images were acquired using a wide-field inverted Olympus IX71 with CMOS camera (500 ms) and illumination with a mercury source (15W).

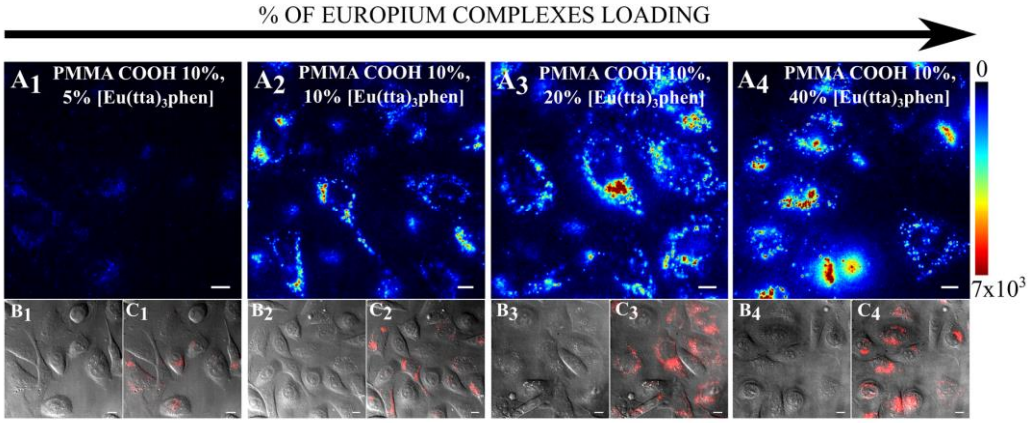

Figure S7. Live-cell images of HeLa cells incubated with ECP-NPs. (A) Time-gated PL signal from PMMA-COOH 10% NPs at 5, 10, 20 and 40% [Eu(tta)$_3$phen] complex loading. (B) Differential interference contrast (DIC) images. (C) Overlay: DIC overlaid with PL (ECP-NPs in red). The TG images were acquired on a wide-field inverted Olympus IX71 microscope with iCCD camera (100 gates/exposure, 0.01 ms delay time 0.6 ms gate time and 100V gain) and pulsed laser excitation at 349 nm and 300 Hz. Scale bars: 10 µm.

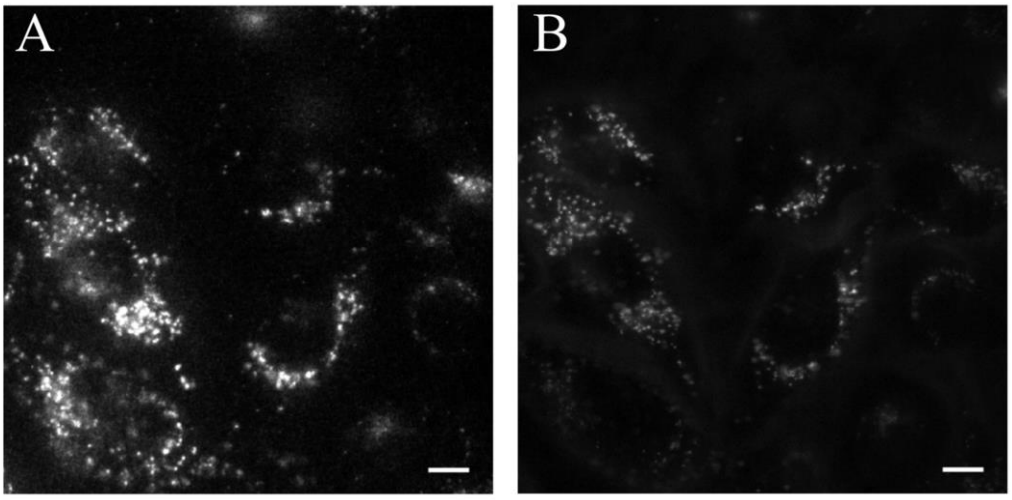

Figure S8. Live-cell images of HeLa cells incubated for 3h with PMMA-COOH 10%, 20% [Eu(tta)$_3$phen] NPs (A) TG PL intensity recorded on a wide-field inverted Olympus IX71 microscope with iCCD camera (100 gates/exposure, 0.01 ms delay time 0.6 ms gate time and 100 V gain) and pulsed laser excitation at 349 nm and 300 Hz. (B) Steady-state image acquired on the same microscope with CMOS camera (333 ms) and illuminated with mercury source (10 W). Intensity scale was adjusted from 0 to 5000 counts. Scale bars: 10 µm.

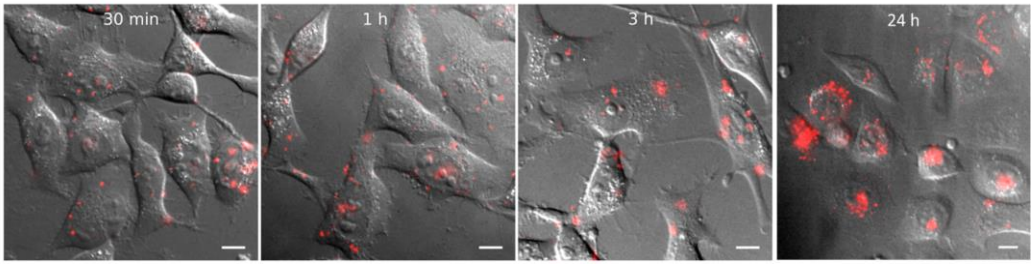

Figure S9. Time-lapse of Eu-NPs PMMA-SO$_3$H 1% at 40% [Eu(tta)$_3$phen] localization in live HeLa cells incubated with Eu-NPs The image after 24h shows the cells after trypsination and transfer to a new well. Merge of DIC image with TG-PL (Eu-NPs are in red). Images were acquired on a wide-field inverted Olympus IX71 microscope with iCCD camera (100 gates/exposure, 0.01 ms delay time 0.6 ms gate time and 100V gain) and pulsed laser excitation at 349 nm and 300 Hz. The NPs intensity range was adapted to each case in order to appreciate the localization and not the intensity of PL signal. Scale bars: 10 µm.

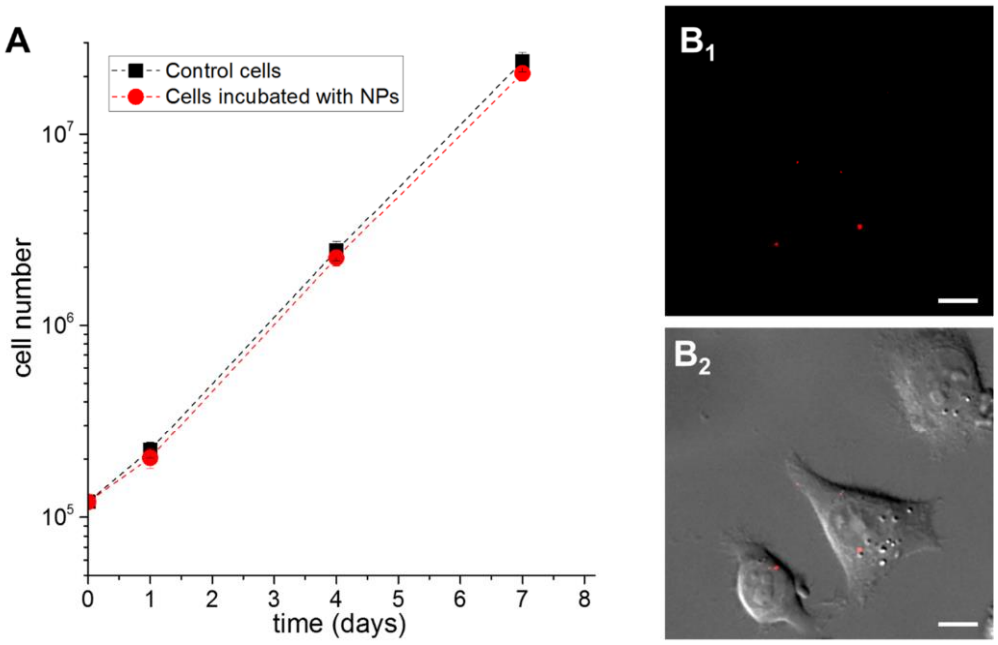

Figure S10. Cell growth of HeLa cells investigated on control cells (black squares) and cells incubated with NPs PMMA-SO_3H 3% (red circles) at 20% [Eu(tta)$_3$phen] loading (A). Error bars correspond to SD. No significant difference between these two conditions were observed (test T concluded no difference between mean cell number values within 95% confidence level at 1 and 4 days and 99% at 7days). (B) Live-cell images of HeLa cells incubated with NPs. TG PL images with NPs after 7 days (B_1) and overlay with DIC images (B_2). Scale bars correspond to 10 µm.

References

(1) Werts, M. H. V.; Jukes, R. T. F.; Verhoeven, J. W. The Emission Spectrum and the Radiative Lifetime of Eu3+ in Luminescent Lanthanide Complexes. *Phys. Chem. Chem. Phys.* **2002**, *4* (9), 1542–1548. https://doi.org/10.1039/B107770H.

4.2 Fluorescence et clignotement des nanoparticules à base de rhodamine

Nous avons vu dans la partie précédente (partie 4.1) qu'il était possible d'améliorer le rapport signal/bruit en supprimant l'autofluorescence des composants cellulaires. Ici, nous nous intéressons à l'optimisation de signal émis par les particules. Plus la sonde est brillante, plus le nombre de photons récoltés sera élevé et il sera facile de la localiser dans le temps et l'espace. Si la brillance de la sonde est suffisamment élevée, l'imagerie de molécules individuelles peut être alors réalisée sur un simple microscope à épifluorescence. Le principe des NPs fluorescentes est d'encapsuler une grande quantité de fluorophores dans la particule pour pallier le manque de brillance des fluorophores seuls. En effet la brillance résultante de la NP sera alors égale à la somme des coefficients d'extinction molaires des fluorophores contenus dans la particule multipliée par le rendement quantique de la particule :

$$B = N \times \varepsilon_{fluo} \times \Phi_{NP}$$

Néanmoins l'augmentation de la brillance pour les NPs de polymères contenant une grande quantité de fluorophores est fortement limitée par la diminution du rendement quantique due à la formation d'agrégats non fluorescents à forte concentration en fluorophores (phénomène d'ACQ).[115,119,120] Récemment, notre groupe a développé une approche basée sur l'insertion d'un contre-ion hydrophobe et très volumineux (un tétraphényl borate perfluoré, F5-TPB), qui sert d'espaceur entre les fluorophores, des dérivés hydrophobes de la rhodamine B (R18) et limite le phénomène d'ACQ (Figure 31).[8] Les NPs de PLGA contenant ces fluorophores atteignent alors des brillances de un à deux ordres de grandeurs supérieures aux QDs.

D'un autre côté, le comportement collectif photocommutable de centaines de fluorophores encapsulés est lié à un transfert d'énergie ultra-rapide entre fluorophores conduisant au clignotement de la particule entière.[8] Il a été démontré que l'organisation spatiale des fluorophores dans les particules de polymères joue un rôle très important concernant la propriété des particules à clignoter. Des résultats préliminaires ont montré que le phénomène de clignotement est lié à une organisation spatiale différente des fluorophores dans la matrice polymérique dépendant de la nature du polymère.[173] En nous basant sur ces premiers résultats, nous avons

postulé que le contrôle du clignotement ainsi qu'une optimisation de la fluorescence des particules étaient possibles par ajustement de leur organisation au sein de la matrice polymérique en jouant notamment sur l'hydrophobie du polymère et celle du fluorophore.

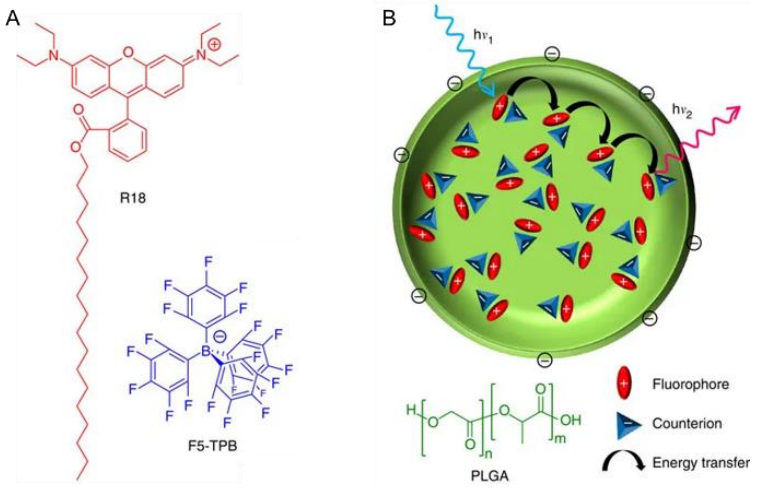

Figure 31. (A) Stuctures chimiques du fluorophore R18 (en rouge) et son contre-ion F5-TPB (en bleu). (B) Schéma d'une nanoparticule de PLGA encapsulant R18/F5-TPB. Reproduit à partir de la référence [8].

Ces travaux ont été scindés en deux parties distinctes : avec une optimisation de la fluorescence d'une part et un contrôle du clignotement d'autre part. Dans un premier temps, nous avons étudié une gamme de NPs chargées avec R18/F5-TPB à base de copolymères d'hydrophobies différentes. L'effet de la chimie du polymère sur l'absorbance et le rendement quantique des NPs a été évalué afin de mieux comprendre et d'optimiser notre système existant au niveau de la fluorescence. Ensuite nous avons essayé de déterminer les paramètres influençant le clignotement des NPs tels que la taille des particules, leur chargement, l'hydrophobie des fluorophores et du polymère.

Optimisation de la fluorescence

Pour étudier l'effet de l'hydrophobie des polymères sur la brillance des particules, nous avons utilisé les copolymères synthétisés par polymérisation radicalaire à partir de différents types de monomères : hydrophiles, hydrophobes et chargés (Partie 3.1, figure 23). Ils contiennent généralement un monomère de chaque type à différents pourcentages. La fraction de l'acide méthacrylique (MAA) est fixée à 1 % (mol). Les

fractions de groupements hydrophiles varient de 0 à 75 %. Pour rendre les NPs fluorescentes, le fluorophore R18/F5-TPB a été encapsulé avec un chargement de 10% en masse relative au polymère. Précédemment l'efficacité d'encapsulation a été évaluée ≥ 95 % pour des NPs de PLGA chargées avec R18/F5-TPB.[135,199]

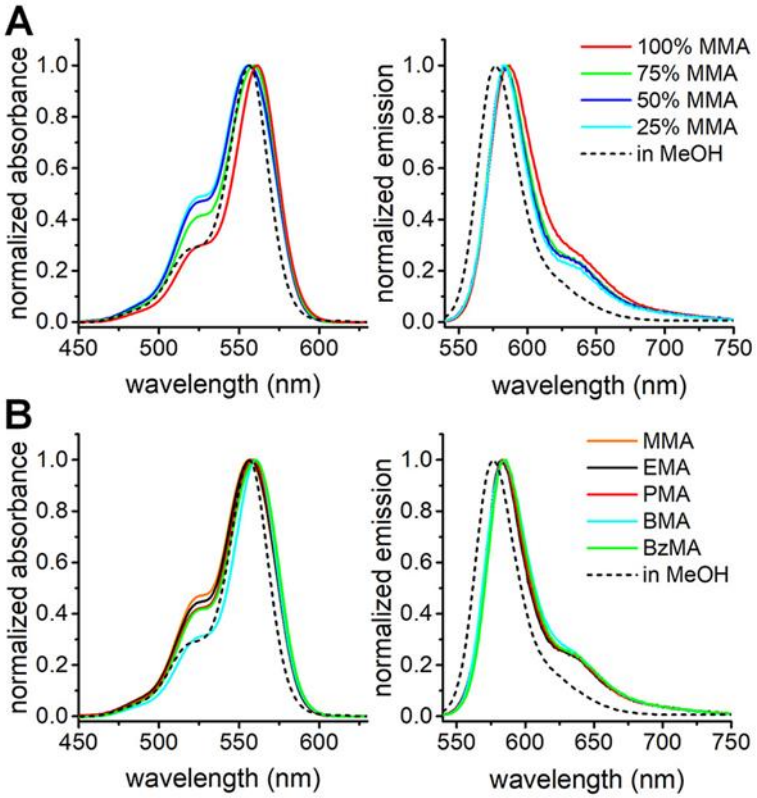

Figure 32. Spectres normalisés d'absorption (gauche) et d'émission (droite) de NPs préparées à partir (A) des copolymères HEMA/MMA à différents ratios (et 1 % MAA) et (B) des copolymères avec 50 % HEMA et différents monomères hydrophobes (et 1 % MAA). Les NPs ont été chargées avec 10 % R18/F5-TPB. L'excitation a été fixée à 530 nm.

Les spectres d'absorption et d'émission sont représentés figure 32. Lorsque l'on augmente la fraction des monomères hydrophiles, on observe une augmentation de l'intensité relative d'absorption au niveau de l'épaulement à 530 nm relatif au pic du maximum d'absorption. Cela indique la formation d'agrégats de R18.[119] Cette augmentation au niveau de l'épaulement, s'accompagne également d'un faible déplacement vers le bleu pour le maximum d'absorption. Le ratio entre l'intensité de l'épaulement à 530 nm et le maximum d'absorption est le même pour les NPs de copolymères composés uniquement de monomères hydrophobes avec 1 % MAA que pour le fluorophore dans le méthanol. La figure 32B montre également que le type de

monomère hydropophobe des copolymères influence la variation d'intensité au niveau de l'épaulement. Concernant l'émission des NPs, les spectres (figure 32A) montrent un léger déplacement du maximum d'émission vers le rouge pour les NPs par rapport au fluorophore dans le solvant organique, accompagné de l'apparition d'un épaulement à 630 nm. Lorsqu'on diminue la fraction des monomères hydrophobes, le spectre d'émission devient légèrement plus fin et est déplacé vers le bleu.

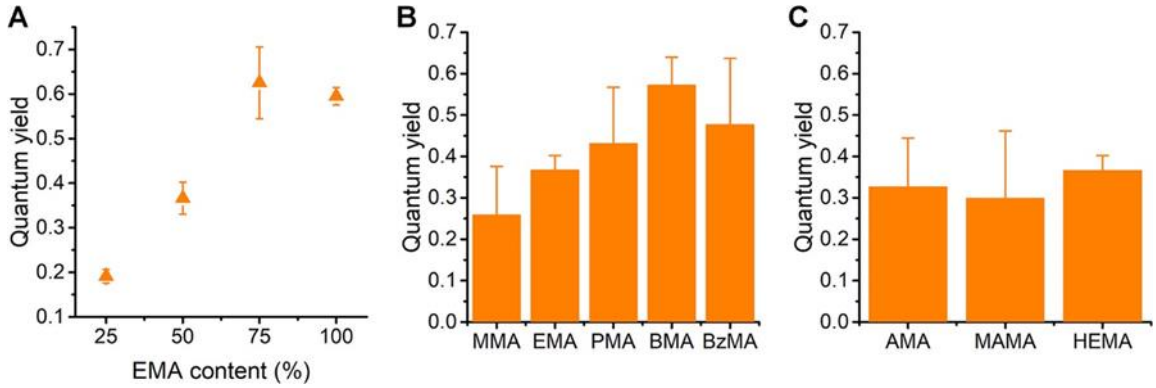

Figure 33. Rendements quantiques des NPs préparées à partir de différents copolymères, chargées avec 10 % R18/F5-TPB. (A) Rendements quantiques en fonction du pourcentage du monomère EMA dans le polymère avec HEMA et 1 % MAA. (B) Influence du type de monomère hydrophobe pour les copolymères avec 50 % HEMA et 1 % MAA. (C) Influence du type de monomère hydrophile pour les copolymères avec 50 % EMA et 1 % MAA. Les NPs ont été préparées dans l'eau. Les barres d'erreur correspondent à l'écart-type sur au moins trois mesures indépendantes.

Le rendement quantique augmente fortement avec l'augmentation de la fraction des monomères hydrophobes dans les polymères (figure 33A). Pour les copolymères EMA/HEMA, le rendement quantique passe de moins de 20 % avec 25 % mol EMA à plus de 60 % avec 75 % mol EMA. Cependant le rendement quantique n'augmente plus au-delà. La nature du monomère hydrophobe influence aussi le rendement quantique. En se plaçant à un ratio de 1 : 1 de HEMA/monomère hydrophobe, le rendement quantique a tendance à augmenter dans l'ordre suivant MMA < EMA < PMA < BzMA ~ BMA (figure 33B). Au contraire la nature des monomères hydrophiles ne montre pas d'influence significative sur le rendement quantique (figure 33C). L'augmentation des rendements quantiques avec l'hydrophobie du polymère, associée aux changements observés précédemment sur les spectres d'absorption suggèrent une tendance des polymères plus hydrophobes à diminuer l'agrégation des fluorophores au sein de la matrice polymérique.

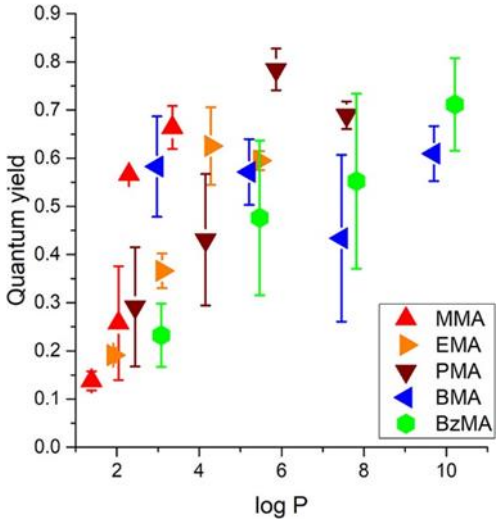

Figure 34. Rendement quantique en fonction du log P calculé des copolymères. Tous les polymères contiennent 1 % MAA et 10 % R18/F5-TPB et ont été encapsulés dans les NPs. Chaque couleur correspond à une série de copolymère contenant un monomère hydrophobe donné. Les NPs ont été préparées dans l'eau. Les barres d'erreur correspondent à l'écart-type sur au moins trois mesures indépendantes.

La figure 34 confirme que le rendement quantique des NPs tend généralement à augmenter avec l'hydrophobie du polymère. Cela est particulièrement vrai pour les polymères ayant un log P < 3 qui donnent des rendements quantiques entre 10 et 35 %. Néanmoins, pour les polymères avec des log P > 3, la variation du rendement quantique des NPs obtenues est moins claire, spécialement pour les rendements quantiques les plus élevés (autour de 60 %).

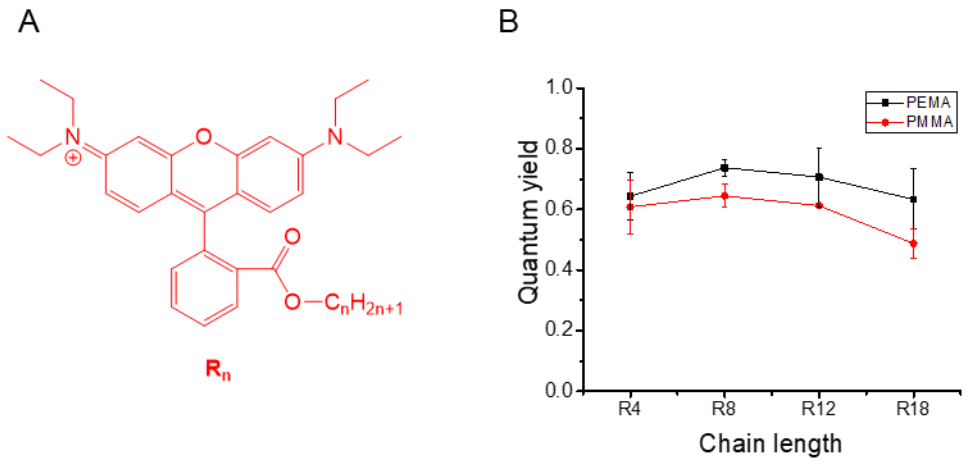

Figure 35. Effet de la longueur de chaine de la rhodamine sur le rendement quantique. (A) Structure de la rhodamine Rn portant une chaine de longueur variable (n=4 à 18). (B) Rendement quantique des NPs de PMMA- ou PEMA-COOH 2% chargées avec 10 % Rn/F5-TPB.

D'un autre côté, la longueur de la chaine de la rhodamine a été diminuée de 18 à 12, 8 puis 4 carbones (R18, R12, R8, R4, figure 35). L'hydrophobie de la rhodamine semble avoir une influence plus faible sur le rendement quantique. Pour les NPs préparées à partir de PMMA-COOH 2%, le rendement quantique passe de 50 % avec la rhodamine R18 à plus de 60 % pour les rhodamines portant une plus courte chaine carbonée. Cependant avec un polymère plus hydrophobe comme le PEMA-COOH 2%, cette légère différence de rendement quantique observée précédemment entre les différentes rhodamines est moins marquée.

Les différences de vitesse de précipitation du fluorophore et des polymères peuvent être à l'origine de ces différences de fluorescence. Le fluorophore R18/F5-TPB seul peut précipiter et former des NPs. Concernant les copolymères les plus hydrophiles, la précipitation des fluorophores est probablement plus rapide que la précipitation des polymères. Cela conduit à la formation de regroupement ou d'agrégats de fluorophores qui diminuent le rendement quantique. Si le fluorophore et le polymère ont des vitesses de précipitation similaires, le fluorophore sera incorporé de manière homogène dans la matrice polymérique donnant des rendements quantiques plus élevés. Les rendements quantiques les plus élevés correspondent aux polymères ayant des vitesses de précipitation les plus proches de celle des fluorophores. Les variations observées précédemment pour les polymères les plus hydrophobes peuvent venir de l'influence de l'environnement direct du fluorophore qui est alors lié à la nature et la

chimie du polymère ou aux différences de températures de transition vitreuse des polymères.[200]

Contrôle du clignotement

Le comportement collectif des fluorophores qui conduit au clignotement de la particule entière, est basé sur le transfert d'énergie ultra-rapide entre eux.[8] Pour que la particule clignote, l'énergie d'excitation doit circuler suffisamment rapidement entre quasi tous les fluorophores pour avoir une chance d'être transférée à une espèce noire ou non fluorescente avant l'émission de fluorescence. Cela va éteindre toute la particule. La vitesse du transfert d'énergie est dépendante de l'orientation relative des fluorophores et de la distance qui les sépare.[201] Dans une étude préliminaire, il a en effet été observé que le clignotement des NPs de PLGA dépend fortement de la distance entre les fluorophores et qu'augmenter leur concentration conduit à un clignotement plus rapide.[173] De plus des différences du clignotement en fonction de différents types de matrice polymérique ont également été observées. Les NPs de PLGA semblent avoir un transfert d'énergie plus rapide qui résulte de distances interfluorophores plus courtes que les NPs de polymères plus hydrophobes tels que le PMMA. On suppose que cela est lié à une organisation différente des fluorophores dans la matrice polymérique. Dans le cas du PLGA, les fluorophores sont condensés et forment un noyau au centre de la particule. Pour le PMMA, les fluorophores sont dispersés dans la matrice de manière plus homogène. Nous avons donc postulé que le contrôle du clignotement ainsi qu'une optimisation de la fluorescence des particules étaient possibles par ajustement de leur organisation au sein de la matrice polymérique en jouant notamment sur la chimie du polymère. Pour essayer de comprendre les paramètres qui régissent le clignotement des particules et le contrôler de manière adéquate, nous avons, dans un premier temps, préparé des NPs à base de polymères d'hydrophobie différente, chargées avec R18/F5-TPB.

La fluorescence de ces NPs a été étudiée par imagerie de particule unique. Pour cela, les NPs ont été déposées sur une surface et imagées par microscopie TIRF. Les images obtenues permettent d'avoir accès à l'intensité de fluorescence en fonction du temps pour chaque particule. Nous considérons qu'une particule clignote lorsqu'elle franchie au moins une fois la barre des 20 % de l'intensité maximale. Les résultats montrent cependant une forte dépendance de la taille des NPs sur le clignotement. En

effet la figure 36 montre que plus la taille des particules est petite, plus le clignotement est important. Or la taille des NPs est également liée à l'hydrophobie.

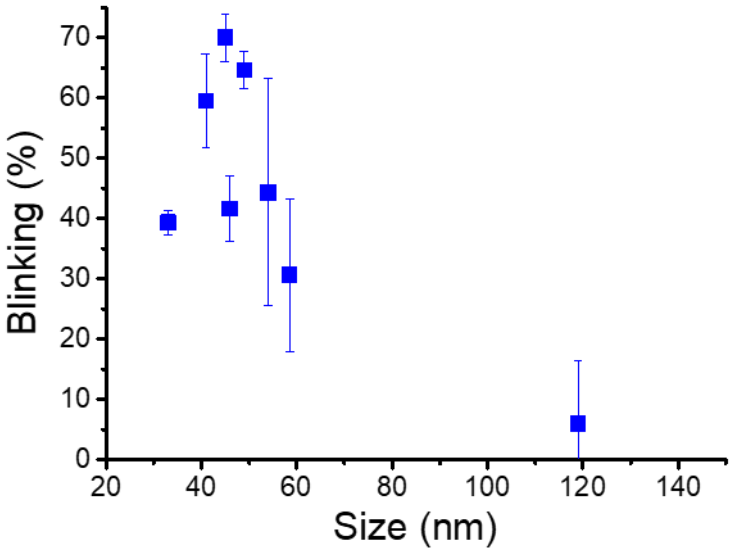

Figure 36.Tracé du clignotement des NPs en fonction de leur taille moyenne. Les NPs préparées à partir de polymères composés de différents monomères hydrophobes et de 2% (mol) de MAA sont chargées avec 10% R18/F5-TPB.

Afin d'obtenir une analyse plus fine et de s'affranchir de l'effet de taille des NPs, nous avons ensuite synthétisé des NPs avec des polymères d'hydrophobie différente mais donnant une taille similaire (Figure 37). Pour cela nous avons utilisé, le travail effectué sur le contrôle de la taille (Partie 3.1) en assemblant différents monomères (hydrophobes/hydrophiles) et en ajustant la taille des NPs avec plus ou moins de groupements chargés. La figure 37B montre la gamme de log P de 8.5 à 2.31 couvert par les NPs de type méthacrylate avec une taille comprise entre 21 et 33 nm. Afin d'agrandir cette gamme vers des hydrophobies plus faibles (jusqu'à -0.23), nous avons ajouté les NPs de PLGA qui donnent des tailles légèrement plus grandes que les NPs de méthacrylate. Les NPs seront imagées ultérieurement de manière individuelle et leur clignotement analysé.

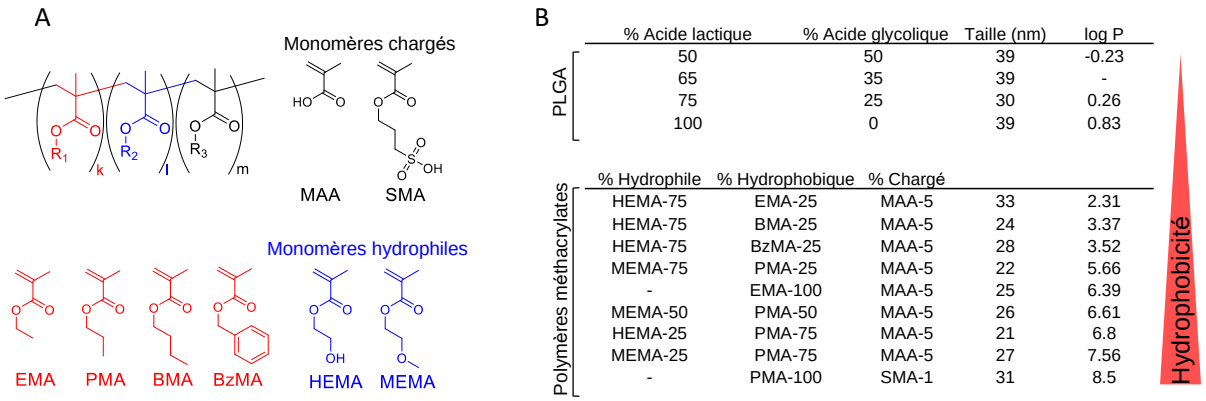

	% Acide lactique	% Acide glycolique	Taille (nm)	log P
PLGA	50	50	39	-0.23
	65	35	39	-
	75	25	30	0.26
	100	0	39	0.83

	% Hydrophile	% Hydrophobique	% Chargé		
Polymères méthacrylates	HEMA-75	EMA-25	MAA-5	33	2.31
	HEMA-75	BMA-25	MAA-5	24	3.37
	HEMA-75	BzMA-25	MAA-5	28	3.52
	MEMA-75	PMA-25	MAA-5	22	5.66
	-	EMA-100	MAA-5	25	6.39
	MEMA-50	PMA-50	MAA-5	26	6.61
	HEMA-25	PMA-75	MAA-5	21	6.8
	MEMA-25	PMA-75	MAA-5	27	7.56
	-	PMA-100	SMA-1	31	8.5

Figure 37. (A) Structure chimique des polymères type méthacrylate et les monomères utilisés. (B) Tableau regroupant la gamme de polymères utilisés pour l'étude du clignotement. Le diamètre des particules résultantes est également indiqué ainsi qu'une estimation de l'hydrophobie des polymères.

L'hydrophobie des polymères utilisés pour former les NPs, a une grande influence sur leurs propriétés photophysiques en particulier sur le rendement quantique. L'organisation des fluorophores au sein de la particule est fortement affectée par la nature du polymère essentiellement en raison de l'influence du polymère sur la formation des NPs. D'un autre côté, l'étude du clignotement des particules a permis de mieux comprendre les éléments intervenant dans la fluctuation de l'intensité de fluorescence et le comportement collectif des fluorophores. La taille des particules semble avoir une influence majeure sur le clignotement des particules. La gamme de NPs de même taille avec différentes hydrophobies devrait nous donner plus d'informations concernant les autres moyens d'influencer l'intermittence du signal fluorescent et surtout à quel point l'hydrophobie du polymère peut impacter celui-ci. Il serait également nécessaire d'appliquer une analyse plus fine des différents profils de clignotement (complet, partiel). Ceci nous permettrait d'aller encore plus loin dans la compréhension de ces systèmes dans le but de contrôler le clignotement des particules.

Une partie de ces résultats a été publié dans l'article joint en annexe :

Article 3 : Controlling Size and Fluorescence of Dye-Loaded Polymer Nanoparticles through Polymer Design. Rosiuk, V., Runser, A., Klymchenko, A. & Reisch, A. *Langmuir* **35**, 7009–7017 (2019).

Partie 5 : Interactions des nanoparticules

Dans ce chapitre, nous nous intéressons tout particulièrement aux interactions des NPs dans l'environnement intracellulaire. D'une part il s'agit de rendre furtives les NPs. Pour cela, la surface des NPs doit être adaptée en parallèle de la taille pour éviter les interactions non spécifiques dans le cytoplasme. D'autre part, il faut créer des interactions spécifiques à l'aide d'un ligand entre la NP et la biomolécule d'intérêt pour pouvoir marquer et suivre cette dernière au niveau intracellulaire.

Nous proposons, ci-dessous, une nouvelle approche pour traiter la surface des NPs à base de groupements zwittérioniques capables de réduire l'adsorption de protéines tout en conservant la petite taille et la brillance des NPs. Par la suite, nous présenterons l'approche et la preuve du concept pour la fonctionnalisation des NPs zwittérioniques.

5.1 Nanoparticules zwittérioniques

Pour se déplacer librement dans les milieux biologiques, les NPs doivent être de petites tailles mais elles doivent également limiter les interactions non spécifiques. Nous avons en effet démontré précédemment que la taille limite pour diffuser librement dans le cytosol était de 23 nm. Mais la surface des NPs joue également un rôle important sur le comportement des NPs dans les systèmes biologiques et peut affecter la diffusion des NPs dans le cytosol. [202,203] La chimie de surface des NPs va en effet déterminer les interactions avec les protéines et macromolécules intracellulaires.[14,204] En particulier, l'adsorption de protéines à la surface de la NP conduit à la formation d'une couche de protéine qui va affecter son comportement.[153,205,206] Cela empêchera notamment la diffusion libre des NPs dans le cytosol. La modification de surface des particules est donc indispensable. Différentes stratégies existent mais la plus courante est l'introduction de groupements PEG sur les NPs.[207,208] Afin d'être efficace, la couche de PEG à la surface augmente considérablement le diamètre des particules d'une dizaine de nm. [15,209,210] Une alternative à la PEGylation est l'utilisation de groupements zwittérioniques (ZI) qui vont mimer le type de surface que l'on retrouve sur la couche externe de la membrane cellulaire.[211,212] Les zwittérions sont des groupements

très hydrophiles composés de leur propre paire d'ions de charges opposées. Leur mécanisme est donc basé sur la forte hydratation de ces groupements et le fait qu'il n'y ait pas de charge nette résultante.[213] L'avantage de l'enrobage des NPs avec des groupements ZI procure une couche très fine limitant l'augmentation du diamètre de la particule contrairement à la PEGylation. Les ZI de type carboxybétaine, sulfobétaine et phosphorylcholine, peuvent être utilisés pour traiter la surface des NPs. Mais ces enrobages à base de groupements ZI ont pour la plupart été développés pour des NPs inorganiques.[214–216]

Afin de rendre nos NPs furtives, nous avons développé une nouvelle approche permettant d'assembler des petites NPs de polymères fluorescentes et résistantes à l'adsorption de protéines par nanoprécipitation. Nous avons synthétisé par polymérisation radicalaire des copolymères de type méthacrylate portant des groupements zwittérioniques (ZI) et sulfonate (SO_3H). Les fractions des groupements ZI et SO_3H varient respectivement de 0 à 10 mol% et de 1 ou 2 mol%. La partie restante du polymère (~90 %) est composée de groupements méthacrylates d'alkyle dont la longueur de la chaine alkyle varie du méthyle au butyle (MMA, EMA, PMA, BMA). La présence de chaines alkyles plus hydrophobes permet de contrebalancer la quantité non négligeable de groupements hydrophiles dans le polymère. L'introduction de 10 % ZI n'a qu'une légère influence sur la taille des NPs de PMMA-ZI-SO_3H. Elles atteignent 11 et 9 nm de diamètre pour les NPs à base de polymères portant respectivement, 1% et 2% de sulfonate indiquant que les groupements ZI n'affectent pas le processus de formation des NPs. Cependant la taille des NPs obtenues à même pourcentage en SO_3H, augmente avec l'hydrophobie du groupe méthacrylate d'alkyle dans l'ordre suivant MMA < EMA < PMA < BMA passant de 11, 14, 22 à 35 nm respectivement.

Pour les rendre fluorescentes, 10 à 20 % de R18/F5-TPB ont été encapsulés dans les NPs ZI. La stabilité de ces particules zwittérioniques a été évaluée par FCS. A 10 % ZI, les NPs ne montrent ni changement de taille, ni signes d'agrégation même dans 1 M de NaCl. De même, en présence de FBS, les NPs à 10% de ZI ne montrent pas de changement significatif de taille indiquant également une excellente résistance à l'adsorption de protéines. Cette stabilité en présence de protéines est cependant moins efficace pour les polymères plus hydrophobes en particulier pour ceux avec BMA. Afin d'étudier le comportement des NPs dans les cellules, ces dernières ont été

microinjectées dans le cytosol et observées au microscope à épifluorescence. Nous avons comparé les NPs ZI composées des différents groupements méthacrylate d'alkyle avec les NPs de PMMA-SO_3H PEGylées. Les NPs de PMMA-ZI 10%-SO_3H 1% et PEMA-ZI 10%-SO_3H 1% montrent une distribution dans tout le cytosol. La diffusion des particules ZI se voit cependant réduite lorsque la taille des particules augmente. La grande brillance de ces particules, nous a ensuite permis de les suivre de manière individuelle. L'étude de leurs trajectoires montre une diffusion de type Brownien pour les NPs PEMA-ZI 10%-SO_3H 1%. Ainsi, les NPs de PEMA-ZI 10%-SO_3H 1%., avec un coefficient moyen de 0.8 $\mu m^2.s^{-1}$, diffusent jusqu'à quatre fois plus vite que les NPs de PMMA-SO_3H 1% PEGylées qui ont un coefficient de diffusion moyen de 0.2 $\mu m^2.s^{-1}$. Les NPs de PMMA-ZI 10%-SO_3H 1% possèdent un coefficient de diffusion légèrement plus faible, de 0.65 $\mu m^2.s^{-1}$ par rapport aux NPs de PEMA-ZI 10%-SO_3H 1%. Concernant les NPs un peu plus grandes, composées de PPMA-ZI 10%-SO_3H 1%, le coefficient de diffusion moyen est de 0.25 $\mu m^2.s^{-1}$, clairement inférieur à celui des NPs de PEMA-ZI 10%-SO_3H 1%.

Grâce à la conception de polymères amphiphiles portant des groupements ZI et chargés, nous pouvons formuler des NPs de la taille de l'ordre des protéines avec des brillances suffisamment élevées pour permettre une bonne précision de localisation par microscopie de fluorescence. La fine pellicule de ZI à la surface des NPs assure une excellente stabilité dans les milieux biologiques. De plus, leur excellente brillance a rendu possible d'imager ces NPs de manière individuelle dans le cytoplasme. L'étude de leur trajectoire a montré que les NPs ZI sont plus efficaces en terme de diffusion que les NPs PEGylées en raison de l'augmentation du volume de la particule par l'enrobage de PEG. Ces petites NPs furtives sont donc prometteuses pour le suivi de molécules uniques avec des résolutions spatio-temporelles élevées dans les cellules vivantes.

Ce travail a été publié dans *ACS Applied Materials and Interfaces* et est joint ci-dessous.

Article 5 : Zwitterionic Stealth Dye-Loaded Polymer Nanoparticles for Intracellular Imaging.

ACS APPLIED MATERIALS & INTERFACES

Research Article

Cite This: ACS Appl. Mater. Interfaces XXXX, XXX, XXX−XXX

www.acsami.org

Zwitterionic Stealth Dye-Loaded Polymer Nanoparticles for Intracellular Imaging

Anne Runser, Denis Dujardin, Pauline Ernst, Andrey S. Klymchenko,* and Andreas Reisch*

Laboratoire de Bioimagerie et Pathologies, Faculté de Pharmacie, CNRS UMR 7021, Université de Strasbourg, 67401 Illkirch Cedex, France

Supporting Information

ABSTRACT: Intracellular applications of fluorescent nanoparticles (NPs) as probes and labels are currently limited by significant molecular crowding and the high level of complexity encountered inside living cells. The solution is to develop very small, bright, and noninteracting (stealth) NPs. Combining these properties requires implementing the stealth behavior through the thinnest possible hydrophilic shell. Here, we propose a one-step process for preparing ultrasmall and bright stealth NPs based on a zwitterionic (ZI) methacrylate-based copolymer. Dye-loaded polymer NPs are assembled through nanoprecipitation of the copolymer together with the salt of a rhodamine B derivative and a bulky hydrophobic counterion to achieve high particle brightness. We found that 10 mol % ZI groups in the polymer yield NPs of less than 15 nm that are stable in physiological salt conditions and practically resistant to protein adsorption, as suggested by fluorescence correlation spectroscopy. The combination of the very small size with the nonfouling nature of these particles enables spreading of ZI polymer NPs in the whole cytosol after their microinjection into living cells. In addition, single-particle tracking showed up to four times faster diffusion of ZI NPs in the cytosol compared to PEGylated NPs. The obtained dye-loaded ZI polymer NPs open the route to intracellular single-particle tracking and biosensing applications.

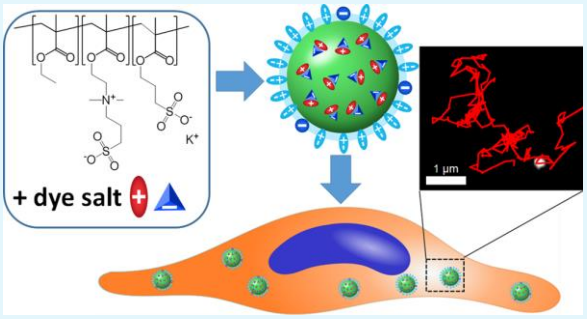

KEYWORDS: *fluorescent nanoparticles, dye-loaded polymer nanoparticles, zwitterion coating, stealth nanoparticles, single-particle tracking, intracellular imaging*

INTRODUCTION

The emergence of single-molecule and super-resolution fluorescence microscopy has opened a new area of sensing and imaging of biological molecules and processes in living cells.[1−3] However, these techniques require very bright fluorescent labels and probes, because their spatiotemporal resolution and sensitivity are directly linked to the number of collected photons.[4] Fluorescent nanoparticles (NPs) such as quantum dots (QDs),[5,6] silica NPs,[7] conjugated polymer NPs,[8] aggregation-induced emission NPs,[9] and dye-loaded NPs[10] can overcome the limited brightness of fluorescent proteins or organic fluorophores. In particular, dye-loaded polymer NPs have recently achieved very high brightness equivalent to 100−1000 organic dyes.[9−11] Achieving such high brightness required the development of new strategies to overcome aggregation-caused quenching of the fluorophores encapsulated at very high concentrations in the polymer matrix of NPs. This was achieved, for example, by using fluorophores that undergo aggregation-induced emission[12] or by using salts of fluorophores with hydrophobic bulky counterions to prevent aggregation.[13] Importantly, the bulky counterions approach enabled generation of ultrabright polymeric NPs with unprecedented energy transfer,[14] which is essential for preparation of NP-based fluorescent biosensors.[15] Furthermore, polymer-based dye-loaded NPs have been shown to be nontoxic, and they can be made from biodegradable polymers, being highly flexible with respect to (co)encapsulation and release of active compounds.[10,16]

However, intracellular applications require small probe sizes and the absence of nonspecific interactions in biological environments, which remain key challenges of current fluorescent NPs.[17] First, in order to increase localization precision, the particle diameter should be comparable to that of the biomolecule (e.g., protein, nucleic acid) it is intended to label/detect. Second, the particle size and the surface coating play a crucial role in defining the intracellular behavior of NPs and impact on the behavior of the labeled biomolecules.[18−20] Diffusion of NPs can be limited because of structural restrictions and macromolecular crowding effects inside cells.[21,22] Etoc. et al. determined that particles of ≤50 nm can have Brownian diffusion in the cytosol.[18] We showed that the critical core size for NPs to reach almost all parts of the

Received: August 27, 2019
Accepted: December 9, 2019

Downloaded via UNIV STRASBOURG on January 6, 2020 at 09:14:26 (UTC).
See https://pubs.acs.org/sharingguidelines for options on how to legitimately share published articles.

cytosol is around 23 nm.[20] At the same time, the surface chemistry has a major effect on the behavior of NPs in biological systems[23,24] and can affect the diffusion and the motion of NPs in the cytosol.[18,19] One reason for this is that the surface chemistry will determine interactions with proteins, notably their adsorption, which can lead to the formation of a protein corona affecting all aspects of NP behavior from the cellular uptake to their degradation.[25−27] Moreover, strong interactions between proteins and the NP surface prevent free movement of NPs in the cytosol.[18] Therefore, their surface treatment against protein adsorption is essential. Grafting polyethylene glycol (PEG) is the best known strategy for suppressing protein adsorption on NPs.[28,29] However, PEGylation is not fully adapted to protein-sized NPs, because the PEG chains of 2000−5000 Da in length, used for this purpose, also significantly increase the particle diameter by ∼10 nm.[30−32] An alternative is the use of zwitterionic (ZI) groups, mimicking the surface of the cell membrane.[33,34] The mechanism of suppression of protein adsorption in the case of zwitterions is linked to their very hydrophilic nature and the fact that they contain their own counterion,[31,34,35] rather than on steric repulsion as in the case of PEG.[36] Therefore, ZI coatings can be very thin, having minimal impact on the particle diameter, unlike PEG coatings.

Several approaches have been developed to implement ZI groups, especially carboxybetaine, sulfobetaine, and phosphorylcholine, on NP surfaces. Most of these have been developed for inorganic NPs as QDs,[37−40] silica NPs,[41,42] or Au NPs.[43,44] ZI surfaces were achieved in these cases either through the direct grafting of suitable ZI small molecules,[38,41,44−46] or the grafting or adsorption of ZI polymers.[37,40,47,48] In the case of polymeric NPs, ZI particles are mainly obtained through the assembly of polymeric micelles, based on block copolymers bearing a polar ZI and a hydrophobic block.[49−52] Statistical copolymers with relatively large amounts of ZI groups (30 to >90%), on the other hand, have been studied as water-soluble systems able to translocate through cellular membranes.[53−55]

Recently, we introduced a concept of charge-controlled nanoprecipitation of hydrophobic polymers,[32] where a small number of charged groups can tune the size of the obtained NPs down to 7 nm.[20] To minimize their interaction with proteins and to ensure their free diffusion in the cytosol, they were stabilized by adsorption of PEGylated surfactants.[20,32] However, so far, no attempts have been done to develop hydrophobic polymers with a limited number of charged and ZI groups for their nanoprecipitation into ultrasmall NPs with stealth shell, compatible with intracellular applications.

In the present work, we developed a novel approach to assemble small fluorescent polymer NPs with a ZI shell in a one-step process. For this, we designed methacrylate-based statistical copolymers, bearing a hydrophobic major monomer (methyl to butyl methacrylate), a small amount of charged monomer to reduce the size,[20,32] and a varying amount of ZI sulfobetaine side groups. We then studied the influence of the presence of the ZI groups on the formation of dye-loaded NPs through nanoprecipitation. The resulting NPs were evaluated with respect to their stability in biological media and the capacity of the sulfobetaine groups to prevent protein adsorption. The behavior of the most promising NPs was then monitored directly at the single particle level in the cytosol of living cells in order to access their suitability as nanoprobes for single-particle tracking. In this way, we could show that polymers bearing 10% ZI groups and 1−2% sulfonate groups formed small (<20 nm) NPs, in which efficient encapsulation of a dye salt was obtained, rendering them brightly fluorescent. These particles showed stealth behavior with respect to biological media and very high mobility in the cytosol, exceeding that of PEGylated particles of a similar core size.

RESULTS AND DISCUSSION

Methacrylate-based copolymers bearing sulfonate and ZI groups were synthetized by free radical copolymerization (Figure 1, Scheme S1, and Figure S1). The fraction of sulfonate groups on polymers was 1 or 2 mol %, whereas that of the ZI group was varied from 0 to 10 mol %. The remaining part of the polymers, corresponding to 88 to 99 mol %, was made up of alkyl methacrylates, with varying lengths of the alkyl groups, ranging from methyl to butyl. Increasing the alkyl chain length should thereby increase the hydrophobicity of the polymers and balance the hydrophilicity of the ZI groups. In consequence, the synthesized polymers had an amphiphilic character and a relatively low net negative charge. Here, the polymers are noted as PXMA−ZI-x%−SO_3H-y%, where XMA stands for the corresponding major monomer (MMA for methyl methacrylate, EMA for ethyl methacrylate, PMA for propyl methacrylate, BMA for butyl methacrylate), x and y give the molar percentage of the ZI and sulfonate groups.

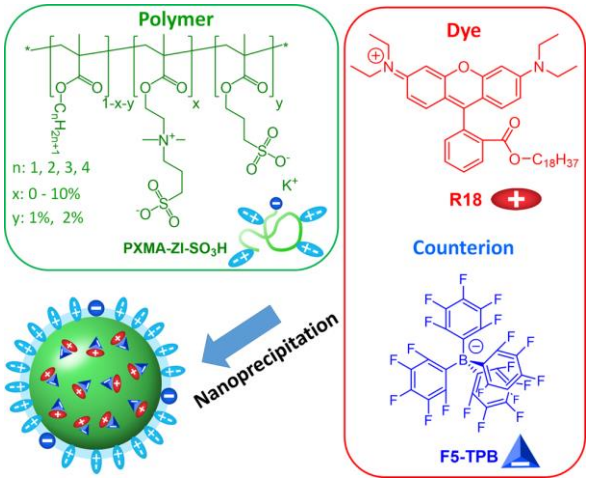

Figure 1. Chemical structures of different polymers, dye R18 and its counterion (F5-TPB) used for preparation of ZI dye-loaded NPs through nanoprecipitation.

These polymers were then used to assemble dye-loaded polymer NPs through nanoprecipitation. For this, solutions of the polymers in acetonitrile (with a small amount of methanol) containing the salt of a rhodamine B derivative (R18) with a perfluorinated tetraphenylborate (F5-TPB, typically 10 wt % with respect to the polymer)[13] were added quickly to a large excess of Milli-Q water. The size of the formed NPs was analyzed through transmission electron microscopy (TEM, Figure 2, Table S1), fluorescence correlation spectroscopy (FCS, Tables S1 and S4), and dynamic light scattering (DLS, Tables S1, S2, S3). In the case of polymers bearing only sulfonate but no ZI groups, very small particles were obtained as observed previously:[20] According to TEM, PMMA−SO_3H-1% yielded NPs of about 13 nm and the particle size decreased

DOI: 10.1021/acsami.9b15396
ACS Appl. Mater. Interfaces XXXX, XXX, XXX−XXX

ACS Applied Materials & Interfaces Research Article

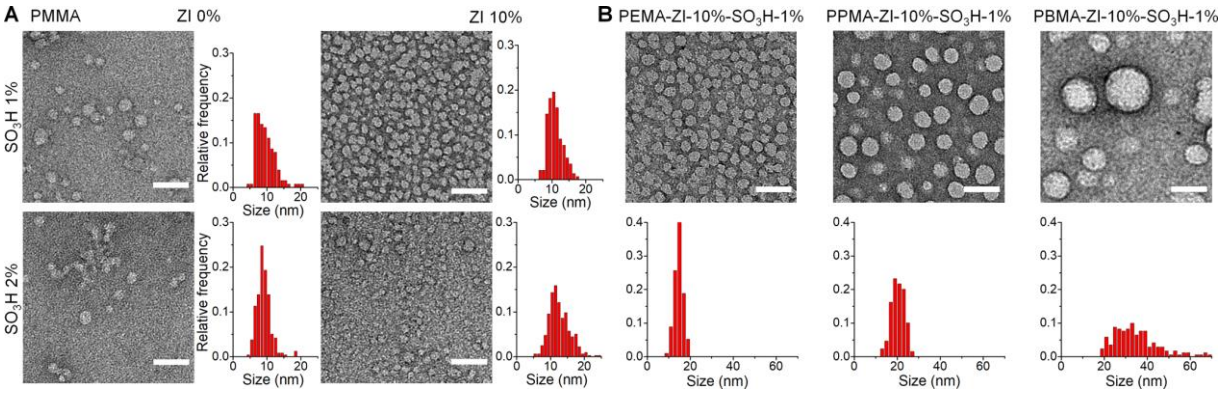

Figure 2. TEM analysis of the sizes of ZI and non-ZI sulfonate NPs. NPs loaded with 10 wt % R18/F5-TPB were prepared by nanoprecipitation from (A) PMMA−SO_3H-1% and 2%, PMMA−ZI-10%−SO_3H-1% and 2%, and (B) different methacrylate polymers with 10% ZI and 1% SO_3H groups. Below each image, size distributions of corresponding NPs are given. Scale bars correspond to 50 nm. At least 100 NPs were analyzed per condition.

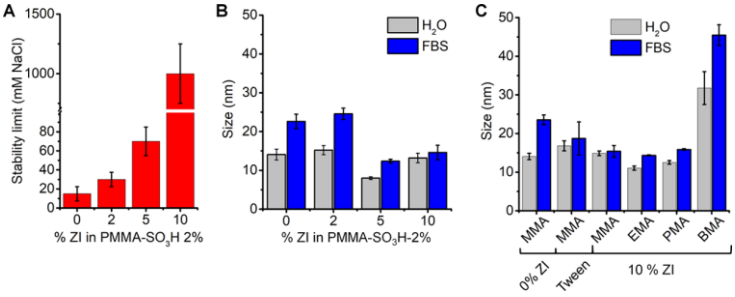

Figure 3. Stability of NPs and their interactions with proteins as determined by FCS. (A) Influence of the ZI content on the maximum NaCl concentration at which the particles remained stable (size increase <20%). Size of (B) PMMA−ZI−SO_3H-2% NPs with different ZI contents and (C) PXMA−SO_3H-1% NPs made from different methacrylate monomers with or without ZI groups, or without ZI groups and treated with Tween 80, in the presence of 10% FBS. (Tween corresponds to PMMA−SO_3H-1% NPs treated with Tween 80. Tween adsorption led to a size increase of ∼5 nm). All NPs were loaded with 1 wt % R18/F5-TPB in order to prevent saturation phenomena involving triplet states. Given are mean values from three independent measurements. The error bars correspond to standard error of the mean (SEM).

to about 9 nm for 2% sulfonate. The introduction of 10% ZI in the polymers had only a minor influence on the particle size of PMMA−ZI−SO_3H-based NPs. They reached 11 and 9 nm of diameter for polymers with 1 and 2% sulfonates, respectively. Hence, the presence of the ZI groups did not affect the nanoprecipitation process, while the expected "ZI shell" is thin enough to preserve the small size of NPs. Increasing the hydrophobicity of the alkyl methacrylate monomers, on the other hand, led to increasing particle size (Figure 2, Table S1) in the order PMMA−ZI-10%−SO_3H-1% < PEMA−ZI-10%−SO_3H-1% < PPMA−ZI-10%−SO_3H-1% < PBMA−ZI-10%−SO_3H-1%, from 11 to 35 nm. This is in agreement with results obtained previously[56] and can be attributed to the fact that increasing hydrophobicity leads to increasing supersaturation, which is the major driving force in nanoprecipitation.[56−58] DLS and FCS results were in good agreement with the sizes obtained by TEM (Table S1). The slightly larger sizes obtained by TEM in some cases were attributed to a preferred immobilization of larger particles on the grids. Zeta-potential measurements of NPs made from different polymers showed that these were always clearly negatively charged with values in the range −20 to −35 mV (Table S3). The ZI groups did not influence significantly the surface charge.

As we showed earlier, the hydrophobic counterion approach works well for dye encapsulation of cationic R18 into NPs from hydrophobic polymers.[10,13,59] As the hydrophobicity of our new polymers is lower because of 10% ZI groups, we evaluated the encapsulation efficiency for several polymers, and notably the least hydrophobic polymer, PMMA−ZI-10%−SO_3H-2%, using dialysis against a special β-cyclodextrin-based release medium.[59] This method has been validated for several series of dye-loaded NPs, showing that dyes that are not well encapsulated are removed in this way.[59,60] Here, dialysis of the dye-loaded NPs for 24 h showed a release of 14% of the used dye for the most hydrophilic polymer, and a release of around 10% for the other tested polymers (Figure S2, Table S5). Hence, the used approach yielded very efficient encapsulation (86−91%) of the dye salt in the particles, in agreement with previous results from dialysis and ultracentrifugation.[32,59] The efficient loading has been attributed to the high hydrophobicity of the dye−counterion pair. Furthermore, the quantum yield of the particles remained high, 31−58% for a 10 wt % loading for all zwitterion bearing polymers (Figure S3, Table S6). A slight decrease was, however, observed upon introduction of the ZI groups, probably because of the lower hydrophobicity of the ZI-bearing polymers.[56] Taking into account the size, the loading, the encapsulation efficiency, and the quantum yield, this resulted in a per particle brightness of 10^6 to over 10^7 M^{-1} cm^{-1} (Table S6). For example, PMMA−ZI-10%−SO_3H-1%-based NPs loaded with 10 wt % R18/F5-TPB reached a

DOI: 10.1021/acsami.9b15396
ACS Appl. Mater. Interfaces XXXX, XXX, XXX−XXX

ACS Applied Materials & Interfaces Research Article

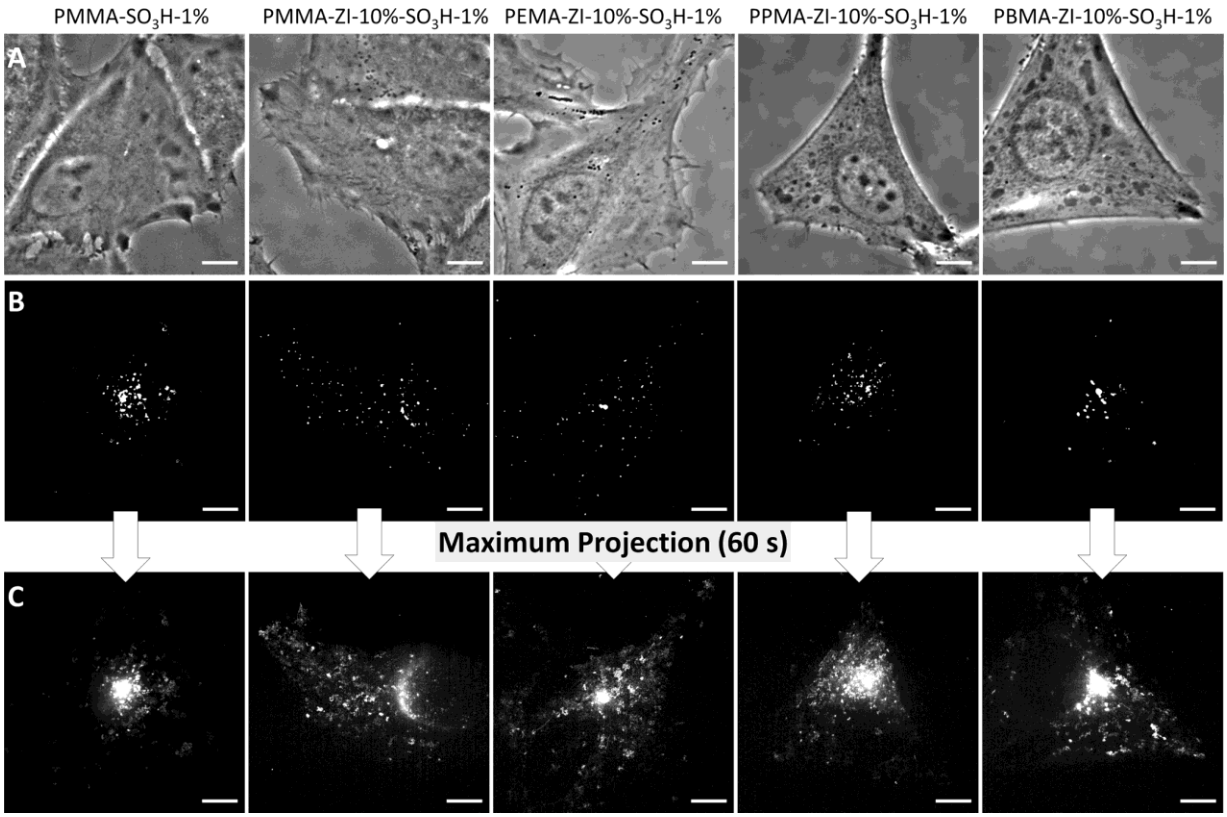

Figure 4. Representative micrographs of HeLa cells microinjected with different types of NPs loaded with 10 wt % R18/F5-TPB: (A) phase contrast images after microinjection and monitoring of particle behavior. (B,C) Epi-fluorescence micrographs representing: (B) a single frame (50 ms exposure) and (C) maximum projections over 60 s. Each column represents the same cell. Scale bars correspond to 10 μm.

brightness of 2.0×10^6 M^{-1} cm^{-1} (for excitation at 565 nm) exceeding by nearly 10-fold the brightness of corresponding QDs (e.g., ~2.2×10^5 M^{-1} cm^{-1} for QD585 from Invitrogen).

The stability of the resulting particles in biological media, and in particular the potential of the ZI groups to improve this, was then investigated (Figure 3, Tables S1, S2, S4).[61] The fraction of ZI groups in the polymers was varied from 0 to 10% in order to modify the density of ZI on the particle surface. In a first step, the stability of NPs was evaluated through addition of NaCl (Figure 3A). The size of the particles was monitored by FCS after addition of increasing salt concentrations. The stability limit was defined as the highest tested NaCl concentration showing no aggregation of NPs. Typically, when exceeding this salt concentration, a marked increase in size was observed. Here, we chose an increase of particle size by >20% to define this limit. NPs made from polymers bearing no ZI groups started to aggregate (and precipitate) already at a relatively small salt concentration (>20 mM), which is far below that in a physiological medium (~150 mM). Addition of ZI groups to the polymer led to an increase in the particle stability. At 10% of ZI groups, the NPs showed neither changes in size nor signs of precipitation up to 1 M NaCl. These ZI-bearing NPs also showed an excellent stability over a wide pH range, from 3.6 to 9, as observed by DLS measurements (Table S2). This should be beneficial for their use in different cellular microenvironments. Furthermore, no significant changes in fluorescence brightness were observed in the presence of proteins (Table S4, Figure S4).

The influence of the ZI groups on interactions of the NPs with proteins and other biomolecules was then studied by FCS in the presence of 10% fetal bovine serum (FBS), a complex mixture containing notably numerous proteins (Figure 3B). In the case of particles without ZI groups, a size increase by about 10 nm was observed, which corresponds to the adsorption of at least a monolayer of proteins and thus the formation of a protein corona.[25] Starting from 5% of ZI groups, the size increase of the NPs upon interaction with proteins was significantly reduced. At 10% of ZI groups, no significant increase in particle size was observed, indicating that the surfaces of these NPs resisted protein adsorption. The stealth properties of NPs with ZI groups were more pronounced for the less hydrophobic MMA polymer, whereas more hydrophobic polymers, especially BMA, showed a significant size increase in the presence of FBS.

These NPs were then directly microinjected in the perinuclear region of the cytosol of living HeLa cells and their behavior was monitored using epifluorescence microscopy (Figures 4 and S5). Direct observation of the cells was conducted over the whole experiment time and showed generally good viability of cells with microinjected NPs (Figure 4A). Microinjection ensures direct delivery of the NPs with minimal modification of their surface and optimal control over the compartment they are delivered to, here the cytosol. The particles were easily visible as bright dots (even when excited with a Xenon lamp), which allowed observing their distribution and movement. In all cases, diffuse staining of

DOI: 10.1021/acsami.9b15396
ACS Appl. Mater. Interfaces XXXX, XXX, XXX−XXX

cytosolic structures was virtually absent. This confirms the efficient and stable encapsulation of the dyes within the NPs and the absence of dye leaching, which has been shown to lead to a strong and characteristic staining of the cell-interior.[59,62,63] Maximum projections of the fluorescence intensities for 60 s of acquisition gave a general idea of the overall distribution and mobility of the particles throughout the cytosol (Figure 4C, Table S7 for a more quantitative analysis): in the absence of ZI groups, a large part of the particles remained stuck at the injection point, indicating strong interactions of NPs with the cellular constituents. In sharp contrast, NPs bearing 10% ZI groups showed a tendency to distribute throughout the cytosol showing traces of their diffusion trajectories, although their behavior depended on the type of alkyl methacrylate used for the polymer synthesis. PMMA-based ZI-bearing NPs showed a distribution all over the cytosol, but often also a "crescent"-like signal around the nucleus close to the injection point. This latter might hint at limitations of the physical stability of the PMMA−ZI particles under the conditions experienced during microinjection. PEMA−ZI particles showed a homogeneous distribution over practically the whole cytosol and only a small clustering around the injection point (Figure 4B), which was also observed for PPMA−ZI particles. These results confirmed that 10% ZI groups are sufficient to strongly reduce interactions of the particles with cellular constituents and enable spreading throughout the cytosol. However, in the case of PBMA-based particles, a static localization at the injection point was observed. As observed previously,[20] the particle size has a major influence on intracellular particle diffusion, and only particles below a critical core size of around 23 nm were able to spread throughout the cytosol because of steric hindrance by cellular structures.[21] The size of PBMA−ZI particles used here was clearly above this threshold, which can explain their confinement to the injection site. In a certain measure, this can also apply to the PPMA-based ZI particles, for which the size distribution (Figure 2) showed that about 20% of these NPs were larger than 23 nm and thus above this threshold.

Observation of NPs microinjected in cells showed that all the NPs made from polymers bearing 10% ZI groups (except PBMA) had a high mobility within the cytosol, in contrast to those made of PMMA−SO_3H-1%. At the same time, the high brightness of our particles enabled studying their movement through single-particle tracking, and thus better understanding the influence of the ZI groups and the type of polymer used on their intracellular behavior. An example of a cytoplasmic trajectory of a PEMA−ZI-10%−SO_3H-1% NP is represented in Figure 5A. Plotting the mean square displacement (MSD) versus lag time for individual trajectories yields detailed information on their diffusion behavior, notably the diffusion coefficients and the type of diffusion (i.e., free/Brownian, restricted, active transport).[64−66] Here, for the ZI-bearing NPs, the MSD showed a linear increase with a lag time of up to about 10 μm^2 for over 90% of the particles (Figure 5B). This indicates normal or Brownian diffusion of these particles in the cytosol, which is described, in two dimensions, as MSD = $4D\Delta t^{\alpha}$ with D, the diffusion coefficient and $\alpha = 1$.[66] The diffusion coefficients of individual NPs were then obtained from the corresponding MSD curves (Figures 5 and S6). Figure 5C shows that for PEMA−ZI NPs the distribution of the diffusion coefficients is centered around 1 $\mu m^2\ s^{-1}$, with a mean D of 0.80 $\mu m^2\ s^{-1}$, in good agreement with values obtained for QDs of a similar size.[18] Only a small fraction

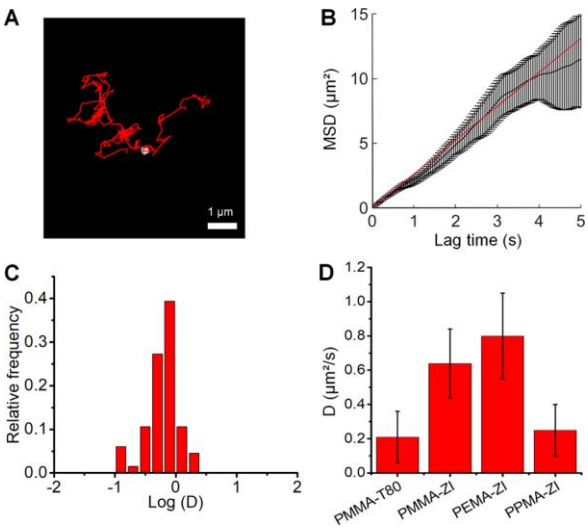

Figure 5. Single-particle tracking. (A) Trajectory (in red) of a PEMA−ZI-10%−SO_3H-1% NP loaded with 20 wt % R18/F5-TPB in the cytoplasm over 30 s. (B) Mean-square displacement (MSD) of PEMA−ZI-10%−SO_3H-1% NPs. The black curve corresponds to the mean MSD curves and the red curve is the fitted plot. The error bars correspond to SEM. (C) Diffusion coefficient distribution of PEMA−ZI-10%−SO_3H-1% NPs. (D) Mean diffusion coefficients of different polymer NPs. The error bars give full width at half-maximum of the distributions. At least 50 trajectories were analyzed per sample.

(<10%) of these NPs had diffusion coefficients below 0.2 $\mu m^2\ s^{-1}$. PMMA−ZI NPs had a similar distribution of diffusion coefficients with a slightly lower mean of 0.65 $\mu m^2\ s^{-1}$ (Figures 5D and S6), in agreement with their slightly larger hydrodynamic size. PPMA−ZI NPs, on the other hand, showed a clearly lower mean diffusion coefficient of 0.25 $\mu m^2\ s^{-1}$. This is probably due to their larger size leading to a restricted cytoplasmic diffusion (though a less complete suppression of interactions with proteins for these more hydrophobic particles may also contribute). As made PMMA−SO_3H-1% NPs without ZI groups remained clustered around the injection point, and hence it was not possible to characterize their diffusion behavior. However, we could show earlier that simple adsorption of Tween 80 (T80), a PEGylated surfactant, on such NPs strongly reduces their interaction with proteins and permits their diffusion in the cytosol.[20,32] Interestingly, the mean diffusion coefficient of these NPs was 0.2 $\mu m^2\ s^{-1}$ that is three- to fourfold lower than those of the PMMA−ZI and PEMA−ZI NPs, even though their core sizes were very close (Figure 2). One reason for this is certainly the fact that the addition of the PEGylated surfactant increases the NP size by >5 nm (from 13 to 18 nm according to FCS).[32] The large difference in diffusion coefficients further indicates that the ZI groups are probably more effective in reducing nonspecific interactions with intracellular biomolecules and structures compared to the adsorbed PEGylated surfactant.

Considering the ensemble of these results in view of previous findings can give a better idea of the structure and function of the obtained ZI fluorescent NPs: here, to develop "stealth" dye-loaded polymer NPs, we designed a series of amphiphilic polymers made up of a majority of hydrophobic monomers, 10% of ZI monomers, and 1−2% of negatively charged monomers. These were nanoprecipitated together

DOI: 10.1021/acsami.9b15396
ACS Appl. Mater. Interfaces XXXX, XXX, XXX−XXX

with a dye salt to assemble the NPs in a single step. The resulting particles combined, on the one hand, efficient dye encapsulation and high fluorescence quantum yields, resulting in high particle brightness with, on the other hand, excellent colloidal stability and resistance to protein adsorption. We have observed previously that high hydrophobicity of the matrix is crucial for achieving good encapsulation and high quantum yields of the encapsulated dyes.[56,67] In consequence, the particles probably have a hydrophobic core made up predominantly of hydrophobic alkyl-methacrylate units and of the dye salt. The excellent resistance to protein adsorption and the high mobility of the particles in the cytosol, on the other hand, suggest a very hydrophilic surface with a high density of ZI groups.[23,34] We hence suppose that upon mixing of the organic solutions of the polymers and dyes with the aqueous phase, supersaturation of the polymers and the dye salt occurs, which then drives nanoprecipitation. During nucleation and growth, the polymers probably arrange in a way that the sulfonate and ZI groups are primarily located at the surface of the particles, whereas the hydrophobic parts are located in the particle interior, where the highly apolar dye-salt is also embedded. Based on the obtained sizes and a molar mass of the used polymer between 40 000 and 50 000, the number of polymer chains per particle can be estimated to be around 10 per NP, that is, ∼350 ZI groups at the particle surface.

Assuming that the ZI groups are located mainly at the particle surface, their surface density can be estimated based on the particle size to be around 1.1 ZI groups per nm^2, for example, for our PMMA−ZI-10%−SO_3H-1% NPs with a size of 11 nm. This is close to the density of phosphorylcholine head groups in closely packed lipid monolayers (1.4−2 per nm^2)[68] and suggests that the ZI groups form a relatively dense layer on the NP surface. The NPs made with MMA and EMA, the least hydrophobic monomers, showed a better resistance to protein adsorption and also the highest mobility. This can be attributed to a better implementation of the ZI groups on the surface and less ZI groups in the particle interior. At the same time, MMA and EMA probably allow for a "softer" particle surface because of dangling polymer loops, contributing steric repulsion to protein adsorption.[36] The observed high mobility of our ZI-bearing particles in the cytosol, notably in comparison with PEGylated NPs, indicates that the ZI groups led to the formation of a very thin shell, capable of resisting protein adsorption.

CONCLUSIONS

In this work, we showed how the design of hydrophobic statistical copolymers bearing ZI and charged groups can be used to assemble very small and bright dye-loaded polymer NPs. For this, we combined different hydrophobic alkylmethacrylate monomers with sulfobetaine- and sulfonate-bearing methacrylate monomers. These polymers were then used to assemble dye-loaded polymer NPs, encapsulating high amounts of the salt of a rhodamine derivative with a hydrophobic bulky counterion. The resulting NPs had sizes from 10 to 35 nm, and even 11 nm NPs reached a fluorescence brightness 10 times higher than that of corresponding QDs. About 10% of ZI groups were sufficient to render these particles stable over a wide range of salt concentrations and pH values as well as resistant to protein adsorption. The high fluorescence brightness of these particles made it possible to monitor their behavior at the single-particle level, showing that the optimized particles diffuse freely within the cytosol of living cells. For equivalent core size the ZI particles showed a higher mobility than the corresponding PEGylated NPs. In consequence, the developed zwitterion approach for dye-loaded polymer NPs opens the route to bright labels and probes for sensing and imaging of single biomolecules at work in living cells with very high spatial and temporal resolution.

MATERIALS AND METHODS

Materials. MMA (99%, M55909), methacrylic acid (99%, 155 721), 3-sulfopropyl methacrylate potassium salt (99%, 251 658) and 2-(*N*-3-sulfopropyl-*N*,*N*-dimethyl ammonium)ethyl methacrylate (99%, 537 284) were purchased from Sigma-Aldrich. Dimethylsulfoxide (DMSO, analytical grade) was obtained from Fisher Scientific. Milli-Q water (Millipore), acetonitrile (≥99.9%, Sigma-Aldrich), and methanol (≥99.9%, Carlo Erba reagents) were used for preparation of NPs. Dichloromethane (≥99.8%) was from Carlo Erba and methanol (HPLC grade) from VWR. 6-Carboxy-tetramethylrhodamine (TMR from Sigma-Aldrich), phosphate buffered saline (PBS, Fisher Scientific), FBS (Lonza) were used for the stability study. Monomers were purified using column chromatography or re-crystallization. Azobis isobutyronitrile (Sigma-Aldrich, ≥98%) was recrystallized twice from ethanol. The other compounds were used as received. R18/F5-TPB was synthesized from rhodamine B octadecyl ester perchlorate (Sigma-Aldrich, >98.0%) and lithium tetrakis-(pentafluorophenyl)borate ethyl etherate (Alfa Aesar, 97%) through ion exchange followed by purification through column chromatography as described previously.[13,69]

Polymer Synthesis. *General Procedure.* The different polymers were synthesized through free radical polymerization. The different monomers were all dissolved in degassed DMSO and mixed at the desired ratio. 0.01 equiv of AIBN were added and the round bottom flask was placed in an oil bath preheated to 70 °C. Once the conversion reached 25%, the reaction was stopped and the polymers reprecipitated twice in methanol and/or water. After drying, the polymers were characterized through NMR and, where possible, size exclusion chromatography (SEC). As an example, the synthesis of PMMA−ZI−SO_3H is given:

Poly(methyl methacrylate-co-3-sulfopropyl methacrylate-co-2-(N-3-sulfopropyl-N,N-dimethyl ammonium)ethyl methacrylate) (PMMA−ZI−SO_3H). MMA, 2-(*N*-3-sulfopropyl-*N*,*N*-dimethyl ammonium)ethyl methacrylate, and 3-sulfopropyl methacrylate potassium salt were dissolved in degassed DMSO at a concentration of 2 M. The three solutions were then mixed in a 50 mL two-neck round bottom flask equipped with a stirring bar at the desired ratio to give a total volume of 20 mL. The mixture was degassed by bubbling argon for 5 min and placed under argon atmosphere. 0.01 equiv of AIBN in DMSO (40 mg/mL) were added and the round-bottom flask was placed in an oil bath preheated to 70 °C. At regular intervals, samples were drawn, dissolved in DMSO-d_6, and analyzed by NMR. Once the conversion reached 25%, the reaction was stopped by quickly cooling it to RT. The reaction mixture was then added dropwise to methanol, or, for higher percentages of the charged and ZI monomers, to water. After filtration, the precipitate was redissolved in a small amount of acetonitrile (when needed with a small amount of methanol) and reprecipitated twice in methanol (water for highest percentages). The obtained polymer was dried under vacuum. ^{1}H NMR (400 MHz, DMSO-d_6, δ): 4.36 (br, 0.04−0.2 H), 3.96 (br s, 0.02−0.04 H), 3.55 (m, 3.4 H), 3.13 (br, 0.12−0.6 H), 2.45 (br, covered by the solvent peak), 2.04 (br, 0.04−0.2 H), 2.00−0.30 (m, 6 H). The fraction obtained of ZI and SO_3H groups was based on the peaks at 4.36 and 3.97 ppm, respectively (feed: obtained): ZI 10%: 10.2%—SO_3H 1%: 1.4%; ZI 10%: 11%—SO_3H 2%: 2.8%. Molecular weight by SEC: 1% SO_3H: M_w = 51 200, M_w/M_n = 1.58; 1% ZI: M_w = 43 100, M_w/M_n = 1.14. For polymers with higher amounts of ZI monomers, no suitable solvent systems for SEC were available.

Poly(ethyl methacrylate-co-3-sulfopropyl methacrylate-co-2-(N-3-sulfopropyl-N,N-dimethyl ammonium)ethyl methacrylate) (PEMA−ZI−SO_3H). ^{1}H NMR (400 MHz, MeOD, δ): 4.50 (br, 0.2 H), 4.34−3.92 (m, 2.02 H), 3.81 (br, 0.2 H), 3.70 (br, 0.2 H), 3.29

DOI: 10.1021/acsami.9b15396
ACS Appl. Mater. Interfaces XXXX, XXX, XXX−XXX

(br, partial covered by the solvent peak), 2.92 (br, 0.2 H), 2.31 (br, 0.2 H), 2.23−0.5 (m, 9 H). Fraction obtained of ZI groups based on the peak at 4.50 ppm: 10.3%.

Poly(propyl methacrylate-co-3-sulfopropyl methacrylate-co-2-(N-3-sulfopropyl-N,N-dimethyl ammonium)ethyl methacrylate) (PPMA−ZI−SO_3H). ^{1}H NMR (400 MHz, MeOD, δ): 4.50 (br, 0.2 H), 4.29−3.54 (m, 2.42 H), 3.29 (br, partial covered by the solvent peak), 2.92 (br, 0.2 H), 2.31 (br, 0.2 H), 2.23−0.5 (m, 11 H).

Fraction obtained of ZI groups based on the peak at 4.50 ppm: 9.4%.

Poly(butyl methacrylate-co-3-sulfopropyl methacrylate-co-2-(N-3-sulfopropyl-N,N-dimethyl ammonium)ethyl methacrylate) (PBMA−ZI−SO_3H). ^{1}H NMR (400 MHz, $CDCl_3$, δ): 4.40 (br, 0.2H), 4.30−3.55 (m, 2.42 H), 3.33 (br, 0.6 H), 2.99 (br, 0.2 H), 2.36 (br, 0.2 H), 2.28−0.4 (m, 13 H). Fraction obtained of ZI groups based on the peak at 4.40 ppm: 8.3%.

Poly(methyl methacrylate-co-3-sulfopropyl methacrylate) (PMMA−SO_3H). ^{1}H NMR (400 MHz, DMSO-d_6, δ): 3.97 (br s, 0.02−0.04 H), 3.57 (s, 3 H), 2.45 (m, partially covered by the solvent peak), 2.1−0.5 (m, 6 H). Fraction of SO_3H groups based on the peak at 3.97 ppm (feed: obtained): SO_3H 1%: 1.1%; SO_3H 2%: 2.3%.

Preparation of NPs. Stock solutions of copolymers were prepared at a concentration of 10 g L^{-1} in acetonitrile (20 vol % methanol for ZI polymers). These solutions were diluted at 2 g L^{-1} in the corresponding solvent containing 1, 10, or 20 wt % of R18/F5-TPB (relative to the polymer). This solution was quickly added to a 10-fold volume excess of water, under shaking (Thermomixer comfort, Eppendorf, 1000 rpm, at 21 °C), followed by a second dilution in water.

Characterization of NPs. *Absorption and Emission Spectra.* Absorption and emission spectra were recorded on a Cary 4000 Scan ultraviolet−visible spectrophotometer (Varian) and on a FS5 Spectrofluorometer (Edinburgh Instruments) equipped with a thermostated cell compartment, respectively. The excitation wavelength was set to 530 nm and emission was recorded from 540 to 750 nm. QYs were calculated using rhodamine 101 in ethanol as reference (QY = 0.9).[70]

Transmission Electron microscopy. NP solution (5 μL) was deposited onto carbon-coated copper−rhodium electron microscopy grids following amylamine glow-discharge. They were then treated for 20 s with a 2% uranyl acetate solution for staining. The obtained grids were observed using a Philips CM120 transmission electron microscope equipped with a LaB6 filament and operating at 100 kV. The acquisition of areas of interest was recorded with a Peltier-cooled CCD camera (model 794, Gatan, Pleasanton, CA). Images were analyzed using Fiji software.

Fluorescence Correlation Spectroscopy. Measurements were performed on a home-built confocal setup based on a Nikon inverted microscope with a Nikon 60× 1.2 NA water immersion objective. Excitation was provided by a continuous wave laser diode (532 nm, Oxxius) and photons were detected with a fibered avalanche photodiode (APD SPCM-AQR-14-FC, PerkinElmer) connected to an online hardware correlator (ALV7000-USB, ALV GmbH, Germany). The solution of NPs containing 1 wt % dyes were diluted two times before depositing 200 μL on 96-well optical-bottom plates for measurements. The NP stability in the presence of salts and proteins was investigated by adding drop-by-drop 50 vol % of 10-fold PBS (10×), FBS, or water to the solutions of NPs in low-binding 1.5 mL Eppendorf tubes. The data were recorded 5 min after addition and then analyzed using the PyCorrFit software. For FCS measurements, which apply relatively high excitation powers in the focal spot, a reduced dye-loading was used in order to avoid saturation phenomena involving triplet states, which would have made the analysis more complicated.

Cellular Experiments. HeLa cells were grown in Dulbecco's modified Eagle medium (without phenolred, Gibco-Invitrogen), supplemented with 10% FBS (Lonza), L-glutamine, and 1% antibiotic solution (penicillin-streptomycin, Gibco-Invitrogen) at 37 °C in humidified atmosphere containing 5% CO_2. The cells were seeded onto round microscope cover glasses (diameter 18 mm) deposited in six-well plates at a density of 125 × 10^3 cells/well 24 h before the microinjection.

Microinjection of NPs and Cellular Imaging. For microinjection experiments, subconfluent HeLa cells plated on glass coverslips were mounted in a Ludin Chamber (Life Imaging Services, Basel, Switzerland). The cells were then placed on a Leica DMIRE 2 microscope and solutions of the different NPs at particle concentrations of 0.5−2 nM were microinjected into the perinuclear region of the cells, using a FemtoJet/InjectMan NI2 microinjector (Eppendorf). Image sequences were then acquired either on the same setup (100× Plan APO 1.4 NA objective, Xenon-source, and Photometrics Prime camera) or on an iMIC microscope (Till Photonics) equipped with a Mutli-LED Spectra X (Lumencor), an Olympus 60× TIRFM (1.45 NA) objective, and a Flash 4 V2+ camera (Hamamatsu) after transfer of the samples. Live cells were maintained at 37 °C in a 5% CO_2 humidified atmosphere using an environmental control system (Life Imaging Services). Time-lapse movies were recorded over 60 s with a frame rate of 50 ms and binning 2. They were then analyzed using the ImageJ software (National Institutes of Health, USA). For single-particle tracking, time-lapse movies were recorded for over 30 s with a frame rate of 43 ms for the Imic microscope or 50 ms for the Leica DMIRE 2 microscope and binning 1. The trajectories were obtained using the TrackMate plugin for Fiji.[71] Then, MSD curves were plotted and slopes extracted from the MSD curves with a MATLAB script for particle tracking analysis. At least 50 trajectories from at least three different cells were used for analysis.

■ ASSOCIATED CONTENT

Supporting Information

The Supporting Information is available free of charge at https://pubs.acs.org/doi/10.1021/acsami.9b15396.

Results and details of synthesis, FCS, DLS, quantum yield measurements, dialysis, and particle tracking (PDF)

■ AUTHOR INFORMATION

Corresponding Authors

*E-mail: andrey.klymchenko@unista.fr (A.S.K.).

*E-mail: reisch@unista.fr (A.R.).

ORCID

Andrey S. Klymchenko: 0000-0002-2423-830X

Andreas Reisch: 0000-0003-1154-7637

Author Contributions

The paper was written through contributions of all the authors. All the authors have given approval to the final version of the paper.

Funding

Agence National de Recherche JC/JC grant "Supertrack" ANR-16-CE09-0007, European Research Council ERC Consolidator grant BrightSens 648528.

Notes

The authors declare no competing financial interest.

■ ACKNOWLEDGMENTS

This work was supported by the Agence National de Recherche JC/JC grant "Supertrack" ANR-16-CE09-0007 and by the European Research Council ERC Consolidator grant BrightSens 648528. The authors thank C. Ruhlmann and C. Crucifix from the FRISBI platform (ANR-10-INBS-05) for help with electron microscopy, M. Legros and C. Foussat for SEC, and Oleksii Dukhno for helpful discussions on single-particle tracking analysis.

DOI: 10.1021/acsami.9b15396
ACS Appl. Mater. Interfaces XXXX, XXX, XXX−XXX

REFERENCES

(1) Shashkova, S.; Leake, M. C. Single-Molecule Fluorescence Microscopy Review: Shedding New Light on Old Problems. *Biosci. Rep.* **2017**, *37*, BSR20170031.

(2) Nelson, A. J.; Hess, S. T. Localization Microscopy: Mapping Cellular Dynamics with Single Molecules. *J. Microsc.* **2014**, *254*, 1−8.

(3) Kusumi, A.; Tsunoyama, T. A.; Hirosawa, K. M.; Kasai, R. S.; Fujiwara, T. K. Tracking Single Molecules at Work in Living Cells. *Nat. Chem. Biol.* **2014**, *10*, 524−532.

(4) Deschout, H.; Zanacchi, F. C.; Mlodzianoski, M.; Diaspro, A.; Bewersdorf, J.; Hess, S. T.; Braeckmans, K. Precisely and Accurately Localizing Single Emitters in Fluorescence Microscopy. *Nat. Methods* **2014**, *11*, 253−266.

(5) Pinaud, F.; Clarke, S.; Sittner, A.; Dahan, M. Probing Cellular Events, One Quantum Dot at a Time. *Nat. Methods* **2010**, *7*, 275−285.

(6) Pierobon, P.; Cappello, G. Quantum Dots to Tail Single Bio-Molecules inside Living Cells. *Adv. Drug Delivery Rev.* **2012**, *64*, 167−178.

(7) Bonacchi, S.; Genovese, D.; Juris, R.; Montalti, M.; Prodi, L.; Rampazzo, E.; Zaccheroni, N. Luminescent Silica Nanoparticles: Extending the Frontiers of Brightness. *Angew. Chem., Int. Ed.* **2011**, *50*, 4056−4066.

(8) Liu, H.; Dong, C.; Ren, J. Tempo-Spatially Resolved Scattering Correlation Spectroscopy under Dark-Field Illumination and Its Application to Investigate Dynamic Behaviors of Gold Nanoparticles in Live Cells. *J. Am. Chem. Soc.* **2014**, *136*, 2775−2785.

(9) Genin, E.; Gao, Z.; Varela, J. A.; Daniel, J.; Bsaibess, T.; Gosse, I.; Groc, L.; Cognet, L.; Blanchard-Desce, M. Nanoparticles: "Hyper-Bright" Near-Infrared Emitting Fluorescent Organic Nanoparticles for Single Particle Tracking (Adv. Mater. 14/2014). *Adv. Mater.* **2014**, *26*, 2257.

(10) Reisch, A.; Klymchenko, A. S. Fluorescent Polymer Nanoparticles Based on Dyes: Seeking Brighter Tools for Bioimaging. *Small* **2016**, *12*, 1968−1992.

(11) Gu, B.; Yong, K.-T.; Liu, B. Strategies to Overcome the Limitations of AIEgens in Biomedical Applications. *Small Methods* **2018**, *2*, 1700392.

(12) Li, K.; Qin, W.; Ding, D.; Tomczak, N.; Geng, J.; Liu, R.; Liu, J.; Zhang, X.; Liu, H.; Liu, B.; Tang, B. Z. Photostable Fluorescent Organic Dots with Aggregation-Induced Emission (AIE Dots) for Noninvasive Long-Term Cell Tracing. *Sci. Rep.* **2013**, *3*, 1150.

(13) Reisch, A.; Didier, P.; Richert, L.; Oncul, S.; Arntz, Y.; Mély, Y.; Klymchenko, A. S. Collective Fluorescence Switching of Counterion-Assembled Dyes in Polymer Nanoparticles. *Nat. Commun.* **2014**, *5*, 4089.

(14) Trofymchuk, K.; Reisch, A.; Didier, P.; Fras, F.; Gilliot, P.; Mely, Y.; Klymchenko, A. S. Giant Light-Harvesting Nanoantenna for Single-Molecule Detection in Ambient Light. *Nat. Photonics* **2017**, *11*, 657.

(15) Melnychuk, N.; Klymchenko, A. S. DNA-Functionalized Dye-Loaded Polymeric Nanoparticles: Ultrabright FRET Platform for Amplified Detection of Nucleic Acids. *J. Am. Chem. Soc.* **2018**, *140*, 10856−10865.

(16) Li, K.; Liu, B. Polymer-Encapsulated Organic Nanoparticles for Fluorescence and Photoacoustic Imaging. *Chem. Soc. Rev.* **2014**, *43*, 6570−6597.

(17) Sahl, S. J.; Hell, S. W.; Jakobs, S. Fluorescence Nanoscopy in Cell Biology. *Nat. Rev. Mol. Cell Biol.* **2017**, *18*, 685−701.

(18) Etoc, F.; Balloul, E.; Vicario, C.; Normanno, D.; Liße, D.; Sittner, A.; Piehler, J.; Dahan, M.; Coppey, M. Non-Specific Interactions Govern Cytosolic Diffusion of Nanosized Objects in Mammalian Cells. *Nat. Mater.* **2018**, *17*, 740−746.

(19) Xu, M.; Soliman, M. G.; Sun, X.; Pelaz, B.; Feliu, N.; Parak, W. J.; Liu, S. How Entanglement of Different Physicochemical Properties Complicates the Prediction of in Vitro and in Vivo Interactions of Gold Nanoparticles. *ACS Nano* **2018**, *12*, 10104−10113.

(20) Reisch, A.; Heimburger, D.; Ernst, P.; Runser, A.; Didier, P.; Dujardin, D.; Klymchenko, A. S. Protein-Sized Dye-Loaded Polymer Nanoparticles for Free Particle Diffusion in Cytosol. *Adv. Funct. Mater.* **2018**, *28*, 1805157.

(21) Luby-Phelps, K. Cytoarchitecture and Physical Properties of Cytoplasm: Volume, Viscosity, Diffusion, Intracellular Surface Area. *Int. Rev. Cytol.* **2000**, *192*, 189−221.

(22) Parry, B. R.; Surovtsev, I. V.; Cabeen, M. T.; O'Hern, C. S.; Dufresne, E. R.; Jacobs-Wagner, C. The Bacterial Cytoplasm Has Glass-like Properties and Is Fluidized by Metabolic Activity. *Cell* **2014**, *156*, 183−194.

(23) Tonga, G. Y.; Saha, K.; Rotello, V. M. 25th Anniversary Article: Interfacing Nanoparticles and Biology: New Strategies for Biomedicine. *Adv. Mater.* **2014**, *26*, 359−370.

(24) Walkey, C. D.; Chan, W. C. W. Understanding and Controlling the Interaction of Nanomaterials with Proteins in a Physiological Environment. *Chem. Soc. Rev.* **2012**, *41*, 2780−2799.

(25) Monopoli, M. P.; Åberg, C.; Salvati, A.; Dawson, K. A. Biomolecular Coronas Provide the Biological Identity of Nanosized Materials. *Nat. Nanotechnol.* **2012**, *7*, 779−786.

(26) Docter, D.; Westmeier, D.; Markiewicz, M.; Stolte, S.; Knauer, S. K.; Stauber, R. H. The Nanoparticle Biomolecule Corona: Lessons Learned − Challenge Accepted? *Chem. Soc. Rev.* **2015**, *44*, 6094−6121.

(27) Ke, P. C.; Lin, S.; Parak, W. J.; Davis, T. P.; Caruso, F. A Decade of the Protein Corona. *ACS Nano* **2017**, *11*, 11773−11776.

(28) Jokerst, J. V.; Lobovkina, T.; Zare, R. N.; Gambhir, S. S. Nanoparticle PEGylation for Imaging and Therapy. *Nanomedicine* **2011**, *6*, 715−728.

(29) Suk, J. S.; Xu, Q.; Kim, N.; Hanes, J.; Ensign, L. M. PEGylation as a Strategy for Improving Nanoparticle-Based Drug and Gene Delivery. *Adv. Drug Delivery Rev.* **2016**, *99*, 28−51.

(30) Rabanel, J.-M.; Hildgen, P.; Banquy, X. Assessment of PEG on Polymeric Particles Surface, a Key Step in Drug Carrier Translation. *J. Controlled Release* **2014**, *185*, 71−87.

(31) Estephan, Z. G.; Schlenoff, P. S.; Schlenoff, J. B. Zwitteration As an Alternative to PEGylation. *Langmuir* **2011**, *27*, 6794−6800.

(32) Reisch, A.; Runser, A.; Arntz, Y.; Mély, Y.; Klymchenko, A. S. Charge-Controlled Nanoprecipitation as a Modular Approach to Ultrasmall Polymer Nanocarriers: Making Bright and Stable Nanoparticles. *ACS Nano* **2015**, *9*, 5104−5116.

(33) Bangham, A. D. Correlation between Surface Charge and Coagulant Action of Phospholipids. *Nature* **1961**, *192*, 1197−1198.

(34) García, K. P.; Zarschler, K.; Barbaro, L.; Barreto, J. A.; O'Malley, W.; Spiccia, L.; Stephan, H.; Graham, B. Zwitterionic-Coated "Stealth" Nanoparticles for Biomedical Applications: Recent Advances in Countering Biomolecular Corona Formation and Uptake by the Mononuclear Phagocyte System. *Small* **2014**, *10*, 2516−2529.

(35) Schlenoff, J. B. Zwitteration: Coating Surfaces with Zwitterionic Functionality to Reduce Nonspecific Adsorption. *Langmuir* **2014**, *30*, 9625−9636.

(36) Jeon, S. I.; Lee, J. H.; Andrade, J. D.; De Gennes, P. G. Protein—surface Interactions in the Presence of Polyethylene Oxide. *J. Colloid Interface Sci.* **1991**, *142*, 149−158.

(37) Tasso, M.; Giovanelli, E.; Zala, D.; Bouccara, S.; Fragola, A.; Hanafi, M.; Lenkei, Z.; Pons, T.; Lequeux, N. Sulfobetaine−Vinylimidazole Block Copolymers: A Robust Quantum Dot Surface Chemistry Expanding Bioimaging's Horizons. *ACS Nano* **2015**, *9*, 11479−11489.

(38) Muro, E.; Pons, T.; Lequeux, N.; Fragola, A.; Sanson, N.; Lenkei, Z.; Dubertret, B. Small and Stable Sulfobetaine Zwitterionic Quantum Dots for Functional Live-Cell Imaging. *J. Am. Chem. Soc.* **2010**, *132*, 4556−4557.

(39) Huang, C.-J.; Chu, S.-H.; Wang, L.-C.; Li, C.-H.; Lee, T. R. Bioinspired Zwitterionic Surface Coatings with Robust Photostability and Fouling Resistance. *ACS Appl. Mater. Interfaces* **2015**, *7*, 23776−23786.

(40) Debayle, M.; Balloul, E.; Dembele, F.; Xu, X.; Hanafi, M.; Ribot, F.; Monzel, C.; Coppey, M.; Fragola, A.; Dahan, M.; Pons, T.; Lequeux, N. Zwitterionic Polymer Ligands: An Ideal Surface Coating

DOI: 10.1021/acsami.9b15396
ACS Appl. Mater. Interfaces XXXX, XXX, XXX−XXX

to Totally Suppress Protein-Nanoparticle Corona Formation? *Biomaterials* **2019**, *219*, 119357.
(41) Rosen, J. E.; Gu, F. X. Surface Functionalization of Silica Nanoparticles with Cysteine: A Low-Fouling Zwitterionic Surface. *Langmuir* **2011**, *27*, 10507−10513.
(42) Estephan, Z. G.; Schlenoff, J. B. Zwitterion Siloxane to Passivate Silica against Nonspecific Protein Adsorption. *Methods Mol. Biol.* **2013**, *1025*, 201−205.
(43) Rouhana, L. L.; Jaber, J. A.; Schlenoff, J. B. Aggregation-Resistant Water-Soluble Gold Nanoparticles. *Langmuir* **2007**, *23*, 12799−12801.
(44) Moyano, D. F.; Saha, K.; Prakash, G.; Yan, B.; Kong, H.; Yazdani, M.; Rotello, V. M. Fabrication of Corona-Free Nanoparticles with Tunable Hydrophobicity. *ACS Nano* **2014**, *8*, 6748−6755.
(45) Zhan, N.; Palui, G.; Safi, M.; Ji, X.; Mattoussi, H. Multidentate Zwitterionic Ligands Provide Compact and Highly Biocompatible Quantum Dots. *J. Am. Chem. Soc.* **2013**, *135*, 13786−13795.
(46) Estephan, Z. G.; Jaber, J. A.; Schlenoff, J. B. Zwitterion-Stabilized Silica Nanoparticles: Toward Nonstick Nano. *Langmuir* **2010**, *26*, 16884−16889.
(47) Dong, Z.; Mao, J.; Yang, M.; Wang, D.; Bo, S.; Ji, X. Phase Behavior of Poly(Sulfobetaine Methacrylate)-Grafted Silica Nanoparticles and Their Stability in Protein Solutions. *Langmuir* **2011**, *27*, 15282−15291.
(48) Giovanelli, E.; Muro, E.; Sitbon, G.; Hanafi, M.; Pons, T.; Dubertret, B.; Lequeux, N. Highly Enhanced Affinity of Multidentate versus Bidentate Zwitterionic Ligands for Long-Term Quantum Dot Bioimaging. *Langmuir* **2012**, *28*, 15177−15184.
(49) Salvage, J. P.; Rose, S. F.; Phillips, G. J.; Hanlon, G. W.; Lloyd, A. W.; Ma, I. Y.; Armes, S. P.; Billingham, N. C.; Lewis, A. L. Novel Biocompatible Phosphorylcholine-Based Self-Assembled Nanoparticles for Drug Delivery. *J. Controlled Release* **2005**, *104*, 259−270.
(50) John, J. V.; Uthaman, S.; Augustine, R.; Manickavasagam Lekshmi, K.; Park, I.-K.; Kim, I. Biomimetic PH/Redox Dual Stimuli-Responsive Zwitterionic Polymer Block Poly(L-Histidine) Micelles for Intracellular Delivery of Doxorubicin into Tumor Cells. *J. Polym. Sci., Part A: Polym. Chem.* **2017**, *55*, 2061−2070.
(51) Xie, G.; Ma, C.; Zhang, X.; Liu, H.; Guo, X.; Yang, L.; Li, Y.; Wang, K.; Wei, Y. Biocompatible Zwitterionic Phosphorylcholine Polymers with Aggregation-Induced Emission Feature. *Colloids Surf., B* **2017**, *157*, 166−173.
(52) Huang, P.; Liu, J.; Wang, W.; Li, C.; Zhou, J.; Wang, X.; Deng, L.; Kong, D.; Liu, J.; Dong, A. Zwitterionic Nanoparticles Constructed with Well-Defined Reduction-Responsive Shell and PH-Sensitive Core for "Spatiotemporally Pinpointed" Drug Delivery. *ACS Appl. Mater. Interfaces* **2014**, *6*, 14631−14643.
(53) Ishihara, K.; Iwasaki, Y.; Nakabayashi, N. Polymeric Lipid Nanosphere Consisting of Water-Soluble Poly(2-Methacryloyloxyethyl Phosphorylcholine-*Co-n*-Butyl Methacrylate). *Polym. J.* **1999**, *31*, 1231−1236.
(54) Goda, T.; Goto, Y.; Ishihara, K. Cell-Penetrating Macromolecules: Direct Penetration of Amphipathic Phospholipid Polymers across Plasma Membrane of Living Cells. *Biomaterials* **2010**, *31*, 2380−2387.
(55) Morimoto, N.; Wakamura, M.; Muramatsu, K.; Toita, S.; Nakayama, M.; Shoji, W.; Suzuki, M.; Winnik, F. M. Membrane Translocation and Organelle-Selective Delivery Steered by Polymeric Zwitterionic Nanospheres. *Biomacromolecules* **2016**, *17*, 1523−1535.
(56) Rosiuk, V.; Runser, A.; Klymchenko, A.; Reisch, A. Controlling Size and Fluorescence of Dye-Loaded Polymer Nanoparticles through Polymer Design. *Langmuir* **2019**, *35*, 7009−7017.
(57) Saad, W. S.; Prud'homme, R. K. Principles of Nanoparticle Formation by Flash Nanoprecipitation. *Nano Today* **2016**, *11*, 212−227.
(58) Lepeltier, E.; Bourgaux, C.; Couvreur, P. Nanoprecipitation and the "Ouzo Effect": Application to Drug Delivery Devices. *Adv. Drug Delivery Rev.* **2014**, *71*, 86−97.
(59) Andreiuk, B.; Reisch, A.; Bernhardt, E.; Klymchenko, A. S. Fighting Aggregation-Caused Quenching and Leakage of Dyes in Fluorescent Polymer Nanoparticles: Universal Role of Counterion. *Chem.—Asian J.* **2019**, *14*, 836−846.
(60) Andreiuk, B.; Reisch, A.; Pivovarenko, V. G.; Klymchenko, A. S. An Aluminium-Based Fluorinated Counterion for Enhanced Encapsulation and Emission of Dyes in Biodegradable Polymer Nanoparticles. *Mater. Chem. Front.* **2017**, *1*, 2309−2316.
(61) Koynov, K.; Butt, H.-J. Fluorescence Correlation Spectroscopy in Colloid and Interface Science. *Curr. Opin. Colloid Interface Sci.* **2012**, *17*, 377−387.
(62) Shulov, I.; Oncul, S.; Reisch, A.; Arntz, Y.; Collot, M.; Mely, Y.; Klymchenko, A. S. Fluorinated Counterion-Enhanced Emission of Rhodamine Aggregates: Ultrabright Nanoparticles for Bioimaging and Light-Harvesting. *Nanoscale* **2015**, *7*, 18198−18210.
(63) Trofymchuk, K.; Valanciunaite, J.; Andreiuk, B.; Reisch, A.; Collot, M.; Klymchenko, A. S. BODIPY-Loaded Polymer Nanoparticles: Chemical Structure of Cargo Defines Leakage from Nanocarrier in Living Cells. *J. Mater. Chem. B* **2019**, *7*, 5199−5210.
(64) Höfling, F.; Franosch, T. Anomalous Transport in the Crowded World of Biological Cells. *Rep. Prog. Phys.* **2013**, *76*, 046602.
(65) Di Rienzo, C.; Gratton, E.; Beltram, F.; Cardarelli, F. Fast Spatiotemporal Correlation Spectroscopy to Determine Protein Lateral Diffusion Laws in Live Cell Membranes. *Proc. Natl. Acad. Sci. U.S.A.* **2013**, *110*, 12307−12312.
(66) Ruthardt, N.; Lamb, D. C.; Bräuchle, C. Single-Particle Tracking as a Quantitative Microscopy-Based Approach to Unravel Cell Entry Mechanisms of Viruses and Pharmaceutical Nanoparticles. *Mol. Ther.* **2011**, *19*, 1199−1211.
(67) Reisch, A.; Trofymchuk, K.; Runser, A.; Fleith, G.; Rawiso, M.; Klymchenko, A. S. Tailoring Fluorescence Brightness and Switching of Nanoparticles through Dye Organization in the Polymer Matrix. *ACS Appl. Mater. Interfaces* **2017**, *9*, 43030−43042.
(68) Zheng, J.; He, Y.; Chen, S.; Li, L.; Bernards, M. T.; Jiang, S. Molecular Simulation Studies of the Structure of Phosphorylcholine Self-Assembled Monolayers. *J. Chem. Phys.* **2006**, *125*, 174714.
(69) Andreiuk, B.; Reisch, A.; Lindecker, M.; Follain, G.; Peyriéras, N.; Goetz, J. G.; Klymchenko, A. S. Fluorescent Polymer Nanoparticles for Cell Barcoding In Vitro and In Vivo. *Small* **2017**, *13*, 1701582.
(70) Würth, C.; Geissler, D.; Behnke, T.; Kaiser, M.; Resch-Genger, U. Critical Review of the Determination of Photoluminescence Quantum Yields of Luminescent Reporters. *Anal. Bioanal. Chem.* **2015**, *407*, 59−78.
(71) Tinevez, J.-Y.; Perry, N.; Schindelin, J.; Hoopes, G. M.; Reynolds, G. D.; Laplantine, E.; Bednarek, S. Y.; Shorte, S. L.; Eliceiri, K. W. TrackMate: An Open and Extensible Platform for Single-Particle Tracking. *Methods* **2017**, *115*, 80−90.

DOI: 10.1021/acsami.9b15396
ACS Appl. Mater. Interfaces XXXX, XXX, XXX−XXX

Supporting Information for:

Zwitterionic Stealth Dye-loaded Polymer Nanoparticles for Intracellular Imaging

Anne Runser, Denis Dujardin, Pauline Ernst, Andrey S. Klymchenko, Andreas Reisch**

Laboratoire de Bioimagerie et Pathologies, CNRS UMR 7021, Université de Strasbourg, Faculté de Pharmacie, 67401 Illkirch Cedex, France.

E-mail: reisch@unista.fr; andrey.klymchenko@unista.fr

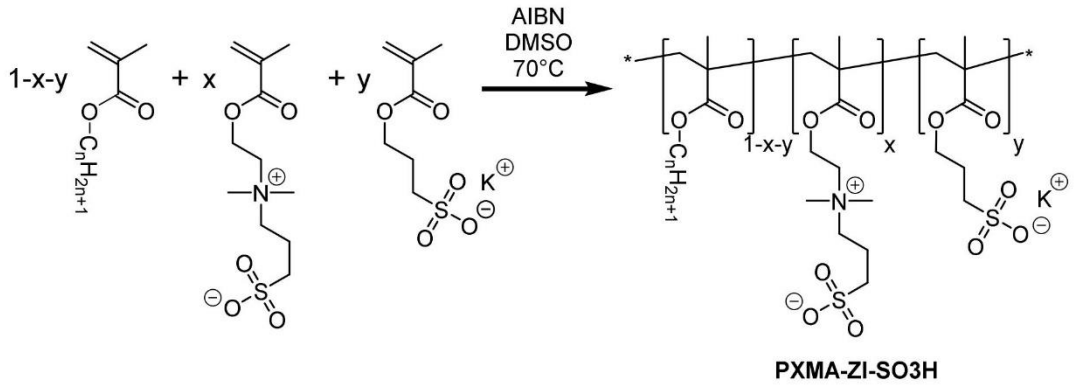

Scheme S1. Polymerization of alkylacrylate, ZI and sulfonate monomers to obtain methacrylate polymers bearing zwitterionic and charged groups.

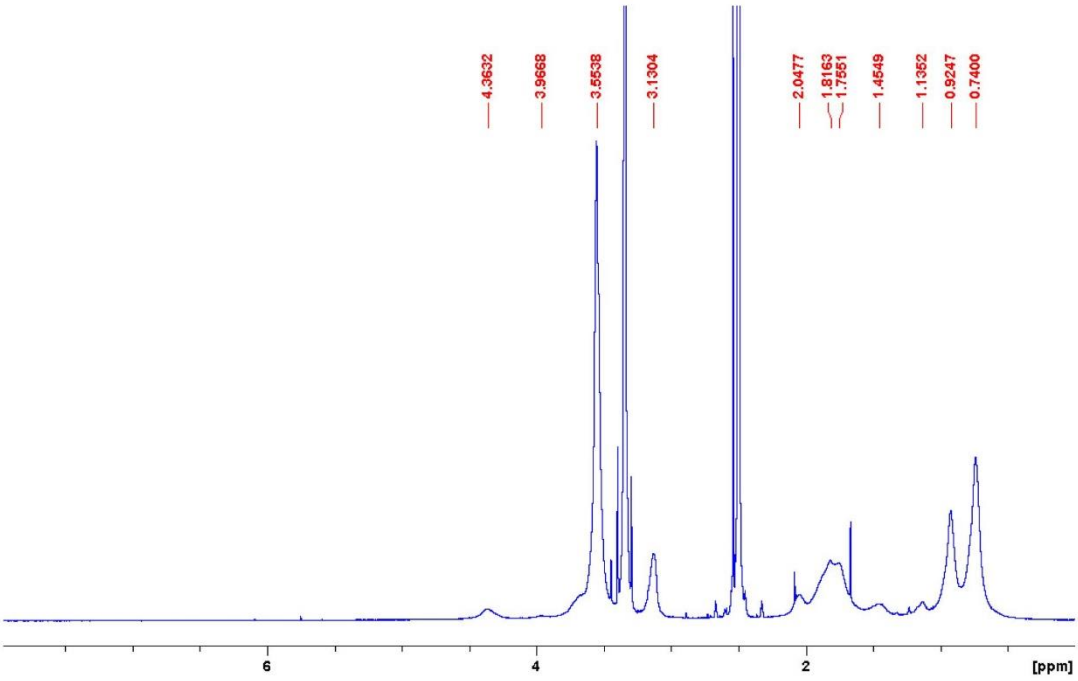

Figure S1. ^{1}H-NMR spectrum of PMMA-ZI-10%-SO_3H-1% in DMSO-d_6.

Table S1. Sizes of NPs made of different polymers as obtained from TEM, DLS, and FCS.[a]

Polymer			Size (nm)		
Main monomer	SO_3H (mol%)	ZI (mol%)	TEM[b]	DLS[b]	FCS[c]
MMA	1	-	13 ± 3	-	14 ± 1
MMA	1	10	11 ± 3	11 ± 1	15 ± 1
MMA	2	-	9 ± 3	-	14 ± 1
MMA	2	10	9 ± 2	-	13 ± 1
EMA	1	10	14 ± 3	10 ± 1	11 ± 1
PMA	1	10	22 ± 4	19 ± 2	13 ± 1
BMA	1	10	35 ± 7	31 ± 2	32 ± 4

[a] Errors correspond to width of the distribution at half maximum (FWHM) for TEM, and standard error of the mean (s.e.m.) over 3 measurements for DLS and FCS.[b] NPs prepared with 10 wt% R18/F5-TPB. [c] NPs prepared with 1 wt% R18/F5-TPB.

Table S2. Sizes of PMMA-ZI-10%-SO_3H-1% NPs at different pH values as measured by DLS.[a]

pH[b]	Mean size (nm)
3.6	14 ± 1
5.0	15 ± 1
7.4	14 ± 1
9.0	15 ± 2

[a] NPs were loaded with 10 wt% of R18/F5-TPB. [b] For adjusting the pH we used the following buffer solutions: acetate buffer for pH 3.6 and 5; phosphate buffer for pH 7.4; borate buffer for pH 9; all at 5mM.

Table S3. Zeta potential of dye-loaded NPs made from different polymers.

polymer	Zeta potential (mV)
PMMA-SO_3H-1%	-24
PMMA-ZI-10%-SO_3H-1%	-21
PEMA-ZI-10%-SO_3H-1%	-28
PPMA-ZI-10%-SO_3H-1%	-34

Table S4. FCS results: concentration, diameter and brightness obtained for the different zwitterionic NP solutions before and 5 min after addition of 10% fetal bovine serum (FBS).[a]

	ZI %	FBS addition (vol%)	Concentration (nM)	Diameter (nm)	Brightness relative to TMR
PMMA-SO_3H-2%	0	-	18.6	14.1	5.0
		10	14.7	22.6	4.3
	2	-	12.9	15.2	5.5
		10	12.2	24.6	4.4
	5	-	30.7	8.0	2.7
		10	23.3	12.4	2.5
	10	-	26.1	13.2	3.1
		10	20.2	14.6	2.9
PMMA-SO_3H-1%	0	-	17.9	14.0	6.0
		10	10.8	23.5	5.9
	10	-	14.8	14.9	5.3
		10	14.5	15.4	4.6
PEMA-SO_3H-1%	10	-	34.5	11.0	2.0
		10	26.4	14.3	2.4
PPMA-SO_3H-1%	10	-	9.6	12.5	5.8
		10	7.8	15.9	5.7
PBMA-SO_3H-1%	10	-	4.2	31.8	22.1
		10	1.6	45.5	26.4

[a] NPs prepared with 1 wt% R18/F5-TPB.

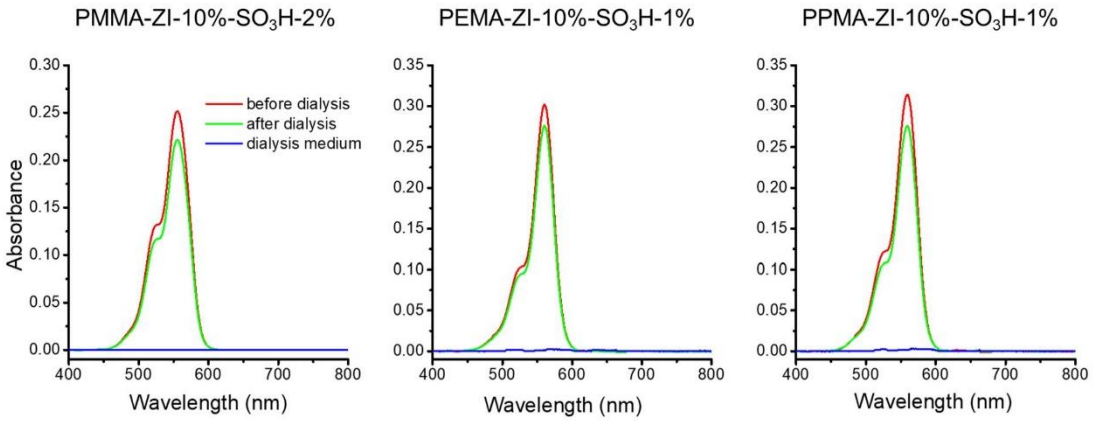

Figure S2. Absorbance spectra measured for solutions of PXMA-ZI-10%-SO_3H-1 or 2% NPs loaded with 10 wt% of R18/F5-TPB before (red) and after (green) dialysis. The blue curve corresponds to the dialysis medium after dialysis.

Table S5. Release of dye from NPs made from different polymers over 48 h.[a]

polymer	loss of R18/F5-TPB[b]
PMMA-ZI-10%-SO_3H-2%	14 %
PEMA-ZI-10%-SO_3H-1%	9 %
PPMA-ZI-10%-SO_3H-1%	12 %

[a] Release was tested by dialysis for 48 h against a 1 mM solution of β-cyclodextrin. Absorbance spectra were recorded for the NP solution before and for the NP solution and the dialysis solution after dialysis (Figure S5). [b] Relative to amount of R18/F5-TPB before dialysis.

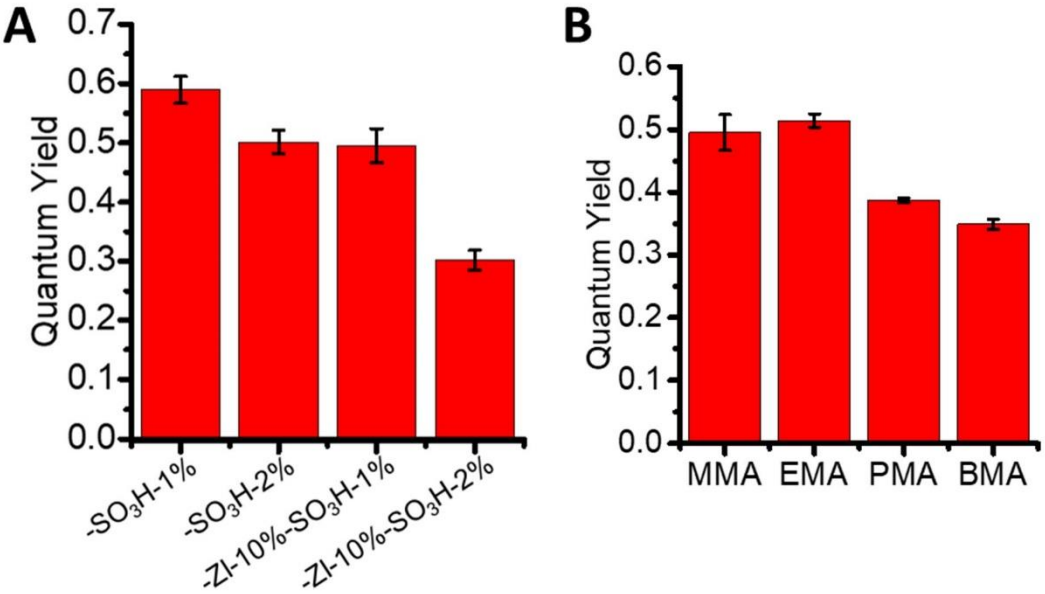

Figure S3. Quantum yield of dye-loaded NPs. NPs were made from (A) PMMA-SO_3H-1% and 2%, PMMA-ZI-10%-SO_3H-1% and 2% and (B) from PMXA-ZI-10%-SO_3H-1% with different hydrophobic monomers. They were loaded with 10 wt% R18/F5-TPB. Given are mean values from three independent measurements. The error bars correspond to SEM.

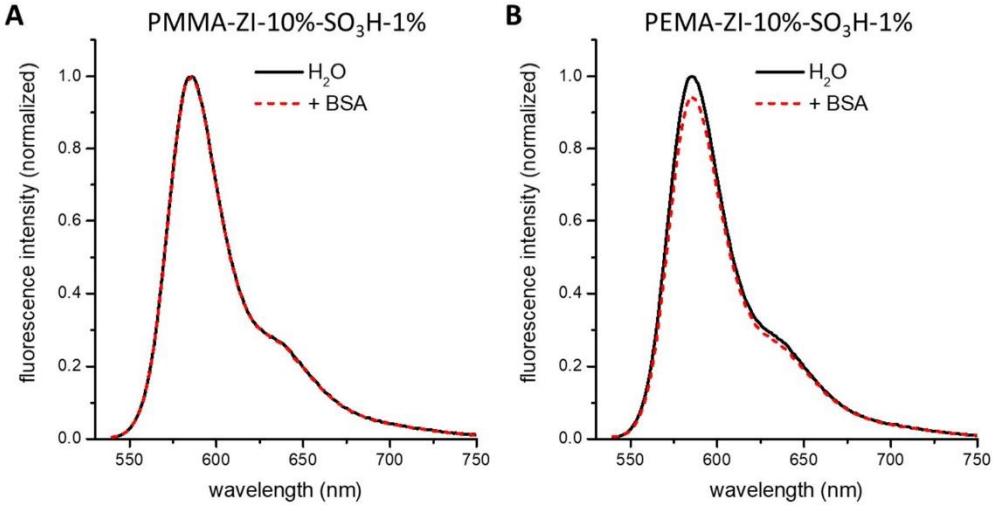

Figure S4. Fluorescence spectra of (A) PMMA-ZI-10%-SO_3H-1% and (B) PEMA-ZI-10%-SO_3H-1% NPs loaded with 10 wt% R18/F5-TPB in water and in the presence of 1 mg/mL bovine serum albumin (BSA).

Table S6. Per particle fluorescence brightness for different zwitterionic NPs loaded with 10 wt% R18/F5-TPB.[a]

Main monomer	SO_3H, (mol%)	ZI (mol%)	TEM (nm)	QY	Brightness ($M^{-1}L^{-1}$)
MMA	1	0	13 ± 3	0.58 ± 0.04	4.2×10^6
MMA	1	10	11 ± 3	0.50 ± 0.02	2.2×10^6
MMA	2	0	9 ± 3	0.50 ± 0.03	1.2×10^6
MMA	2	10	9 ± 2	0.31 ± 0.03	0.9×10^6
EMA	1	10	14 ± 3	0.51 ± 0.04	4.6×10^6
PMA	1	10	22 ± 4	0.39 ± 0.03	1.4×10^6
BMA	1	10	35 ± 7	0.35 ± 0.04	4.9×10^7

[a] Brightness was calculated as: Brightness = $N*\varepsilon_{R18}*QY$, where N is the number of fluorophores based on the loading and the NP size, ε_{R18} is the absorbance of R18 at 565 nm (125 000 $M^{-1}L^{-1}$) and QY is the measured quantum yield.

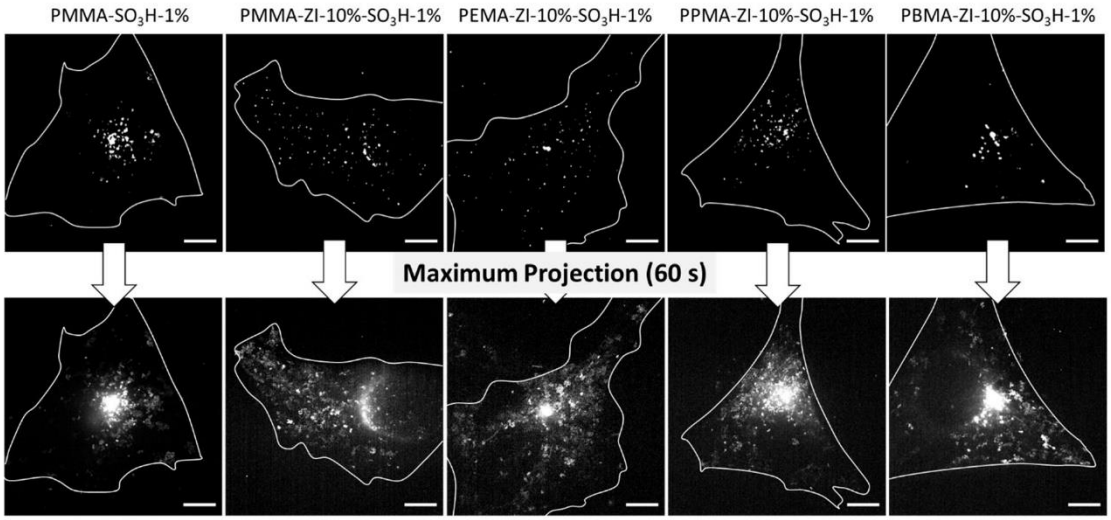

Figure S5. Approximate outline of cells obtained from phase-contrast images marked on representative epi-fluorescence micrographs of HeLa cells microinjected with different types of NPs loaded with 10 wt% R18/F5-TPB. Top: single frame (50 ms exposure); bottom: maximum projections over 60 s. Scale bars correspond to 10 µm.

Table S7. Percentage of fluorescence at the injection point to total NP fluorescence in cells microinjected with different types of NPs loaded with 10 wt% R18/F5-TPB.

polymer	Fluorescence at the injection point (%)[a]
PMMA-SO_3H-1%	39 ± 10
PMMA-ZI-10%-SO_3H-1%	6 ± 2
PEMA-ZI-10%-SO_3H-1%	10 ± 1
PPMA-ZI-10%-SO_3H-1%	7 ± 2
PBMA-ZI-10%-SO_3H-1%	35 ± 12

[a] The fluorescence in the entire cell and the fluorescence in a circle of about 5 µm around the injection point were measured for at least 3 different fields of view per condition. Given is the ratio of fluorescence at the injection point to the total fluorescence in the NP channel in the cell.

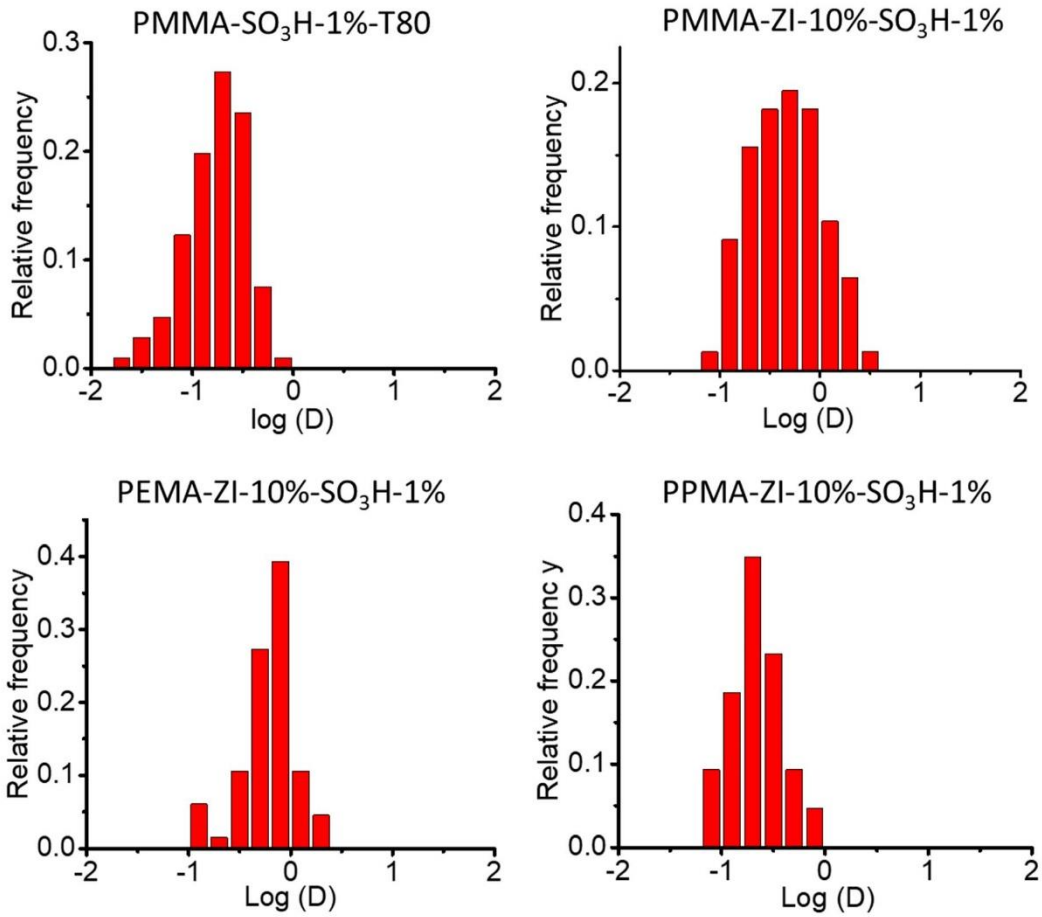

Figure S6. Distribution of diffusion coefficients ($\mu m^2.s^{-1}$) of NPs in the cytosol obtained from MSD curves.

5.2 Fonctionnalisation des nanoparticules

Le but de ces NPs est de pouvoir marquer de manière spécifique des molécules ou complexes intracellulaires comme la dynéine. Pour un marquage spécifique, ces NPs doivent être fonctionnalisées par ajout d'un ligand à leur surface capable de se lier spécifiquement à la protéine intracellulaire. Idéalement, les biomolécules d'intérêts ne devront portées qu'une seule copie du marqueur fluorescent et vice versa afin de ne pas altérer leurs fonctions et leur diffusion.

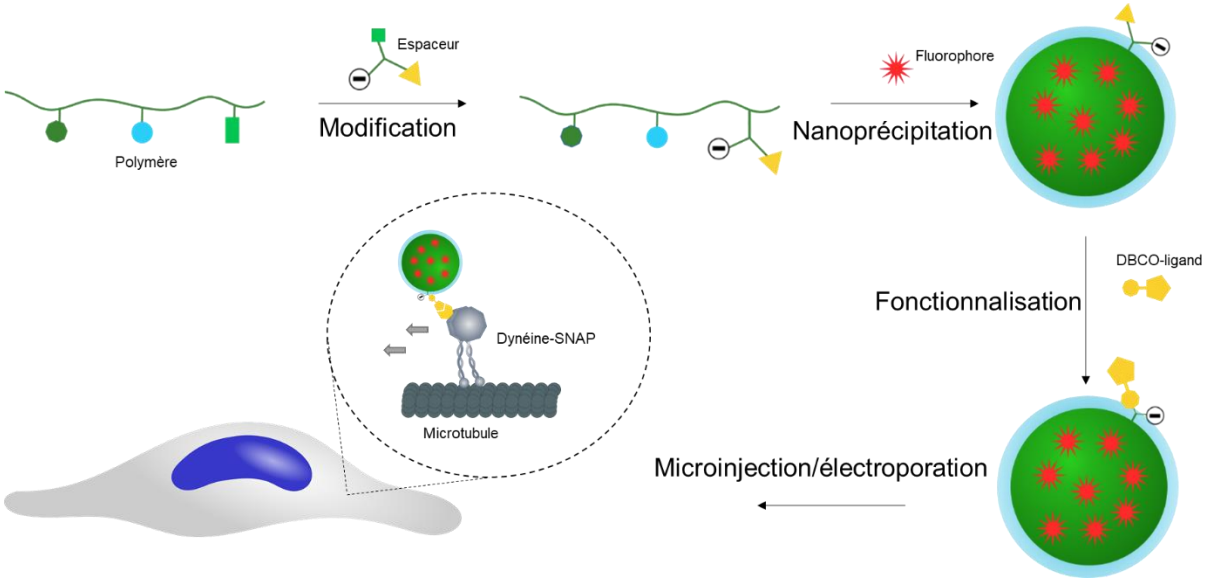

Figure 38. Stratégie pour le marquage de biomolécules intracellulaires.

L'approche retenue pour fonctionnaliser les NPs est montrée figure 38. Certaines stratégies de marquage de protéines reposent sur la fusion de la biomolécule à suivre avec un fragment d'enzyme qui peut ensuite réagir avec des groupements ou substrats spécifiques.[217] Parmi elles, la technologie SNAP-tag a déjà été utilisée avec succès pour le marquage de protéines avec des QDs.[218–220] Elle permet de produire une protéine de fusion portant le tag O6-alkylguanine-DNA alkyl transférase humaine (AGT) qui réagit spécifiquement avec un groupement O6-benzylguanine (BG) porté par la NP.[221] Cela nécessite d'introduire la BG sur la NP. L'introduction de ce groupement sera effectuée par chimie clic *via* un dibenzocyclooctyne-amine (DBCO).[222] Cette réaction requiert la présence d'un groupement azide à la surface de la particule. Mais la difficulté est de s'assurer que le groupement réactif, ici le groupement azide, soit exposé à la surface des particules et non encapsulé à l'intérieur

de la particule lors de la nanoprécipitation. Dernièrement, notre groupe a démontré que la présence d'un groupement chargé tel qu'un groupement carboxylate sur un espaceur assurait l'exposition du groupement réactionnel à la surface de la particule après nanoprécipitation.[132,133] La fonctionnalisation s'effectura donc en deux temps. La première étape consistera à modifier le polymère avec un espaceur portant le groupement azide et un groupement chargé. Après formation des NPs, ces dernières pourront réagir par chimie clic avec DBCO portant le groupement BG.

Dans cette partie, nous avons validé cette stratégie de fonctionnalisation par un système de transfert d'énergie par résonance de type Förster (FRET). Pour cela nous avons synthétisé l'espaceur portant un groupement réactionnel azide et un groupement sulfonate qui a pour rôle de maintenir l'espaceur vers l'extérieur de la particule et d'assurer la petite taille des NPs.

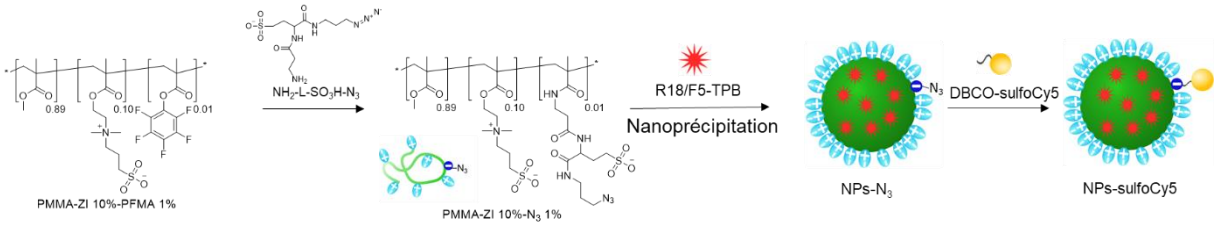

Figure 39. Preuve du concept pour la fonctionnalisation : modification d'un polymère zwittérionique PMMA-ZI 10%-PFMA 1% avec un espaceur portant un groupement sulfonate et azide. Après nanoprécipitation les NPs sont fonctionnalisées avec une sulfoCy5.

Celui-ci a ensuite été inséré sur un polymère de type méthacrylate de méthyle portant 1 % de groupement méthacrylate de pentafluorophényle (PFMA) (figure 39).[223] Après formation de NPs chargées avec 20 % R18/F5-TPB, elles ont réagi avec DBCO portant une sulfo cyanine 5 (sulfoCy5). La fonctionnalisation a ensuite été confirmée par observation d'un signal FRET après purification des NPs sulfoCy5.

La synthèse de l'espaceur NH_2-L-SO_3H-N_3 commence à partir de l'acide cystéique (Figure 40). Dans un premier temps, la fonction amine est protégée par un groupement boc. Puis le couplage avec l'azidopropyl amine par réaction peptidique permet d'obtenir le synthon **1** avec un rendement de 42 %. Dans un premier temps, la modification du polymère a été réalisée directement avec le synthon **1** mais a échoué. Nous avons donc supposé que la charge du sulfonate empêche la modification du polymère s'il est trop près du groupement amine réactionnel. C'est pourquoi, le second

synthon porte une chaine de trois carbones qui sert à éloigner le groupement sulfonate de l'espaceur du groupement amine qui devra réagir avec le polymère ultérieurement. La réaction peptidique entre **1** et **2** est réalisée *via* un ester NHS activé. L'espaceur obtenu boc-NH-L-SO_3H-N_3 a été caractérisé par RMN-^{1}H et spectrométrie de masse.

Pour la modification du polymère, un poly(méthacrylate de méthyle) portant 10 %(mol) ZI et 1 %(mol) de groupement méthacrylate de pentafluorophényle (PFMA) (PMMA-ZI 10%-PFMA 1%, Figure 39) a été synthétisé par polymérisation radicalaire. Le spectre RMN-^{19}F indique la présence du groupement PFMA après purification du polymère. Ce groupement permet d'activer le groupement COOH et de réaliser la modification dans des conditions plus douces qui faciliteront ensuite la purification du polymère modifié.[223,224] Le groupement PFMA est alors remplacé par l'espaceur déprotégé NH_2-L-SO_3H-N_3 par simple mélange du polymère et de l'espaceur dans le solvant approprié. Le suivi de la modification par RMN-^{1}H est impossible du fait de la faible fraction du groupement PFMA initial sur le polymère (1%). Cependant la RMN-^{19}F du polymère modifié montre une quasi-totale disparition des pics du groupement PFMA suggérant une modification partielle du polymère.

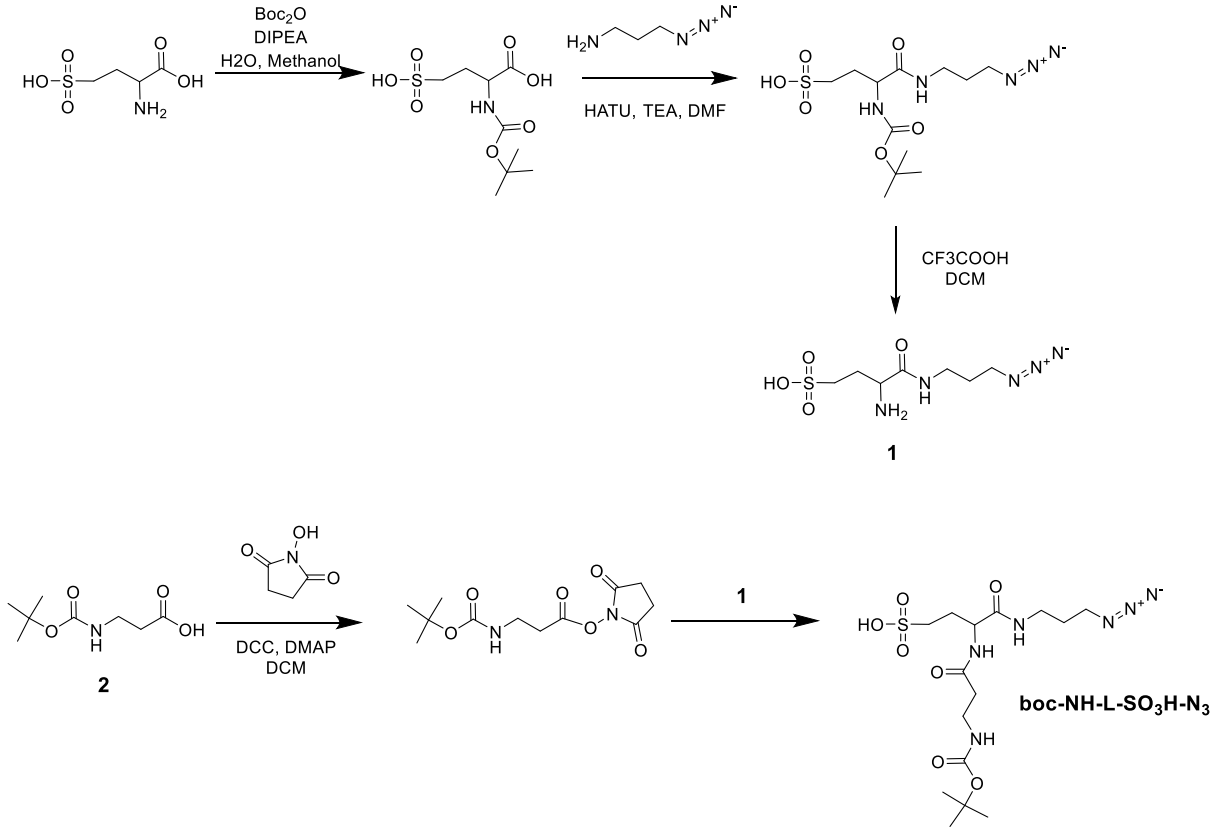

Figure 40. Synthèse de l'espaceur boc-NH-L-SO_3H-N_3.

Afin de démontrer la preuve du concept, nous avons utilisé un système FRET. Pour cela les polymères PMMA-ZI 10%-N_3 1% et PMMA-ZI 10%- PFMA 1% ont été dissous dans un mélange acétonitrile/méthanol (8 : 2) à 10g.l^{-1}. Des NPs de PMMA-ZI 10%-N_3 1% et PMMA-ZI 10%- PFMA 1% contenant 20 % R18/F5-TPB ont été préparées par nanoprécipitation. Les mesures de taille par DLS de ces NPs (Figure 41A) montrent une diminution du diamètre pour les particules de PMMA-ZI 10%-N_3 1% suggérant, ici aussi, la présence du groupement SO_3H de l'espaceur NH_2-L-SO_3H-N_3 sur le polymère. La taille des NPs est cependant significativement plus grande que les NPs de PMMA-ZI 10 %-SO_3H 1% indiquant que la modification n'est pas complète et/ou que le groupement sulfonate de l'espaceur est moins efficace que le groupement sulfonate du polymère PMMA-ZI 10 %-SO_3H 1%.

A

Polymères		Taille (nm)
PMMA-ZI 10%	PFMA 1%	98 ± 3
	N_3 1%	43 ± 1
	SO_3H 1%	13 ± 1

B

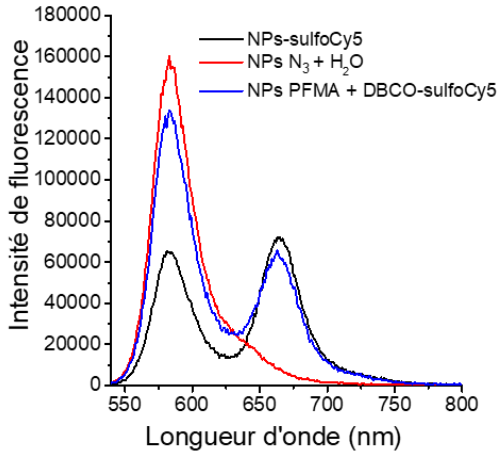

Figure 41. (A) Tailles des NPs de PMMA-ZI 10%-PFMA 1% ou -N3 1% chargées à 20 % R18/F5-TPB et les NPs de PMMA-ZI 10%-SO3H 1% chargées avec 10 % R18/F5-TPB obtenues par DLS. (B) Spectres de fluorescence pour les NPs PMMA-ZI 10%-N_3 fonctionnalisées (en noir) ou non (en rouge) avec DBCO-sulfoCy5 et des NPs PMMA-ZI 10%-PFMA 1% en présence de DBCO-sulfoCy5 (en bleu) après purification. Les NPs ont été excitées à 530 nm. Elles sont chargées avec 20 % R18/F5-TPB avec un ratio D/A égal à 12.

Enfin ces NPs-N_3 ont ensuite été fonctionnalisées par chimie clic avec DBCO-sulfoCy5 avec un ratio de 12 donneur/accepteur (Figure 39). Après purification par chromatographie d'exclusion stérique, les NPs-sulfoCy5 ont été caractérisées par spectrométrie de fluorescence. Les spectres obtenus sont représentés figure 41B. On observe une diminution de l'intensité du pic à 580 nm pour les NPs sulfoCy5 (spectre noir) accompagnée d'une apparition du pic à 670 nm indiquant un transfert d'énergie

entre la rhodamine R18/F5-TPB et la sulfoCy5. Le contrôle négatif pour les NPs non fonctionnalisées mais mises en présence de DBCO-sulfoCy5 (NPs PFMA + DBCO-sulfoCy5, spectre bleu) montre également un transfert d'énergie moindre entre l'accepteur et le donneur. Ce signal FRET ne devrait pas être présent pour ces NPs suggérant un problème de purification. Cet effet n'a pas été observé sur les premiers essais avec les polymères non ZI. Il résulte probablement des sulfoCy5 piégées par les groupements ZI à la surface des particules qui ne sont pas éliminées lors de la purification.

Les résultats ci-dessus ont permis de démontrer la preuve du concept de fonctionnalisation des NPs PMMA-ZI 10%-N_3 1%. Le polymère PMMA-ZI 10%-N_3 1% a été modifié partiellement avec l'espaceur synthétisé NH_2-L-SO_3H-N_3. Les NPs PMMA-ZI 10%-N_3 1% à 20 % R18/F5-TPB ont été ensuite assemblées donnant une taille de 43 nm. La seconde partie de la fonctionnalisation a été validée par FRET par observation d'un transfert d'énergie entre les fluorophores R18/F5-TPB à l'intérieur des particules et la sulfoCy5 à la surface. La stratégie décrite ci-dessus nécessite encore une optimisation au niveau de la taille des NPs en ajoutant un groupement SO_3H sur le polymère afin d'atteindre des tailles de l'ordre des protéines et une amélioration de la purification des NPs ZI fonctionnalisées. Ces NPs pourront alors être fonctionnalisées avec la BG avant d'être microinjectées dans le cytosol de cellules transfectées et ainsi marquées les dynéines portant un SNAP-tag.

Conclusion et perspectives

L'objectif de ce projet de thèse était de développer des NPs de polymères fluorescentes comme marqueurs pour l'imagerie intracellulaire et super-résolutive en prenant en compte toutes les contraintes liées à l'imagerie intracellulaire telles que la taille, la fluorescence et les interactions des particules.

Dans un premier temps nous avons mis au point une méthode permettant de contrôler la taille des NPs de polymères préparées par nanoprécipitation. Cette méthode permet de maitriser le diamètre des NPs obtenues par ajout de groupements chargés, en variant la composition du polymère, la concentration ou encore par ajout de sels dans la fraction aqueuse de nanoprécipitation. Cette étude sur la taille des particules a montré que nous pouvions diminuer le diamètre jusqu'à 7 nm tout en conservant une brillance suffisante pour leur détection en microscopie de fluorescence. Nous sommes donc en mesure de formuler des NPs ultrapetites < 15 nm mais aussi de construire des gammes de taille de NPs pour un polymère donné ou des gammes de NPs de même taille mais de composition différente. Ces gammes de NPs peuvent être utiles pour étudier divers paramètres dans les cellules. Les NPs ayant des tailles différentes, ont contribué à déterminer une taille critique < 25 nm permettant de franchir la membrane cytoplasmique par électroporation puis une taille ≤ 23 nm pour diffuser librement dans le cytosol.

L'optimisation de la brillance est indispensable afin d'augmenter la précision et la vitesse de localisation des NPs fluorescentes en imagerie de molécules uniques. Les NPs chargées avec des complexes de lanthanide et chargées avec la rhodamine ont montré des brillances supérieures à 10^7 $M^{-1}cm^{-1}$. Cela non seulement facilite leur détection mais permet en même temps de diminuer la puissance d'illumination des échantillons et donc la phototoxicité sur les cellules vivantes. D'un autre côté, l'organisation des fluorophores au sein de la particule et donc la fluorescence est fortement affectée par la nature du polymère cela est due en grande partie à la l'influence du polymère sur la formation des NPs. Néanmoins la taille des particules joue un rôle majeur concernant le phénomène clignotement et masque l'influence d'autres paramètres.

Enfin l'élaboration de NPs furtives a conduit à la conception de NPs zwittérioniques Leur comportement dans le cytosol en fonction de la taille des particules et de leur chimie de surface a montré une meilleure diffusion des NPs zwittérioniques par rapport aux NPs PEGylés et une excellente stabilité vis-à-vis des milieux biologiques. D'autre part, la preuve du concept concernant la fonctionnalisation des NPs a été démontrée par un système FRET. Celle-ci s'effectue en deux étapes. Le concept n'a pour l'instant été démontré qu'en couplant DBCO-sulfocy5 sur les NPs ZI. Mais cela reste encourageant. Leur petite taille, leur grande brillance et leur surface non interactives rendent déjà ces particules prometteuses pour des applications de suivi de molécules individuelles au niveau intracellulaire en particulier pour le suivi de biomolécules qui se déplacent rapidement dans le cytoplasme telles que les moteurs moléculaires.

Les points clés restant à éclairer concernent essentiellement le contrôle du clignotement des NPs et l'optimisation de la fonctionnalisation. L'utilisation d'une gamme de NPs de même taille avec variation de l'hydrophobie du polymère devrait nous aider à comprendre l'influence de l'hydrophobie et ses limites sur le comportement collectif des fluorophores. En second lieu, la classification des différents profils de clignotement (continu, complet ou partiel) ainsi que la fréquence de la fluctuation du signal fluorescent, nous apporteraient encore une plus grande compréhension et peut-être un contrôle du clignotement des particules à terme. Par ailleurs, la stratégie de fonctionnalisation doit être optimisée au niveau de la taille des NPs, afin d'atteindre des tailles de l'ordre des protéines et au niveau de la purification des NPs ZI fonctionnalisées. En même temps, il serait intéressant d'avoir un moyen de suivre la réaction de modification du polymère et d'estimer le pourcentage de modification. Ces NPs pourront ensuite être fonctionnalisées avec la BG avant d'être microinjectées dans le cytosol de cellules transfectées et ainsi marquées les dynéines portant un SNAP-tag.

A plus ou moins moyen terme, ces NPs, biocompatibles, faciles à synthétiser et à assembler ont le potentiel de surpasser les NPs fluorescentes actuellement sur le marché et peuvent aspirer être à l'origine d'une nouvelle génération de marqueurs fluorescents en particulier pour le suivi de molécule individuelle. Les potentiels progrès dans ce domaine pourraient également ouvrir la voie à de nouveaux types de microscopie de fluorescence permettant d'imager des molécules individuelles en plein travail directement dans les cellules par imagerie super-résolutive. A terme, cela

permettrait non seulement de mieux comprendre les mécanismes moléculaires à l'origine de diverses pathologies mais aussi de contribuer au développement d'outils diagnostics de plus en plus efficaces, faciles d'accès et d'emploi ainsi qu'à l'émergence de nouvelles thérapies.

Références

1. Shashkova S, Leake MC. Single-molecule fluorescence microscopy review: shedding new light on old problems. Biosci Rep [Internet]. 2017 Jul 21 [cited 2018 Nov 7];37(4). Available from: https://www.ncbi.nlm.nih.gov/pmc/articles/PMC5520217/

2. Nelson AJ, Hess ST. Localization microscopy: mapping cellular dynamics with single molecules. J Microsc. 2014 Apr;254(1):1–8.

3. Deschout H, Zanacchi FC, Mlodzianoski M, Diaspro A, Bewersdorf J, Hess ST, et al. Precisely and accurately localizing single emitters in fluorescence microscopy. Nature Methods. 2014 Mar;11(3):253–66.

4. Rösch TC, Oviedo-Bocanegra LM, Fritz G, Graumann PL. SMTracker: a tool for quantitative analysis, exploration and visualization of single-molecule tracking data reveals highly dynamic binding of B. subtilis global repressor AbrB throughout the genome. Sci Rep. 2018 Oct 24;8(1):15747.

5. Betzig E, Patterson GH, Sougrat R, Lindwasser OW, Olenych S, Bonifacino JS, et al. Imaging intracellular fluorescent proteins at nanometer resolution. Science. 2006 Sep 15;313(5793):1642–5.

6. Pinaud F, Clarke S, Sittner A, Dahan M. Probing cellular events, one quantum dot at a time. Nat Meth. 2010 Apr;7(4):275–85.

7. Montalti M, Prodi L, Rampazzo E, Zaccheroni N. Dye-doped silica nanoparticles as luminescent organized systems for nanomedicine. Chem Soc Rev. 2014 May 27;43(12):4243–68.

8. Reisch A, Didier P, Richert L, Oncul S, Arntz Y, Mély Y, et al. Collective fluorescence switching of counterion-assembled dyes in polymer nanoparticles. Nat Commun [Internet]. 2014 Jun 9 [cited 2014 Aug 5];5. Available from: http://www.nature.com.scd-rproxy.u-strasbg.fr/ncomms/2014/140609/ncomms5089/full/ncomms5089.html

9. Li K, Liu B. Polymer-encapsulated organic nanoparticles for fluorescence and photoacoustic imaging. Chem Soc Rev. 2014 Aug 18;43(18):6570–97.

10. Provance DW, McDowall A, Marko M, Luby-Phelps K. Cytoarchitecture of size-excluding compartments in living cells. Journal of Cell Science. 1993 Oct 1;106(2):565–77.

11. Luby-Phelps K. The physical chemistry of cytoplasm and its influence on cell function: an update. Mol Biol Cell. 2013 Sep;24(17):2593–6.

12. Etoc F, Balloul E, Vicario C, Normanno D, Liße D, Sittner A, et al. Non-specific interactions govern cytosolic diffusion of nanosized objects in mammalian cells. Nature Materials. 2018 Aug;17(8):740–6.

13. Rao JP, Geckeler KE. Polymer nanoparticles: Preparation techniques and size-control parameters. Progress in Polymer Science. 2011 Jul;36(7):887–913.

14. Tonga GY, Saha K, Rotello VM. 25th Anniversary Article: Interfacing Nanoparticles and Biology: New Strategies for Biomedicine. Advanced Materials. 2014 Jan;26(3):359–70.

15. Rabanel J-M, Hildgen P, Banquy X. Assessment of PEG on polymeric particles surface, a key step in drug carrier translation. Journal of Controlled Release. 2014 Jul 10;185:71–87.

16. Estephan ZG, Schlenoff PS, Schlenoff JB. Zwitteration As an Alternative to PEGylation. Langmuir. 2011 Jun 7;27(11):6794–800.

17. Prasad PN. Introduction to Biophotonics. John Wiley & Sons; 2004. 623 p.

18. Valeur B, Berberan-Santos MN. Molecular Fluorescence: Principles and Applications. 2nd edition. Wiley-VCH; 2012. 569 p.

19. Lichtman JW, Conchello J-A. Fluorescence microscopy. Nat Methods. 2005 Dec;2(12):910–9.

20. Zhang KY, Yu Q, Wei H, Liu S, Zhao Q, Huang W. Long-Lived Emissive Probes for Time-Resolved Photoluminescence Bioimaging and Biosensing. 2018 Feb 2 [cited 2019 Sep 10]; Available from: https://pubs-acs-org.scd-rproxy.u-strasbg.fr/doi/abs/10.1021/acs.chemrev.7b00425

21. Antibody Conjugates - Fluorophore and Enzyme Tags | StressMarq [Internet]. StressMarq Biosciences Inc. 2015 [cited 2019 Oct 6]. Available from: https://www.stressmarq.com/primary-antibody-conjugates/

22. Lavis LD, Raines RT. Bright Ideas for Chemical Biology. ACS Chem Biol. 2008 Mar 1;3(3):142–55.

23. Pansare VJ, Hejazi S, Faenza WJ, Prud'homme RK. Review of Long-Wavelength Optical and NIR Imaging Materials: Contrast Agents, Fluorophores, and Multifunctional Nano Carriers. Chem Mater. 2012 Mar 13;24(5):812–27.

24. Resch-Genger U, Grabolle M, Cavaliere-Jaricot S, Nitschke R, Nann T. Quantum dots versus organic dyes as fluorescent labels. Nat Meth. 2008 Sep;5(9):763–75.

25. Buschmann V, Weston KD, Sauer M. Spectroscopic Study and Evaluation of Red-Absorbing Fluorescent Dyes. Bioconjugate Chem. 2003 Jan 1;14(1):195–204.

26. A Homogeneous, Nonradioactive High-Throughput Fluorogenic Protein Phosphatase Assay - Kevin Kupcho, Kevin Hsiao, Bob Bulleit, Said A. Goueli, 2004 [Internet]. [cited 2019 Oct 4]. Available from: https://journals-sagepub-com.scd-rproxy.u-strasbg.fr/doi/abs/10.1177/1087057103262840

27. Qi J, Liu D, Liu X, Guan S, Shi F, Chang H, et al. Fluorescent pH Sensors for Broad-Range pH Measurement Based on a Single Fluorophore. Anal Chem. 2015 Jun 16;87(12):5897–904.

28. Burdette SC, Lippard SJ. The Rhodafluor Family. An Initial Study of Potential Ratiometric Fluorescent Sensors for Zn2+. Inorg Chem. 2002 Dec 1;41(25):6816–23.

29. Crissman HA, Hirons GT. Chapter 13 Staining of DNA in Live and Fixed Cells. In: Darzynkiewicz Z, Paul Robinson J, Crissman HA, editors. Methods in Cell Biology [Internet]. Academic Press; 1994 [cited 2019 Oct 4]. p. 195–209. (Flow Cytometry Second Edition, Part A; vol. 41). Available from: http://www.sciencedirect.com/science/article/pii/S0091679X08617185

30. Chalfie M, Tu Y, Euskirchen G, Ward WW, Prasher DC. Green fluorescent protein as a marker for gene expression. Science. 1994 Feb 11;263(5148):802–5.

31. Tomosugi W, Matsuda T, Tani T, Nemoto T, Kotera I, Saito K, et al. An ultramarine fluorescent protein with increased photostability and pH insensitivity. Nature Methods. 2009 May;6(5):351–3.

32. Hu C-D, Kerppola TK. Simultaneous visualization of multiple protein interactions in living cells using multicolor fluorescence complementation analysis. Nat Biotechnol. 2003 May;21(5):539–45.

33. Matz MV, Fradkov AF, Labas YA, Savitsky AP, Zaraisky AG, Markelov ML, et al. Fluorescent proteins from nonbioluminescent Anthozoa species. Nat Biotechnol. 1999 Oct;17(10):969–73.

34. Merzlyak EM, Goedhart J, Shcherbo D, Bulina ME, Shcheglov AS, Fradkov AF, et al. Bright monomeric red fluorescent protein with an extended fluorescence lifetime. Nature Methods. 2007 Jul;4(7):555–7.

35. Ando R, Hama H, Yamamoto-Hino M, Mizuno H, Miyawaki A. An optical marker based on the UV-induced green-to-red photoconversion of a fluorescent protein. PNAS. 2002 Oct 1;99(20):12651–6.

36. Stiel AC, Trowitzsch S, Weber G, Andresen M, Eggeling C, Hell SW, et al. 1.8 A bright-state structure of the reversibly switchable fluorescent protein Dronpa guides the generation of fast switching variants. Biochem J. 2007 Feb 15;402(1):35–42.

37. Chudakov DM, Matz MV, Lukyanov S, Lukyanov KA. Fluorescent proteins and their applications in imaging living cells and tissues. Physiol Rev. 2010 Jul;90(3):1103–63.

38. Drepper T, Eggert T, Circolone F, Heck A, Krauß U, Guterl J-K, et al. Reporter proteins for in vivo fluorescence without oxygen. Nature Biotechnology. 2007 Apr;25(4):443–5.

39. Shu X, Lev-Ram V, Deerinck TJ, Qi Y, Ramko EB, Davidson MW, et al. A genetically encoded tag for correlated light and electron microscopy of intact cells, tissues, and organisms. PLoS Biol. 2011 Apr;9(4):e1001041.

40. Chapman S, Faulkner C, Kaiserli E, Garcia-Mata C, Savenkov EI, Roberts AG, et al. The photoreversible fluorescent protein iLOV outperforms GFP as a reporter of plant virus infection. Proc Natl Acad Sci USA. 2008 Dec 16;105(50):20038–43.

41. Kumagai A, Ando R, Miyatake H, Greimel P, Kobayashi T, Hirabayashi Y, et al. A bilirubin-inducible fluorescent protein from eel muscle. Cell. 2013 Jun 20;153(7):1602–11.

42. Karasev MM, Stepanenko OV, Rumyantsev KA, Turoverov KK, Verkhusha VV. Near-Infrared Fluorescent Proteins and Their Applications. Biochemistry Mosc. 2019 Jan;84(Suppl 1):S32–50.

43. Dabbousi BO, Rodriguez-Viejo J, Mikulec FV, Heine JR, Mattoussi H, Ober R, et al. (CdSe)ZnS Core−Shell Quantum Dots: Synthesis and Characterization of a Size Series of Highly Luminescent Nanocrystallites. J Phys Chem B. 1997 Nov 1;101(46):9463–75.

44. Pinaud F, Clarke S, Sittner A, Dahan M. Probing cellular events, one quantum dot at a time. Nat Meth. 2010 Apr;7(4):275–85.

45. Michalet X, Pinaud FF, Bentolila LA, Tsay JM, Doose S, Li JJ, et al. Quantum Dots for Live Cells, in Vivo Imaging, and Diagnostics. Science. 2005 Jan 28;307(5709):538–44.

46. Hoyer P, Staudt T, Engelhardt J, Hell SW. Quantum Dot Blueing and Blinking Enables Fluorescence Nanoscopy. Nano Letters. 2011 Jan 12;11(1):245–50.

47. Hanne J, Falk HJ, Görlitz F, Hoyer P, Engelhardt J, Sahl SJ, et al. STED nanoscopy with fluorescent quantum dots. ncomms. 2015 May 18;6:7127.

48. Wang Q, Xu Y, Zhao X, Chang Y, Liu Y, Jiang L, et al. A Facile One-Step in situ Functionalization of Quantum Dots with Preserved Photoluminescence for Bioconjugation. J Am Chem Soc. 2007 May 1;129(20):6380–1.

49. Gao X, Cui Y, Levenson RM, Chung LWK, Nie S. In vivo cancer targeting and imaging with semiconductor quantum dots. Nat Biotechnol. 2004 Aug;22(8):969–76.

50. Nann T. Phase-transfer of CdSe@ZnS quantum dots using amphiphilic hyperbranched polyethylenimine. Chem Commun. 2005 Mar 23;(13):1735–6.

51. Wang X, Li W, Zhao B, Zhang D, Sun K, An X, et al. Highly fluorescent quantum dot@silica nanoparticles by a novel post-treatment for live cell imaging. RSC Adv. 2013 Feb 18;3(11):3553–6.

52. Dubertret B, Skourides P, Norris DJ, Noireaux V, Brivanlou AH, Libchaber A. In Vivo Imaging of Quantum Dots Encapsulated in Phospholipid Micelles. Science. 2002 Nov 29;298(5599):1759–62.

53. Roullier V, Clarke S, You C, Pinaud F, Gouzer GG, Schaible D, et al. High-affinity labeling and tracking of individual histidine-tagged proteins in live cells using Ni2+ tris-nitrilotriacetic acid quantum dot conjugates. Nano Lett. 2009 Mar;9(3):1228–34.

54. Pinaud F, Clarke S, Sittner A, Dahan M. Probing cellular events, one quantum dot at a time. Nat Methods. 2010 Apr;7(4):275–85.

55. Clarke S, Pinaud F, Beutel O, You C, Piehler J, Dahan M. Covalent monofunctionalization of peptide-coated quantum dots for single-molecule assays. Nano Lett. 2010 Jun 9;10(6):2147–54.

56. Hines DA, Kamat PV. Recent Advances in Quantum Dot Surface Chemistry. ACS Appl Mater Interfaces. 2014 Mar 12;6(5):3041–57.

57. Wang Y, Hu R, Lin G, Roy I, Yong K-T. Functionalized Quantum Dots for Biosensing and Bioimaging and Concerns on Toxicity. ACS Appl Mater Interfaces. 2013 Apr 24;5(8):2786–99.

58. Wegner KD, Hildebrandt N. Quantum dots: bright and versatile in vitro and in vivo fluorescence imaging biosensors. Chem Soc Rev. 2015 Jul 7;44(14):4792–834.

59. Kochuveedu ST, Kim DH. Surface plasmon resonance mediated photoluminescence properties of nanostructured multicomponent fluorophore systems. Nanoscale. 2014 Apr 23;6(10):4966–84.

60. Tsukamoto D, Shiraishi Y, Sugano Y, Ichikawa S, Tanaka S, Hirai T. Gold Nanoparticles Located at the Interface of Anatase/Rutile TiO2 Particles as Active Plasmonic Photocatalysts for Aerobic Oxidation. J Am Chem Soc. 2012 Apr 11;134(14):6309–15.

61. Ni M, Zhuo S. Nonlinear optical microscopy: Endogenous signals and exogenous probes. Annalen der Physik. 2015;527(7–8):471–89.

62. He H, Xie C, Ren J. Nonbleaching fluorescence of gold nanoparticles and its applications in cancer cell imaging. Anal Chem. 2008 Aug 1;80(15):5951–7.

63. Santos RFS, Andrade CAS, dos Santos CG, de Melo CP. Visible luminescence in polyaniline/(gold nanoparticle) composites. J Nanopart Res. 2013 Jan 18;15(1):1408.

64. Huang T, Murray RW. Visible Luminescence of Water-Soluble Monolayer-Protected Gold Clusters. J Phys Chem B. 2001 Dec 1;105(50):12498–502.

65. Negishi Y, Tsukuda T. Visible photoluminescence from nearly monodispersed Au12 clusters protected by meso-2,3-dimercaptosuccinic acid. Chemical Physics Letters. 2004 Jan 1;383(1):161–5.

66. Pellegrotti JV, Acuna GP, Puchkova A, Holzmeister P, Gietl A, Lalkens B, et al. Controlled Reduction of Photobleaching in DNA Origami–Gold Nanoparticle Hybrids. Nano Lett. 2014 May 14;14(5):2831–6.

67. Khan S, Verma NC, Gupta A, Nandi CK. Reversible Photoswitching of Carbon Dots. Scientific Reports. 2015 Jun 16;5:11423.

68. Yang S-T, Wang X, Wang H, Lu F, Luo PG, Cao L, et al. Carbon Dots as Nontoxic and High-Performance Fluorescence Imaging Agents. J Phys Chem C Nanomater Interfaces. 2009 Sep 28;113(42):18110–4.

69. Lim SY, Shen W, Gao Z. Carbon quantum dots and their applications. Chem Soc Rev. 2014 Dec 8;44(1):362–81.

70. Sun Y-P, Zhou B, Lin Y, Wang W, Fernando KAS, Pathak P, et al. Quantum-Sized Carbon Dots for Bright and Colorful Photoluminescence. J Am Chem Soc. 2006 Jun 1;128(24):7756–7.

71. Chen G, Qiu H, Prasad PN, Chen X. Upconversion Nanoparticles: Design, Nanochemistry, and Applications in Theranostics. Chem Rev. 2014 May 28;114(10):5161–214.

72. Gargas DJ, Chan EM, Ostrowski AD, Aloni S, Altoe MVP, Barnard ES, et al. Engineering bright sub-10-nm upconverting nanocrystals for single-molecule imaging. Nat Nanotechnol. 2014 Apr;9(4):300–5.

73. Shan J, Uddi M, Wei R, Yao N, Ju Y. The Hidden Effects of Particle Shape and Criteria for Evaluating the Upconversion Luminescence of the Lanthanide Doped Nanophosphors. J Phys Chem C. 2010 Feb 18;114(6):2452–61.

74. Tang S, Moayeri M, Chen Z, Harma H, Zhao J, Hu H, et al. Detection of Anthrax Toxin by an Ultrasensitive Immunoassay Using Europium Nanoparticles. Clin Vaccine Immunol. 2009 Mar;16(3):408–13.

75. Sun W, Yu J, Deng R, Rong Y, Fujimoto B, Wu C, et al. Highly Bright Eu-complex Doped Semiconducting Polymer Dots with Ultranarrow Emission and Long Luminescence Lifetime for Time-Gated Cellular Imaging. Angew Chem Int Ed Engl [Internet]. 2013 Oct 18 [cited 2020 Jan 14];52(43). Available from: https://www.ncbi.nlm.nih.gov/pmc/articles/PMC3883514/

76. Chen Y, Chi Y, Wen H, Lu Z. Sensitized Luminescent Terbium Nanoparticles: Preparation and Time-Resolved Fluorescence Assay for DNA. Anal Chem. 2007 Feb 1;79(3):960–5.

77. Qian D-J, Liu H-G, Huang H-X, Fu Q, Feng X-S. Europium complex nanoparticles: preparation, characterization and optical properties. Materials Letters. 2001 Dec 1;51(6):525–8.

78. Härmä H, Soukka T, Lövgren T. Europium nanoparticles and time-resolved fluorescence for ultrasensitive detection of prostate-specific antigen. Clin Chem. 2001 Mar;47(3):561–8.

79. Cardoso Dos Santos M, Goetz J, Bartenlian H, Wong K-L, Charbonnière LJ, Hildebrandt N. Autofluorescence-Free Live-Cell Imaging Using Terbium Nanoparticles. Bioconjug Chem. 2018 18;29(4):1327–34.

80. Afsari HS, Santos MCD, Lindén S, Chen T, Qiu X, Henegouwen PMP van B en, et al. Time-gated FRET nanoassemblies for rapid and sensitive intra- and extracellular fluorescence imaging. Science Advances. 2016 Jun 1;2(6):e1600265.

81. Väisänen V, Härmä H, Lilja H, Bjartell A. Time-resolved fluorescence imaging for quantitative histochemistry using lanthanide chelates in nanoparticles and conjugated to monoclonal antibodies. Luminescence. 2000;15(6):389–97.

82. Yan J, Estévez MC, Smith JE, Wang K, He X, Wang L, et al. Dye-doped nanoparticles for bioanalysis. Nano Today. 2007 Jun 1;2(3):44–50.

83. Tapec R, Zhao XJ, Tan W. Development of organic dye-doped silica nanoparticles for bioanalysis and biosensors. J Nanosci Nanotechnol. 2002 Aug;2(3–4):405–9.

84. Van Blaaderen A, Vrij A. Synthesis and characterization of colloidal dispersions of fluorescent, monodisperse silica spheres. Langmuir. 1992 Dec 1;8(12):2921–31.

85. Zhang W-H, Hu X-X, Zhang X-B. Dye-Doped Fluorescent Silica Nanoparticles for Live Cell and In Vivo Bioimaging. Nanomaterials (Basel) [Internet]. 2016 Apr 27 [cited 2019 Sep 13];6(5). Available from: https://www.ncbi.nlm.nih.gov/pmc/articles/PMC5302498/

86. Zhao X, Bagwe RP, Tan W. Development of Organic-Dye-Doped Silica Nanoparticles in a Reverse Microemulsion. Advanced Materials. 2004;16(2):173–6.

87. Montalti M, Prodi L, Rampazzo E, Zaccheroni N. Dye-doped silica nanoparticles as luminescent organized systems for nanomedicine. Chem Soc Rev. 2014 May 27;43(12):4243–68.

88. Rampazzo E, Genovese D, Palomba F, Prodi L, Zaccheroni N. NIR-fluorescent dye doped silica nanoparticles for in vivo imaging, sensing and theranostic. Methods Appl Fluoresc. 2018 Mar;6(2):022002.

89. Wang L, Wang K, Santra S, Zhao X, Hilliard LR, Smith JE, et al. Watching Silica Nanoparticles Glow in the Biological World. Anal Chem. 2006 Feb 1;78(3):646–54.

90. Wu C, Szymanski C, Cain Z, McNeill J. Conjugated Polymer Dots for Multiphoton Fluorescence Imaging. J Am Chem Soc. 2007 Oct 1;129(43):12904–5.

91. Wu C, Schneider T, Zeigler M, Yu J, Schiro PG, Burnham DR, et al. Bioconjugation of ultrabright semiconducting polymer dots for specific cellular targeting. J Am Chem Soc. 2010 Nov 3;132(43):15410–7.

92. Wu C, Bull B, Szymanski C, Christensen K, McNeill J. Multicolor Conjugated Polymer Dots for Biological Fluorescence Imaging. ACS Nano. 2008 Nov 25;2(11):2415–23.

93. Efficient Photoluminescence and Electroluminescence from a Soluble Polyfluorene | Journal of the American Chemical Society [Internet]. [cited 2019 Sep 30]. Available from: https://pubs-acs-org.scd-rproxy.u-strasbg.fr/doi/10.1021/ja9615233

94. Reisch A, Klymchenko AS. Fluorescent Polymer Nanoparticles Based on Dyes: Seeking Brighter Tools for Bioimaging. Small. 2016 Apr 1;12(15):1968–92.

95. Wang C, Sun J, Mei H, Gao F. Semiconducting-polymer-dot based fluorescent probe for turn-on sensing of phytic acid. Anal Methods. 2016 Nov 3;8(43):7755–61.

96. Lin H, Tabaei SR, Thomsson D, Mirzov O, Larsson P-O, Scheblykin IG. Fluorescence Blinking, Exciton Dynamics, and Energy Transfer Domains in Single Conjugated Polymer Chains. J Am Chem Soc. 2008 Jun 1;130(22):7042–51.

97. Barbara PF, Gesquiere AJ, Park S-J, Lee YJ. Single-Molecule Spectroscopy of Conjugated Polymers. Acc Chem Res. 2005 Jul 1;38(7):602–10.

98. Yu J, Zhang X, Hao X, Zhang X, Zhou M, Lee C-S, et al. Near-infrared fluorescence imaging using organic dye nanoparticles. Biomaterials. 2014 Mar;35(10):3356–64.

99. Ye F, Wu C, Jin Y, Wang M, Chan Y-H, Yu J, et al. A compact and highly fluorescent orange-emitting polymer dot for specific subcellular imaging. Chem Commun (Camb). 2012 Feb 7;48(12):1778–80.

100. Wu C, Schneider T, Zeigler M, Yu J, Schiro PG, Burnham DR, et al. Bioconjugation of Ultrabright Semiconducting Polymer Dots for Specific Cellular Targeting. J Am Chem Soc. 2010 Nov 3;132(43):15410–7.

101. Sauer R, Turshatov A, Baluschev S, Landfester K. One-Pot Production of Fluorescent Surface-Labeled Polymeric Nanoparticles via Miniemulsion Polymerization with Bodipy Surfmers. Macromolecules. 2012 May 8;45(9):3787–96.

102. Zupke O, Distler E, Baumann D, Strand D, Meyer RG, Landfester K, et al. Preservation of dendritic cell function upon labeling with amino functionalized polymeric nanoparticles. Biomaterials. 2010 Sep;31(27):7086–95.

103. Grazon C, Rieger J, Méallet-Renault R, Charleux B, Clavier G. Ultrabright Fluorescent Polymeric Nanoparticles Made from a New Family of BODIPY Monomers. Macromolecules. 2013 Jul 9;46(13):5167–76.

104. Geng J, Li K, Qin W, Ma L, Gurzadyan GG, Tang BZ, et al. Eccentric Loading of Fluorogen with Aggregation-Induced Emission in PLGA Matrix Increases

Nanoparticle Fluorescence Quantum Yield for Targeted Cellular Imaging. Small. 2013;9(11):2012–9.

105. Riess G. Micellization of block copolymers. Progress in Polymer Science. 2003 Jul;28(7):1107–70.

106. Lu H, Su F, Mei Q, Tian Y, Tian W, Johnson RH, et al. Using fluorine-containing amphiphilic random copolymers to manipulate the quantum yields of aggregation-induced emission fluorophores in aqueous solutions and the use of these polymers for fluorescent bioimaging. J Mater Chem. 2012 May 1;22(19):9890–900.

107. Joralemon MJ, O'Reilly RK, Hawker CJ, Wooley KL. Shell Click-Crosslinked (SCC) Nanoparticles: A New Methodology for Synthesis and Orthogonal Functionalization. J Am Chem Soc. 2005 Dec 1;127(48):16892–9.

108. Mora-Huertas CE, Fessi H, Elaissari A. Influence of process and formulation parameters on the formation of submicron particles by solvent displacement and emulsification–diffusion methods: Critical comparison. Advances in Colloid and Interface Science. 2011 Apr 14;163(2):90–122.

109. Breul AM, Hager MD, Schubert US. Fluorescent monomers as building blocks for dye labeled polymers: synthesis and application in energy conversion, biolabeling and sensors. Chem Soc Rev. 2013 Jun 21;42(12):5366–407.

110. Chen J, Zhang P, Fang G, Yi P, Zeng F, Wu S. Design and Synthesis of FRET-Mediated Multicolor and Photoswitchable Fluorescent Polymer Nanoparticles with Tunable Emission Properties. J Phys Chem B. 2012 Apr 12;116(14):4354–62.

111. Dossi M, Ferrari R, Dragoni L, Martignoni C, Gaetani P, D'Incalci M, et al. Synthesis of Fluorescent PMMA-Based Nanoparticles. Macromol Mater Eng. 2013 Jul 1;298(7):771–8.

112. Zhang X, Zhang X, Yang B, Liu M, Liu W, Chen Y, et al. Fabrication of aggregation induced emission dye-based fluorescent organic nanoparticles via emulsion polymerization and their cell imaging applications. Polym Chem. 2013 Dec 11;5(2):399–404.

113. Sauer R, Turshatov A, Baluschev S, Landfester K. One-Pot Production of Fluorescent Surface-Labeled Polymeric Nanoparticles via Miniemulsion Polymerization with Bodipy Surfmers. Macromolecules. 2012 May 8;45(9):3787–96.

114. Monguzzi A, Frigoli M, Larpent C, Meinardi F. Laser dye doped nanoparticles for highly photostable optical nanoamplifiers. RSC Adv. 2012 Nov 5;2(31):11731–6.

115. Wagh A, Qian SY, Law B. Development of Biocompatible Polymeric Nanoparticles for in Vivo NIR and FRET Imaging. Bioconjugate Chem. 2012 May 16;23(5):981–92.

116. Wagh A, Jyoti F, Mallik S, Qian S, Leclerc E, Law B. Polymeric Nanoparticles with Sequential and Multiple FRET Cascade Mechanisms for Multicolor and Multiplexed Imaging. Small. 2013 Jun 24;9(12):2129–39.

117. Trofymchuk K, Reisch A, Shulov I, Mély Y, Klymchenko AS. Tuning the color and photostability of perylene diimides inside polymer nanoparticles: towards biodegradable substitutes of quantum dots. Nanoscale. 2014 Oct 10;6(21):12934–42.

118. Behnke T, Würth C, Laux E-M, Hoffmann K, Resch-Genger U. Simple strategies towards bright polymer particles via one-step staining procedures. Dyes and Pigments. 2012 Aug;94(2):247–57.

119. MacDonald RI. Characteristics of self-quenching of the fluorescence of lipid-conjugated rhodamine in membranes. J Biol Chem. 1990 Aug 15;265(23):13533–9.

120. Klymchenko AS, Roger E, Anton N, Anton H, Shulov I, Vermot J, et al. Highly lipophilic fluorescent dyes in nano-emulsions: towards bright non-leaking nano-droplets. RSC Adv. 2012 Oct 29;2(31):11876–86.

121. Tian Z, Shaller AD, Li ADQ. Twisted perylene dyes enable highly fluorescent and photostable nanoparticles. Chem Commun (Camb). 2009 Jan 8;(2):180–2.

122. Méallet-Renault R, Hérault A, Vachon J-J, Pansu RB, Amigoni-Gerbier S, Larpent C. Fluorescent nanoparticles as selective Cu(II) sensors. Photochem Photobiol Sci. 2006 Mar 6;5(3):300–10.

123. Bwambok DK, El-Zahab B, Challa SK, Li M, Chandler L, Baker GA, et al. Near-Infrared Fluorescent NanoGUMBOS for Biomedical Imaging. ACS Nano. 2009 Dec 22;3(12):3854–60.

124. Yao H, Ashiba K. Highly fluorescent organic nanoparticles of thiacyanine dye : A synergetic effect of intermolecular H-aggregation and restricted intramolecular rotation. RSC Advances. 2011;1(5):834–8.

125. Mei J, Hong Y, Lam JWY, Qin A, Tang Y, Tang BZ. Aggregation-Induced Emission: The Whole Is More Brilliant than the Parts. Adv Mater. 2014 Aug 1;26(31):5429–79.

126. Qin W, Li K, Feng G, Li M, Yang Z, Liu B, et al. Bright and Photostable Organic Fluorescent Dots with Aggregation-Induced Emission Characteristics for Noninvasive Long-Term Cell Imaging. Adv Funct Mater. 2014 Feb 1;24(5):635–43.

127. Geng J, Li K, Qin W, Ma L, Gurzadyan GG, Tang BZ, et al. Eccentric Loading of Fluorogen with Aggregation-Induced Emission in PLGA Matrix Increases Nanoparticle Fluorescence Quantum Yield for Targeted Cellular Imaging. Small. 2013 Jun 10;9(11):2012–9.

128. Li K, Jiang Y, Ding D, Zhang X, Liu Y, Hua J, et al. Folic acid-functionalized two-photon absorbing nanoparticles for targeted MCF-7 cancer cell imaging. Chem Commun. 2011 Jun 21;47(26):7323–5.

129. Zhang X, Chen Z, Würthner F. Morphology control of fluorescent nanoaggregates by co-self-assembly of wedge- and dumbbell-shaped amphiphilic perylene bisimides. J Am Chem Soc. 2007 Apr 25;129(16):4886–7.

130. Genovese D, Rampazzo E, Bonacchi S, Montalti M, Zaccheroni N, Prodi L. Energy transfer processes in dye-doped nanostructures yield cooperative and versatile fluorescent probes. Nanoscale. 2014 Mar 21;6(6):3022–36.

131. Trofymchuk K, Reisch A, Didier P, Fras F, Gilliot P, Mely Y, et al. Giant light-harvesting nanoantenna for single-molecule detection in ambient light. Nature Photon. 2017 Oct;11(10):657–63.

132. Melnychuk N, Klymchenko AS. DNA-Functionalized Dye-Loaded Polymeric Nanoparticles: Ultrabright FRET Platform for Amplified Detection of Nucleic Acids. J Am Chem Soc. 2018 Aug 29;140(34):10856–65.

133. Melnychuk N, Egloff S, Runser A, Reisch A, Klymchenko AS. Light-harvesting nanoparticle probes for FRET-based detection of oligonucleotides with single-molecule sensitivity. Angewandte Chemie [Internet]. [cited 2020 Jan 28];n/a(n/a). Available from: https://onlinelibrary-wiley-com.scd-rproxy.u-strasbg.fr/doi/abs/10.1002/ange.201913804

134. Jeon SI, Lee JH, Andrade JD, De Gennes PG. Protein—surface interactions in the presence of polyethylene oxide. Journal of Colloid and Interface Science. 1991 Mar 1;142(1):149–58.

135. Reisch A, Runser A, Arntz Y, Mély Y, Klymchenko AS. Charge-controlled nanoprecipitation as a modular approach to ultrasmall polymer nanocarriers: making bright and stable nanoparticles. ACS Nano. 2015 May 26;9(5):5104–16.

136. Müller J, Bauer KN, Prozeller D, Simon J, Mailänder V, Wurm FR, et al. Coating nanoparticles with tunable surfactants facilitates control over the protein corona. Biomaterials. 2017 Jan;115:1–8.

137. Lee Y-D, Lim C-K, Kim S, Kwon IC, Kim J. Squaraine-Doped Functional Nanoprobes: Lipophilically Protected Near-Infrared Fluorescence for Bioimaging. Adv Funct Mater. 2010;20(17):2786–93.

138. Sapsford KE, Algar WR, Berti L, Gemmill KB, Casey BJ, Oh E, et al. Functionalizing Nanoparticles with Biological Molecules: Developing Chemistries that Facilitate Nanotechnology. Chem Rev. 2013 Mar 13;113(3):1904–2074.

139. Jo A, Zhang R, Allen IC, Riffle JS, Davis RM. Design and Fabrication of Streptavidin-Functionalized, Fluorescently Labeled Polymeric Nanocarriers. Langmuir. 2018 Dec 26;34(51):15783–94.

140. Wang D, Qian J, He S, Park JS, Lee K-S, Han S, et al. Aggregation-enhanced fluorescence in PEGylated phospholipid nanomicelles for in vivo imaging. Biomaterials. 2011 Sep 1;32(25):5880–8.

141. Krovi SA, Smith D, Nguyen ST. “Clickable” polymer nanoparticles: a modular scaffold for surface functionalization. Chem Commun (Camb). 2010 Aug 7;46(29):5277–9.

142. Kamphuis MMJ, Johnston APR, Such GK, Dam HH, Evans RA, Scott AM, et al. Targeting of Cancer Cells Using Click-Functionalized Polymer Capsules. J Am Chem Soc. 2010 Nov 17;132(45):15881–3.

143. Dunst S, Tomancak P. Imaging Flies by Fluorescence Microscopy: Principles, Technologies, and Applications. Genetics. 2019 Jan 1;211(1):15–34.

144. Croce AC, Bottiroli G. Autofluorescence spectroscopy and imaging: a tool for biomedical research and diagnosis. Eur J Histochem. 2014 Dec 12;58(4):2461.

145. Sy M, Nonat A, Hildebrandt N, Charbonnière LJ. Lanthanide-based luminescence biolabelling. Chem Commun. 2016 Mar 31;52(29):5080–95.

146. Yildiz A, Selvin PR. Fluorescence Imaging with One Nanometer Accuracy: Application to Molecular Motors. Acc Chem Res. 2005 Jul 1;38(7):574–82.

147. Hell SW, Wichmann J. Breaking the diffraction resolution limit by stimulated emission: stimulated-emission-depletion fluorescence microscopy. Opt Lett. 1994 Jun 1;19(11):780–2.

148. Klar TA, Jakobs S, Dyba M, Egner A, Hell SW. Fluorescence microscopy with diffraction resolution barrier broken by stimulated emission. Proc Natl Acad Sci USA. 2000 Jul 18;97(15):8206–10.

149. Hess ST, Girirajan TPK, Mason MD. Ultra-high resolution imaging by fluorescence photoactivation localization microscopy. Biophys J. 2006 Dec 1;91(11):4258–72.

150. Sharonov A, Hochstrasser RM. Wide-field subdiffraction imaging by accumulated binding of diffusing probes. PNAS. 2006 Dec 12;103(50):18911–6.

151. Dunst S, Tomancak P. Imaging Flies by Fluorescence Microscopy: Principles, Technologies, and Applications. Genetics. 2019 Jan 1;211(1):15–34.

152. Magidson V, Khodjakov A. Chapter 23 - Circumventing Photodamage in Live-Cell Microscopy. In: Sluder G, Wolf DE, editors. Methods in Cell Biology [Internet]. Academic Press; 2013 [cited 2020 Jan 13]. p. 545–60. (Digital Microscopy; vol. 114). Available from: http://www.sciencedirect.com/science/article/pii/B9780124077614000233

153. Docter D, Westmeier D, Markiewicz M, Stolte S, Knauer SK, Stauber RH. The nanoparticle biomolecule corona: lessons learned – challenge accepted? Chem Soc Rev. 2015 Aug 17;44(17):6094–121.

154. Tyagi S. Imaging intracellular RNA distribution and dynamics in living cells. Nat Methods. 2009 May;6(5):331–8.

155. Zhang J, Fei J, Leslie BJ, Han KY, Kuhlman TE, Ha T. Tandem Spinach Array for mRNA Imaging in Living Bacterial Cells. Sci Rep. 2015 Nov 27;5:17295.

156. Anderluh A, Klotzsch E, Ries J, Reismann AWAF, Weber S, Fölser M, et al. Tracking Single Serotonin Transporter Molecules at the Endoplasmic Reticulum and Plasma Membrane. Biophys J. 2014 May 6;106(9):L33–5.

157. Anderluh A, Hofmaier T, Klotzsch E, Kudlacek O, Stockner T, Sitte HH, et al. Direct PIP 2 binding mediates stable oligomer formation of the serotonin transporter. Nat Commun. 2017 Jan 19;8(1):1–9.

158. Di Paolo D, Afanzar O, Armitage JP, Berry RM. Single-molecule imaging of electroporated dye-labelled CheY in live Escherichia coli. Philos Trans R Soc Lond, B, Biol Sci. 2016 05;371(1707).

159. Hansen SD, Zuchero JB, Mullins RD. Cytoplasmic Actin: Purification and Single Molecule Assembly Assays. Methods Mol Biol. 2013;1046:145–70.

160. Kuhn JR, Pollard TD. Single Molecule Kinetic Analysis of Actin Filament Capping POLYPHOSPHOINOSITIDES DO NOT DISSOCIATE CAPPING PROTEINS. J Biol Chem. 2007 Sep 21;282(38):28014–24.

161. Zimmermann D, Santos A, Kovar DR, Rock RS. Actin Age Orchestrates Myosin-5 and Myosin-6 Runlengths. Curr Biol. 2015 Aug 3;25(15):2057–62.

162. Hansen SD, Mullins RD. VASP is a processive actin polymerase that requires monomeric actin for barbed end association. J Cell Biol. 2010 Nov 1;191(3):571–84.

163. Pierobon P, Achouri S, Courty S, Dunn AR, Spudich JA, Dahan M, et al. Velocity, processivity, and individual steps of single myosin V molecules in live cells. Biophys J. 2009 May 20;96(10):4268–75.

164. Nelson SR, Ali MY, Trybus KM, Warshaw DM. Random walk of processive, quantum dot-labeled myosin Va molecules within the actin cortex of COS-7 cells. Biophys J. 2009 Jul 22;97(2):509–18.

165. Genin E, Gao Z, Varela JA, Daniel J, Bsaibess T, Gosse I, et al. “Hyper-bright” near-infrared emitting fluorescent organic nanoparticles for single particle tracking. Adv Mater Weinheim. 2014 Apr 9;26(14):2258–61, 2257.

166. Fang X, Chen X, Li R, Liu Z, Chen H, Sun Z, et al. Multicolor Photo-Crosslinkable AIEgens toward Compact Nanodots for Subcellular Imaging and STED Nanoscopy. Small. 2017;13(41):1702128.

167. Jin D, Xi P, Wang B, Zhang L, Enderlein J, Oijen AM van. Nanoparticles for super-resolution microscopy and single-molecule tracking. Nat Methods. 2018 Jun;15(6):415–23.

168. Zhan Q, Liu H, Wang B, Wu Q, Pu R, Zhou C, et al. Achieving high-efficiency emission depletion nanoscopy by employing cross relaxation in upconversion nanoparticles. Nat Commun. 2017 20;8(1):1058.

169. Leménager G, Luca ED, Sun Y-P, Pompa PP. Super-resolution fluorescence imaging of biocompatible carbon dots. Nanoscale. 2014 Jul 11;6(15):8617–23.

170. Yu J, Wu C, Sahu SP, Fernando LP, Szymanski C, McNeill J. Nanoscale 3D Tracking with Conjugated Polymer Nanoparticles. J Am Chem Soc. 2009 Dec 30;131(51):18410–4.

171. Chen X, Li R, Liu Z, Sun K, Sun Z, Chen D, et al. Small Photoblinking Semiconductor Polymer Dots for Fluorescence Nanoscopy. Advanced Materials. 2017;29(5):1604850.

172. Liu M, Li Q, Liang L, Li J, Wang K, Li J, et al. Real-time visualization of clustering and intracellular transport of gold nanoparticles by correlative imaging. Nat Commun [Internet]. 2017 May 31 [cited 2020 Feb 12];8. Available from: https://www.ncbi.nlm.nih.gov/pmc/articles/PMC5460036/

173. Reisch A, Trofymchuk K, Runser A, Fleith G, Rawiso M, Klymchenko AS. Tailoring Fluorescence Brightness and Switching of Nanoparticles through Dye Organization in the Polymer Matrix. ACS Appl Mater Interfaces. 2017 Dec 13;9(49):43030–42.

174. Bhattacharjee S. DLS and zeta potential – What they are and what they are not? Journal of Controlled Release. 2016 Aug 10;235:337–51.

175. Atomic World - Transmission electron microscope(TEM) - Principle of TEM [Internet]. [cited 2019 Dec 13]. Available from: http://www.hk-phy.org/atomic_world/tem/tem02_e.html

176. Thompson NL. Fluorescence Correlation Spectroscopy. In: Lakowicz JR, editor. Topics in Fluorescence Spectroscopy: Techniques [Internet]. Boston, MA: Springer US; 1999 [cited 2020 Jan 28]. p. 337–78. (Topics in Fluorescence Spectroscopy). Available from: https://doi.org/10.1007/0-306-47057-8_6

177. Krichevsky O, Bonnet G. Fluorescence correlation spectroscopy: the technique and its applications. Rep Prog Phys. 2002 Jan;65(2):251–297.

178. Lakowicz JR. Principles of Fluorescence Spectroscopy [Internet]. 3rd ed. Springer US; 2006 [cited 2019 Aug 8]. Available from: https://www.springer.com/gp/book/9780387312781

179. Mobility & Interaction Measurements [Internet]. [cited 2019 Dec 13]. Available from: https://malone.bioquant.uni-heidelberg.de/methods/mobility/mobility.html

180. Würth C, Geissler D, Behnke T, Kaiser M, Resch-Genger U. Critical review of the determination of photoluminescence quantum yields of luminescent reporters. Anal Bioanal Chem. 2015 Jan;407(1):59–78.

181. lynn.savage@photonics.com LS Features Editor. Improving Plant Cell Analysis Requires Good TIRF [Internet]. [cited 2020 Jan 10]. Available from: https://www.photonics.com/Articles/Improving_Plant_Cell_Analysis_Requires_Good_TIRF/a48690

182. Tinevez J-Y, Perry N, Schindelin J, Hoopes GM, Reynolds GD, Laplantine E, et al. TrackMate: An open and extensible platform for single-particle tracking. Methods. 2017 Feb 15;115:80–90.

183. Luby-Phelps K. Cytoarchitecture and physical properties of cytoplasm: volume, viscosity, diffusion, intracellular surface area. Int Rev Cytol. 2000;192:189–221.

184. Etoc F, Balloul E, Vicario C, Normanno D, Liße D, Sittner A, et al. Non-specific interactions govern cytosolic diffusion of nanosized objects in mammalian cells. Nature Mater. 2018 Aug;17(8):740–6.

185. Lince F, Marchisio DL, Barresi AA. Strategies to control the particle size distribution of poly-ε-caprolactone nanoparticles for pharmaceutical applications. Journal of Colloid and Interface Science. 2008 Jun 15;322(2):505–15.

186. Johnson BK, Prud'homme RK. Chemical processing and micromixing in confined impinging jets. AIChE Journal. 2003;49(9):2264–82.

187. D'Addio SM, Prud'homme RK. Controlling drug nanoparticle formation by rapid precipitation. Advanced Drug Delivery Reviews. 2011 May 30;63(6):417–26.

188. Beck-Broichsitter M, Nicolas J, Couvreur P. Solvent selection causes remarkable shifts of the "Ouzo region" for poly(lactide- co -glycolide) nanoparticles prepared by nanoprecipitation. Nanoscale. 2015;7(20):9215–21.

189. Khan SA, Schneider M. Improvement of Nanoprecipitation Technique for Preparation of Gelatin Nanoparticles and Potential Macromolecular Drug Loading. Macromolecular Bioscience. 2013;13(4):455–63.

190. Seremeta KP, Chiappetta DA, Sosnik A. Poly(ε-caprolactone), Eudragit® RS 100 and poly(ε-caprolactone)/Eudragit® RS 100 blend submicron particles for the sustained release of the antiretroviral efavirenz. Colloids and Surfaces B: Biointerfaces. 2013 Feb 1;102:441–9.

191. Mora-Huertas CE, Fessi H, Elaissari A. Influence of process and formulation parameters on the formation of submicron particles by solvent displacement and emulsification–diffusion methods: Critical comparison. Advances in Colloid and Interface Science. 2011 Apr 14;163(2):90–122.

192. Schneider J, Jallouk AP, Vasquez D, Thomann R, Forget A, Pino CJ, et al. Surface Functionality as a Means to Impact Polymer Nanoparticle Size and Structure. Langmuir. 2013 Mar 26;29(12):4092–5.

193. Horn D, Rieger J. Organic Nanoparticles in the Aqueous Phase—Theory, Experiment, and Use. Angewandte Chemie International Edition. 2001;40(23):4330–61.

194. Saad WS, Prud'homme RK. Principles of nanoparticle formation by flash nanoprecipitation. Nano Today. 2016 Apr 1;11(2):212–27.

195. Stephens DJ, Pepperkok R. The many ways to cross the plasma membrane. Proc Natl Acad Sci U S A. 2001 Apr 10;98(8):4295–8.

196. E. Grady M, Parrish E, A. Caporizzo M, C. Seeger S, J. Composto R, M. Eckmann D. Intracellular nanoparticle dynamics affected by cytoskeletal integrity. Soft Matter. 2017;13(9):1873–80.

197. Kalwarczyk T, Zięba cz N, Bielejewska A, Zaboklicka E, Koynov K, Szymański J, et al. Comparative Analysis of Viscosity of Complex Liquids and Cytoplasm of Mammalian Cells at the Nanoscale. Nano Lett. 2011 May 11;11(5):2157–63.

198. Li H, Dou S-X, Liu Y-R, Li W, Xie P, Wang W-C, et al. Mapping intracellular diffusion distribution using single quantum dot tracking: compartmentalized diffusion defined by endoplasmic reticulum. J Am Chem Soc. 2015 Jan 14;137(1):436–44.

199. Andreiuk B, Reisch A, Bernhardt E, Klymchenko AS. Fighting Aggregation-Caused Quenching and Leakage of Dyes in Fluorescent Polymer Nanoparticles: Universal Role of Counterion. Chemistry – An Asian Journal. 2019;14(6):836–46.

200. Middleton JC, Tipton AJ. Synthetic biodegradable polymers as orthopedic devices. Biomaterials. 2000 Dec 1;21(23):2335–46.

201. Colby KA, Burdett JJ, Frisbee RF, Zhu L, Dillon RJ, Bardeen CJ. Electronic Energy Migration on Different Time Scales: Concentration Dependence of the Time-Resolved Anisotropy and Fluorescence Quenching of Lumogen Red in Poly(methyl methacrylate). J Phys Chem A. 2010 Mar 18;114(10):3471–82.

202. Etoc F, Balloul E, Vicario C, Normanno D, Liße D, Sittner A, et al. Non-specific interactions govern cytosolic diffusion of nanosized objects in mammalian cells. Nature Materials. 2018 Aug;17(8):740–6.

203. Xu M, Soliman MG, Sun X, Pelaz B, Feliu N, Parak WJ, et al. How Entanglement of Different Physicochemical Properties Complicates the Prediction of in Vitro and in Vivo Interactions of Gold Nanoparticles. ACS Nano. 2018 Oct 23;12(10):10104–13.

204. Walkey CD, Chan WCW. Understanding and controlling the interaction of nanomaterials with proteins in a physiological environment. Chem Soc Rev. 2012 Mar 12;41(7):2780–99.

205. Monopoli MP, Åberg C, Salvati A, Dawson KA. Biomolecular coronas provide the biological identity of nanosized materials. Nat Nano. 2012 Dec;7(12):779–86.

206. Ke PC, Lin S, Parak WJ, Davis TP, Caruso F. A Decade of the Protein Corona. ACS Nano. 2017 26;11(12):11773–6.

207. Jokerst JV, Lobovkina T, Zare RN, Gambhir SS. Nanoparticle PEGylation for imaging and therapy. Nanomedicine. 2011 Jun 1;6(4):715–28.

208. Suk JS, Xu Q, Kim N, Hanes J, Ensign LM. PEGylation as a strategy for improving nanoparticle-based drug and gene delivery. Advanced Drug Delivery Reviews. 2016 Apr 1;99, Part A:28–51.

209. Estephan ZG, Schlenoff PS, Schlenoff JB. Zwitteration As an Alternative to PEGylation. Langmuir. 2011 Jun 7;27(11):6794–800.

210. Reisch A, Runser A, Arntz Y, Mély Y, Klymchenko AS. Charge-Controlled Nanoprecipitation as a Modular Approach to Ultrasmall Polymer Nanocarriers: Making Bright and Stable Nanoparticles. ACS Nano. 2015 May 26;9(5):5104–16.

211. Bangham AD. A Correlation between Surface Charge and Coagulant Action of Phospholipids. Nature. 1961 Dezember;192(4808):1197–8.

212. García KP, Zarschler K, Barbaro L, Barreto JA, O'Malley W, Spiccia L, et al. Zwitterionic-Coated "Stealth" Nanoparticles for Biomedical Applications: Recent Advances in Countering Biomolecular Corona Formation and Uptake by the Mononuclear Phagocyte System. Small. 2014 Jul 1;10(13):2516–29.

213. Schlenoff JB. Zwitteration: Coating Surfaces with Zwitterionic Functionality to Reduce Nonspecific Adsorption. Langmuir. 2014 Aug 19;30(32):9625–36.

214. Tasso M, Giovanelli E, Zala D, Bouccara S, Fragola A, Hanafi M, et al. Sulfobetaine–Vinylimidazole Block Copolymers: A Robust Quantum Dot Surface Chemistry Expanding Bioimaging's Horizons. ACS Nano. 2015 Nov 24;9(11):11479–89.

215. Rosen JE, Gu FX. Surface Functionalization of Silica Nanoparticles with Cysteine: A Low-Fouling Zwitterionic Surface. Langmuir. 2011 Sep 6;27(17):10507–13.

216. Moyano DF, Saha K, Prakash G, Yan B, Kong H, Yazdani M, et al. Fabrication of Corona-Free Nanoparticles with Tunable Hydrophobicity. ACS Nano. 2014 Jul 22;8(7):6748–55.

217. O'Hare HM, Johnsson K, Gautier A. Chemical probes shed light on protein function. Curr Opin Struct Biol. 2007 Aug;17(4):488–94.

218. Petershans A, Wedlich D, Fruk L. Bioconjugation of CdSe/ZnS nanoparticles with SNAP tagged proteins. Chem Commun. 2011 Sep 20;47(38):10671–3.

219. Farlow J, Seo D, Broaders KE, Taylor MJ, Gartner ZJ, Jun Y. Formation of targeted monovalent quantum dots by steric exclusion. Nat Methods. 2013 Dec;10(12):1203–5.

220. Wichner SM, Mann VR, Powers AS, Segal MA, Mir M, Bandaria JN, et al. Covalent Protein Labeling and Improved Single-Molecule Optical Properties of Aqueous CdSe/CdS Quantum Dots. ACS Nano. 2017 25;11(7):6773–81.

221. Keppler A, Pick H, Arrivoli C, Vogel H, Johnsson K. Labeling of fusion proteins with synthetic fluorophores in live cells. PNAS. 2004 Jul 6;101(27):9955–9.

222. C. Jewett J, R. Bertozzi C. Cu-free click cycloaddition reactions in chemical biology. Chemical Society Reviews. 2010;39(4):1272–9.

223. Eberhardt M, Mruk R, Zentel R, Théato P. Synthesis of pentafluorophenyl(meth)acrylate polymers: New precursor polymers for the synthesis of multifunctional materials. European Polymer Journal. 2005 Jul 1;41(7):1569–75.

224. Singha NK, Gibson MI, Koiry BP, Danial M, Klok H-A. Side-Chain Peptide-Synthetic Polymer Conjugates via Tandem “Ester-Amide/Thiol–Ene” Post-Polymerization Modification of Poly(pentafluorophenyl methacrylate) Obtained Using ATRP. Biomacromolecules. 2011 Aug 8;12(8):2908–13.

Annexes

Article 2 : Protein-Sized Dye-Loaded Polymer Nanoparticles for Free Particle Diffusion in Cytosol.

FULL PAPER

Nanoparticles in the Cytosol

ADVANCED FUNCTIONAL MATERIALS
www.afm-journal.de

Protein-Sized Dye-Loaded Polymer Nanoparticles for Free Particle Diffusion in Cytosol

Andreas Reisch, Doriane Heimburger, Pauline Ernst, Anne Runser, Pascal Didier, Denis Dujardin, and Andrey S. Klymchenko**

How small should nanoparticles be in order to travel freely through the cytosol similar to proteins? Answering this question remains a challenge, because the majority of nanoparticles are relatively large and their size cannot be finely tuned to match that of proteins. Here, poly(methyl methacrylate) copolymers with varied fraction and type of charged groups (carboxylate, sulfonate, and trimethylammonium) are developed, yielding nanoparticles with controlled sizes from 50 to 7 nm through nanoprecipitation. Loading these nanoparticles with a rhodamine dye/bulky counterion pair at 10wt% makes them highly fluorescent. After their coating with polyethylene glycol groups for preventing non-specific protein binding and microinjection into living cells, the first systematic study of the size effect on diffusion in the cytosol for solid nanoparticles of the same nature is realized. Single-particle-tracking data provide evidence for distinct particle sieving in the cytosol, suggesting that only nanoparticles below a critical size of 23 nm exhibit free diffusion and spreading. These findings show the size limitations imposed by intracellular crowding and compartmentalization, which is critical for applications of nanomaterials in the cytosol. The proposed concept of polymer design opens the route to organic nanoparticles of ultrasmall sizes and high loading for bioimaging and drug-delivery applications.

1. Introduction

Proteins are nature's ultimate nanoparticles (NPs), combining a large spectrum of functionalities with highest specificity, a size small enough to access nearly any desired location, and biodegradability. In consequence, ultrasmall polymer NPs mimicking their behavior have a high potential as bioimaging agents and drug carriers.[1,2] They could, for example, play a key role in single-molecule imaging of biomolecules inside living cells using fluorescence microscopy. Studying the behavior of single molecules is of key importance for the understanding of biological processes at the molecular level, but requires labeling of the biomolecules of interest with fluorescent probes.[3–5] The speed and resolution, with which the biomolecules can then be tracked, depend on the number of collected photons.[6] In consequence, the brightness of the probe is particularly important, especially as already quite low light intensities can alter the behavior of cells.[7–9] At the same time, the probes themselves should not interfere with the studied biological systems. Ideal probes would thus combine high brightness with small size, close to that of single proteins,[10,11] and absence of non-specific interactions.[12–14]

The limited brightness of organic fluorophores and fluorescent proteins, can be overcome by using fluorescent NPs.[15–17] The most popular examples include quantum dots (QDs),[13,18–20] dye-doped silica NPs,[21] NPs based on the assembly of dyes,[22,23] conjugated polymer NPs,[24–27] aggregation induced emission NPs,[28,29] dye-loaded polymer NPs,[30,31] etc. The latter appeared recently as systems with exceptional brightness,[32,33] which already found applications in super-resolution imaging,[32] amplified single-molecule detection,[34] and multicolor cellular imaging.[35,36]

Non-specific interactions of NPs with biological molecules, on the other hand, can be suppressed through modification of the surface with polyethylene glycol (PEG) or other hydrophilic groups as zwitterions.[37,38] However, what is the ideal size of NPs for intracellular applications, notably in view of the crowded and complex structure of the cytosol?[39–44] Do NPs have to be as small as proteins, or is the size of endosomes sufficient? Indeed, while the influence of NP size on their fate in vivo[45,46] or on the interactions with cells has been evaluated in detail,[47,48] studies on its influence on intracellular diffusion of solid NPs, especially on the single-particle level, are largely missing. Size dependence of intracellular behavior has, up to now, mainly been studied for macromolecules as dextrans[49] and DNA[50] using ensemble methods.[41,42,51] These macromolecular nanoscale objects are, however, expected to behave, in view of their deformability, totally different from "hard" (solid) NPs, such as QDs, magnetic, carbon, and silica NPs or NPs based on hydrophobic polymers. Although solid particles have been extensively studied in biological and biomedical fields for imaging to drug-delivery applications,[15,16,52–54] the effect of their size on the intracellular diffusion at the single-particle level has not been systematically

Dr. A. Reisch, D. Heimburger, P. Ernst, A. Runser, Prof. P. Didier, Dr. D. Dujardin, Dr. A. S. Klymchenko
Laboratoire de Bioimagerie et Pathologies
UMR 7021 CNRS
Faculté de Pharmacie
Université de Strasbourg
67401 Illkirch, France
E-mail: reisch@unistra.fr; andrey.klymchenko@unistra.fr

The ORCID identification number(s) for the author(s) of this article can be found under https://doi.org/10.1002/adfm.201805157.

DOI: 10.1002/adfm.201805157

 © 2018 WILEY-VCH Verlag GmbH & Co. KGaA, Weinheim

ADVANCED SCIENCE NEWS
www.advancedsciencenews.com

ADVANCED FUNCTIONAL MATERIALS
www.afm-journal.de

investigated. A probable reason is that it remains a challenge to prepare a series of fluorescent NPs of the same nature with finely tuned sizes down to the level of single proteins, while maintaining a sufficient brightness for single-particle visualization.[55] To evaluate the optimal size for intracellular imaging, we consider dye-loaded polymer NPs to be excellent candidates.

Approaches to the synthesis of small polymeric NPs include notably different types of emulsion polymerizations[56,57] and self-assembly of block copolymers.[58,59] Nanoprecipitation of preformed polymers is a simple technique for preparation of NPs, which also allows encapsulation of drugs and contrast agents.[60,61] In order to reduce the size of polymeric NPs in the latter case, controlling the parameters of nanoprecipitation, e.g. the presence of charged groups,[62] concentration,[63] mixing speed,[64] and type of solvent,[65] can be successfully employed. However, so far, dye-loaded polymer NPs, assembled through nanoprecipitation, had never reached sizes of ≤10 nm, which would match the dimensions of proteins. Here, we varied the type and the fraction of charged groups on poly(methyl methacrylate) (PMMA) to reduce maximally the size of dye-loaded polymer NPs. This allowed us to create series of particles of the same nature and surfaces but varying size. We then studied the influence of the size and surface of these particles on their behavior in the cytosol. The observed size-dependent diffusion of the particles has profound consequences for understanding steric restrictions imposed by the cytosol on nanomaterials, which is of key importance for their intracellular applications.

2. Results and Discussion

2.1. Polymer Synthesis and Nanoparticle Assembly and Characterization

Three series of methyl methacrylate-based copolymers bearing either carboxylic acid, sulfonate or trimethylammonium groups in their side chains were synthesized (**Scheme 1**). The percentage of charged groups was varied from 1 to 10 mol%. Polymerization yielded copolymers with molecular weights around 50 000 for carboxylate and sulfonate polymers and 90 000 for trimethylammonium polymers. The fraction of charged groups in the polymers could be well controlled and was, according to NMR, close to the fraction in the feed. These polymers, dissolved in acetonitrile, were then nanoprecipitated in water to yield NPs. Their size decreased systematically with increasing percentage of charged groups (**Figure 1**). For sulfonate and trimethylammonium-bearing polymers the size reached 8 and 7 nm, respectively, at ≥5% of charged groups. This corresponds to approximately 8 and 4 polymer chains per NP at the obtained molecular weights. At 10% of sulfonate groups transmission electron microscopy (TEM) images did not show particles anymore, but rather deposition of unstructured polymer, indicating a limit to particle formation. Particles made from carboxylate bearing polymers were systematically larger, though the size was reduced using buffer at pH 7.4 (Figure S2, Supporting Information). Fluorescence correlation spectroscopy (FCS) was used to measure the hydrodynamic diameter of the particles (**Figure 2**). These results confirmed the trends observed by TEM, giving nearly identical sizes for the small sulfonate particles [17, 13, and 9 nm for 1, 2, and 5% PMMA-SO_3H (poly(methyl methacrylate-co-3-sulfopropyl methacrylate)) NPs, respectively]. A bit larger sizes were observed for the larger NPs [86 nm for poly(methyl methacrylate-comethacrylic acid) (PMMA-COOH) 1% NPs and 53 nm for PMMA-SO_3H 1% NPs made in 30×10^{-3} M NaCl] due to the stronger contribution of larger particles to the fluorescence signal.

For sulfonate and trimethylammonium polymers, the number of charged groups per particle was around 100 independently of polymer composition and thus particle size (Table S1, Supporting Information). Particle growth and thus incorporation of new polymers in the NPs, hence, stopped once this threshold was reached, probably due to electrostatic repulsion.

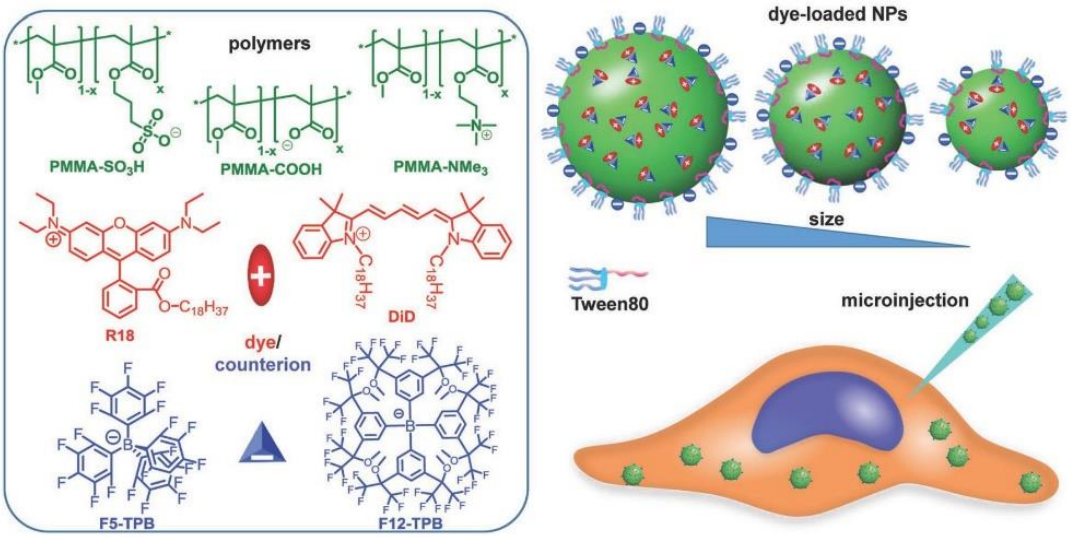

Scheme 1. Structures of polymers, dyes, and counterions used in this study, and schematic representation of preparation of dye-loaded NPs of different sizes and their microinjection.

© 2018 WILEY-VCH Verlag GmbH & Co. KGaA, Weinheim

ADVANCED SCIENCE NEWS
www.advancedsciencenews.com

ADVANCED FUNCTIONAL MATERIALS
www.afm-journal.de

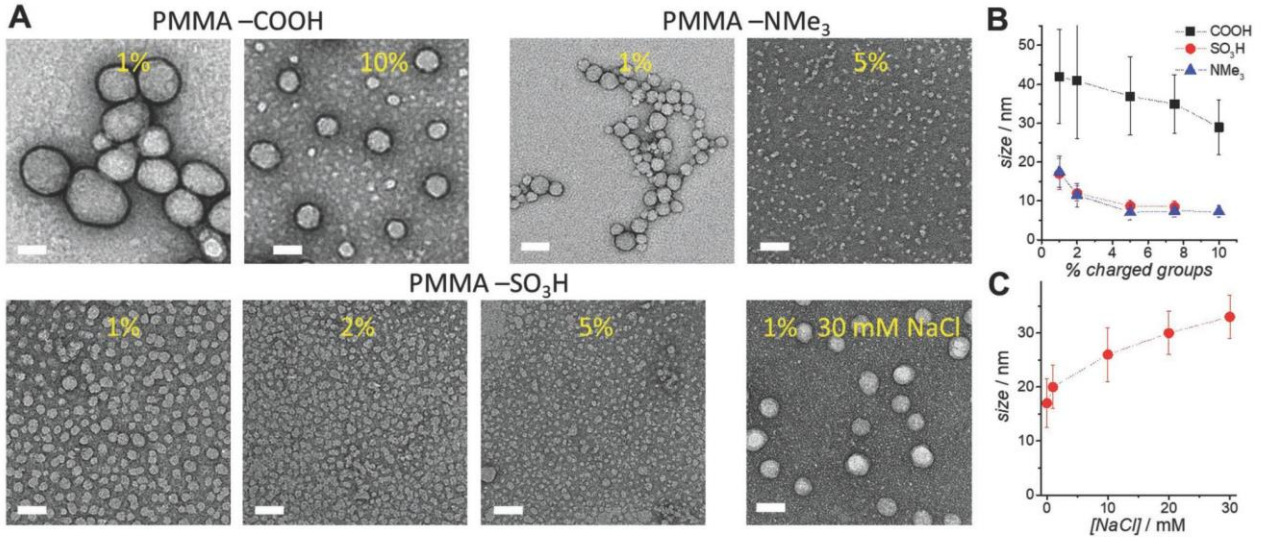

Figure 1. Sizes of NPs made by nanoprecipitation: A) TEM images of NPs made from different polymers in water or 30×10^{-3} M NaCl. Scale bars, 50 nm. B) Influence of the fraction of charged groups on the size of NPs. C) Influence of NaCl concentration in the precipitation medium on the size of PMMA-SO_3H 1% NPs. In (B) and (C), mean values of sizes determined by TEM are given for NPs loaded with 10 wt% of R18/F5-TPB. At least 200 NPs were analyzed per condition. Error bars give full width at half-maximum of the distribution.

In consequence, the particle size decreased for more charged polymer. In MilliQ water, the Debye screening length exceeds 10 nm and thus all the charges on these small NPs can contribute to repulsion of an incoming chain. By contrast, the effective charge of the carboxylate groups in MilliQ water is lower, and the particles thus reach sizes lager than the Debye screening length. In consequence, particle growth is stopped only when a given surface charge density is reached, as observed previously.[66,67] Importantly, addition of NaCl in the precipitation medium that decreases these repulsive forces allowed us to increase the size of particles made from a given polymer (Figure 1).

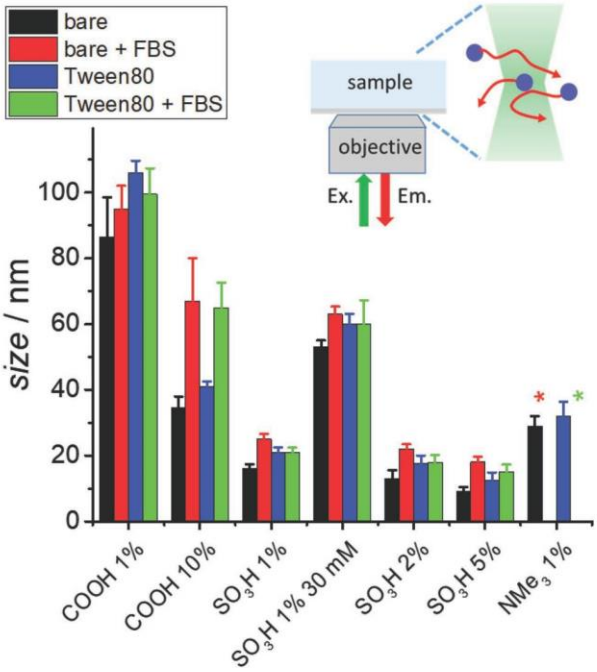

Figure 2. FCS on dye-loaded polymer NPs: hydrodynamic sizes of NPs with and without surface treatment with Tween 80 in different conditions as determined by FCS. Given are the sizes of as made NPs, NPs exposed to 10 vol% FBS solution, NPs pre-treated with 0.05 mg mL^{-1} Tween 80 and then exposed or not to 10 vol% FBS solution. NPs were loaded with 1 or 2 wt% of R18/F5-TPB. Error bars give SEM over three measurements. *Aggregation or no particles were detected. Inset: Schematic view of the FCS technique.

These NPs were made fluorescent through the encapsulation of 10 wt% of a rhodamine dye salt (R18/F5-TPB, wt% relative to polymer, Scheme 1).[32] The bulky counterion prevents aggregation of dyes in the polymer matrix, leading to high fluorescence quantum yields ≈50% even at this high loading (Table S2, Supporting Information). Consequently, the estimated brightness of 17, 12, and 9 nm PMMA-SO_3H NPs was 7×10^6, 2×10^6, and 7×10^5 M cm^{-1}, respectively, that is 25, 10, and 3 times higher than that of corresponding quantum dots (QD585) at 532 nm excitation. Fluorescence microscopy of single particles immobilized on surfaces confirmed these estimations (**Figure 3**A and Figure S4, Supporting Information), showing that our NPs are brighter than QDs despite their much smaller size.

2.2. Microinjection of Nanoparticles

In order to render these NPs resistant to protein adsorption they were treated with Tween 80, a PEG-bearing surfactant.[62] Their interaction with serum proteins was then studied with FCS (Figure 2). Adsorption of Tween 80 led to an increase of the particle size by ≈5 nm, which suggests adsorption of a monolayer. When solutions of 10% fetal bovine serum (FBS) were added to the resulting particles, the particle size for PMMA-SO_3H and 1%-PMMA-COOH NPs did not change, suggesting that a monolayer of Tween 80 is sufficient to suppress

 © 2018 WILEY-VCH Verlag GmbH & Co. KGaA, Weinheim

ADVANCED SCIENCE NEWS
www.advancedsciencenews.com

ADVANCED FUNCTIONAL MATERIALS
www.afm-journal.de

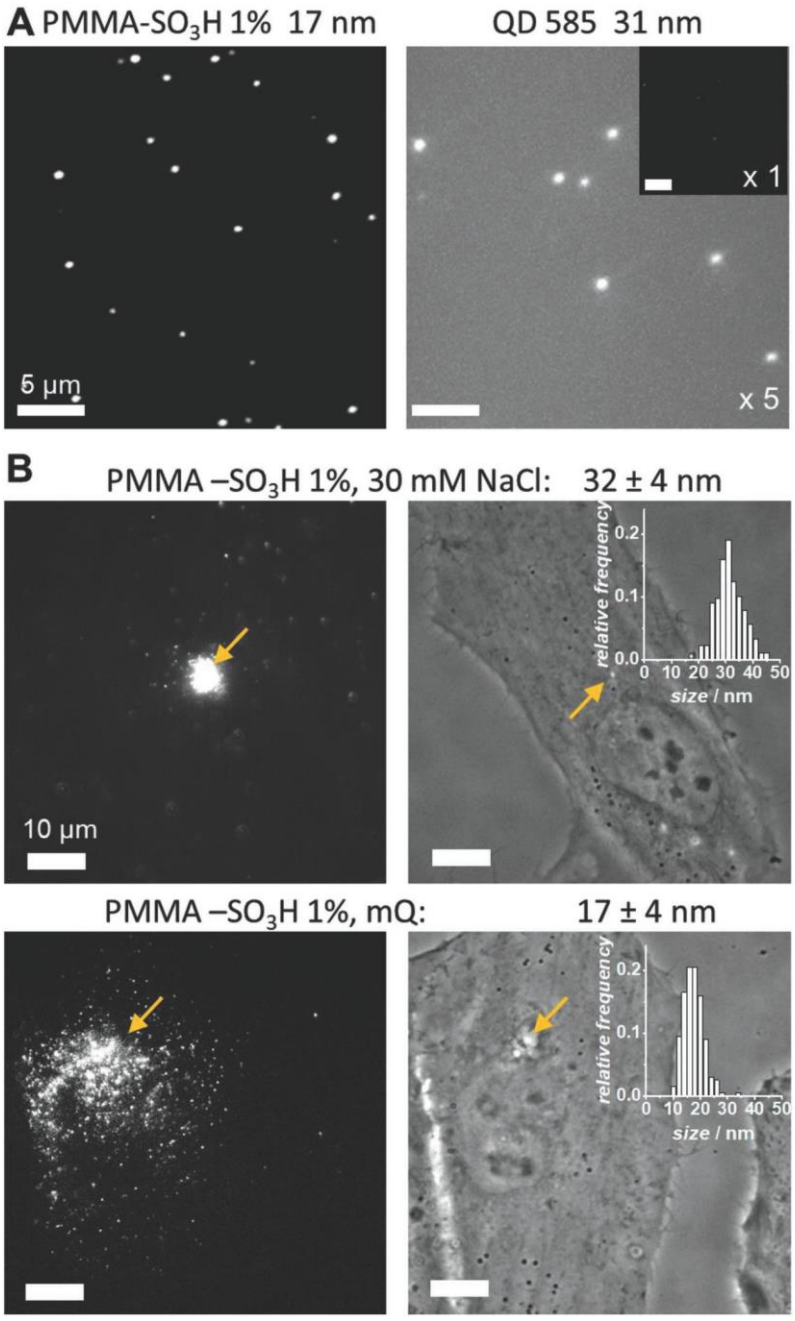

Figure 3. Microscopy of NPs on surfaces and in the cytosol. A) Microscopy images of PMMA-SO_3H 1% NPs loaded with 10 wt% R18/F5-TPB and of QDs 585 immobilized on a surface in TIRF mode (532 nm laser excitation, 12 W cm^{-2}). For better visibility, the QD intensity was increased fivefold (original in inset). Scale bars, 5 µm. B) Microinjection of NPs in living HeLa cells. Left hand: epi-fluorescence micrographs of 32 and 17 nm PMMA-SO_3H 1% NPs made in 30×10^{-3} M NaCl and MilliQ water, respectively. Right hand: phase-contrast images of the corresponding cells. Injection points are indicated by arrows. Scale bars, 10 µm. Insets show distributions of particle sizes obtained by TEM. NPs were loaded with 10 wt% of R18/F5-TPB and coated with Tween 80.

non-specific interactions with serum proteins. The behavior of these NPs treated with Tween 80 and having different sizes was then studied in the cytosol. For this, we microinjected solutions of NPs directly into the cytosol of living HeLa cells (Figure 3B, and Figure S5 for other NP types and videos in SI). Dye leaching from all used NPs was virtually absent, at least on the time scale of our study. Indeed, no diffuse intracellular labeling (notably of mitochondria) was observed, as would be expected for the case of leaching of the used R18 dye.[68,69] Individual NPs and their movement could be easily observed and tracked inside cells at low illumination intensities (2 W cm^{-2}). The vast majority of larger NPs (42 nm, and 29 nm NPs made of PMMA-COOH 1% and 10%, respectively, and 32 nm PMMA-SO_3H 1% particles, made in 30×10^{-3} M NaCl) remained close to the point of injection. Only very few of these particles actually moved inside the cell and their movements were restricted to the immediate surroundings of the injection point. However, smaller NPs of 17 nm, made from PMMA-SO_3H 1% in MilliQ water, spread practically through the entire cell. Most (≈90%) of these particles moved quickly throughout the cytosol (Figure 3B and Supporting Videos). This suggests a critical size required for efficient spreading throughout the cytosol. A closer look at the image sequences shows that some particles from 32-nm formulation spread inside the cells, whereas about 10% of particles from 17-nm formulation remained close to the point of injection. This phenomenon can be explained by non-negligible size distribution in these two formulations of NPs. The particle size distribution of the NPs from the 17-nm formulation (insets in Figure 3B) shows that about 10% of the particles are larger than 23 nm, while about 5% of NPs from the 32-nm formulation are smaller than 23 nm. This indicates that the actual critical size of the hard particle core for spreading throughout the cytosol is situated at around 23 nm.

We then studied the intracellular movement of these NPs in more detail. In particular, we wanted to know, whether and how a further reduction in the size of NPs would influence their movement inside cells. PMMA-SO_3H NPs of 12 and 9 nm size, as those of 17 nm, spread well throughout the cells and retained a high mobility (**Figure 4** and Figure S5, Supporting Information). A particularly good impression of the spreading of the particles can notably be obtained through a maximum projection of the particle fluorescence over a given observation time (**Figures 4A and 5**). We then performed single-particle-tracking analysis on 17 and 9 nm particles using threefold lower particle concentration

 © 2018 WILEY-VCH Verlag GmbH & Co. KGaA, Weinheim

ADVANCED SCIENCE NEWS
www.advancedsciencenews.com

ADVANCED FUNCTIONAL MATERIALS
www.afm-journal.de

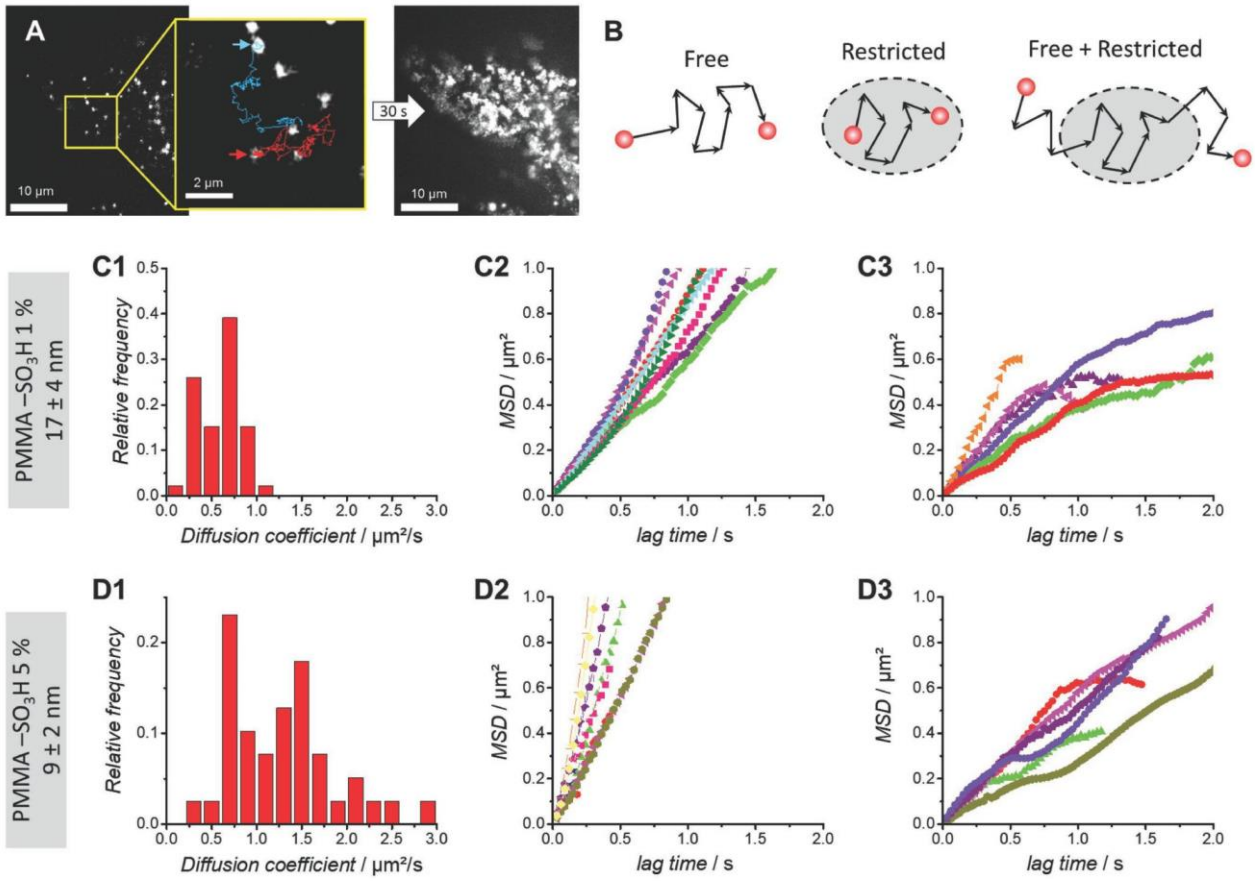

Figure 4. Diffusion of NPs in the cytosol studied by single-particle fluorescence microscopy. A) 17 nm PMMA-SO_3H NPs in a HeLa cell (HiLo mode, 532 nm laser excitation, 2 W cm^{-2}, 30 ms per frame). The trajectories of two particles (arrows) are shown. Right hand: maximum projection of the acquisition over 30 s. NPs were loaded with 10 wt% of R18/F5-TPB and coated with Tween 80. B) Three simplified cases of intracellular diffusion: free, restricted, and combination of free and restricted diffusion. Analysis of single-particle trajectories for PMMA-SO_3H 1% 17 nm NPs (C1–C3) and PMMA-SO_3H 5% 9 nm NPs (D1–D3). C1, D1) Distribution of diffusion coefficients as obtained from the initial slope of the MSD curves. C2, C3, D2, D3) MSD versus lag time for several representative trajectories, showing straight curves (C2, D2) and kinks (C3, D3). At least 60 trajectories from three different cells were analyzed per condition.

and a microscope operating in highly inclined and laminated optical sheet (HILO) mode[70] with laser illumination and an EMCCD camera. Plotting mean square displacement (MSD) versus time for individual trajectories allows characterizing the diffusion behavior, such as diffusion coefficient and type of diffusion (i.e., free, restricted diffusion or their combination, Figure 4B).[42,71,72] First, the initial slope can be used to extract the diffusion coefficient on a local scale for the 2D projection.[71,72] Both 17 and 9 nm NPs showed a broad (nearly bimodal) distribution of diffusion times, indicating that the diffusion of part of NPs (about 30%) was significantly slowed, probably due to non-specific interactions or a strong spatial restriction (Figure 4B, C1, and D1). The diffusion coefficients were centered ≈0.7 $\mu m^2\ s^{-1}$ for the 17 nm NPs and ≈1.5 $\mu m^2\ s^{-1}$ for the 9 nm NPs, corresponding to the higher mobility of the smaller particles. These values are considerably higher than diffusion coefficients obtained for QDs in the cytosol,[73–75] in line with the smaller size of our NPs. Second, further information on the movement of the particles can be obtained from the shape of the plots of MSD as a function of lag time (Figure 4C2, C3, D2, and D3): free Brownian diffusion is seen as a straight line; occurrence of plateaus or kinks indicates confined (restricted) diffusion, with the position of the plateau giving access to the size of the involved structures; and upward bending of the curves indicates superdiffusion often due to an active transport or a flow.[42,71,72] The latter was virtually absent for both particle sizes analyzed here. The relative importance of free-diffusive and subdiffusive behavior, however, was significantly different for 17 versus 9 nm NPs. In the case of 9 nm NPs more than 60% of the MSD curves were entirely straight indicating free diffusion. These corresponded mainly to those having high initial diffusion coefficients. Interestingly from the curves having visual kinks, corresponding to restricted diffusion, about 75% showed a stabilization or even a regain in the slope of the curve after the kink (Figure 4C, bottom right). This behavior indicates that the particles were able to overcome the spatial restrictions.[42,72] In the case of the 17 nm NPs only about 40% of the particles showed relatively straight MSD curves corresponding to free Brownian diffusion. Furthermore, in the cases where the MSD curves showed

 © 2018 WILEY-VCH Verlag GmbH & Co. KGaA, Weinheim

ADVANCED SCIENCE NEWS
www.advancedsciencenews.com

ADVANCED FUNCTIONAL MATERIALS
www.afm-journal.de

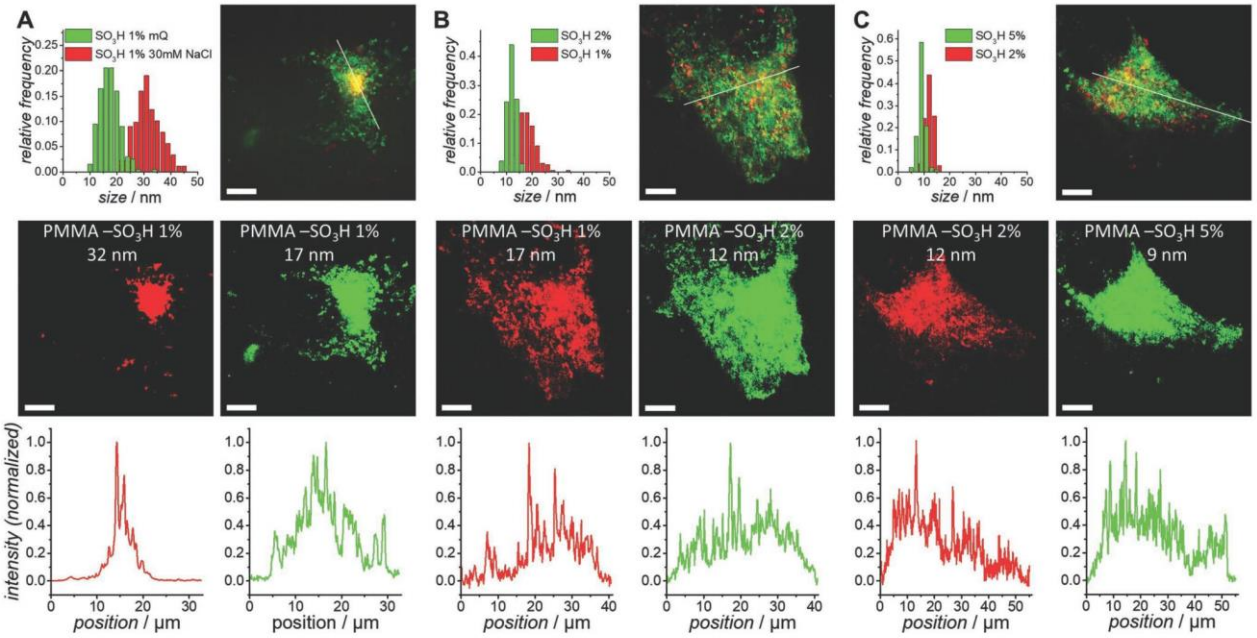

Figure 5. Two-color imaging of different sets of PMMA-SO_3H NPs co-microinjected into the cytosol. A) 32 nm (red) and 17 nm (green) NPs, prepared from PMMA-SO_3H 1% in 30×10^{-3} M NaCl and MilliQ water, respectively. B) 17 nm (red) and 12 nm (green) NPs. C) 12 nm (red) and 9 nm (green) NPs. Particles presented in red were loaded with 20×10^{-3} M DiD/F12-TPB, particles in green with 10 wt% of R18/F5-TPB, all were coated with Tween 80. In each part, the panels represent: top left: size distributions from TEM; top right: superposition of maximum projections over 1 min; middle: threshold images obtained from the projections; and bottom: intensity profiles along the lines indicated in top right. Scale bars, 10 µm.

kinks, most actually reached plateau values, indicating that particle movement was indeed restricted to certain regions.

In order to directly compare the intracellular behavior of different NPs of close sizes (and thus overcome cell-to-cell variations in injection or morphology), we performed pairwise comparison of a subset of NPs co-injected in the same cell. For this, we labeled two different types of NPs to be compared with dyes of different colors, a rhodamine (R18/F5-TPB) and a cyanine 5 (DiD/F12-TPB) (Scheme 1), mixed them at equivalent particle concentrations, and injected them together, before imaging them in two separate channels (Figure 5). Comparison of the 32 and 17 nm PMMA-SO_3H NPs confirmed the differences observed when injecting the particles in different cells (Figures 5A and 3B): localization and immobilization of the larger NPs around the injection point and spreading of the smaller ones. Co-injecting 17 and 12 nm PMMA-SO_3H NPs showed that both spread through the entire cell (Figure 5B). However, the 17 nm NPs were excluded from several intracellular regions where the 12 nm NPs had access (lower panels in Figure 5B). Finally, a comparison of 12 and 9 nm PMMA-SO_3H NPs showed slightly better accessibility of the latter mainly at the edge of cells with a flat morphology (Figure 5C).

We thus observed distinct diffusion behavior of solid NPs depending on their size: particles with sizes of 32 nm remained (on the time scale of our experiments) confined to the region of injection. Particles of 17 nm already spread throughout the entire cell. Comparison of the size distributions for these two types of NPs gave a critical size of 23 nm, below which NPs tended to spread well inside the cells. Smaller NPs of 12 and 9 nm showed improved access to some regions of the cytosol. Especially, the 9 nm NPs were capable to access regions at the edge of the cell, and were, based on the MSD curves better capable to escape from restricted compartments. It should be taken into account that the particle sized described here correspond to hard-sphere diameters estimated from TEM, whereas intracellular diffusion should be governed by the hydrodynamic diameter, which is somewhat larger (Figure 2).

These results can be compared to previous experimental data using mostly ensemble methods and deformable macromolecules as well as to different approaches to model diffusion in the cytosol.[39,40,42,51,76] From a structural point of view, a major barrier to diffusion is the cytoskeleton. Using different methods, mesh sizes in the range of 30–100 nm were found,[77,78] although even smaller particles of 10 nm were restricted in their movement by the actin cytoskeleton.[79] A second barrier to diffusion, notably in the perinuclear region, is constituted by the endoplasmatic reticulum (ER) and the Golgi apparatus. It has notably been observed that QDs of 27 nm and macromolecules of 48 nm were restricted in their movement by the ER and the trans-Golgi.[73,77] The increased density and finely divided filaments of the cytoskeleton at the edge of the cells were noted to restrict the access of macromolecules further, leading to strongly decreased partitioning for macromolecules larger than 20 nm.[77,80] The nucleus finally was only accessible to macromolecules smaller than 7 nm.[49] This suggests that spreading of our larger particles, injected in the perinuclear region, is limited by the ER and the Golgi in combination with the cytoskeleton. The critical size of 23 nm revealed in our work for hard particles is in good agreement with the lower mesh sizes found for the cytoskeleton (30 nm). This suggests that

 © 2018 WILEY-VCH Verlag GmbH & Co. KGaA, Weinheim

ADVANCED SCIENCE NEWS
www.advancedsciencenews.com

ADVANCED FUNCTIONAL MATERIALS
www.afm-journal.de

the smallest mesh sizes are effective for restricting the motion of hard particles. The diffusion restrictions for intermediate-sized particles of 17 nm, could notably stem from the spaces in-between cisternae of the Golgi and in voids of the ER, which create small compartments. Smaller particles can probably still escape relatively quickly from such compartments. Our results showed that particles larger than 10 nm were at least partially excluded from the edges of the cells, indicating again that the critical sizes for hard particles are smaller than those for deformable macromolecules. Finally, our particles did not significantly enter the nucleus and did not appear to localize specifically inside other intracellular compartments, in line with the size restrictions mentioned above.

In a different approach, the so-called length-scale-dependent viscosity model, the cytosol is considered as a heterogeneous, crowded mixture, and the viscosity experienced by a probe depends on its size (relative to that of the crowding agent) and on the relative crowding.[42,51] Two limiting dimensions of the diffusing particles emerge from this model: particles smaller than the correlation length feel the nanoscale viscosity of the solution and basically move freely in-between the obstacles. Particles with sizes above the limiting length, on the other hand, are subject to the macroscale viscosity. For these particles, the cytosol resembles a gel or even a colloidal glass strongly restricting their motion. For HeLa and Swiss 3T3 cells, these lengths were found, mainly based on DNA and dextrans, to be respectively 5 and 7 nm for the correlation length and 86 and 30 nm for the limiting size. Similar results were found for bacterial cytoplasm, with a critical size in the range of 30–40 nm for the diffusion of protein-based particles. Above this size the bacterial cytoplasm showed glass-like properties in the absence of metabolic activity.[81] With respect to this model even the sizes of the smallest particles studied here were already above the correlation length. The critical size of 23 nm found here is of the same order, yet again below that found for deformable macromolecules. Together these results show the influence and importance of particle size for the behavior of solid NPs, and, how these differ from the results obtained for deformable macromolecules, even though they follow the same trends.

3. Conclusions

In order to address the question of the optimal size of NPs for intracellular applications, we designed a series of dye-loaded polymer NPs with finely tuned sizes. The control of the fraction of charged groups, notably sulfonate and trimethylammonium, allowed achieving particle sizes below 10 nm, and thus attaining the sizes of proteins. Despite their small size these particles could be made brightly fluorescent (3–25-fold brighter than corresponding QDs) by encapsulating dyes at high concentration. This in turn made them suitable for single-particle tracking inside the cytosol even at low light excitation intensities. Using a series of NPs with sizes of 9, 12, 17, and 32 nm, we could evaluate for the first time the influence of particle size on the movement of solid particles in the cytosol: NPs below a critical size of ≤23 nm were required to obtain spreading throughout the living cell. Still smaller particle sizes are required to quickly reach all regions of the cytosol. Our findings on the size-dependent intracellular diffusion of solid particles are of highest importance for practically any application of NPs in the complex intracellular environment. Moreover, our concept of polymer design opens the route to organic NPs of ultrasmall sizes, which should enable high-speed tracking of single biomolecules with high localization precision.

4. Experimental Section

Materials: Methyl methacrylate (99%), methacrylic acid (99%), 3-sulfopropyl methacrylate potassium salt (98%), [2-(methacryloyloxy) ethyl]trimethylammonium chloride (75% in water), acetonitrile (anhydrous, 99.8%), rhodamine B octadecyl ester perchlorate (>98.0%), lithium tetrakis(pentafluorophenyl)borate ethyl etherate were purchased from Sigma–Aldrich.

R18/F5-TPB, the salt of Rhodamine B octadecyl ester with tetrakis(pentafluorophenyl)borate, and Cy5/F12-TPB (or DiD/F12-TPB), the salt of DiD with sodium tetrakis[3,5-bis(1,1,1,3,3,3-hexafluoro-2-methoxy-2-propyl)phenyl]borate trihydrate were synthesized through dye exchange followed by purification through column chromatography as described previously.[32,35] MilliQ-water (Millipore) was used in all experiments. Qdot 585 Streptavidin Conjugates were purchased from Thermo-Fisher Scientific.

Synthesis of Polymers: The different polymers were synthesized through free radical polymerization. Methyl methacrylate and the corresponding charged monomer were both dissolved in degased acetonitrile or DMSO and mixed at the desired ratio. 0.01 eq. of AIBN were added and the round bottom flask was placed in an oil bath preheated to 70 °C. Once the conversion reached 25%, the reaction was stopped and the polymers reprecipitated twice in methanol and/or water. After drying, the polymers were characterized through NMR and size exclusion chromatography.

Poly(Methyl Methacrylate-co-Methacrylic Acid): Methyl methacrylate and methacrylic acid were both dissolved in degased acetonitrile at a concentration of 1 M. The two solutions were then mixed in a 100 mL two-neck round bottom flask equipped with a stirring bar at the desired ratio to give a total volume of 40 mL (e.g., for 1% of methacrylic acid: 39.6 mL of methyl methacrylate solution and 0.4 mL of methacrylic acid solution). The mixture was degazed by bubbling argon for 5 min and placed under argon atmosphere. 0.01 eq of AIBN in acetonitrile (40 mg mL^{-1}) were added and the round bottom flask was placed in an oil bath preheated to 70 °C. At regular intervals, samples were drawn, dissolved in DMSO-d_6 and analyzed by NMR. Once the conversion reached 25%, the reaction was stopped by quickly cooling it to RT. Part of the acetonitrile was evaporated under reduced pressure and the reaction mixture was added dropwise to methanol. After filtration, the precipitate was redissolved in a small amount of acetonitrile and reprecipitated twice in methanol. The obtained polymer was dried under vacuum. ^{1}H NMR (400 MHz, $CDCl_3$, δ): 3.60 (s, 3 H), 2.2–0.5 (m, 6 H). Molecular weight by GPC: 1%: M_w = 38 100, M_w/M_n = 1.35; 5%: M_w = 46 800, M_w/M_n = 1.34.

Poly(Methyl Methacrylate-co-3-Sulfopropyl Methacrylate): Methyl methacrylate and 3-sulfopropyl methacrylate potassium salt were dissolved in degased DMSO at a concentration of 2 M. The two solutions were then mixed in a 50 mL two-neck round bottom flask equipped with a stirring bar at the desired ratio to give a total volume of 20 mL. The mixture was degased by bubbling argon for 5 min and placed under argon atmosphere. 0.01 eq. of AIBN in DMSO (40 mg mL^{-1}) were added and the round bottom flask was placed in an oil bath preheated to 70 °C. At regular intervals samples were drawn, dissolved in DMSO-d_6 and analyzed by NMR. Once the conversion reached 25%, the reaction was stopped by quickly cooling it to RT. The reaction mixture was then added dropwise to methanol, or, for higher percentages of the charged monomer, to water. After filtration, the precipitate was redissolved in a small amount of acetonitrile and reprecipitated twice in methanol (water for highest percentages). The obtained polymer was dried under vacuum. ^{1}H NMR (400 MHz, DMSO-d_6, δ): 3.97 (br. s, 0.02-0.2 H),

 © 2018 WILEY-VCH Verlag GmbH & Co. KGaA, Weinheim

ADVANCED SCIENCE NEWS
www.advancedsciencenews.com

ADVANCED FUNCTIONAL MATERIALS
www.afm-journal.de

3.57 (s, 3 H), 2.45 (m, partial covered by the solvent peak), 2.1–0.5 (m, 6 H). Fraction of SO_3H groups based on the peak at 3.97 ppm (feed: obtained): 1%:1.1%; 2%:2.3%; 5%:5.5%, 10%:12%. Molecular weight by GPC: 1%: $M_w = 51\,200$, $M_w/M_n = 1.58$; 5%: $M_w = 48\,400$, $M_w/M_n = 1.08$.

Poly(Methyl Methacrylate-co-[2-(Methacryloyloxy)ethyl]trimethylammonium) (PMMA-NMe$_3$): Methyl methacrylate was dissolved in degased DMSO at a concentration of 2 M. [2-(methacryloyloxy)ethyl]-trimethylammonium chloride was diluted with DMSO to yield a 2 M solution. The two solutions were then mixed in a 50 mL two-neck round bottom flask equipped with a stirring bar at the desired ratio to give a total volume of 20 mL. The mixture was degased by bubbling argon for 5 min and placed under argon atmosphere. 0.01 eq. of AIBN in DMSO (40 mg mL^{-1}) were added and the round bottom flask was placed in an oil bath preheated to 70 °C. At regular intervals, samples were drawn, dissolved in DMSO-d$_6$ and analyzed by NMR. Once the conversion reached 25%, the reaction was stopped by quickly cooling it to RT. The reaction mixture was then added dropwise to methanol, or, for higher percentages of the charged monomer, to water. After filtration, the precipitate was redissolved in a small amount of acetonitrile and reprecipitated twice in methanol (water for highest percentages). The obtained polymer was dried under vacuum. ^{1}H NMR (400 MHz, DMSO-d_6, δ): 4.37 (br. s, 0.02-0.2 H), 3.70 (br. S, 0.02-0.2), 3.55 (s, 3 H), 3.17 (s, 0.09–0.9 H), 2.1–0.4 (m, 6 H). Fraction of NMe_3 groups based on the peak at 3.17 ppm (feed: obtained): 1%:1.1%; 2%:2.4%; 5%:5.8%, 10%:12.2%. Molecular weight by GPC: 1%:$M_w = 99\,900$, $M_w/M_n = 1.62$; 5%: $M_w = 95\,300$, $M_w/M_n = 1.22$.

Preparation of NPs: Solutions of the polymers at 2 mg mL^{-1} in acetonitrile (up to 15 vol% methanol for >5% charged groups), containing the desired amount of dye (1, 10, or 20 wt% relative to the polymer) were added quickly and under stirring (shaking) using a micropipette to a tenfold volume excess of water, NaCl solution, or 20×10^{-3} M pH 7.4 phosphate buffer at 21 °C. The particle solution was then quickly diluted fivefold in water.

For FCS experiments these solutions were diluted twofold, and Tween 80 was added to obtain a Tween 80 concentration of 0.05 g L^{-1}. For cell experiments, the particle solutions were diluted to a particle concentration of 2–5 nM, followed by the addition of Tween 80 to obtain a Tween 80 concentration of 0.05 g L^{-1}.

Characterization of NPs: Absorption and emission spectra were recorded on a Cary 4000 Scan ultraviolet–visible spectrophotometer (Varian) and FluoroMax-4 spectrofluorometer (Horiba Jobin Yvon) equipped with a thermostated cell compartment, respectively. QYs were calculated using rhodamine 101 in ethanol as standard (QY = 0.9).[82]

Electron Microscopy: 5 µL of the particle solution were deposited onto carbon-coated copper–rhodium electron microscopy grids that were used either as obtained or following an air or amylamine glow-discharge. The grids were then treated for 1 min with a 2% uranyl acetate solution for staining and observed with a Philips CM120 TEM equipped with an LaB_6 filament and operating at 100 kV. Areas covered with NPs of interest were recorded at different magnifications on a Peltier cooled CCD camera (Model 794, Gatan, Pleasanton, CA). Image analysis was performed using the Fiji software.

Fluorescence Correlation Spectroscopy: FCS measurements were performed on a home-built confocal set-up based on a Nikon inverted microscope with a Nikon 60 × 1.2NA water immersion objective. Excitation was provided by a continuous wave (CW) laser diode (532 nm, Oxxius) and photons were detected with a fibered avalanche photodiode (APD SPCM-AQR-14-FC, Perkin Elmer) connected to an online hardware correlator (ALV7000-USB, ALV GmbH, Germany). Typical acquisition time was 5 min (10 × 30 s) with an excitation power of 0.5 mW at the sample level. The data were analyzed using the PyCorrFit software.[83]

Fluorescence Microscopy: Two set-ups were used for fluorescence microscopy: microinjection itself and part of the cellular single-particle imaging (notably the two-color imaging) were performed on a Leica DMIRE 2 microscope equipped with a control system of 37 °C, 5% CO_2 (Life Imaging Services), a 100 × HCX PL APO CS (1.4 NA) objective using a Photometrics Prime sCMOS camera piloted by the Metamorph software, a Xenon-lamp and Leica Y3 and Y5 filter cubes. Single-particle measurements and part of the intracellular single-particle tracking were performed in the TIRF (Total Internal Reflection Fluorescence) or HILO mode on a home-made wide-field setup based on an Olympus IX-71 microscope with an oil immersion objective (NA = 1.49, 100x). A DPPS (Cobolt) CW laser emitting at 532 nm was used for excitation at 12 W cm^{-2} for immobilized single particles, and at 2 W cm^{-2} for cellular imaging. The fluorescence signal was recorded with an EMCCD (ImagEM Hamamatsu) using an exposure of 30.5 ms per image frame. For single-particle fluorescence microscopy measurements, the NPs were immobilized either on glass surfaces on which a polyethyleneimine layer was initially adsorbed or in 15 wt% poly(vinyl alcohol), as described previously.[11,32] The surfaces were left in MilliQ-water during microscopy. QDs were immobilized and imaged in the same way as the NPs. Single-particle analysis was performed using the Fiji software as described previously.[32,33]

Cellular Experiments: HeLa cells were grown in Dulbecco's modified Eagle medium (without phenolred, Gibco-Invitrogen), supplemented with 10% FBS (Lonza), L-glutamine, and 1% antibiotic solution (penicillin-streptomycin, Gibco-Invitrogen) at 37 ° C in humidified atmosphere containing 5% CO_2. Cells were seeded onto round microscope cover glasses (diameter 18 mm) deposited in six well plates at a density of 125×10^3 cells per well 24 h before the microinjection.

Microinjection of NPs and Cellular Imaging: For microinjection experiments, subconfluent HeLa cells plated on glass coverslips were mounted in a Ludin Chamber (Life Imaging Services, Basel, Switzerland). The cells were then placed on the Leica DMIRE 2 microscope and solutions of the different NPs at particle concentrations of 0.5–2 nM were microinjected into the perinuclear region of the cells, using a Femtojet/InjectMan NI2 microinjector (Eppendorf). Images sequences were then acquired either on the same setup or with the Olympus set-up used for single-particle imaging after transfer of the samples. Time-lapse movies were analyzed using the ImageJ (National Institutes of Health, USA) software with the Mosaic module for single-particle tracking.[84] Obtained trajectories were checked for artefacts (e.g., wrong connections, which were rare). At least three cells with 60 trajectories per condition were analyzed.

Supporting Information

Supporting Information is available from the Wiley Online Library or from the author.

Acknowledgements

D.H. and P.E. contributed equally to this work. This work was supported by the European Research Council ERC Consolidator grant BrightSens 648528 and by the Agence National de Recherche JC/JC grant "Supertrack" ANR-16-CE09-0007. The authors thank C. Ruhlmann and C. Crucifix from the FRISBI platform (ANR-10-INBS-05) for help with electron microscopy, R. Vauchelles and the QUEST platform imaging facility for help with fluorescence microscopy, and M. Legros and C. Foussat for size exclusion chromatography.

Conflict of Interest

The authors declare no conflict of interest.

Keywords

diffusion in the cytosol, fluorescent polymer nanoparticles, intracellular particle sieving, single-particle tracking

Received: July 26, 2018
Revised: September 5, 2018
Published online:

© 2018 WILEY-VCH Verlag GmbH & Co. KGaA, Weinheim

ADVANCED SCIENCE NEWS
www.advancedsciencenews.com

ADVANCED FUNCTIONAL MATERIALS
www.afm-journal.de

[1] C. Wong, T. Stylianopoulos, J. Cui, J. Martin, V. P. Chauhan, W. Jiang, Z. Popović, R. K. Jain, M. G. Bawendi, D. Fukumura, *Proc. Natl. Acad. Sci. USA* **2011**, *108*, 2426.
[2] Y. Tsvetkova, N. Beztsinna, M. Baues, D. Klein, A. Rix, S. K. Golombek, W. Al Rawashdeh, F. Gremse, M. Barz, K. Koynov, S. Banala, W. Lederle, T. Lammers, F. Kiessling, *Nano Lett.* **2017**, *17*, 4665.
[3] S. Shashkova, M. C. Leake, *Biosci. Rep.* **2017**, *37*, BSR20170031.
[4] A. Kusumi, T. A. Tsunoyama, K. M. Hirosawa, R. S. Kasai, T. K. Fujiwara, *Nat. Chem. Biol.* **2014**, *10*, 524.
[5] A. J. Nelson, S. T. Hess, *J. Microsc.* **2014**, *254*, 1.
[6] H. Deschout, F. C. Zanacchi, M. Mlodzianoski, A. Diaspro, J. Bewersdorf, S. T. Hess, K. Braeckmans, *Nat. Methods* **2014**, *11*, 253.
[7] R. Dixit, R. Cyr, *Plant J.* **2003**, *36*, 280.
[8] J. Icha, M. Weber, J. C. Waters, C. Norden, *BioEssays* **2017**, *39*, 1700003.
[9] P. P. Laissue, R. A. Alghamdi, P. Tomancak, E. G. Reynaud, H. Shroff, *Nat. Methods* **2017**, *14*, 657.
[10] P. Çakir, A. Cutivet, M. Resmini, B. T. S. Bui, K. Haupt, *Adv. Mater.* **2013**, *25*, 1048.
[11] I. Shulov, R. V. Rodik, Y. Arntz, A. Reisch, V. I. Kalchenko, A. S. Klymchenko, *Angew. Chem., Int. Ed.* **2016**, *55*, 15884.
[12] C. Veigel, C. F. Schmidt, *Nat. Rev. Mol. Cell Biol.* **2011**, *12*, 163.
[13] F. Pinaud, S. Clarke, A. Sittner, M. Dahan, *Nat. Methods* **2010**, *7*, 275.
[14] S. J. Sahl, S. W. Hell, S. Jakobs, *Nat. Rev. Mol. Cell Biol.* **2017**, *18*, 685.
[15] O. S. Wolfbeis, *Chem. Soc. Rev.* **2015**, *44*, 4743.
[16] P. D. Howes, R. Chandrawati, M. M. Stevens, *Science* **2014**, *346*, 1247390.
[17] M. Elsabahy, G. S. Heo, S.-M. Lim, G. Sun, K. L. Wooley, *Chem. Rev.* **2015**, *115*, 10967.
[18] P. Pierobon, G. Cappello, *Adv. Drug Delivery Rev.* **2012**, *64*, 167.
[19] L. Cognet, C. Leduc, B. Lounis, *Curr. Opin. Chem. Biol.* **2014**, *20*, 78.
[20] X. Michalet, F. F. Pinaud, L. A. Bentolila, J. M. Tsay, S. Doose, J. J. Li, G. Sundaresan, A. M. Wu, S. S. Gambhir, S. Weiss, *Science* **2005**, *307*, 538.
[21] S. Bonacchi, D. Genovese, R. Juris, M. Montalti, L. Prodi, E. Rampazzo, N. Zaccheroni, *Angew. Chem., Int. Ed.* **2011**, *50*, 4056.
[22] A. Kaeser, A. P. H. J. Schenning, *Adv. Mater.* **2010**, *22*, 2985.
[23] E. Genin, Z. Gao, J. A. Varela, J. Daniel, T. Bsaibess, I. Gosse, L. Groc, L. Cognet, M. Blanchard-Desce, *Adv. Mater.* **2014**, *26*, 2258.
[24] J. Yu, C. Wu, S. P. Sahu, L. P. Fernando, C. Szymanski, J. McNeill, *J. Am. Chem. Soc.* **2009**, *131*, 18410.
[25] J. Pecher, S. Mecking, *Chem. Rev.* **2010**, *110*, 6260.
[26] C. Wu, D. T. Chiu, *Angew. Chem., Int. Ed.* **2013**, *52*, 3086.
[27] H. Wang, P. Zhang, Y. Hong, B. Zhao, P. Yi, J. Chen, *Polym. Chem.* **2017**, *8*, 5795.
[28] K. Li, B. Liu, *Chem. Soc. Rev.* **2014**, *43*, 6570.
[29] X. Gu, R. T. K. Kwok, J. W. Y. Lam, B. Z. Tang, *Biomaterials* **2017**, *146*, 115.
[30] A. Reisch, A. S. Klymchenko, *Small* **2016**, *12*, 1968.
[31] M. P. Robin, R. K. O'Reilly, *Polym. Int.* **2015**, *64*, 174.
[32] A. Reisch, P. Didier, L. Richert, S. Oncul, Y. Arntz, Y. Mély, A. S. Klymchenko, *Nat. Commun.* **2014**, *5*, 4089.
[33] A. Reisch, K. Trofymchuk, A. Runser, G. Fleith, M. Rawiso, A. S. Klymchenko, *ACS Appl. Mater. Interfaces* **2017**, *9*, 43030.
[34] K. Trofymchuk, A. Reisch, P. Didier, F. Fras, P. Gilliot, Y. Mely, A. S. Klymchenko, *Nat. Photonics* **2017**, *11*, 657.
[35] B. Andreiuk, A. Reisch, M. Lindecker, G. Follain, N. Peyriéras, J. G. Goetz, A. S. Klymchenko, *Small* **2017**, *13*, 1701582.
[36] J. Chen, W. Zhong, Y. Tang, Z. Wu, Y. Li, P. Yi, J. Jiang, *Macromolecules* **2015**, *48*, 3500.
[37] J. S. Suk, Q. Xu, N. Kim, J. Hanes, L. M. Ensign, *Adv. Drug Delivery Rev.* **2016**, *99*, 28.
[38] Z. G. Estephan, P. S. Schlenoff, J. B. Schlenoff, *Langmuir* **2011**, *27*, 6794.
[39] K. Luby-Phelps, *Int. Rev. Cytol.* **2000**, *192*, 189.
[40] K. Luby-Phelps, *Mol. Biol. Cell* **2013**, *24*, 2593.
[41] K. Norregaard, R. Metzler, C. M. Ritter, K. Berg-Sørensen, L. B. Oddershede, *Chem. Rev.* **2017**, *117*, 4342.
[42] F. Höfling, T. Franosch, *Rep. Prog. Phys.* **2013**, *76*, 046602.
[43] D. Wirtz, *Annu. Rev. Biophys.* **2009**, *38*, 301.
[44] J. A. Dix, A. S. Verkman, *Annu. Rev. Biophys.* **2008**, *37*, 247.
[45] H. S. Choi, W. Liu, F. Liu, K. Nasr, P. Misra, M. G. Bawendi, J. V. Frangioni, *Nat. Nanotechnol.* **2010**, *5*, 42.
[46] H. Cabral, Y. Matsumoto, K. Mizuno, Q. Chen, M. Murakami, M. Kimura, Y. Terada, M. R. Kano, K. Miyazono, M. Uesaka, N. Nishiyama, K. Kataoka, *Nat. Nanotechnol.* **2011**, *6*, 815.
[47] R. Ferrari, M. Lupi, F. Falcetta, P. Bigini, K. Paolella, F. Fiordaliso, C. Bisighini, M. Salmona, M. D'Incalci, M. Morbidelli, D. Moscatelli, P. Ubezio, *Nanotechnology* **2014**, *25*, 045102.
[48] L. Shang, K. Nienhaus, G. U. Nienhaus, *J. Nanobiotechnol.* **2014**, *12*, 5.
[49] K. Luby-Phelps, D. L. Taylor, F. Lanni, *J. Cell Biol.* **1986**, *102*, 2015.
[50] E. Dauty, A. S. Verkman, *J. Biol. Chem.* **2005**, *280*, 7823.
[51] T. Kalwarczyk, N. Ziębacz, A. Bielejewska, E. Zaboklicka, K. Koynov, J. Szymański, A. Wilk, A. Patkowski, J. Gapiński, H.-J. Butt, R. Hołyst, *Nano Lett.* **2011**, *11*, 2157.
[52] L. H. Reddy, J. L. Arias, J. Nicolas, P. Couvreur, *Chem. Rev.* **2012**, *112*, 5818.
[53] F. Tang, L. Li, D. Chen, *Adv. Mater.* **2012**, *24*, 1504.
[54] F. Danhier, E. Ansorena, J. M. Silva, R. Coco, A. Le Breton, V. Preat, *J. Controlled Release* **2012**, *161*, 505.
[55] M. J. Saxton, *J. Phys. Chem. B* **2014**, *118*, 12805.
[56] K. Landfester, *Angew. Chem., Int. Ed.* **2009**, *48*, 4488.
[57] F. Candau, M. Pabon, J.-Y. Anquetil, *Colloids Surf. A* **1999**, *153*, 47.
[58] F. Gu, L. Zhang, B. A. Teply, N. Mann, A. Wang, A. F. Radovic-Moreno, R. Langer, O. C. Farokhzad, *Proc. Natl. Acad. Sci. USA* **2008**, *105*, 2586.
[59] G. Riess, *Prog. Polym. Sci.* **2003**, *28*, 1107.
[60] E. Lepeltier, C. Bourgaux, P. Couvreur, *Adv. Drug Delivery Rev.* **2014**, *71*, 86.
[61] S. Schubert, J. T. Delaney, U. S. Schubert, *Soft Matter* **2011**, *7*, 1581.
[62] A. Reisch, A. Runser, Y. Arntz, Y. Mély, A. S. Klymchenko, *ACS Nano* **2015**, *9*, 5104.
[63] F. Lince, D. L. Marchisio, A. A. Barresi, *J. Colloid Interface Sci.* **2008**, *322*, 505.
[64] W. S. Saad, R. K. Prud'homme, *Nano Today* **2016**, *11*, 212.
[65] M. Beck-Broichsitter, J. Nicolas, P. Couvreur, *Nanoscale* **2015**, *7*, 9215.
[66] M. Li, M. Jiang, L. Zhu, C. Wu, *Macromolecules* **1997**, *30*, 2201.
[67] D. Horn, J. Rieger, *Angew. Chem., Int. Ed.* **2001**, *40*, 4330.
[68] B. Andreiuk, A. Reisch, V. G. Pivovarenko, A. S. Klymchenko, *Mater. Chem. Frontiers* **2017**, *1*, 2309.
[69] I. Shulov, S. Oncul, A. Reisch, Y. Arntz, M. Collot, Y. Mely, A. S. Klymchenko, *Nanoscale* **2015**, *7*, 18198.
[70] M. Tokunaga, N. Imamoto, K. Sakata-Sogawa, *Nat. Methods* **2008**, *5*, 159.
[71] N. Ruthardt, D. C. Lamb, C. Bräuchle, *Mol. Ther.* **2011**, *19*, 1199.
[72] C. D. Rienzo, E. Gratton, F. Beltram, F. Cardarelli, *Proc. Natl. Acad. Sci. USA* **2013**, *110*, 12307.
[73] H. Li, S.-X. Dou, Y.-R. Liu, W. Li, P. Xie, W.-C. Wang, P.-Y. Wang, *J. Am. Chem. Soc.* **2015**, *137*, 436.
[74] K. Susumu, E. Oh, J. B. Delehanty, F. Pinaud, K. B. Gemmill, S. Walper, J. Breger, M. J. Schroeder, M. H. Stewart, V. Jain, C. M. Whitaker, A. L. Huston, I. L. Medintz, *Chem. Mater.* **2014**, *26*, 5327.

 © 2018 WILEY-VCH Verlag GmbH & Co. KGaA, Weinheim

ADVANCED SCIENCE NEWS
www.advancedsciencenews.com

ADVANCED FUNCTIONAL MATERIALS
www.afm-journal.de

[75] E. Derivery, E. Bartolami, S. Matile, M. Gonzalez-Gaitan, *J. Am. Chem. Soc.* **2017**, *139*, 10172.
[76] T. Kalwarczyk, K. Sozanski, A. Ochab-Marcinek, J. Szymanski, M. Tabaka, S. Hou, R. Holyst, *Adv. Colloid Interface Sci.* **2015**, *223*, 55.
[77] D. W. Provance, A. McDowall, M. Marko, K. Luby-Phelps, *J. Cell Sci.* **1993**, *106*, 565.
[78] C. Kronlage, M. Schäfer-Herte, D. Böning, H. Oberleithner, J. Fels, *Biophys. J.* **2015**, *109*, 687.
[79] M. E. Grady, E. Parrish, M. A. Caporizzo, S. C. Seeger, R. J. Composto, D. M. Eckmann, *Soft Matter* **2017**, *13*, 1873.
[80] L. W. Janson, K. Ragsdale, K. Luby-Phelps, *Biophys. J.* **1996**, *71*, 1228.
[81] B. R. Parry, I. V. Surovtsev, M. T. Cabeen, C. S. O'Hern, E. R. Dufresne, C. Jacobs-Wagner, *Cell* **2014**, *156*, 183.
[82] C. Würth, D. Geißler, T. Behnke, M. Kaiser, U. Resch-Genger, *Anal. Bioanal. Chem.* **2015**, *407*, 59.
[83] P. Müller, P. Schwille, T. Weidemann, *Bioinformatics* **2014**, *30*, 2532.
[84] I. F. Sbalzarini, P. Koumoutsakos, *J. Struct. Biol.* **2005**, *151*, 182.

 © 2018 WILEY-VCH Verlag GmbH & Co. KGaA, Weinheim

Copyright WILEY-VCH Verlag GmbH & Co. KGaA, 69469 Weinheim, Germany, 2018.

ADVANCED FUNCTIONAL MATERIALS

Supporting Information

for *Adv. Funct. Mater.,* DOI: 10.1002/adfm.201805157

Protein-Sized Dye-Loaded Polymer Nanoparticles for Free Particle Diffusion in Cytosol

Andreas Reisch, Doriane Heimburger, Pauline Ernst, Anne Runser, Pascal Didier, Denis Dujardin, and Andrey S. Klymchenko**

WILEY-VCH

Copyright WILEY-VCH Verlag GmbH & Co. KGaA, 69469 Weinheim, Germany, 2016.

Supporting Information

Protein-sized Dye-loaded Polymer Nanoparticles for Free Particle Diffusion in Cytosol

Andreas Reisch, Doriane Heimburger, Pauline Ernst, Anne Runser, Pascal Didier, Denis Dujardin, and Andrey S. Klymchenko**

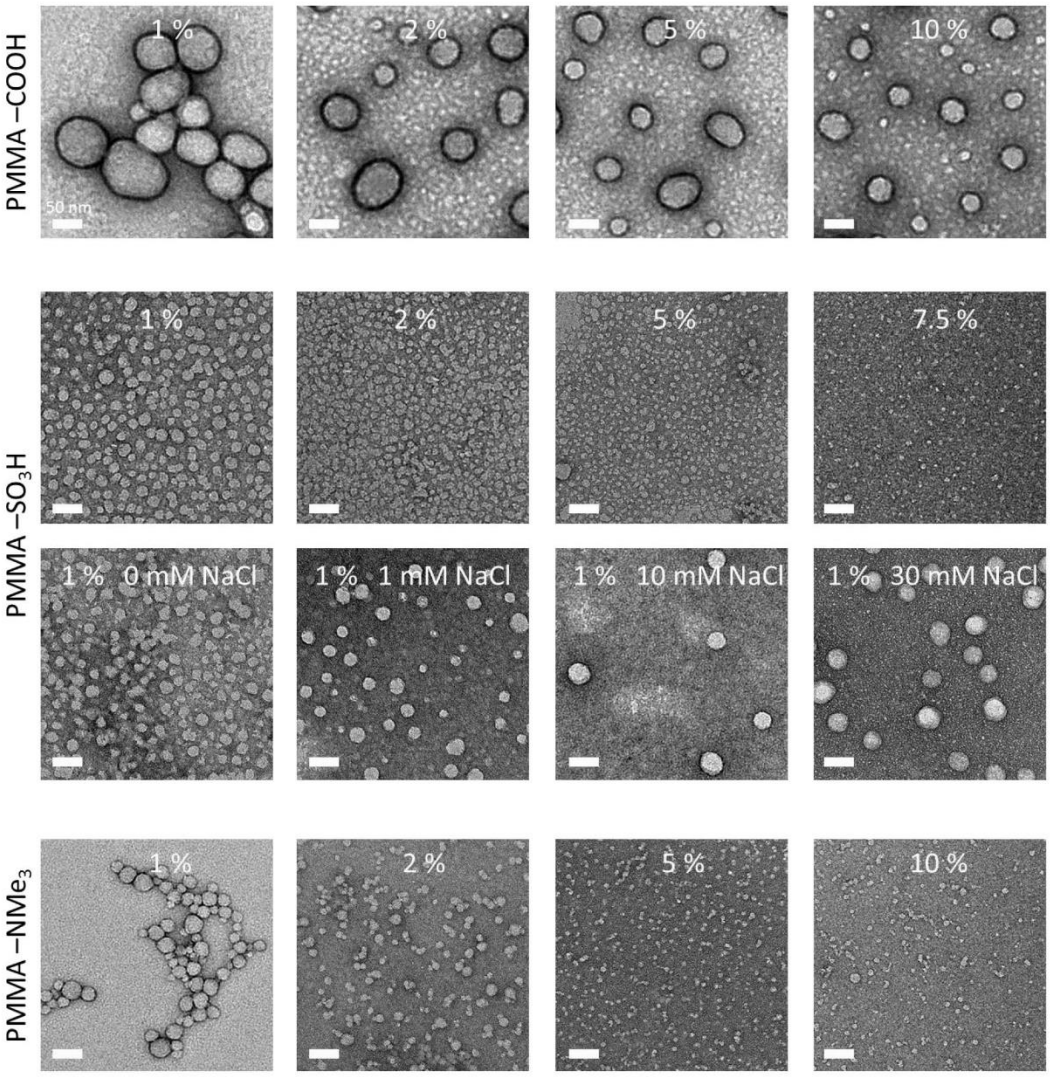

Figure S1. Transmission electron microscopy (TEM) images of particles made by nanoprecipitation for different percentages and type of charged groups. NPs were loaded with 10 wt% of R18/F5-TPB. Where not mentioned, nanoprecipitation was carried out in milliQ water. For PMMA-SO_3H at 1% nanoprecipitations were carried out in different NaCl concentrations as noted. Scale bars correspond to 50 nm.

WILEY-VCH

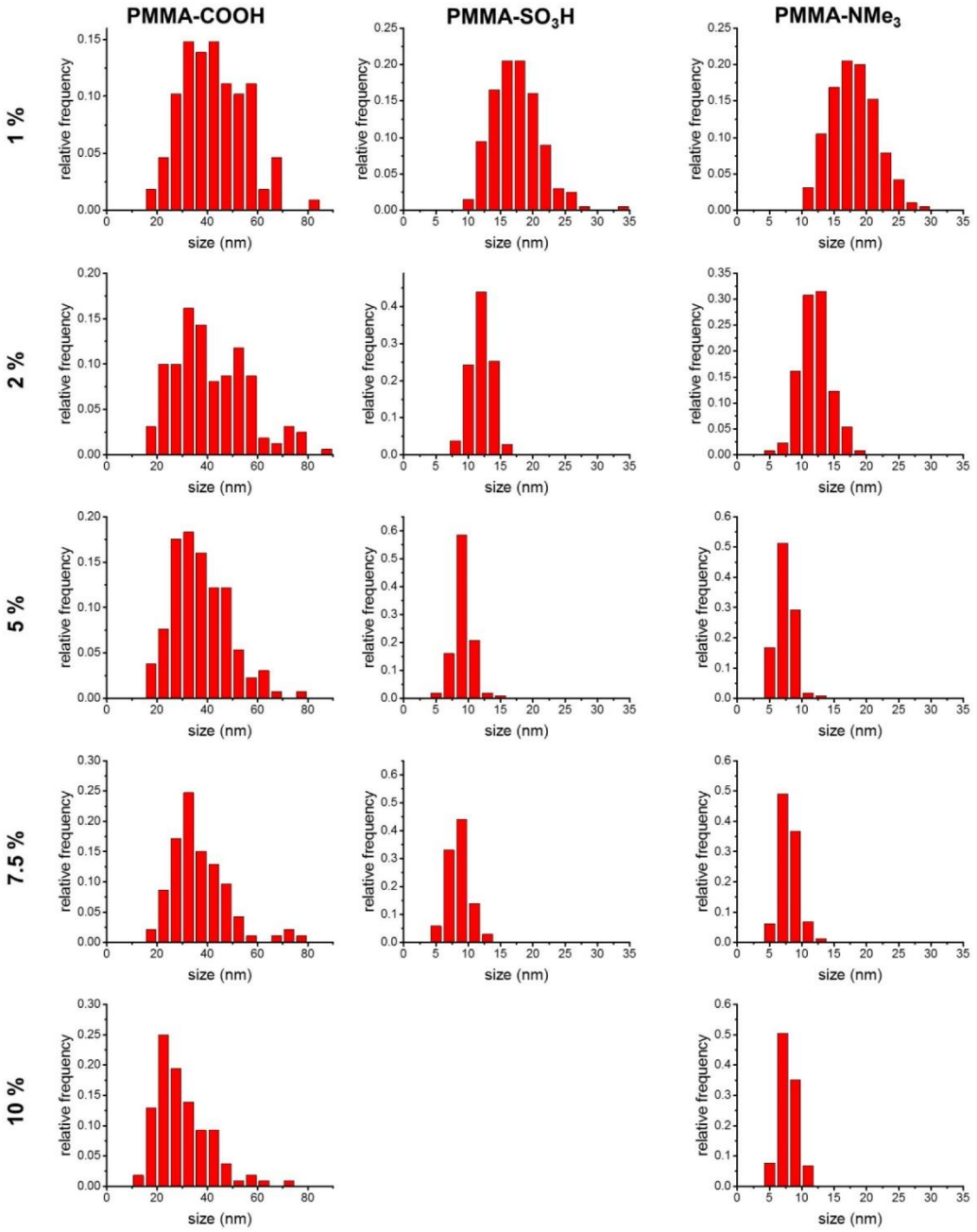

Figure S2. Histograms of sizes of particles made by nanoprecipitation as a function on percentage and type of charged groups as determined by TEM. Mean values of sizes determined by transmission electron microscopy are given for NPs loaded with 10 wt% of R18/F5-TPB. At least 200 NPs were analyzed per condition. Error bars give full width at half maximum of the distribution.

Table S1. Particle sizes as determined by TEM and estimated number of charged groups per nm² of particle surface and total number per particle.

%	COOH			SO_3H			NMe_3		
	size (nm)	charged groups per nm²	charged groups per NP	size (nm)	charged groups per nm²	charged groups per NP	size (nm)	charged groups per nm²	charged groups per NP
1	42	0.4	2300	17	0.17	150	18	0.18	180
2	41	0.8	4300	12	0.24	107	12	0.24	110
5	37	1.9	8042	9	0.43	109	7	0.34	52
7.5	35	2.6	9400	8	0.56	112	7	0.53	90
10	29	2.9	7800				7	0.66	100

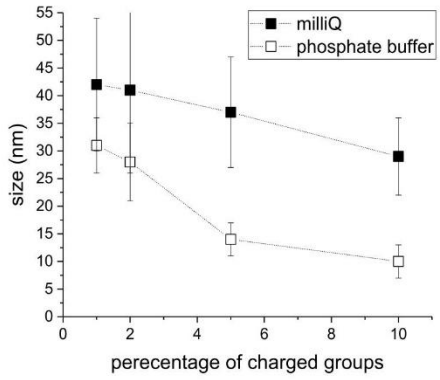

Figure S3. Influence of the precipitation medium on the size of nanoparticles made by nanoprecipitation of carboxylate bearing polymers. Mean values of sizes determined by transmission electron microscopy are given for NPs loaded with 10 wt% of R18/F5-TPB. At least 200 NPs were analyzed per condition. Error bars give full width at half maximum of the distribution.

Table S2. Steady state fluorescence properties of selected nanoparticles loaded with 10 wt% R18/F5-TPB. Measurements were carried out in a FlouroMax-4 spectrofluorometer with an excitation at 530 nm and an intensity of about 1 mW/cm².

	Charged groups %	Size nm	Fluorophores per NP	QY %	Brightness $M.cm^{-1}$	Fluorescence cross section cm^2
PMMA-COOH	1	42	1700	59 ± 2	1.0×10^{8}	3.8×10^{-13}
	10	29	560	59 ± 2	4.3×10^{7}	1.3×10^{-13}
PMMA-SO_3H	1	17	110	61 ± 3	6.9×10^{6}	2.6×10^{-14}
	2	12	40	55 ± 1	2.2×10^{6}	8.4×10^{-15}
	5	9	18	41 ± 2	7.0×10^{5}	2.7×10^{-15}
PMMA-NMe_3	1	18	120	35 ± 3	4.3×10^{6}	1.6×10^{-14}

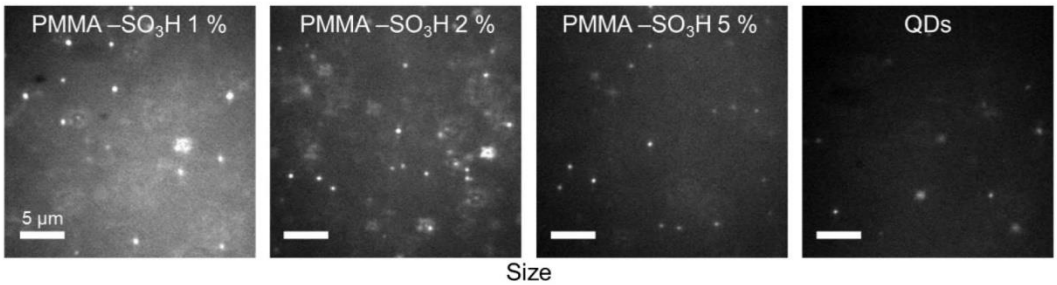

	PMMA –SO_3H 1 %	PMMA –SO_3H 2 %	PMMA –SO_3H 5 %	QDs
Size	17 nm	12 nm	9 nm	31 nm
Single NP brightness				
Photons / s:	22 000	5 800	3 300	2 100
σ (cm²):	6.8×10^{-15}	1.8×10^{-15}	1.1×10^{-15}	0.6×10^{-15}

Figure S4. Single-particle fluorescence microscopy. The nanoparticles were immobilized in solutions of polyvinylalcohol (PVA) in water with a PVA concentration of 15 wt%. Images were acquired using an excitation at 532 nm with an intensity of 1 W/cm². The conditions for excitation, recording and presentation are identical for all images. The mean number of emitted photons per particle per second and the per particle fluorescence cross-sections are given. At least 50 particles were analyzed per condition.

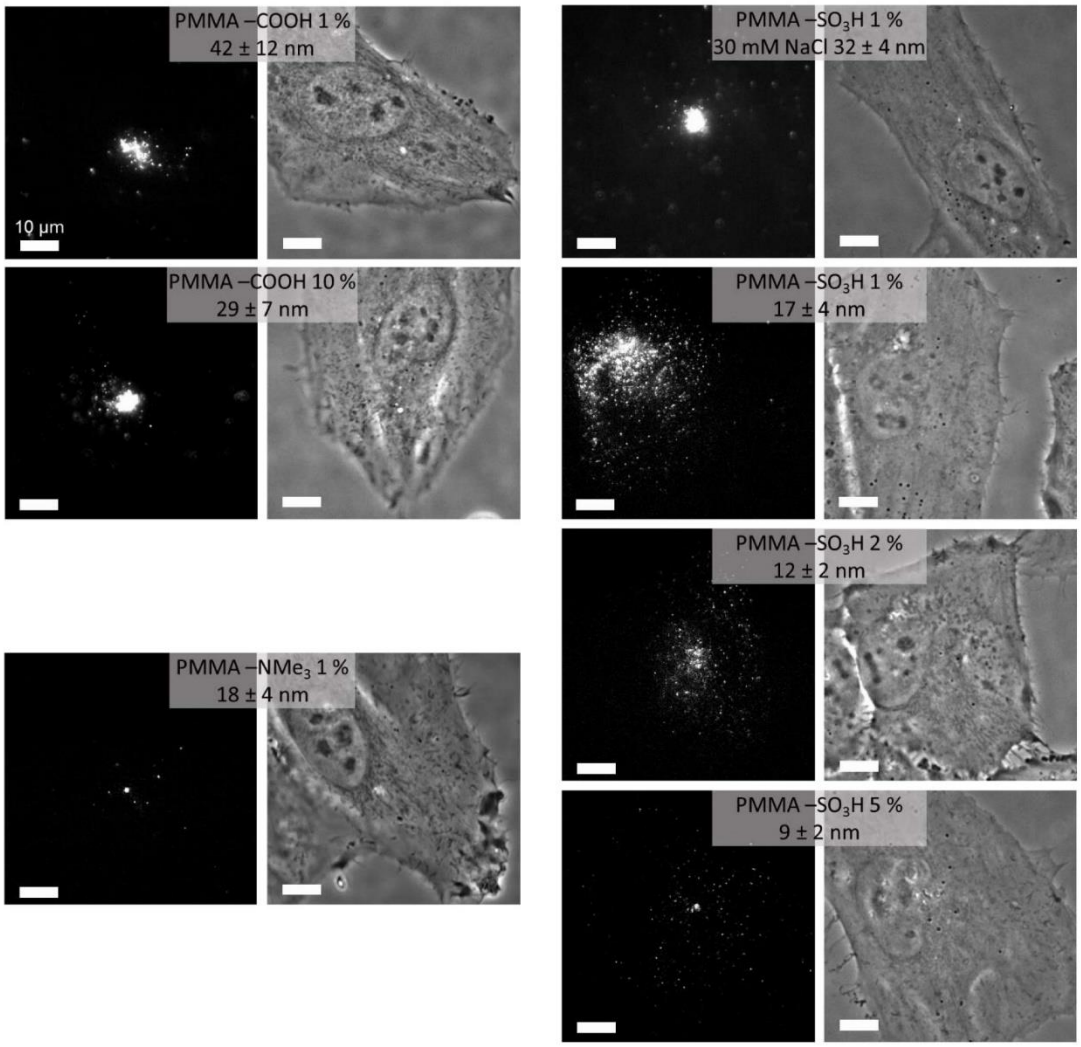

Figure S5. Microinjection of nanoparticles in living HeLa cells. The left hand images are maximum projections of fluorescence micrographs collected over 1 min (50 ms per frame) of nanoparticles made from different polymers, loaded with 10 wt% of R18/F5-TPB and coated with Tween 80. Right hand images are phase-contrast images of the corresponding cells. Scale bars correspond to 10 µm.

Article 3 : Controlling Size and Fluorescence of Dye-Loaded Polymer Nanoparticles through Polymer Design

LANGMUIR Article
Cite This: Langmuir 2019, 35, 7009−7017 pubs.acs.org/Langmuir

Controlling Size and Fluorescence of Dye-Loaded Polymer Nanoparticles through Polymer Design

Vitalii Rosiuk, Anne Runser, Andrey Klymchenko, and Andreas Reisch*

Laboratoire de Bioimagerie et Pathologies, CNRS UMR 7021, Faculté de Pharmacie, Université de Strasbourg, Cedex 67401 Illkirch, France

Supporting Information

ABSTRACT: Nanoprecipitation is a straightforward yet powerful technique to synthesize polymer nanoparticles loaded with various biologically active compounds or contrast agents. Particle formation in this approach is kinetically controlled, and various assembly parameters have been used to control the size distribution and properties of the formed nanoparticles. Here, the influence of the nature of the polymer on the formation of nanoparticles in nanoprecipitation is studied systematically by varying its hydrophobicity and charge over a broad range. For this, methacrylate copolymers with different types and fractions of hydrophobic, hydrophilic, and charged side groups are synthesized. Nanoprecipitation of these polymers shows that particle size increases with increasing global hydrophobicity of the polymers. At the same time, both hydrophilic and charged groups reduce particle size. In this way, we achieve control over particle size from ∼10 to 200 nm. Furthermore, the effect of the polymer nature on the photophysical properties of nanoparticles loaded with a fluorescent dye, a rhodamine B derivative with a bulky hydrophobic counterion (fluorinated tetraphenylborate), is studied. It is found that the hydrophobic/hydrophilic balance of the polymer modulates to a large extent the spectral properties and fluorescence quantum yield of the dye encapsulated at high concentration, which reflects changes in the dye aggregation within the polymer matrix. Thus, we show how polymer chemistry can tune kinetically controlled formation of nanoparticles and encapsulation of the load. The concepts introduced here should be valuable tools for the design of nanoparticles for imaging and drug-delivery applications.

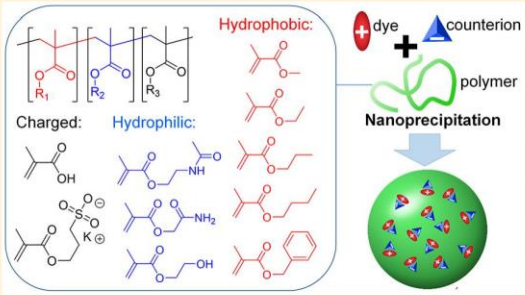

Downloaded via UNIV STRASBOURG on January 7, 2020 at 10:22:37 (UTC).
See https://pubs.acs.org/sharingguidelines for options on how to legitimately share published articles.

INTRODUCTION

Polymer nanoparticles (NPs) have attracted increasing attention and gained considerable importance over the past two decades.[1−3] In particular, the possibility to load them with various active or functional compounds has made them valuable tools in the biomedical field, for example, in drug delivery,[4,5] or, when loaded with different contrast agents,[6,7] in bioimaging.[2,8] Several approaches have been developed for the synthesis of such loaded NPs, either using different types of emulsion polymerizations or using different techniques for the assembly of preformed polymers.[9] Among the latter, nanoprecipitation is a particularly straightforward approach.[10−12] The possibility to encapsulate very high amounts of load in the NPs in this way has been exploited, for example, for the synthesis of fluorescent dye-loaded polymer NPs and aggregation-induced emission NPs.[13−15] In particular, the combination of charged fluorophores with hydrophobic bulky counterions could be used to prevent aggregation caused quenching and thus achieve particles with very high brightness, which can reach a hundred times that of quantum dots.[16,17] The high brightness and biocompatibility of these particles have enabled color coding of cells and the design of probes for intracellular imaging.[18,19] At the same time, energy transfer between the encapsulated dyes is very efficient in these particles, which could be used to construct nanoantennas that allowed observing single molecules at very low excitation light intensities.[20]

In nanoprecipitation, solutions of the polymers and/or the load in a water miscible organic solvent are added to an aqueous phase (Scheme 1). Interdiffusion of the two phases leads to a mixture in which the polymer/load are not soluble anymore, and thus to supersaturation of the polymer/load, which is the driving force of particle formation. As nanoprecipitation is a kinetically controlled process, a precise control of the NP properties is challenging.[1,21,22] Several assembly parameters such as polymer concentration,[21,23,24] type of solvent,[23] type and speed of mixing,[22,25,26] and concentration and nature of stabilizing compounds[27−29] have been found to exert a strong effect on particle formation and in particular on mean particle size and size distribution.[10,30−32] Even so, nanoprecipitation has been applied routinely to various polymers, including poly(lactic acid) (PLA), poly(lactic-*co*-glycolic acid) (PLGA), poly(alkyl cyanoacrylates) (PACA), poly(caprolactone) (PCL), and poly(methyl meth-

Received: March 11, 2019
Revised: April 18, 2019
Published: May 13, 2019

ACS Publications © 2019 American Chemical Society

DOI: 10.1021/acs.langmuir.9b00721
Langmuir 2019, 35, 7009−7017

Scheme 1. (A) Schematic View of the Assembly of Dye-Loaded Polymer NPs through Nanoprecipitation (the Structure of the Dye−Counterion Pair Used in This Study Is Given); (B) Overview of the Monomers Used in the Design of Copolymers (Typically, One Charged, One Hydrophilic, and One Hydrophobic Monomer Were Combined in Different Ratios To Synthesize the Copolymer)

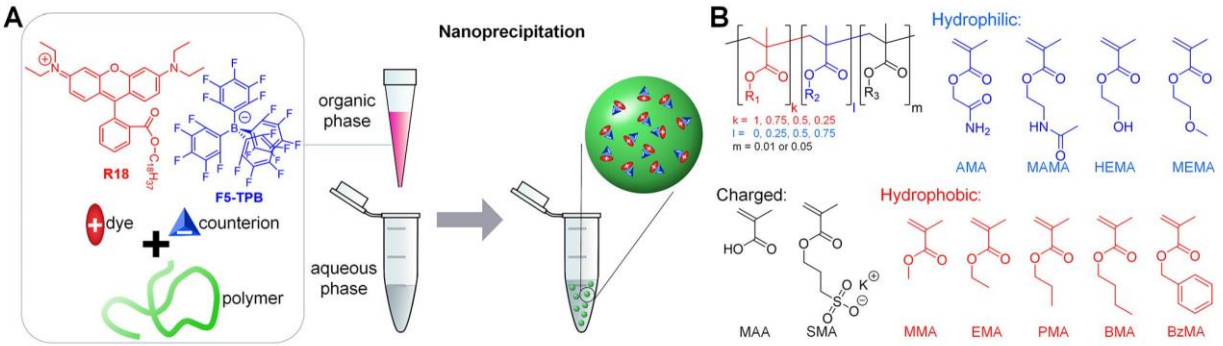

acrylate) (PMMA) and their copolymers with poly(ethylene glycol) (PEG); the influence of polymer chemistry on particle formation in nanoprecipitation has been insufficiently investigated.[10] In several cases the influence of the molecular weight of the polymer was evaluated but did not show a major effect on particle size.[33−35] We have recently determined the influence of the nature and the concentration of charged groups on the polymers on the size of NPs made through nanoprecipitation.[19,36] Already small amounts of charged groups made it possible to assemble dye-loaded polymer NPs with sizes down to 10 nm. By comparing dye-loaded polymer NPs made from PLGA, PMMA, and PCL with respect to their fluorescence properties, we could show how polymer chemistry can be used to improve their brightness but also to control the collective behavior of the fluorophores and thus particle blinking.[16] However, more general studies on the role of polymer chemistry are largely missing to date.

The aim of this study was to investigate systematically the influence of the nature of the polymer on NPs made through nanoprecipitation. To elucidate this question, we synthesized series of copolymers with different types and ratios of hydrophilic, hydrophobic, and charged monomers (Scheme 1). These copolymers were then used to assemble (dye-loaded) polymer NPs through nanoprecipitation. We were particularly interested in two aspects of the formed particles: their size and the photophysical properties of the encapsulated dyes. The latter reflect the organization and the environment of the dyes and thus characterize the encapsulation of the load. Particle size, on the other hand, depends on particle formation as a whole. Together, this work is the first attempt to provide a comprehensive picture of how polymer chemistry influences nanoprecipitation and how it can be used to control particle properties.

■ MATERIALS AND METHODS

Materials. Methyl methacrylate (MMA, 99%), methacrylic acid (MAA, 99%), 2-aminoethyl methacrylate hydrochloride (90%), 3-sulfopropyl methacrylate potassium salt (SMA, 98%), ethyl methacrylate (EMA, 99%), *n*-propyl methacrylate (PMA, 97%), butyl methacrylate (BMA, 99%), benzyl methacrylate (BzMA, 96%), hydroxyethyl methacrylate (HEMA, ≥99%), ethylene glycol methyl ether methacrylate (MEMA, 99%), iodoacetamide (99%), and acetanhydride (>99%) were purchased from Sigma-Aldrich. Acetonitrile (HPLC grade), diisopropylethylamine (DIPEA, >98%), dimethylformamide (DMF, analytical grade), potassium carbonate (K_2CO_3, ≥99.5%), and dimethyl sulfoxide (DMSO, analytical grade) were obtained from Fisher-Scientific. Dichloromethane (DCM, ≥99.8%) was from CarloErba, and methanol (HPLC grade) was from VWR. Monomers were purified using column chromatography or recrystallization. Azobisisobutyronitrile (Aldrich, ≥98%) was recrystallized twice from ethanol. The other compounds were used as received. Milli-Q water (Millipore) was used in all experiments.

R18/F5-TPB was synthesized from rhodamine B octadecyl ester perchlorate (Aldrich, >98.0%) and lithium tetrakis(pentafluorophenyl)borate ethyl etherate (AlfaAesar, 97%) through ion exchange followed by purification through column chromatography as described previously.[17,18]

2-Acetamidoethyl Methacrylate (MAMA). 1.59 g of 2-aminoethyl methacrylate hydrochloride (8.6 mmol) was added to 20 mL of DCM in a 100 mL round-bottom flask, and then 2.43 mL of DIPEA (15 mmol) was added. 1.38 g of acetanhydride (14 mmol) was added dropwise to the mixture, and the reaction was left for 30 min. The reaction mixture was extracted with HCl (1 M), then with aqueous solutions of K_2CO_3 and finally with distilled water. After evaporation of the organic phase, 1.37 g (8 mmol) of a clear liquid was obtained (yield 90%). ^{1}H NMR (400 MHz, DMSO-d_6) δ (ppm): 8.03 (s, 1H), 6.06 (s, 1H), 5.69 (s, 1H), 4.08 (t, 2H), 3.32 (t, 2H), 1.88 (s, 3H), 1.82 (s, 3H). ^{13}C NMR (500 MHz, MeOD) δ (ppm): 173.5, 168.7, 137.6, 126.4, 64.3, 39.5, 22.5, 18.3. HRMS (m/z): $[M]^+$ calcd for $C_8H_{14}NO_3$, 172.0968; found, 172.0965.

2-Amino-2-oxoethyl Methacrylate (AMA). 3.17 g of methacrylic acid (37 mmol), 7.72 g of iodoacetamide (42 mmol), and 6.9 g of K_2CO_3 (50 mmol) were added successively to 30 mL of DMF in a 100 mL round-bottom flask. The mixture was heated at 50 °C over 18 h. After this time the mixture was filtered and extracted with brine/ethyl acetate and two times distilled water/ethyl acetate. Drying under reduced pressure afforded 1.98 g of a white solid (yield 38%). ^{1}H NMR (400 MHz, DMSO-d_6) δ (ppm): 7.43 (s, 1H), 7.24 (s, 1H), 6.16 (s, 1H), 5.74 (s, 1H), 4.52 (s, 2H), 1.92 (s, 3H). ^{13}C NMR (500 MHz, MeOD) δ (ppm): 172.6, 167.9, 137.1, 127.2, 63.4, 18.3. HRMS (m/z): $[M]^+$ calcd for $C_6H_{10}NO_3$, 144.0655; found, 144.0652.

Polymer Synthesis. Polymers were synthesized through free radical polymerization. Monomers were dissolved in DMSO and mixed at the desired ratio in a 1.5 mL Eppendorf tube. 0.01 equiv of AIBN was added, and the mixture was placed in a shaker preheated to 70 °C. Once the conversion reached around 25%, the reaction was stopped, and the polymers reprecipitated twice in methanol/water mixtures. Detailed information about synthesized polymers is given in the Supporting Information.

We used NMR spectroscopy for evaluating the polymerization and the resulting polymers: NMR spectra were recorded at 20 °C on a BrukerAvance III 400 spectrometer. First, the feed composition is analyzed. Second, the conversion of the polymerization is monitored.

DOI: 10.1021/acs.langmuir.9b00721
Langmuir 2019, 35, 7009−7017

Finally, the dried polymers are analyzed to obtain the composition of the synthesized polymers.

As an example the copolymerization of 49.5 mol % ethyl methacrylate, 49.5 mol % 2-hydroxyethyl methacrylate, and 1 mol % methacrylic acid is given:

Poly(ethyl methacrylate-co-2-hydroxyethyl methacrylate-co-methacrylic acid). Monomers were dissolved in DMSO at a concentration of 1 M. The three solutions were then mixed in a 1.5 mL Eppendorf tube at the desired ratio to give a total volume of 1 mL:0.495 mL of ethyl methacrylate solution, 0.495 mL of 2-hydroxyethyl methacrylate solution, and 0.01 mL of methacrylic acid solution. NMR analysis gave a feed composition of 50.5 mol % of HEMA, 48.5 mol % of EMA, and 1 mol % of MAA. 0.01 equiv of AIBN in DMSO (40 mg/mL) was then added, and the Eppendorf tube was placed in a shaker preheated to 70 °C. Samples were drawn and analyzed by NMR to monitor conversion. Once the conversion reached 25% (after 28 min), the reaction was stopped by quickly cooling the Eppendorf tube in the fridge. The reaction mixture was added dropwise to a methanol:water (1:4) mixture. After filtration the precipitate was redissolved in a small amount of acetone and reprecipitated twice in methanol–water mixtures. The obtained polymer was dried under vacuum to give 21 mg of a white solid (global yield 17%). NMR gave 50 mol % of HEMA and 50 mol % of EMA (MAA is not clearly identifiable in the final polymer). Molar mass by size exclusion chromatography (SEC, Shimadzu, equipped with triple detection based on light scattering, refractive index, and viscosimetry, using 3 PLgel mixte B columns as stationary and tetrahydrofuran with 0.01 M tetrabutylammonium tetrafluoroborate as mobile phase with a flow rate of 1 mL min^{-1}) for poly(methyl methacrylate-*co*-methacrylic acid): 1% MAA: M_w = 38100, M_w/M_n = 1.35; 5% MAA: M_w = 46800, M_w/M_n = 1.34.

For simplicity the MAA percentage will be omitted from the global composition, i.e., a 1% MAA, 49.5% EMA, 49.5% HEMA copolymer will be noted 1% MAA, 50% EMA, 50% HEMA. ChemDraw 15 Professional was used to calculate octanol–water partition coefficients (log *P* values) for four repeat units (see Supporting Information for details).

Turbidimetry. For turbidimetry measurements the optical density (absorbance) was measured at 400 nm using a Cary 4000 Scan ultraviolet–visible spectrophotometer (Varian). 800 μL of polymer solution in acetonitrile/acetone (4:1 v/v) was placed in a quartz cuvette. Defined volumes of water were then added to this solution followed by mixing and recording of the absorbance. To determine the onset of precipitation, the absorbance was plotted versus the water fraction of the solution.

Preparation of NPs. Solutions of the polymers at 2 g/L in acetonitrile/acetone mixtures (4:1 v/v, up to 15 vol % methanol for polymers with high content of hydrophilic monomers, in special cases with addition of some amount of DMSO extra acetone and methanol) were prepared. For assembly of dye-loaded NPs these solutions contained 10 wt % (relative to the polymer) of the R18/F5-TPB dye salt. These solutions were then added quickly and under stirring (shaking) using a micropipet to a 10-fold volume excess of water or pH 7.4 phosphate buffer at 21 °C. The particle solution was then quickly diluted 5-fold in water.

Characterization of NPs. *Dynamic Light Scattering (DLS).* Size and ζ-potential measurements were performed on a Zetasizer Nano series ZSP (Malvern Instruments S.A.). For size determination each sample was measured 10 times with a run length of 10 s each. The volume average values were used, which are determined by the Zetasizer software (Malvern) based on Mie theory. For ζ-potential determination three successive measurements combining electrophoretic mobility and laser Doppler velocimetry with >10 runs each were performed with an applied potential of ±150 V.

Absorption and emission spectra were recorded on a Cary 4000 Scan ultraviolet–visible spectrophotometer (Varian) and an Edinburgh FS5 spectrofluorometer equipped with a thermostated cell compartment, respectively. Excitation was performed at 530 nm.

Quantum yields (QYs) were determined using a simplified relative method:[37,38] Absorption and emission spectra (λ_{ex} = 530 nm) of the dye-loaded NPs in water and of rhodamine 101 in ethanol as reference were recorded for solutions with peak absorbances below 0.1. The QYs were then calculated according to

$$QY_{NP} = QY_{r101}\frac{F_{NP}A_{NP,530\,nm}n_{H_2O}^{2}}{F_{r101}A_{r101,530\,nm}n_{EtOH}^{2}} \quad (1)$$

where F_{NP} and F_{r101} correspond to the emission intensity integrated over the whole emission wavelength range of the NP and rhodamine 101 solutions, respectively, $A_{x,530\,nm}$ to their absorbance at the excitation wavelength, and n to the refractive indices of the solvents (1.33 for water and 1.36 for ethanol). QY_{r101} is the quantum yield of the standard, rhodamine 101, which was taken to be 0.95.[37,38]

RESULTS AND DISCUSSION

Polymer Design. Copolymers were synthesized through combination of three types of methacrylate monomers: a hydrophilic monomer, bearing either OH or amide groups, a hydrophobic monomer with different length of the alkyl side chain or a benzyl group, and the (potentially) charged methacrylic acid and sulfopropyl methacrylate (MAA and SMA, Scheme 1). Methacrylic acid was used at low fractions of either 1 or 5 mol %; the sulfonate monomer was used only at 1 mol %, which has proven sufficient to control particle size.[19,36] In the reaction mixture, the fraction of the hydrophilic monomers was varied from 0 to 75%. Polymerizations were stopped once the conversion reached about 20% to limit heterogeneities of the composition of the copolymers. The resulting polymers were analyzed with respect to their composition using NMR spectroscopy based on the protons of the CH_2 groups α and β to the ester group (Figure 1 and Table S1). In general, the obtained ratio of the hydrophobic and hydrophilic monomers in the purified polymers corresponded to the feed ratio (within ±2%). In this way, a set of over 50 amphiphilic copolymers with varying types and ratios of the different groups were obtained (Table S1).

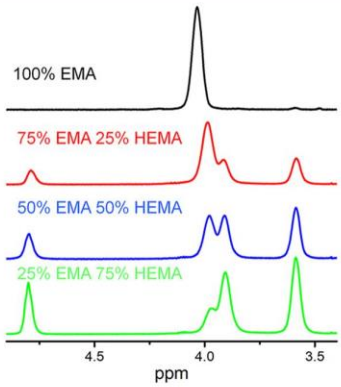

Figure 1. ^{1}H NMR spectra of polymers with different EMA/HEMA ratios. The region used for the determination of the ratios of comonomers is shown. Spectra were recorded in $CDCl_3$ for 100% EMA and in DMSO-d_6 for the others.

Hydrophobicity of Copolymers. The resulting set of amphiphilic polymers were first analyzed with respect to their hydrophobicities/hydrophilicities. A key parameter in nanoprecipitation is the solubility of the polymer in mixtures of organic solvent and water, and especially the water content at which the polymers start aggregating, as it determines the obtained supersaturation, which is the driving force of particle

DOI: 10.1021/acs.langmuir.9b00721
Langmuir 2019, 35, 7009–7017

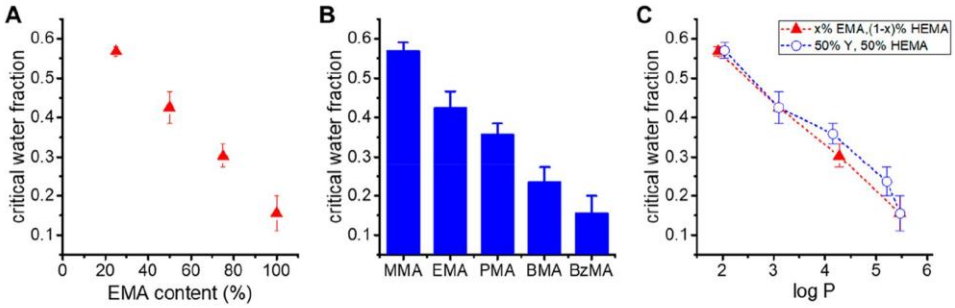

Figure 2. Critical water fraction (volume fraction) leading to precipitation as determined from turbidity measurements as a function of (A) EMA fraction in a EMA/HEMA/MAA copolymer with 1 mol % MAA and (B) the hydrophobic monomer in copolymers with 50 mol % HEMA and 1 mol % MAA. (C) Critical water fraction for the two series of copolymers versus calculated log *P* values. Error bars give the uncertainty of onset of turbidity. Dashed lines are guides to the eye.

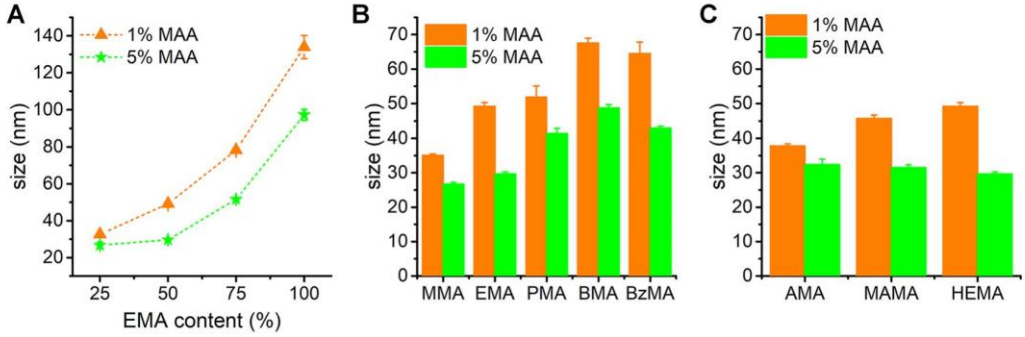

Figure 3. Influence of copolymer composition on size of particles obtained through nanoprecipitation: (A) Influence of ratio of monomers for HEMA/EMA/MAA copolymers. (B) Influence of the type of hydrophobic monomer for copolymers with HEMA (50 mol %) and MAA. (C) Influence of the type of hydrophilic monomer for copolymers with EMA (50 mol %) and MAA. Sizes were determined through dynamic light scattering and give the average of three independent measurements of the volume weighted diameter. Error bars give the standard error of the mean.

formation. We measured this critical water content through turbidity measurements by adding increasing amounts of water to solutions of the different polymers in acetonitrile/acetone mixtures. Results showed a continuous decrease of the critical water fraction with increasing fraction of hydrophobic monomer (Figure 2A). For a given ratio of hydrophilic to hydrophobic monomer, this parameter decreased in the following order: MMA > EMA > PMA > BMA > BzMA (Figure 2B). The critical water fractions correlated well with calculated octanol–water partition coefficients (log *P* values) for the different copolymer compositions (Figure 2C and Figure S1), indicating that the global hydrophobicity determines the solubility of the copolymers in organic solvent/water mixtures and thus the starting point of the precipitation.

Influence of Copolymer Composition on NP Size and Charge. The copolymers were then used for the assembly of nanoparticles through nanoprecipitation. For this, they were dissolved in a water miscible organic solvent (acetonitrile/acetone 4:1, with a small amount of methanol for the least hydrophilic polymers). These solutions were then added quickly to a 10-fold excess of an aqueous solution as the nonsolvent, followed by further dilution, where needed (Scheme 1). The sizes of the resulting NPs were analyzed by dynamic light scattering (DLS), which showed monomodal distributions with PDI values <0.2 for practically all formulations, and confirmed by transmission electron microscopy (Figure S5). For all combinations of monomers, increasing the fraction of the hydrophilic monomer led to a continuous decrease in the size of the resulting particles (Figure 3A). The polymers made only from the hydrophobic monomers (and 1% of MAA) yielded particles of size >100 nm. For the highest fractions of hydrophilic monomers (75 mol %), the sizes decreased to <40 nm. Going from 1 to 5 mol % of the charged MAA yielded a decrease in size of ~20 nm, yet a bit less for the least hydrophobic systems. For the highest ratios of hydrophilic monomers this thus lead to particle sizes of 20–30 nm. A further decrease in size could be obtained by using the sulfonate bearing SMA, even at 1 mol %, leading to particle sizes close to 10 nm (Figure 4A).

The type of hydrophobic monomer also influenced the size of the NPs (Figure 3B, for HEMA as hydrophilic monomer and a 1:1 ratio). For practically all ratios the size increased in the order MMA < EMA < PMA < BMA ~ BzMA, thus following the increase in hydrophobicity of the monomer. Similarly, the type of hydrophilic monomer also had an influence on the size: For a given hydrophobic monomer and monomer ratio, the size increased in the order AMA < MAMA < HEMA (< MEMA) (Figure 3C), again in line with increasing hydrophobicity. However, differences between AMA, MAMA, and HEMA copolymers were relatively small,

DOI: 10.1021/acs.langmuir.9b00721
Langmuir 2019, 35, 7009–7017

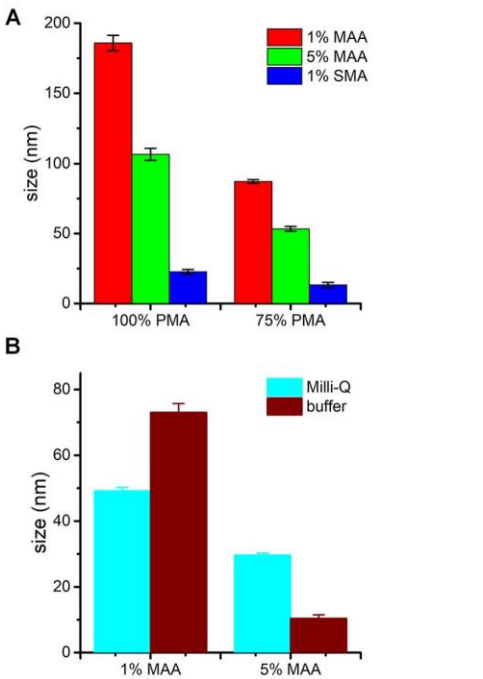

Figure 4. Influence of the nature of the charged group and of the precipitation medium: (A) Size of NPs made from copolymers containing a small fraction of charged monomer (MAA or SMA) and PMA or 75% PMA with 25% HEMA. Prepared in Milli-Q water. (B) Size of NPs formed in either Milli-Q water or 20 mM phosphate buffer at pH 7.4, from HEMA/EMA/MAA copolymers with 50% EMA content and 1 or 5 mol % of charged monomer.

and the trend could even be inversed (or at least vanished) for 5 mol % of charged monomer.

Variation of the polymer composition also influenced the ζ-potential of the formed particles, which was negative for all systems studied here (Tables S3 and S4). Increasing the fraction of hydrophobic monomer resulted in a more negative ζ-potential for the most hydrophobic compositions. Moreover, for a given hydrophilic to hydrophobic ratio the ζ-potential became more negative with increasing hydrophobicity of the alkyl methacrylate monomer, going from −17 mV for MMA to −39 mV for BMA and BzMA (Table S4). As expected, going from 1 to 5% of carboxylate groups also led to a more negative ζ-potential, going for example for 1:1 HEMA/EMA copolymers from −18 mV for 1 mol % MAA to −27 mV for 5 mol % MAA. Even though some of the NPs had ζ-potentials less negative than −30 mV, no signs of aggregation were seen in DLS over the time frame of the experiments (several hours).

The precipitation medium influenced the size of the obtained NPs depending on the amount of charged monomer: In the case of 5 mol % MAA the use of phosphate buffer (pH 7.4) led to a decrease in size compared to Milli-Q water as precipitation medium. In the case of 1 mol % MAA, however, the opposite was true (Figure 4B). At low (1 mol %) fraction of MAA it is likely that the degree of ionization does not significantly differ between both media (at the end of the first precipitation step: [COOH] = 0.0002 mol L^{-1}, log[COOH] = −4.7). The higher ionic strength in the buffer thus decreases the repulsion between polymers/particles, leading to larger particles. At higher (5 mol %) MAA fraction ([COOH] = 0.001 mol L^{-1}, log[COOH] = −4, <pK_a), the ionization should be increased in buffer at higher pH, increasing the number of charged groups per polymer and in consequence the repulsion between chains and/or particles.

Influence of Copolymer Composition on Photophysical Properties. We then analyzed the influence of the copolymer composition on the photophysical properties of dyes encapsulated in these NPs. For this, 10 wt % (relative to the polymer) of the salt of a hydrophobic rhodamine B derivative (R18) with a bulky hydrophobic counterion (perfluorinated tetraphenyl borate, F5-TPB) was added to the organic solution of the polymers. The use of such counterions has been shown to strongly reduce aggregation caused quenching of dyes upon their encapsulation in polymer NPs and thus allowed to assemble very bright fluorescent NPs.[14,16,17] Furthermore, it resulted in ≥95% encapsulation efficiency of the dyes.[36,39] The polymer/dye salt solutions were then used for the formation of NPs through nanoprecipitation in Milli-Q water as before. Absorption spectra showed an increasing relative intensity of the shoulder around 530 nm with respect to the absorption maximum for increasing fraction of hydrophilic monomer, accompanied by a slight blue-shift of the absorption maxima (Figure 5A). In NPs made from

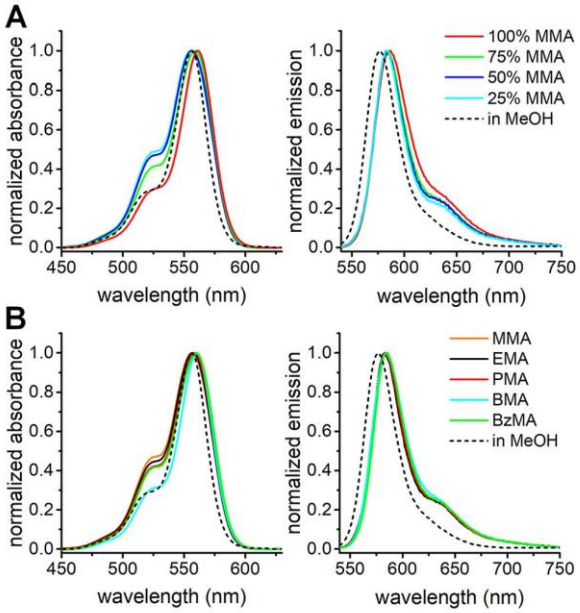

Figure 5. Normalized absorption (left) and emission (right) spectra of NPs made (A) from HEMA/MMA copolymers with different ratios (1 mol % MAA) and (B) from copolymers with 50% HEMA and different hydrophobic monomers (1 mol % MAA). NPs were loaded with 10 wt % of R18/F5-TPB. Excitation was performed at 530 nm.

polymers containing only the hydrophobic monomer (and MAA) the ratio of the shoulder to the maximum was practically the same as for the fluorophore in organic solvent (methanol). This indicates decreasing aggregation of the fluorophores inside the NPs with increasing hydrophobicity of the polymers. The type of hydrophobic monomer influenced how the intensity of the shoulder increased with the fraction of hydrophilic monomer (Figure 5B and Figure S2).

DOI: 10.1021/acs.langmuir.9b00721
Langmuir 2019, 35, 7009−7017

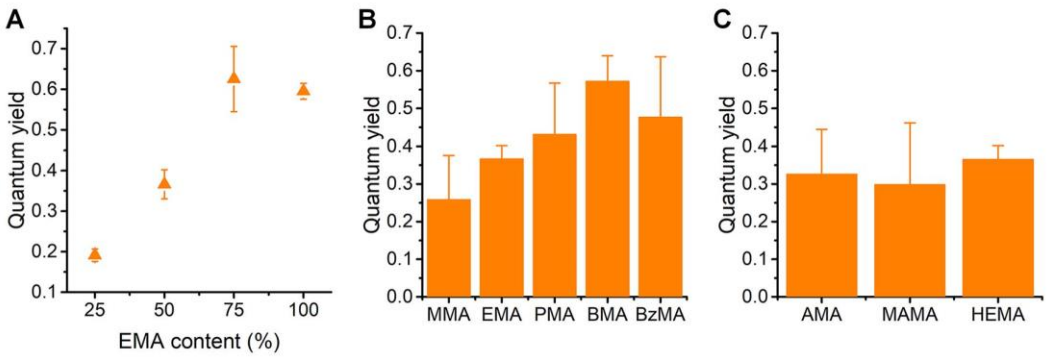

Figure 6. Fluorescence quantum yields of NPs made from different copolymers and loaded with 10 wt % of R18/F5-TPB. (A) Quantum yields vs EMA content for copolymers with HEMA and 1 mol % of MAA. (B) Influence of type of hydrophobic monomer for copolymers with HEMA (50 mol %) and MAA (1 mol %). (C) Influence of type of hydrophilic monomer for copolymers with EMA (50 mol %) and MAA (1 mol %). NPs were prepared in Milli-Q water. Error bars give standard error of the mean over at least three independent experiments.

Emission spectra of the encapsulated dye showed a slight red-shift of the emission maximum with respect to its solution in methanol and the appearance of a small shoulder around 630 nm. With decreasing fraction of hydrophobic monomer in the polymers the emission spectra became slightly narrower and blue-shifted (Figure 5A). On the other hand, the fluorescence quantum yield (QY) increased strongly with increasing fraction of hydrophobic monomer in the polymers (Figure 6). For example, in the case of EMA/HEMA copolymers, the QY increased from <20% for 25 mol % EMA content to >60% for 75 mol % EMA. A further increase in EMA content did not lead to a further increase in the QY. The nature of the hydrophobic monomer also influenced significantly the QY values. For a 1:1 ratio of HEMA and the hydrophobic monomer, the QY increased in the order MMA < EMA < PMA < BzMA ~ BMA. However, the actual dependence of the QY on the monomer ratio was quite different depending on the type of hydrophobic monomer (Figure S3): While for MMA and BzMA a continuous increase with hydrophobic monomer content was observed, the QYs went through a maximum for EMA and PMA at 75 mol % of hydrophobic monomer. For BMA no clear trend was observed. The type of hydrophilic monomer had no significant influence on the QYs (Figure 6C). In the case of QY measurements, we observed a particular variation of the experimental errors (Figure S3). Indeed, the reproducibility was quite good for the systems with the lowest and highest content of hydrophobic monomers, leading to a standard error of the mean of typically <10% (relative). The QY variability within repeated experiments was much larger for intermediate monomer concentrations, and sometimes even two groups of QY values were observed with the standard error of the mean reaching >40% (relative).

■ DISCUSSION

Thus, the nature of the polymer used for nanoprecipitation has a strong influence on the obtained NPs. In Figure 7, the size and the quantum yield of the assembled dye-loaded polymer particles are plotted versus the global hydrophobicity (calculated log P) of the polymer used for their preparation. Concerning the particle size there seemed to be three major influences of the polymer composition: (i) The size increased, in general, with increasing global hydrophobicity of the polymer. (ii) For equal global hydrophobicities, the sizes were smaller for polymers with a larger percentage of charged monomer (MAA). At the same time, the size of NPs made from polymers bearing 1 mol % MAA increased faster with increasing hydrophobicity than for polymers bearing 5 mol % MAA. (iii) Polymers containing only the hydrophobic monomer and charged MAA, but no hydrophilic monomer, gave significantly larger particles. The size of these particles depended less clearly on polymer hydrophobicity.

To understand how the nature of the polymer influences the properties of particles, the mechanism of particle formation in nanoprecipitation has to be considered (Figure 8):[1,11,21] Upon addition of the organic phase to the aqueous phase interdiffusion of the solvents leads to an increasing water content of the organic phase. At some point the polymer (and/or the dye salt) is not soluble anymore in the mixture, leading to supersaturation. This will in turn be the driving force for nucleation. The formed nuclei will then grow through incorporation of polymers and dye salts. In the absence of suitable stabilization, aggregation of the particles will occur. Particle formation in nanoprecipitation is under kinetic control, and so the rates of the different steps will define particle properties as the size distribution. Theoretical approaches are often based on theories developed for crystallization, e.g., classical nucleation theory.[1] Smallest particles will be formed for high nucleation rates, low growth rates, and very low aggregation rates.

The nucleation rate can be estimated by[1,21,22]

$$J = K_1 \exp\left(-\frac{16\pi\gamma^3 v^2}{3k^3T^3[\ln(S)]^2}\right) \tag{2}$$

where γ is the surface tension of the formed nuclei and v the molar volume. The supersaturation S is given by

$$S = \frac{c}{c_{sol}} \tag{3}$$

where c is the actual polymer concentration (in fact, the local effective concentration) and c_{sol} the polymer solubility.[1,22] Thus, at constant temperature (and molar volume of the polymer), the nucleation rate depends largely on supersaturation and surface tension. In particular, it increases with increasing supersaturation and decreases with increasing surface tension. The growth rate also increases with supersaturation. However, different growth types and dependencies

DOI: 10.1021/acs.langmuir.9b00721
Langmuir 2019, 35, 7009−7017

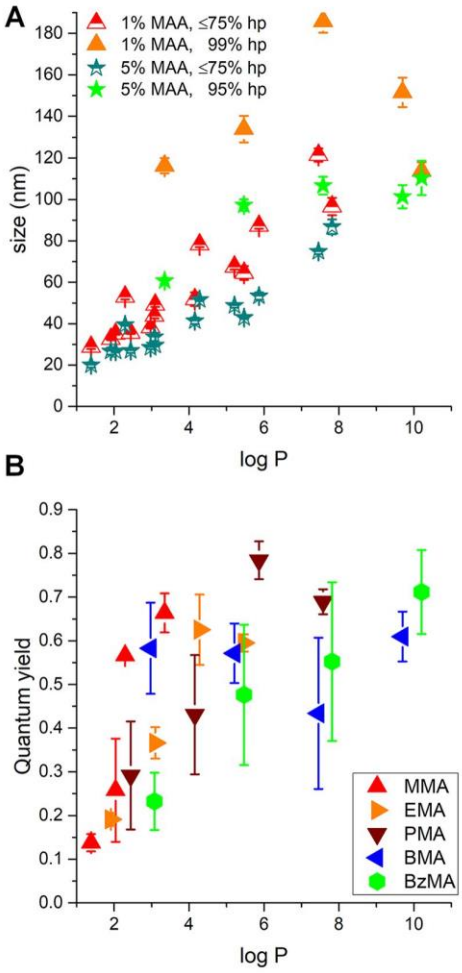

Figure 7. (A) Size and (B) quantum yield of nanoparticles plotted versus calculated log P values of the polymers used for their preparation. In (A) results are given for polymers with 1 mol % (triangles) and 5 mol % (stars) of MAA. Half-filled symbols are used for the NPs made from polymers containing hydrophilic and hydrophobic monomers (≤75% hp), and filled symbols are used for those containing only the hydrophobic monomer (99 or 95% hp) and MAA. In (B) all polymers contained 1 mol % MAA, and 10 wt % R18/F5-TPB were encapsulated. Each series with a given hydrophobic monomer is shown in a distinct color. All NPs were prepared in Milli-Q water. Error bars give standard error of the means over at least three measurements.

have been postulated and observed depending on precipitation conditions and supersaturation regime.[1,21,22,40]

Here, the same conditions of temperature, concentration, and preparation (mixing) have been used for all polymers. The observed differences can thus be attributed to the differences in polymer chemistry through a combination of several effects, assuming that the charged and hydrophilic groups are preferentially situated at the surface of the particles: (i) An increase in the global hydrophobicity and lower fraction of hydrophilic groups should lead to an increase in surface tension of formed nuclei and thus a decrease in nucleation rate. In particular, NPs made from polymers containing only the hydrophobic monomer (and MAA) are much larger than those containing at least a small fraction of hydrophilic monomer,

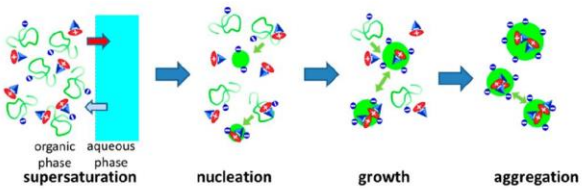

Figure 8. Schematic view of the process of nanoprecipitation of polymers and dye salt yielding dye-loaded polymer NPs: Upon adding the organic phase to the aqueous phase interdiffusion of the solvents occurs, leading to supersaturation of the polymer and/or the dye salt. This triggers nucleation, followed by particle growth and possibly aggregation.

which can reduce surface tension of forming nuclei. This also suggests a high importance of the nucleation rate. (ii) The general trend of increasing size with increasing global hydrophobicity indicates that the ratio of particle growth rate to nucleation rate increases with supersaturation. This is in agreement with earlier observations that the particle size for given polymers increases with polymer concentration.[21,24,33,36] (iii) Charged groups, finally, could contribute to the reduction in surface tension but should also be very effective in preventing aggregation. Furthermore, they could slow down transport of (charged) polymers to the charged surface of growing particles and thus the particle growth.[19,36] In any of these cases, a higher amount of charged groups would result in a reduction of the particle size. Besides charged groups, hydrophilic groups could also contribute to the stabilization of the NPs, possibly through the formation of loops protruding from the particle surface. The presence of increasing amounts of hydrophilic groups on the NP surface is supposed to be at the origin of the decreasing absolute ζ-potential with increasing fraction of hydrophilic groups in the polymers.

In the case of quantum yields we observed a general trend of increasing quantum yield with increasing hydrophobicity of the used polymer (Figure 7B), but the increase was less clearly expressed than for the NP size. Indeed, on a global scale two large groups can be distinguished: (i) Polymers with a log P < 3 gave particles with QYs between 10 and 35% that increased with increasing hydrophobicity. (ii) Polymers with log P > 3 gave NPs with QYs around 60% that varied less clearly with hydrophobicity. Some crossover between these two populations exists, but these were typically the systems showing the largest variations from sample to sample.

Differences notably in the speed of precipitation of the dye salt and the polymer could explain such a behavior.[16] Indeed, it has been shown that the dye salt alone can (nano)precipitate and even form NPs.[41] For the most hydrophilic polymers, precipitation of the dye salt is expected to be faster than that of the polymers. This could then lead to clustering and aggregation of dyes and result in reduced QYs. A similar precipitation speed of both should, on the other hand, lead to a homogeneous distribution of the dyes in the matrix and higher QYs. The highest QYs would then correspond to the best matching of precipitation speeds. The 10 times higher amount of polymer is probably the reason that no clearly defined QY maximum, corresponding to the optimal speed matching, is observed, as the dye salt is simply integrated during polymer precipitation. Variations of the QYs in the second group might also come from distinct influences of the environment

DOI: 10.1021/acs.langmuir.9b00721
Langmuir 2019, 35, 7009−7017

encountered by the dyes inside the particle and thus due to the specific chemical nature of the polymer.

CONCLUSIONS

Here we present a comprehensive study of the influence of the nature of the polymer on the formation of nanoparticles through nanoprecipitation. The composition of the polymers and in particular their global hydrophobicity and the presence of charged groups had a major influence on the sizes of the obtained particles, allowing to control them over a range from ~10 to 200 nm. The specific chemical nature of the building blocks had, on the other hand, at most a minor influence on the particle size. The global hydrophobicity of the polymers also strongly influenced the photophysical properties, in particular the quantum yields of fluorescent dyes encapsulated in the particles, which is linked to their modulated aggregation behavior. Both size of particles and organization of load are thus profoundly affected by the nature of the polymer. These effects are due to the influence of the polymer chemistry on nanoparticle formation in nanoprecipitation: Global hydrophobicity and the presence of hydrophilic and charged groups determine how the polymer behaves on addition of water and thus should influence the kinetics of precipitation. Increasing hydrophobicity led to increasing size, probably due to variations of the ratio of nucleation and growth speeds, which controls the size distribution. At the same time, it led to increasing quantum yields of encapsulated dyes, probably through a better matching of the precipitation of polymer and dye salt. Polymer chemistry thus appears as a powerful tool for tailoring the properties of loaded polymer NPs, notably size and brightness of dye-loaded polymer NPs. The principles developed here should also be of highest interest for the design of aggregation induced emission nanoparticles and drug-delivery systems.

ASSOCIATED CONTENT

Supporting Information

The Supporting Information is available free of charge on the ACS Publications website at DOI: 10.1021/acs.langmuir.9b00721.

Details on the synthesized polymers (polymerization times, conversion, actual composition) and on the assembled NPs (size, ζ-potential, spectra, QYs) (PDF)

AUTHOR INFORMATION

Corresponding Author

*E-mail: reisch@unista.fr.

ORCID

Andrey Klymchenko: 0000-0002-2423-830X

Andreas Reisch: 0000-0003-1154-7637

Notes

The authors declare no competing financial interest.

ACKNOWLEDGMENTS

This work was supported by the Agence National de Recherche JC/JC grant "Supertrack" ANR-16-CE09-0007 and by the European Research Council ERC Consolidator grant BrightSens 648528. The authors thank M. Legros and C. Foussat for size exclusion chromatography and C. Crucifix from the FRISBI platform (ANR-10-INBS-05) for help with electron microscopy.

REFERENCES

(1) Horn, D.; Rieger, J. Organic Nanoparticles in the Aqueous Phase—Theory, Experiment, and Use. *Angew. Chem., Int. Ed.* **2001**, *40* (23), 4330−4361.

(2) Elsabahy, M.; Heo, G. S.; Lim, S.-M.; Sun, G.; Wooley, K. L. Polymeric Nanostructures for Imaging and Therapy. *Chem. Rev.* **2015**, *115* (19), 10967−11011.

(3) Kamaly, N.; Yameen, B.; Wu, J.; Farokhzad, O. C. Degradable Controlled-Release Polymers and Polymeric Nanoparticles: Mechanisms of Controlling Drug Release. *Chem. Rev.* **2016**, *116* (4), 2602−2663.

(4) Ramasamy, T.; Ruttala, H. B.; Gupta, B.; Poudel, B. K.; Choi, H.-G.; Yong, C. S.; Kim, J. O. Smart Chemistry-Based Nanosized Drug Delivery Systems for Systemic Applications: A Comprehensive Review. *J. Controlled Release* **2017**, *258*, 226−253.

(5) Li, N.; Zhao, L.; Qi, L.; Li, Z.; Luan, Y. Polymer Assembly: Promising Carriers as Co-Delivery Systems for Cancer Therapy. *Prog. Polym. Sci.* **2016**, *58*, 1−26.

(6) Oh, J. K.; Park, J. M. Iron Oxide-Based Superparamagnetic Polymeric Nanomaterials: Design, Preparation, and Biomedical Application. *Prog. Polym. Sci.* **2011**, *36* (1), 168−189.

(7) Wolfbeis, O. S. An Overview of Nanoparticles Commonly Used in Fluorescent Bioimaging. *Chem. Soc. Rev.* **2015**, *44*, 4743−4768.

(8) Chen, M.; Yin, M. Design and Development of Fluorescent Nanostructures for Bioimaging. *Prog. Polym. Sci.* **2014**, *39* (2), 365−395.

(9) Rao, J. P.; Geckeler, K. E. Polymer Nanoparticles: Preparation Techniques and Size-Control Parameters. *Prog. Polym. Sci.* **2011**, *36* (7), 887−913.

(10) Lepeltier, E.; Bourgaux, C.; Couvreur, P. Nanoprecipitation and the "Ouzo Effect": Application to Drug Delivery Devices. *Adv. Drug Delivery Rev.* **2014**, *71*, 86−97.

(11) Saad, W. S.; Prud'homme, R. K. Principles of Nanoparticle Formation by Flash Nanoprecipitation. *Nano Today* **2016**, *11* (2), 212−227.

(12) Martínez Rivas, C. J.; Tarhini, M.; Badri, W.; Miladi, K.; Greige-Gerges, H.; Nazari, Q. A.; Galindo Rodríguez, S. A.; Román, R. A.; Fessi, H.; Elaissari, A. Nanoprecipitation Process: From Encapsulation to Drug Delivery. *Int. J. Pharm.* **2017**, *532* (1), 66−81.

(13) Li, K.; Liu, B. Polymer-Encapsulated Organic Nanoparticles for Fluorescence and Photoacoustic Imaging. *Chem. Soc. Rev.* **2014**, *43* (18), 6570−6597.

(14) Reisch, A.; Klymchenko, A. S. Fluorescent Polymer Nanoparticles Based on Dyes: Seeking Brighter Tools for Bioimaging. *Small* **2016**, *12* (15), 1968−1992.

(15) Gu, X.; Kwok, R. T. K.; Lam, J. W. Y.; Tang, B. Z. AIEgens for Biological Process Monitoring and Disease Theranostics. *Biomaterials* **2017**, *146*, 115−135.

(16) Reisch, A.; Trofymchuk, K.; Runser, A.; Fleith, G.; Rawiso, M.; Klymchenko, A. S. Tailoring Fluorescence Brightness and Switching of Nanoparticles through Dye Organization in the Polymer Matrix. *ACS Appl. Mater. Interfaces* **2017**, *9* (49), 43030−43042.

(17) Reisch, A.; Didier, P.; Richert, L.; Oncul, S.; Arntz, Y.; Mély, Y.; Klymchenko, A. S. Collective Fluorescence Switching of Counterion-Assembled Dyes in Polymer Nanoparticles. *Nat. Commun.* **2014**, *5*, 4089.

(18) Andreiuk, B.; Reisch, A.; Lindecker, M.; Follain, G.; Peyriéras, N.; Goetz, J. G.; Klymchenko, A. S. Fluorescent Polymer Nanoparticles for Cell Barcoding In Vitro and In Vivo. *Small* **2017**, *13* (38), 1701582.

(19) Reisch, A.; Heimburger, D.; Ernst, P.; Runser, A.; Didier, P.; Dujardin, D.; Klymchenko, A. S. Protein-Sized Dye-Loaded Polymer Nanoparticles for Free Particle Diffusion in Cytosol. *Adv. Funct. Mater.* **2018**, *28* (48), 1805157.

(20) Trofymchuk, K.; Reisch, A.; Didier, P.; Fras, F.; Gilliot, P.; Mely, Y.; Klymchenko, A. S. Giant Light-Harvesting Nanoantenna for Single-Molecule Detection in Ambient Light. *Nat. Photonics* **2017**, *11* (10), 657.

DOI: 10.1021/acs.langmuir.9b00721
Langmuir 2019, 35, 7009−7017

(21) Lince, F.; Marchisio, D. L.; Barresi, A. A. Strategies to Control the Particle Size Distribution of Poly-ε-Caprolactone Nanoparticles for Pharmaceutical Applications. *J. Colloid Interface Sci.* **2008**, *322* (2), 505−515.
(22) D'Addio, S. M.; Prud'homme, R. K. Controlling Drug Nanoparticle Formation by Rapid Precipitation. *Adv. Drug Delivery Rev.* **2011**, *63* (6), 417−426.
(23) Beck-Broichsitter, M.; Nicolas, J.; Couvreur, P. Solvent Selection Causes Remarkable Shifts of the "Ouzo Region" for Poly(Lactide-Co-Glycolide) Nanoparticles Prepared by Nanoprecipitation. *Nanoscale* **2015**, *7* (20), 9215−9221.
(24) Aubry, J.; Ganachaud, F.; Cohen Addad, J.-P.; Cabane, B. Nanoprecipitation of Polymethylmethacrylate by Solvent Shifting:1. Boundaries. *Langmuir* **2009**, *25* (4), 1970−1979.
(25) Johnson, B. K.; Prud'homme, R. K. Chemical Processing and Micromixing in Confined Impinging Jets. *AIChE J.* **2003**, *49* (9), 2264−2282.
(26) Jara, M. O.; Catalan-Figueroa, J.; Landin, M.; Morales, J. O. Finding Key Nanoprecipitation Variables for Achieving Uniform Polymeric Nanoparticles Using Neurofuzzy Logic Technology. *Drug Delivery Transl. Res.* **2018**, *8* (6), 1797−1806.
(27) Khan, S. A.; Schneider, M. Improvement of Nanoprecipitation Technique for Preparation of Gelatin Nanoparticles and Potential Macromolecular Drug Loading. *Macromol. Biosci.* **2013**, *13* (4), 455−463.
(28) Contado, C.; Vighi, E.; Dalpiaz, A.; Leo, E. Influence of Secondary Preparative Parameters and Aging Effects on PLGA Particle Size Distribution: A Sedimentation Field Flow Fractionation Investigation. *Anal. Bioanal. Chem.* **2013**, *405* (2−3), 703−711.
(29) Geng, J.; Li, K.; Qin, W.; Ma, L.; Gurzadyan, G. G.; Tang, B. Z.; Liu, B. Eccentric Loading of Fluorogen with Aggregation-Induced Emission in PLGA Matrix Increases Nanoparticle Fluorescence Quantum Yield for Targeted Cellular Imaging. *Small* **2013**, *9* (11), 2012−2019.
(30) Galindo-Rodriguez, S.; Allemann, E.; Fessi, H.; Doelker, E. Physicochemical Parameters Associated with Nanoparticle Formation in the Salting-out, Emulsification-Diffusion, and Nanoprecipitation Methods. *Pharm. Res.* **2004**, *21* (8), 1428−1439.
(31) de Oliveira, A. M.; Jäger, E.; Jäger, A.; Stepánek, P.; Giacomelli, F. C. Physicochemical Aspects behind the Size of Biodegradable Polymeric Nanoparticles: A Step Forward. *Colloids Surf., A* **2013**, *436*, 1092−1102.
(32) Bilati, U.; Allémann, E.; Doelker, E. Development of a Nanoprecipitation Method Intended for the Entrapment of Hydrophilic Drugs into Nanoparticles. *Eur. J. Pharm. Sci.* **2005**, *24* (1), 67−75.
(33) Beck-Broichsitter, M.; Rytting, E.; Lebhardt, T.; Wang, X.; Kissel, T. Preparation of Nanoparticles by Solvent Displacement for Drug Delivery: A Shift in the "Ouzo Region" upon Drug Loading. *Eur. J. Pharm. Sci.* **2010**, *41* (2), 244−253.
(34) Legrand, P.; Lesieur, S.; Bochot, A.; Gref, R.; Raatjes, W.; Barratt, G.; Vauthier, C. Influence of Polymer Behaviour in Organic Solution on the Production of Polylactide Nanoparticles by Nanoprecipitation. *Int. J. Pharm.* **2007**, *344* (1−2), 33−43.
(35) Stepanyan, R.; Lebouille, J. G. J. L.; Slot, J. J. M.; Tuinier, R.; Stuart, M. A. C. Controlled Nanoparticle Formation by Diffusion Limited Coalescence. *Phys. Rev. Lett.* **2012**, *109* (13), 138301.
(36) Reisch, A.; Runser, A.; Arntz, Y.; Mély, Y.; Klymchenko, A. S. Charge-Controlled Nanoprecipitation as a Modular Approach to Ultrasmall Polymer Nanocarriers: Making Bright and Stable Nanoparticles. *ACS Nano* **2015**, *9* (5), 5104−5116.
(37) Würth, C.; Geißler, D.; Behnke, T.; Kaiser, M.; Resch-Genger, U. Critical Review of the Determination of Photoluminescence Quantum Yields of Luminescent Reporters. *Anal. Bioanal. Chem.* **2015**, *407* (1), 59−78.
(38) Würth, C.; Grabolle, M.; Pauli, J.; Spieles, M.; Resch-Genger, U. Comparison of Methods and Achievable Uncertainties for the Relative and Absolute Measurement of Photoluminescence Quantum Yields. *Anal. Chem.* **2011**, *83* (9), 3431−3439.
(39) Andreiuk, B.; Reisch, A.; Bernhardt, E.; Klymchenko, A. S. Fighting Aggregation-Caused Quenching and Leakage of Dyes in Fluorescent Polymer Nanoparticles: Universal Role of Counterion. *Chem. - Asian J.* **2019**, *14*, 836.
(40) Mahajan, A. J.; Kirwan, D. J. Nucleation and Growth Kinetics of Biochemicals Measured at High Supersaturations. *J. Cryst. Growth* **1994**, *144* (3), 281−290.
(41) Shulov, I.; Oncul, S.; Reisch, A.; Arntz, Y.; Collot, M.; Mely, Y.; Klymchenko, A. S. Fluorinated Counterion-Enhanced Emission of Rhodamine Aggregates: Ultrabright Nanoparticles for Bioimaging and Light-Harvesting. *Nanoscale* **2015**, *7* (43), 18198−18210.

DOI: 10.1021/acs.langmuir.9b00721
Langmuir 2019, 35, 7009−7017

Supporting Information For

Controlling Size and Fluorescence of Dye-Loaded Polymer Nanoparticles through Polymer Design

Vitalii Rosiuk, Anne Runser, Andrey Klymchenko, Andreas Reisch*

Laboratoire de Bioimagerie et Pathologies, CNRS UMR 7021, Université de Strasbourg, Faculté de Pharmacie, 67401 Illkirch Cedex, France.

Table S1. Overview of synthesized polymers with polymerization time and conversion, AND amounts of monomers in the polymerization mixture before polymerization and in the final purified polymer as determined by NMR.

	Hydrophilic monomer	Amount (mol%)	Hydrophobic monomer	Amount (mol%)	Charged monomer	Amount (mol%)	Polymerization time (min)	Conversion (%)	Amount of hydrophilic monomer in final polymer (%)	Amount of hydrophobic monomer in final polymer (%)
1	HEMA	0	MMA	100	MAA	1	60	33	0	100
2	HEMA	27	MMA	73	MAA	1	30	20	26	74
3	HEMA	52	MMA	48	MAA	1	30	25	53	47
4	HEMA	76	MMA	24	MAA	1	30	29	75	25
5	HEMA	0	MMA	100	MAA	5	60	36	0	100
6	HEMA	24	MMA	76	MAA	5	30	23	25	75
7	HEMA	50	MMA	50	MAA	5	30	24	48	52
8	HEMA	76	MMA	24	MAA	5	30	27	75	25
9	HEMA	0	EMA	100	MAA	1	60	36	0	100
10	HEMA	26	EMA	74	MAA	1	28	28	30	70
11	HEMA	51	EMA	49	MAA	1	28	29	50	50
12	HEMA	75	EMA	25	MAA	1	28	30	77	23
13	HEMA	0	EMA	100	MAA	5	28	<10	0	100
14	HEMA	25	EMA	75	MAA	5	28	24	25	75
15	HEMA	50	EMA	50	MAA	5	28	29	51	49
16	HEMA	74	EMA	26	MAA	5	28	32	76	24
17	HEMA	0	PMA	100	MAA	1	60	39	0	100
18	HEMA	26	PMA	74	MAA	1	30	20	22	78
19	HEMA	50	PMA	50	MAA	1	30	31	50	50
20	HEMA	74	PMA	26	MAA	1	30	35	76	24
21	HEMA	0	PMA	100	MAA	5	60	38	0	100
22	HEMA	26	PMA	74	MAA	5	30	22	22	78
23	HEMA	49	PMA	51	MAA	5	30	24	49	51
24	HEMA	74	PMA	26	MAA	5	30	29	76	24
25	HEMA	0	BMA	100	MAA	1	60	17	0	100
26	HEMA	24	BMA	76	MAA	1	30	19	20	80
27	HEMA	48	BMA	52	MAA	1	30	30	43	57
28	HEMA	72	BMA	28	MAA	1	30	33	74	26
29	HEMA	0	BMA	100	MAA	5	60	11	0	100
30	HEMA	24	BMA	76	MAA	5	30	10	20	80
31	HEMA	48	BMA	52	MAA	5	30	29	43	57
32	HEMA	72	BMA	28	MAA	5	30	31	75	25

Table S1. continued

	Hydrophilic monomer	Amount (mol%)	Hydrophobic monomer	Amount (mol%)	Charged monomer	Amount (mol%)	Polymerization time (min)	Conversion (%)	Amount of hydrophilic monomer in final polymer (%)	Amount of hydrophobic monomer in final polymer (%)
33	HEMA	0	BzMA	100	MAA	1	45	43	0	100
34	HEMA	27	BzMA	73	MAA	1	30	34	30	70
35	HEMA	51	BzMA	49	MAA	1	30	36	52	48
36	HEMA	75	BzMA	25	MAA	1	30	37	75	25
37	HEMA	0	BzMA	100	MAA	5	45	40	0	100
38	HEMA	26	BzMA	74	MAA	5	30	30	31	69
39	HEMA	51	BzMA	49	MAA	5	30	33	52	48
40	HEMA	74	BzMA	26	MAA	5	30	35	74	26
41	AMA	22	EMA	78	MAA	1	30	21	21	79
42	AMA	45	EMA	55	MAA	1	30	27	45	55
43	AMA	72	EMA	28	MAA	1	30	23	72	28
44	AMA	21	EMA	79	MAA	5	30	20	21	79
45	AMA	47	EMA	53	MAA	5	30	18	47	53
46	AMA	73	EMA	27	MAA	5	30	24	70	30
47	MAMA	23	EMA	77	MAA	1	30	22	22	78
48	MAMA	46	EMA	54	MAA	1	30	25	46	54
49	MAMA	72	EMA	28	MAA	1	30	30	72	28
50	MAMA	45	EMA	55	MAA	5	30	25	45	55
51	MEMA	26	PMA	74	MAA	1	20	<10	26	74
52	MEMA	54	PMA	46	MAA	1	20	<10	54	46
53	MEMA	71	PMA	29	MAA	1	20	10	74	26
54	MEMA	100	PMA	0	MAA	1	20	21	100	0
55	MEMA	31	PMA	69	MAA	5	20	10	31	69
56	MEMA	49	PMA	51	MAA	5	20	<10	49	51
57	MEMA	72	PMA	28	MAA	5	20	10	72	28
58	MEMA	100	PMA	0	MAA	5	20	17	100	0
59	HEMA	0	PMA	100	SMA	1	50	40	0	100
60	HEMA	25	PMA	75	SMA	1	40	38	25	75

Estimation of octanol-water partition coefficients (log P values):

Log P values were estimated using the ChemDraw 15 Professional software. For this the structure of four linked repeat units was drawn representing the relative percentages of the hydrophilic and hydrophobic monomers. Log P values are then obtained from the built-in function ClogP, which is based on Molecular Networks' cheminformatics platform MOSES.

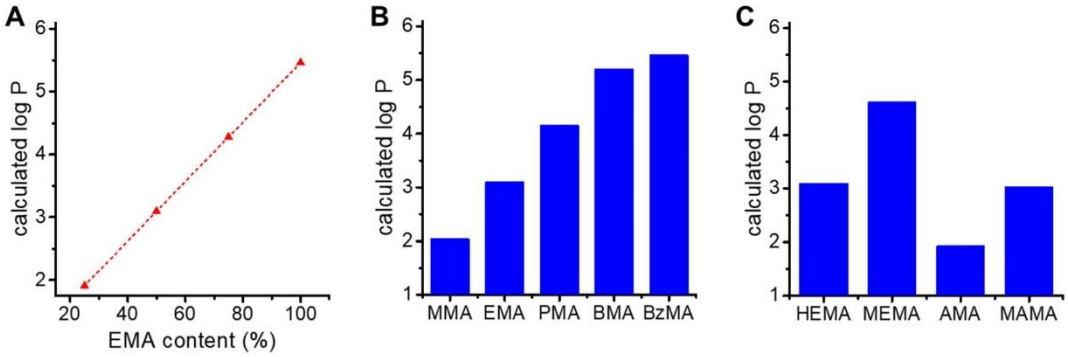

Figure S1. Calculated log P values for different copolymer compositions: (A) EMA/HEMA copolymers with varying EMA (and HEMA) content. (B) Copolymers with 50% HEMA and different hydrophobic monomers. (C) Copolymers with 50% EMA and different hydrophilic monomers.

Table S2. Sizes of prepared particles as analyzed by DLS. Volume average and standard error of the mean for at least 3 measurements are given.

Hydrophilic monomer	Amount (mol%)	Hydrophobic monomer	Amount (mol%)	Charged monomer	Amount (mol%)	Size (nm) for precipitation in	
						MilliQ	Buffer[1)]
HEMA	0	MMA	100	MAA	1	116 ± 4	508 ± 51
HEMA	26	MMA	74	MAA	1	53 ± 2	123 ± 7
HEMA	53	MMA	47	MAA	1	35 ± 1	59 ± 3
HEMA	76	MMA	24	MAA	1	28 ± 2	82 ± 3
HEMA	0	MMA	100	MAA	5	60 ± 2	15 ± 3
HEMA	25	MMA	75	MAA	5	39 ± 1	17 ± 2
HEMA	48	MMA	52	MAA	5	26 ± 1	13 ± 2
HEMA	75	MMA	25	MAA	5	20 ± 2	10 ± 3
HEMA	0	EMA	100	MAA	1	133 ± 7	142 ± 4
HEMA	30	EMA	70	MAA	1	78 ± 2	119 ± 7
HEMA	50	EMA	50	MAA	1	49 ± 2	73 ± 3
HEMA	77	EMA	23	MAA	1	32 ± 2	71 ± 3
HEMA	0	EMA	100	MAA	5	97 ± 3	22 ± 2
HEMA	25	EMA	75	MAA	5	51 ± 1	14 ± 2
HEMA	51	EMA	49	MAA	5	29 ± 2	10 ± 2
HEMA	76	EMA	24	MAA	5	26 ± 2	14 ± 2
HEMA	0	PMA	100	MAA	1	185 ± 6	270 ± 40
HEMA	22	PMA	78	MAA	1	51 ±4	74 ± 3
HEMA	50	PMA	50	MAA	1	87 ± 2	133 ± 41
HEMA	76	PMA	24	MAA	1	35 ± 2	77 ± 3
HEMA	0	PMA	100	MAA	5	106 ± 5	32 ± 1
HEMA	22	PMA	78	MAA	5	53 ± 2	24 ± 2
HEMA	49	PMA	51	MAA	5	41 ± 2	13 ± 2
HEMA	76	PMA	24	MAA	5	27 ± 2	13 ± 2
HEMA	0	BMA	100	MAA	1	133 ± 7	187 ± 13
HEMA	20	BMA	80	MAA	1	78 ± 2	176 ± 8
HEMA	43	BMA	57	MAA	1	49 ± 2	103 ± 4
HEMA	74	BMA	26	MAA	1	32 ± 2	88 ± 3
HEMA	0	BMA	100	MAA	5	97 ± 3	30 ± 2
HEMA	20	BMA	80	MAA	5	51 ± 2	25 ± 2
HEMA	43	BMA	57	MAA	5	29 ± 1	17 ± 1
HEMA	75	BMA	25	MAA	5	26 ± 2	14 ± 2

Table S2. continued

Hydrophilic monomer	Amount (mol%)	Hydrophobic monomer	Amount (mol%)	Charged monomer	Amount (mol%)	Size (nm) for precipitation in	
						MilliQ	buffer
HEMA	0	BzMA	100	MAA	1	113 ± 5	163 ± 12
HEMA	30	BzMA	70	MAA	1	96 ± 5	600 ± 99
HEMA	52	BzMA	48	MAA	1	64 ± 4	480 ± 82
HEMA	75	BzMA	25	MAA	1	43 ± 2	77 ± 4
HEMA	0	BzMA	100	MAA	5	110 ± 9	243 ± 36
HEMA	31	BzMA	69	MAA	5	86 ± 4	102 ± 41
HEMA	52	BzMA	48	MAA	5	42 ± 1	22 ± 5
HEMA	74	BzMA	26	MAA	5	33 ± 3	14 ± 2
AMA	21	EMA	79	MAA	1	27± 2	261± 90
AMA	45	EMA	55	MAA	1	37 ± 2	1100 ± 54
AMA	72	EMA	28	MAA	1	50 ± 1	1100 ± 60
AMA	21	EMA	79	MAA	5	24 ± 2	14 ± 2
AMA	47	EMA	53	MAA	5	32 ± 2	(<10)
AMA	70	EMA	30	MAA	5	33 ± 2	(<10)
MAMA	22	EMA	78	MAA	1	67 ± 3	840 ± 150
MAMA	46	EMA	54	MAA	1	45 ± 2	118 ± 3
MAMA	72	EMA	28	MAA	1	35 ± 3	700 ± 146
MAMA	45	EMA	55	MAA	5	31 ± 2	15 ± 2
MEMA	26	PMA	74	MAA	1	153 ± 8	107 ± 4
MEMA	54	PMA	46	MAA	1	120 ± 5	79 ± 3
MEMA	74	PMA	26	MAA	1	110 ± 3	93 ± 3
MEMA	100	PMA	0	MAA	1	96 ± 3	80 ± 3
MEMA	31	PMA	69	MAA	5	114 ± 3	121 ± 3
MEMA	49	PMA	51	MAA	5	87 ± 2	22 ± 2
MEMA	72	PMA	28	MAA	5	79 ± 2	21 ± 2
MEMA	100	PMA	0	MAA	5	66 ± 2	16 ± 2
HEMA	0	PMA	100	SMA	1	23 ± 2	
HEMA	22	PMA	78	SMA	1	13 ±2	

[1)] In the case of samples giving sizes < 15 nm the measurement quality was limited due to the low scattering signal at the used concentrations.

Table S3. ζ–potentials of nanoparticles prepared in MilliQ water from copolymers of EMA and HEMA with 1 mol% MAA. Measurements were performed in triplicate, errors give the standard error of the mean.

Copolymer composition		ζ–potential (mV)
HEMA	EMA	
25	75	-22 ± 4
50	50	-18 ± 6
75	25	-25 ± 6
100	0	-31 ± 2

Table S4. ζ–potentials of nanoparticles prepared in MilliQ water from copolymers of HEMA with different hydrophobic monomers in a 1:1 ratio. Measurements were performed in triplicate, errors give the standard error of the mean.

Copolymer composition			ζ–potential (mV)
hydrophobic	hydrophilic	MAA	
MMA	HEMA	1%	-17 ± 5
EMA	HEMA	1%	-18 ± 6
PMA	HEMA	1%	-28 ± 2
BMA	HEMA	1%	-39 ± 4
BzMA	HEMA	1%	-39 ± 3
EMA	HEMA	5%	-27 ± 3

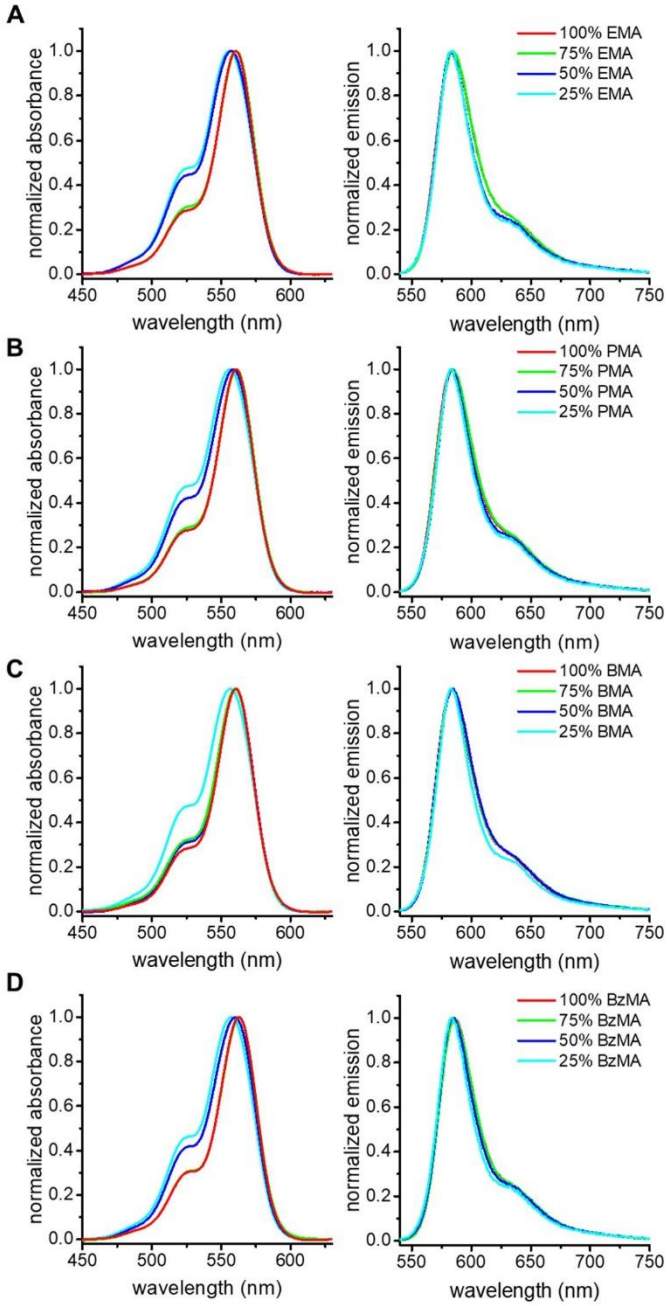

Figure S2. Normalized absorption (left) and emission (right) spectra of NPs made from copolymers with 50% HEMA and different hydrophobic monomers (1 mol% MAA) and loaded with 10 wt% of R18/F5-TPB: (A) EMA, (B) PMA, (C) BMA, (D) BzMA. Excitation was performed at 530 nm.

Table S5. Quantum yields of nanoparticles prepared from different polymers with 10 wt% R18/F5-TPB. The average of at least three measurements with the corresponding standard error of the mean is given.

Hydrophilic monomer	Amount (mol%)	Hydrophobic monomer	Amount (mol%)	Charged monomer	Amount (mol%)	Quantum yield
HEMA	0	MMA	100	MAA	1	0.66 ± 0.05
HEMA	26	MMA	74	MAA	1	0.57 ± 0.01
HEMA	53	MMA	47	MAA	1	0.26 ± 0.12
HEMA	76	MMA	24	MAA	1	0.14 ± 0.02
HEMA	0	EMA	100	MAA	1	0.60 ± 0.02
HEMA	30	EMA	70	MAA	1	0.62 ± 0.08
HEMA	50	EMA	50	MAA	1	0.37 ± 0.04
HEMA	77	EMA	23	MAA	1	0.20 ± 0.02
HEMA	0	PMA	100	MAA	1	0.69 ± 0.03
HEMA	50	PMA	50	MAA	1	0.78 ± 0.04
HEMA	22	PMA	78	MAA	1	0.43 ± 0.14
HEMA	76	PMA	24	MAA	1	0.29 ± 0.13
HEMA	0	BMA	100	MAA	1	0.61 ± 0.06
HEMA	20	BMA	80	MAA	1	0.43 ± 0.18
HEMA	43	BMA	57	MAA	1	0.57 ± 0.07
HEMA	74	BMA	26	MAA	1	0.58 ± 0.11
HEMA	0	BzMA	100	MAA	1	0.71 ± 0.10
HEMA	30	BzMA	70	MAA	1	0.55 ± 0.19
HEMA	52	BzMA	48	MAA	1	0.48 ± 0.17
HEMA	75	BzMA	25	MAA	1	0.23 ± 0.07
AMA	21	EMA	79	MAA	1	0.59 ± 0.09
AMA	45	EMA	55	MAA	1	0.32 ± 0.12
AMA	72	EMA	28	MAA	1	0.22 ± 0.13
MAMA	22	EMA	78	MAA	1	0.59 ± 0.09
MAMA	46	EMA	54	MAA	1	0.30 ± 0.17
MAMA	72	EMA	28	MAA	1	0.23 ± 0.10
MEMA	26	PMA	74	MAA	1	0.65 ± 0.07
MEMA	54	PMA	46	MAA	1	0.85 ± 0.16
MEMA	74	PMA	26	MAA	1	0.78 ± 0.08
MEMA	100	PMA	0	MAA	1	0.75 ± 0.1

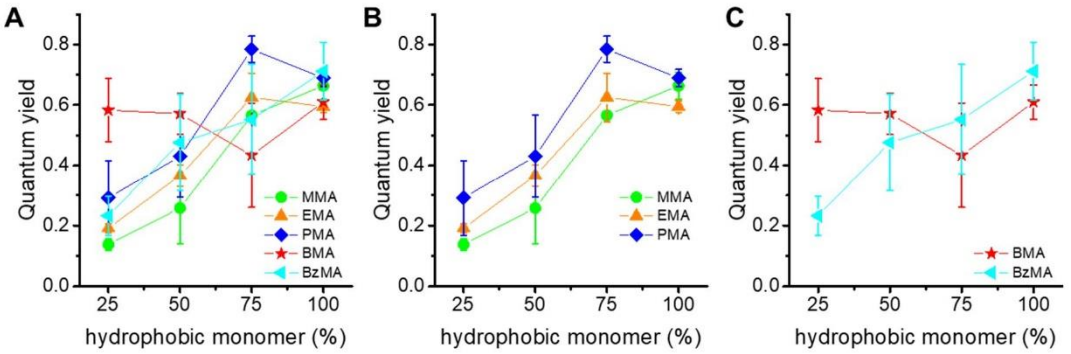

Figure S3. Fluorescence quantum yields of NPs made from different copolymers and loaded with 10 wt% of R18/F5-TPB (A: all polymers, B and C: selected series for better visibility). Quantum yields are plotted *vs* content of the hydrophobic monomer for copolymers with HEMA and 1 mol% of MAA. NPs were prepared in MilliQ water. Error bars give standard error of the mean over at least three independent experiments.

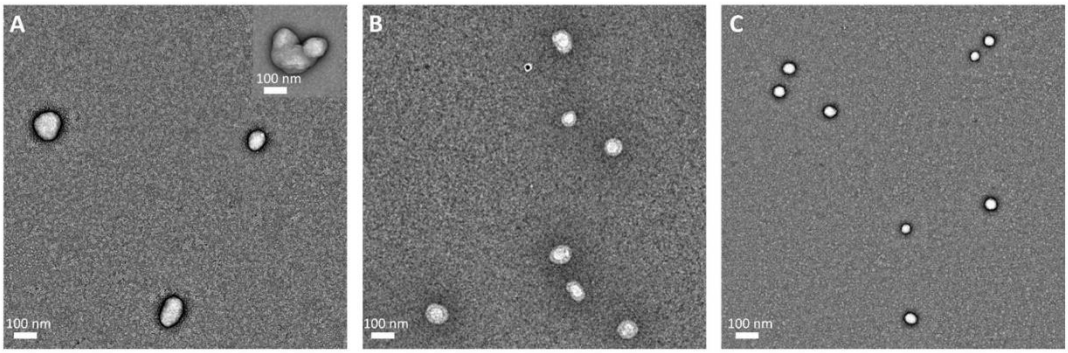

Figure S4. Transmission electron microscopy (TEM) images of NPs made from EMA/HEMA copolymers with 1 mol% MAA (A) 100% EMA (inset: example of aggregates), (B) 75% EMA, (C) 50% EMA in MilliQ water. NPs were deposited onto carbon-coated copper rhodium electron microscopy grids and treated for 1 min with a 2% uranyl acetate solution for staining.

UNIVERSITÉ DE STRASBOURG

EDSC
École Doctorale des Sciences Chimiques

Anne RUNSER

Nanoparticules de polymères fluorescentes, ultrapetites, ultrabrillantes et furtives pour le suivi intracellulaire et l'imagerie super-résolutive

Résumé

L'observation de processus biologique à l'échelle moléculaire est possible aujourd'hui grâce à l'imagerie de fluorescence. Cependant suivre des biomolécules individuelles à l'intérieur de cellules requiert des sondes très brillantes, capables de se déplacer dans tout le cytosol en interagissant uniquement avec la cible intracellulaire. Les nanoparticules de polymères fluorescentes ont l'avantage d'être biocompatibles, flexibles en plus d'être très brillantes. Dans ce projet de thèse, nous avons développé des nanoparticules de polymères chargées en fluorophores en tant que sondes pour l'imagerie intracellulaire. Nous avons ainsi élaboré une méthode permettant de contrôler la taille des particules et d'obtenir des particules avec un diamètre < 9 nm. La brillance de ces nanoparticules à base de complexes de lanthanides ou de rhodamine facilite leur détection et permet en même temps de diminuer la phototoxicité sur les cellules vivantes. D'un autre côté, la conception de nanoparticules zwittérioniques a permis de limiter les interactions non spécifiques dans le cytoplasme sans augmenter le diamètre des particules. Enfin, la fonctionnalisation de ces particules de polymères offre la possibilité d'être des outils très performants pour le suivi de biomolécules intracellulaires.

Mots-clés : nanoparticules de polymères fluorescentes, zwittérion, furtives, ultrapetites, imagerie intracellulaire

Résumé en anglais

Visualization of biological processes at molecular level is made possible by fluorescence imaging. However tracking single biomolecules inside cells requires very bright probes capable to move in the whole cytosol and interacting exclusively with the intracellular target. Fluorescent polymer nanoparticles have the advantages of the biocompatibility and flexibility in addition to be very bright. In this thesis project, we developed dye-loaded polymer nanoparticles for intracellular imaging. We then developed a method allowing to control size of particles and to reach particle sizes < 9 nm. The brightness of the nanoparticles loaded with lanthanide complexes or rhodamine made easier their detection and decreased their phototoxicity in living cells. On the other hand, the design of zwitterionic nanoparticles was able to prevent non-specific interactions in the cytosol without increasing the particle diameter. Finally, the functionalisation of these polymer nanoparticles offered the possibility to be very powerful tools for tracking intracellular biomolecules.

Keywords: polymer fluorescent nanoparticles, zwitterion, stealth, utlrasmall, intracellular imaging